Ultracold Atoms in Traps: Theoretical Approaches, Resonances, and Quantum Simulations

D I S S E R T A T I O N

zur Erlangung des akademischen Grades
doctor rerum naturalium
(Dr. rer. nat.)
im Fach Physik

eingereicht an der
Mathematisch-Naturwissenschaftlichen Fakultät
der Humboldt-Universität zu Berlin

von

Dipl.-Phys. Simon Johannes Sala

Präsident der Humboldt-Universität zu Berlin:
Prof. Dr. Jan-Hendrik Olbertz

Dekan der Mathematisch-Naturwissenschaftlichen Fakultät:
Prof. Dr. Elmar Kulke

Gutachter/innen:
1. Prof. Dr. Alejandro Saenz
2. Prof. Brett Esry, Ph.D.
3. Prof. Dr. Wolfgang Nolting

Tag der mündlichen Prüfung: 23. März 2016

Abstract

This thesis aims for a theoretical description of ultracold trapped atoms. The main focus are resonance phenomena due to the coupling of center-of-mass and relative motion, the development of a theoretical approach to treat ultracold few-body systems in versatile trap potentials, and the quantum simulation of attosecond physics with ultracold atoms.

By developing a model and applying it together with *ab initio* calculations to a system of two ultracold atoms in anharmonic trap potentials, it is shown that recent experimental findings of particle loss and heating in a many-body system of ultracold Cesium atoms and the coherent molecule formation in a two-body system of distinguishable ^{6}Li atoms are caused by so called inelastic confinement-induced resonances. Additionally, a thorough validation of the model and an investigation of these resonances in multi-well systems is provided. The findings provide unique evidence for the origin of the detected loss features and hereby resolve a controversial debate.

Motivated by the momentous anharmonicity-induced effects in two-body systems, a theoretical approach is developed that allows for the computational treatment of a variable number of ultracold fermionic atoms in trap potentials of almost arbitrary shape. The method is validated to reproduce the essential scattering properties of ultracold atoms confined in an isotropic harmonic trap. The approach uses concepts of electronic-structure theory by performing a mapping that replaces electrons by atoms and the Coulomb potential of the nuclei by an external trap potential.

Finally, the mapping of electrons in an atom or molecule on ultracold trapped atoms is extended by a magnetic-field gradient that results in a linear time-dependent term in the Hamiltonian. This Hamiltonian is shown to be formally equivalent to the strong-field Hamiltonian of attosecond physics. The mapping builds the basis of a versatile quantum simulator. An experimental realization of the quantum simulator is proposed. Based on this proposal it is demonstrated under the use of experimentally realistic parameters that the quantum simulator is capable of reproducing accurately essential effects of strong-field physics such as above-threshold ionization, rescattering, or frustrated tunneling ionization in accordance to the results obtained for atomic hydrogen exposed to a strong laser pulse. In fact, it is shown that the very popular strong-field approximation is more accurately fulfilled for the simulator system that thus delivers the first method to stringently probe its validity for many-electron atoms and molecules. Hence, due to the flexibility of ultracold atom experiments, the quantum simulator offers a novel tool to systematically deepen the understanding of many-body strong-field physics where classical computations fail and the accuracy of widespread simplified models is unknown.

Zusammenfassung

Diese Dissertation widmet sich der theoretischen Beschreibung ultrakalter Atome in einem optischen Einschluss. Das Hauptaugenmerk liegt hierbei auf inelastischen Resonanzen, die durch die Kopplung von Schwerpunkts- und Relativbewegung durch Anharmonizitäten im externen Potenzial Zustande kommen, der Entwicklung einer Methode zur theoretischen Beschreibung von ultrakalten Wenigteilchensystemen in einem vielseitigen Einschlusspotenzial und der Quantensimulation von Attosekundenphysik mit ultrakalten Atomen.

Die Anwendung eines entwickelten Modells und ab initio Rechnungen auf ein System bestehend aus zwei ultrakalten Atomen in anharmonischen Fallen liefert eine Erklärung für die kürzlichen experimentellen Beobachtungen von Teilchenverlusten in einem Vielteilchensystem von ultrakalten ^{133}Cs Atomen und kohärenter Molekülbildung in einem Zweiteilchensystem aus unterscheidbaren ^{6}Li Atomen. Beide Effekte lassen sich eindeutig auf inelastische einschlussinduzierte Resonanzen zurückführen und lösen hierdurch eine anhaltenden Debatte über den Ursprung der beobachteten Teilchenverluste auf. Darüber hinaus wird das Modell sorgfältig validiert und eine Untersuchung der Resonanzen im Vergleich zu neuesten experimentellen Ergebnissen in Mehrmuldenfallen präsentiert.

Motiviert durch die bedeutsamen Effekte basierend auf Anharmonizitäten im externen Potential, wird eine numerische Methode zur Beschreibung einer variablen Anzahl ultrakalter fermionischer Atome entwickelt. Das externe Potential kann durch beliebige Polynome approximiert werden und ist somit sehr flexibel. Die Anwendbarkeit der Methode wird im Vergleich zur analytischen Lösung von zwei ultrakalten Atomen in einem harmonischen Einschluss validiert. Die essentiellen Streueigenschaften können reproduziert werden. Die Methode bedient sich bewährter Verfahren der elektronischen Strukturrechnung und einer formalen Identifizierung von Elektronen mit Atomen und der Ersetzung des Kernpotenzials durch ein externes optisches Potenzial.

Schließlich wird die formale Abbildung von Elektronen im Atom (oder Molekül) zu ultrakalten Atomen in einem externen Einschluss um einen linearen zeitabhängigen Term in Form eines Magnetfeldgradienten erweitert. Der resultierende Hamiltonoperator für das ultrakalte System wird hierdurch formal äquivalent zu einem der Starkfeldphyik. Diese Abbildung formt das Herzstück eines Quantensimulators für die Attosekundenphysik. Es wird eine experimentelle Realisierung des Quantensimulators vorgeschlagen. Basierend auf dieser Realisierung wird gezeigt, dass mit dem Quantensimulator unter Verwendung experimentell realistischer Parameter wesentliche Effekte der Starkfeldphysik, wie etwa der charakteristischen Ionisierung im Multiphotonenregime, der Rückstreuphysik im adiabatischen Regime oder frustrierte Tunnelionisierung akkurat reproduziert werden können im Vergleich zum Wasserstoffatom in einem starken Laserpuls. Es kann sogar demonstriert werden, dass die Starkfeldnäherung, die extrem populär ist in der theoretischen Beschreibung von Starkfeldsystemen, besser für den Quantensimulator erfüllt ist. Hierdurch avanciert dieser zu einem wertvollen Werkzeug um die Gültigkeit der

Starkfeldnährung für Attosekundensysteme zu überprüfen. Durch die mannigfaltige Realisierbarkeit experimenteller ultrakalter Systeme kann der vorgeschlagene Quantensimulator benutzt werden um das grundlegende Verständnis des Verhaltens von Vielteilchenstarkfeldsystemen systematisch zu vertiefen, wo es mit klassischen Rechnungen nicht mehr möglich ist und die Gültigkeit vereinfachter Modelle unbekannt ist.

Contents

List of publications

(i) Simon Sala, Philipp-Immanuel Schneider, and Alejandro Saenz,
Inelastic Confinement-Induced Resonances in Low-Dimensional Quantum Systems,
Phys. Rev. Lett. **109**, 073201 (2012)

(ii) Simon Sala, Gerhard Zürn, Thomas Lompe, Andre N. Wenz, Simon Murmann, Friedhelm Serwane, Selim Jochim, and Alejandro Saenz,
Coherent molecule formation in anharmonic potentials near confinement-induced resonances,
Phys. Rev. Lett. **110**, 203202 (2013)

(iii) Simon Sala, Johann Förster, and Alejandro Saenz,
Ultracold-atom quantum simulator for attosecond science,
submitted for publication in *Phys. Rev. Lett.*, arXiv:1311.2304

(iv) Simon Sala, and Alejandro Saenz,
Inelastic resonances due to the coupling of center-of-mass to relative motion,
submitted for publication in *Phys. Rev. A*, arXiv:1509.05799

(v) Sergey Grishkevich, Simon Sala, and Alejandro Saenz,
Theoretical description of two ultracold atoms in finite three-dimensional optical lattices using realistic interatomic interaction potentials,
Phys. Rev. A **84**, 062710 (2012)

(vi) M. J. Mark, S. Sala, F. Meinert, K. Lauber, E. Kirilov, A. Saenz, and H.-C. Nägerl,
Observation of Ultra-narrow Feshbach Resonances and Inelastic Confinement-Induced Resonances in a Three Dimensional Optical Lattice,
in preparation

(vii) Maria Troppenz, Simon Sala, Philipp-Immanuel Schneider, and Alejandro Saenz
Inelastic Confinement-Induced Resonances in Quantum Dots,
submitted for publication in *Phys. Rev. B*, arXiv:1509.01159

(viii) Bruno Schulz, Simon Sala, and Alejandro Saenz,
Resonances in ultracold dipolar atomic and molecular gases,
New J. Phys. **17**, 065002 (2015)

Introduction

The first experimental realization of a Bose-Einstein condensate (BEC) in 1995 by Eric A. Cornell, Carl E. Wieman, and Wolfgang Ketterle [1, 2] who received the Nobel price for their works marked the beginning of a rapid ascend of the field of ultracold atoms. Spectacularly, in a BEC the atoms form a *single collective* quantum wave. Hence, a BEC manifests a macroscopic quantum phenomenon.

A unique feature of ultracold atom experiments is the possibility to tune interatomic interactions with the help of magnetic Feshbach resonances [3–5]. By applying an external magnetic field, the effective interparticle interaction can be tuned to arbitrary values. This provides the rare possibility to prepare quantum systems from quasi free to strongly correlated by tuning a single external parameter.

As a second key feature, miscellaneous external confinements can be realized by the use of optical trap potentials such as dipole traps and optical lattices. The latter are built from counter-propagating interfering laser beams and can be adapted to various geometries [6], such as quasi-1D cigar-shaped potentials, quasi-2D pancake-shaped potentials, almost harmonic single-well potentials or periodic structures similar to the one of solid-state systems. While solids are bound to restrictions of electronegativity, impurities, or coupling to phonons, artificial crystals made of light can be prepared free of these reservations. Nowadays, it became even possible to arbitrarily distribute and detect single atoms over an optical lattice [7, 8] in a controlled way which enabled the observation of quantum-phase transitions on the single-atom level [9].

While in the early years of ultracold experiments the observation of macroscopic quantum phenomena such as coherent matter waves [10] attracted great attention, in recent years ultracold atoms have become a flexible tool for numerous topical applications like quantum information processing [11–14], precision measurements [15–19], quantum simulation [20–26], or phenomena in reduced dimensionality [27–34].

The present thesis reflects different aspects of the fascinating physics of ultracold atoms. The first part is motivated by investigations of systems of reduced dimensionality. There, elastic confinement-induced resonances (CIR) [35, 36] have become the tool to manipulate the effective low-dimensional interaction strength. In theory, a mapping of the (partial) spectrum of the relative-motion Hamiltonian

of two atoms confined in a harmonic trap at large anisotropies onto the spectrum of the corresponding purely one-dimensional system leads to a divergence in the 1D effective interaction strength g_{1D} [35]. The divergent behavior of g_{1D} at the elastic CIR allows not only to experimentally control the effective 1D interaction strength [30–34], but also leads to the creation of a Tonks-Girardeau gas [27–29, 37] and a fermionization of bosonic systems in accordance with the model of Lieb and Liniger [38]. Later it was revealed [36] that the resonance shows similarities to a Feshbach resonance. In 2010, an experiment [39] in the group of Hanns-Christoph Nägerl in Innsbruck confirmed a loss resonance in the region where the elastic CIR should occur which seemed to prove the validity of the Feshbach-type resonance picture. However, detailed analysis [40, 41] demonstrated that there are severe discrepancies of the structure of resonances seen in the experiment and the theory of elastic CIR when adopting different confinement geometries. This initiated a lively, controversial debate.

One major achievement of this thesis is to provide unique evidence that the loss resonances in [39] are caused by so called inelastic CIR, i. e. resonances caused by the confinement-induced center-of-mass to relative-motion coupling of bound states and states of unbound atom pairs. The theory of inelastic CIR describes quantitatively all aspects of the Innsbruck experiment. Moreover, unique evidence is delivered that other proposed mechanisms can be excluded. The latter reasoning is achieved by comparing the theory of inelastic CIR to a subsequently performed experiment [42] that was designed to uniquely identify and characterize inelastic CIR. Additionally, a model is introduced and validated [43] which allows for the prediction of the position and coupling strengths in closed-form expressions as alternative to heavy numerical *ab initio* calculations. The emergence of inelastic CIR in multi-well systems is demonstrated [44] in agreement to an ultracold many-body experiment in a shallow-optical lattice. The calculated two-body Mott-insulator state that couples to a center-of-mass excited molecular bound state in the vicinity of an inelastic CIR is shown in Figure 1.

The molecule formation at an inelastic CIR is controllable fully coherently, even by a variation of the external confinement. This paves the way for a controlled molecule association and variation of the interaction strength in analogy to a magnetic Feshbach resonance. Hence, such a method might become valuable in cases where the use of magnetic Feshbach resonances is hampered, such as for earth-alkaline atoms.

A consequence of the investigation of inelastic CIR is that one of the absolutely standard and routinely adopted approximations for the description of ultracold atoms – the harmonic approximation for the external trap potential – has to be abandoned in order to describe instabilities and molecule formation in recent ex-

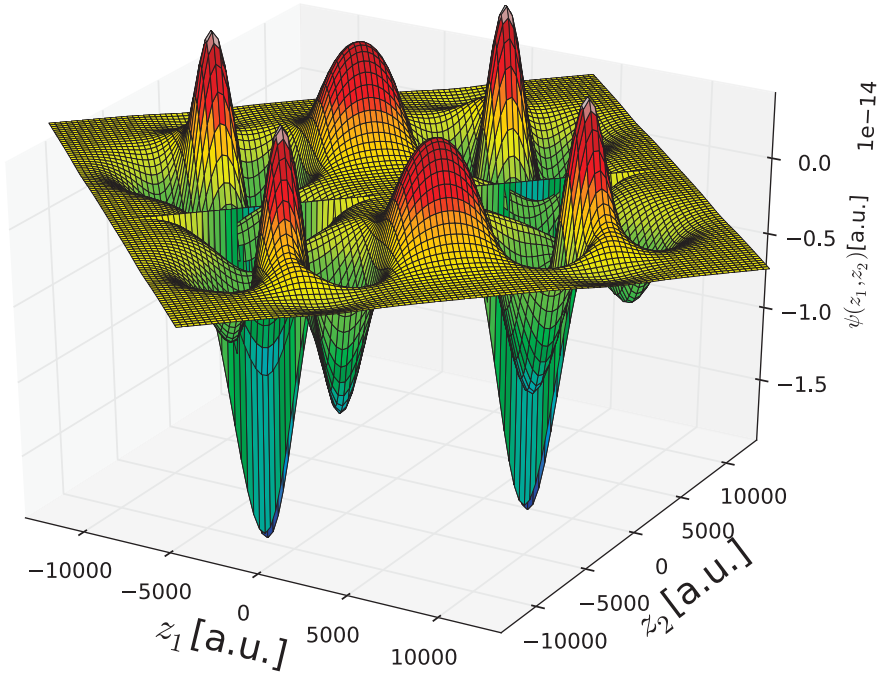

Figure 1: Cut $\psi(z_1, z_2; x_1 = x_2 = y_1 = y_2 = 0)$ through the wavefunction of an two-body Mott-insulator state in a quadruple-well potential that resonantly couples to a center-of-mass excited bound state in the vicinity of an inelastic CIR. The two local maxima on the anti-diagonal ($z_1 = -z_2$) reflect the Mott-insulator state where the two particles reside in different wells. The sharp maxima on the diagonal ($z_1 = z_2$) reflect the resonant bound state admixture of a molecular state in which both atoms are (almost) at the same position delocalized over the wells. The off-diagonal structure is due to interference.

periments. Moreover, the mechanism of inelastic CIR might be further generalized to more-body bound states such as Efimov trimers. However, recent computational methods for the treatment of 3D ultracold few-body systems adopt the harmonic approximation [45] (and references therein). Hence, in Part II a theoretical approach is developed to investigate a variable number of particles in versatile external potentials. The method adopts concepts of electronic-structure theory. In a first step, a Hartree-Fock calculation is performed. Mean-field calculations (such as the solution of the Gross-Pitaevskii equation) have gained popularity in the theoretical treatment of ultracold atoms. However, the method introduced here also aims for a description of strongly correlated systems. Therefore, in a post-Hartree-Fock step correlations are included by a configuration-interaction (exact diagonalization) cal-

culation. It turns out that correlations are indeed crucial to describe the physics at large scattering lengths for interaction potentials of finite range. It is demonstrated, that the essential features of two s-wave interacting atoms can be reproduced. Yet, a renormalization procedure is necessary in order to obtain meaningful results for the implementation of a zero-range potential. It is shown how, in principle, the energy spectrum for arbitrary scattering lengths can be constructed.

In order to adopt concepts of quantum chemistry for the description of ultracold atoms in Part II, electrons are formally replaced by ultracold atoms and the Coulomb potential of the nuclei is replaced by an external trapping potential. In Part III an additional time-dependent magnetic-field gradient is included in the ultracold-atom Hamiltonian that is then shown to become formally equivalent to the Hamiltonian of atoms and molecules in short, high-intense laser fields. In fact, this mapping paves the way for the quantum simulation of attosecond science with ultracold atoms in "slow motion". After proposing an explicit experimental realization of the simulator by extending an already existing experiment, the simulator is shown to reproduce various aspect of strong-field ionization within experimentally accessible parameters. For example, it is demonstrated that differential yields can be quantitatively reproduced in the multiphoton regime. Moreover, it is explicitly worked out that the quantum simulator captures the rescattering physics – that nowadays is perhaps the major research area within attosecond science – even more accurately than a hydrogen atom. Additionally, it is worked out how strong-field effects such as channel closing, n-photon resonances and frustrated tunneling ionization emerge in the quantum simulator system.

Moreover, the widespread strong-field approximation (SFA) is shown to be better satisfied for the quantum simulator. Hence, the evaluation of the SFA for the simulator system together with a comparison to a strong-field experiment directly provide insights into its validity. Finally, the accuracy of the SFA in velocity gauge in the simulator system provides a new method for the imaging of momentum-space densities in trapped ultracold atomic systems.

By the extreme flexibility and control of the quantum simulator, systematic investigations become accessible that are far beyond the possibilities in strong-field systems. In fact, strong-field physics of complex molecules is to a high extent not understood. Exact numerical treatments of the non-relativistic time-dependent Schrödinger equation become quickly unfeasible (two-electron systems such as H_2 are presently state of the art) and the validity of popular simplified approximations is unclear for many-body strong-field systems. Hence, quantum simulation can be a precious assistance to the experimental investigation of attosecond systems in order to deepen the understanding of strong-field experiments and to provide valuable

insights into the validity of approximations and models.

This thesis covers interdisciplinary topics. It is thus organized such that a non-expert reader should be able to follow the discussions. An introduction to basic, yet important theoretical concepts is given in Chapter 1. Part I deals with confinement-induced resonances. After a description of the initial situation that highlights the need for a new theory, elastic CIR are introduced in Chapter 2. Important properties of the spectra of two harmonically trapped ultracold atoms in reduced dimensionality are worked out which allow for a presentation of a mechanism for elastic CIR in a different view than in the original works [35, 36]. The approach delivers an understanding of the discrepancies of the theory and the loss resonances of [39]. In Chapter 3, the theory of inelastic CIR is introduced including the mechanism, a model, and *ab initio* calculations. A thorough validation [43] of the model for different confinement geometries including the description of higher-order resonances is presented in Chapter 4. In Chapter 5 the theory of inelastic CIR is then applied [46] to explain the loss experiment [39]. The challenge to prove that the losses and heating in [39] are uniquely caused by inelastic CIR and not by one of the other proposed mechanisms, was solved by performing a sophisticated experiment [42] as described in Chapter 6. Finally, the emergence of inelastic CIR in multiwell systems is revealed in comparison with very recent loss measurements in a shallow optical lattice [44] in Chapter 7. Chapter 8 concludes Part I.

Part II starts with an introduction into the concepts of electronic-structure theory in second quantization in Chapter 9. Chapter 10 describes the complex implementation of the methods that is partly based on an open-source quantum chemistry program package. In Chapter 11, a discussion of two types of interaction potentials is presented and the applicability of the potentials within the numerical method in view of ultracold interactions is validated. Part II ends with a conclusion (Chapter 12).

Part III begins with a brief survey on strong-field physics in Chapter 13. The attoscience simulator [47], including the basic concept, the Hamiltonian and parameter mapping, an experimental proposal, and application suggestions is described in Chapter 14. After pointing out different aspects of the solution of the time-dependent Schrödinger equation (Chapter 15) and the SFA (Chapter 16), a validation of the quantum simulator in different regimes of the laser-matter interaction and a validation of the applicability of the SFA are provided in terms of differential yields in Chapter 17. Frustrated tunneling ionization is considered in Chapter 18 including an evaluation of static tunneling rates for different computational approaches. The computation of static rates is necessary to compare to semiclassical Monte-Carlo calculations in order to validate a simple tunneling picture. Finally, the behavior

of the total yield is considered in Chapter 19. Part III ends with a conclusion in Chapter 20.

A final summary of the thesis and an outlook is presented in Chapter 21.

1 Trapped ultracold atoms – basic theoretical concepts

Ultracold quantum systems have become versatile systems for probing fundamental physics [48–52] ranging from quantum optics and quantum information to condensed-matter physics. Two cornerstones for the rapid success of the field can be identified: First, the manipulation and control of ultracold atoms in optical potentials allows for the creation of various, almost tailor-made structures. Second, the interaction strength of bosonic and distinguishable ultracold atoms can be parametrized by a single parameter, the s-wave scattering length, which can be tuned by the use of magnetic Feshbach resonances. With focus on these two key features, in Chapter 1 the basic concepts for the theoretical treatment of ultracold atoms is summarized.

1.1 The Born-Oppenheimer approximation

From a most general perspective, a collection of neutral atoms in an external potential is described in non-relativistic quantum mechanics by the many-body Hamiltonian (in atomic units)

$$\begin{aligned} H_{\text{full}} =& T_{\text{e}} + T_{\text{nuc}} + V_{\text{e,e}} + V_{\text{e,nuc}} + V_{\text{nuc,nuc}} + V_{\text{trap}} \\ =& -\frac{1}{2}\sum_{i}^{N_{\text{e}}} \nabla^2_{\mathbf{r}_i^{(\text{el})}} - \frac{1}{2}\sum_{i}^{N} \frac{\nabla^2_{\mathbf{r}_i}}{M_i} + \frac{1}{2}\sum_{i\neq j} \frac{1}{|\mathbf{r}_i^{(\text{el})} - \mathbf{r}_j^{(\text{el})}|} \\ & - \sum_{i,j} \frac{Z_i}{|\mathbf{r}_i - \mathbf{r}_j^{(\text{el})}|} + \frac{1}{2}\sum_{i\neq j} \frac{Z_i Z_j}{|\mathbf{r}_i - \mathbf{r}_j|} + V_{\text{trap}}(\mathbf{r}_i^{(\text{el})}, \mathbf{r}_i) \end{aligned} \tag{1.1}$$

consisting of N_{e} electrons and N nuclei. T_{e} (T_{nuc}) denotes the kinetic energy of the electrons (nuclei), $V_{\text{e,e}}$ is the Coulomb interaction between the electrons, $V_{\text{e,nuc}}$ the Coulomb interaction of the nuclei and the electrons, and $V_{\text{nuc,nuc}}$ the nuclear Coulomb interaction. The summation indices $\{i, j\}$ run over the number of nuclei at $\mathbf{r}_i$ with mass M_i or over the number of electrons which are positioned at $\mathbf{r}_i^{(\text{el})}$ with masses m_{e} (which are set to unity in atomic units). Because of the coupled electronic and nuclear motion the Schrödinger equation of this general many-body Hamiltonian is only for the most simple systems computationally feasible. The

transformation of the Hamiltonian in Eq. (1.1) to the well known Hamiltonian of electronic-structure theory or the electronic Hamiltonian of strong-field physics, in which the electrons are described in the potential of spatially fixed nuclei, or the Hamiltonian of ultracold atoms describing atoms as interacting entities is obtained by the *Born-Oppenheimer approximation*. It states that the solution Ψ_{full} of the time-independent Schrödinger equation of the general Hamiltonian given in Eq. (1.1) can be written as a single product $\Psi_{\text{full}} = \Psi_{\text{el}}\Psi_{\text{nuc}}$ of an electronic part Ψ_{el} and a nuclear part Ψ_{nuc}. This assumption is motivated by the large mass difference between an electron and a nucleus which leads to different timescales in their motion. With this assumption, the nuclear motion influences only adiabatically the electronic Hamiltonian $H_{\text{el}} = T_{\text{e}} + V_{\text{e,e}} + V_{\text{e,nuc}} + V_{\text{nuc,nuc}}$ for which $T_{\text{nuc}} = 0$. For each nuclear geometry, the stationary Schrödinger equation for the electronic Hamiltonian is solved. For a static geometry of the electronic problem, also the potential term $V_{\text{nuc,nuc}}$ reduces to a constant.

The solution is a fermionic wavefunction and must be antisymmetric. Since the total non-relativistic Hamiltonian Eq. (1.1) contains no spin-orbit coupling, the total electronic wavefunction factorizes $|\Psi_{\text{el}}\rangle = |\psi_{\text{el}}\rangle\,|\chi_{\text{el}}\rangle$ into a spatial wavefunction $|\psi\rangle$ and a spin wavefunction $|\chi_{\text{el}}\rangle$. Furthermore, for systems containing only two atoms, the solution depends only on the absolute values r of the internuclear separation $\mathbf{r}$ and not on its orientation. Hence, in the electronic Schrödinger equation

$$H_{\text{el}}\,|\psi_{\text{el}}(\mathbf{r}^{(\text{el})};r)\rangle\;|\chi_{\text{el}}\rangle = E_{\text{el}}(r)\,|\psi_{\text{el}}(\mathbf{r}^{(\text{el})};r)\rangle\;|\chi_{\text{el}}\rangle\,. \tag{1.2}$$

the dependence on the nuclear separation is parametric, i. e. the equation is solved for a fixed nuclear geometry. The only systems involving interatomic interaction considered in this thesis are composed by alkali atoms. In the case of alkali atoms, it is common in molecular physics to consider valence electrons only. The core electrons occupy fully occupied orbitals which add up to zero total angular momentum. Hence, the possible combinations for an antisymmetric product is an antisymmetric spatial wavefunction and a symmetric spin triplet or a symmetric spatial wavefunction and an antisymmetric spin singlet.

In order to classify electronic molecular states of diatomics (or other molecules with $\mathrm{C}_{v,\infty}$ or $\mathrm{D}_{\infty,h}$ symmetry) the following notation is commonly used: The z component of the total angular momentum $\mathbf{M} = \sum_i \mathbf{m}_i$ is a good quantum number because the electronic Hamiltonian is symmetric under azimuthal rotation. It is conserved and denoted by capital Greek letters $\Lambda = \Sigma, \Pi, \Delta, \ldots$ for $M = 0, 1, 2, \ldots$ in the style of the nomenclature of the angular momentum quantum numbers in atomic spectra. The spin multiplicity is $2S + 1$. Another symmetry arises from mirroring the wavefunction at an arbitrary plane through both nuclei. A symmetric

(antisymmetric) wavefunction is indicated by a $+(-)$ superscript. The last symmetry to uniquely define the electronic state is only present in the case of homonuclear systems and arises from the symmetry at the perpendicular plane to the axis connecting both nuclei. Symmetric (antisymmetric) wavefunctions are denoted *gerade* (*ungerade*) in form of a subscript g(u). In case of the ground state, usually a X is written in front, in the case of excited singlet states a capital (Latin) letter L, in the case of excited triplet states a lower case Latin letter l is written in front. The specific notation is thus

$$\{X, l, L\}\ {}^{2S+1}\Lambda^{\pm}_{g/u}. \tag{1.3}$$

The electronic states mainly considered in the calculations of this thesis are the $a^3\Sigma_g^+$ triplet states of ^{7}Li-^{7}Li and ^{6}Li-^{6}Li systems.

Next, it is demonstrated how the Schrödinger equation for the nuclei is extracted for a two-body system of alkali atoms. After solving Eq. (1.2) for different r the electronic part of the full Hamiltonian can be eliminated by multiplying the full Schrödinger equation in Born-Oppenheimer approximation

$$\begin{aligned} H_{\text{full}} \left|\Psi_{\text{nuc}}(\mathbf{r})\, \psi_{\text{el}}(\mathbf{r}_i^{(\text{el})}, s_i; r)\right\rangle &= \left[T_{\text{nuc}}(\mathbf{r}) + H_{\text{el}}(\mathbf{r}_\mathbf{i}^{(\text{el})}, s_i; r)\right] \left|\Psi_{\text{nuc}}(\mathbf{r})\, \psi_{\text{el}}(\mathbf{r}_i^{(\text{el})}, s_i; r)\right\rangle \\ &= E \left|\Psi_{\text{nuc}}(\mathbf{r})\, \psi_{\text{el}}(\mathbf{r}_i^{(\text{el})}, s_i; r)\right\rangle \end{aligned} \tag{1.4}$$

with the adjoint $\langle\psi_{\text{el}}|$. Here, $r = |\mathbf{r}|$ and $i = 1, 2$ for the two valence electrons. Having in mind that the nuclear kinetic energy operator has a second derivative which is parametric for the electronic wavefunctions, its action on the electronic wavefunction can be neglected in Born-Oppenheimer approximation and leads to

$$\langle\psi_{\text{el}}|\, T_{\text{nuc}}(|\psi_{\text{el}}\rangle\, |\Psi_{\text{nuc}}\rangle) + \langle\psi_{\text{el}}|H_{\text{el}}|\psi_{\text{el}}\rangle\, |\Psi_{\text{nuc}}\rangle = \langle\psi_{\text{el}}|\psi_{\text{el}}\rangle\, E\, |\Psi_{\text{nuc}}\rangle = E\, |\Psi_{\text{nuc}}\rangle\ . \tag{1.5}$$

Using the orthogonality of the electronic states leads to the desired Schrödinger equation for the nuclei

$$T_{\text{nuc}}\, |\Psi_{\text{nuc}}\rangle + E_{\text{el}}(r)\, |\Psi_{\text{nuc}}\rangle = E\, |\Psi_{\text{nuc}}\rangle \tag{1.6}$$

As visible in Figure 1.1 the Born-Oppenheimer potential curves $E_{\text{el}}(r)$ consist of a strongly repulsive part for small internuclear distances which is dominantly caused by the overlapping of electron clouds [5].

If the attractive part of the potential curve (for large r) is dominated by the van-der-Waals force, it can be well described in leading order by the functional form $-C_6/r^6$, where C_6 is the van-der-Waals coefficient. The van-der-Waals force is caused by the induced dipole moments in the atomic shells. The singlet ground-state curve of ^{6}Li ^{133}Cs is much deeper than the ^{7}Li^{7}Li excited triplet curve which leads

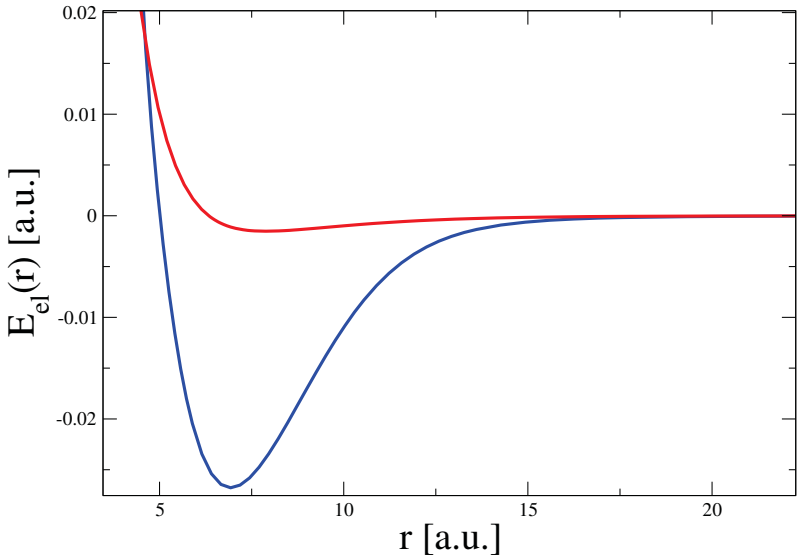

Figure 1.1: Born-Oppenheimer potential curves [53] for the singlet ground state of ^{6}Li ^{133}Cs (blue) and the excited triplet state of ^{7}Li^{7}Li (red).

to a larger number of bound states. This effect is enhanced by the larger reduced mass μ of ^{6}Li ^{133}Cs compared to ^{7}Li^{7}Li which leads to a higher density of states.

A high-precision *ab initio* calculation of the electronic potential curves to an extent where it predicts accurately the scattering length is numerically very demanding and can be achieved only for simple systems such as He_2 [54]. For more complicated structures such as alkali atoms, a successful approach can be to parametrize the curves and extract the correct parameters from comparison with experimental and numerical data.

1.2 Scattering theory

The interaction of confined atoms can be described with concepts of scattering theory. A basic potential-scattering setup usually consists of an open scattering channel with an asymptotical energy of zero. Despite the fact that the asymptotic energies for large interatomic distances are non-zero due to the trap potential also the interaction of trapped ultracold atoms can be described by scattering concepts. This is possible since at small interatomic distances the influence of the trap potential can be neglected. On the other hand, the influence of the interaction is negligible in the regime where the wavefunction of the system is dominated by the trap. This behavior manifests itself in two characteristic length scales. First, the length scale

to characterize the trap is the harmonic oscillator length

$$d_{\mathrm{ho}} = \sqrt{\frac{\hbar}{\mu\omega}} \tag{1.7}$$

with the harmonic oscillator frequency ω and the reduced mass μ, which is given for two particles with mass m_1 and m_2 as

$$\mu = \frac{m_1 m_2}{m_1 + m_2} \quad . \tag{1.8}$$

Typical trap-length scales vary between 10^3 a.u. and 10^4 a.u. For the systems of neutral alkali atoms considered in this thesis, the long-range part of Born-Oppenheimer curves can be approximated by a van-der-Waals tail (of the form $-C_6/r^6$). The range of the this potential is given by [5]

$$r_0^{\mathrm{vdW}} = \left(\frac{2mC_6}{\hbar^2}\right)^{\frac{1}{4}} \quad . \tag{1.9}$$

For example, the range of the ^{7}Li -^{7}Li system is about 30 a.u. (as can be also seen in Figure 1.1) and for other systems of alkali atoms on the order of 100 a.u. [55]. Since the effective length scale of the interatomic interaction and the trap potential differ by at least one order of magnitude, in order to adopt scattering concepts the interaction regime can be regarded as independent of the trap regime.

The effective Schrödinger equation of the relative-motion Hamiltonian in Born-Oppenheimer approximation has the same form as the equation for a particle scattering at a spherically symmetric potential. The asymptotic solution is then given by the Sommerfeld condition

$$\psi(\mathbf{r}) = \mathrm{e}^{i\mathbf{k}\cdot\mathbf{r}} + f(\theta)\frac{\mathrm{e}^{ikr}}{r} \quad . \tag{1.10}$$

It has the form of an incoming plane wave and a spherical wave weighted by the *scattering amplitude* $f(\theta)$. In general, the scattering amplitude depends also on the azimuthal angle ϕ. The interatomic potentials treated in the present thesis are spherically symmetric[1] which leads to the conservation of the the z component of the angular momentum and makes the problem independent on ϕ. Different than implied by Eq. (1.10) the scattering process is not a stationary process. Wave packets propagate in time from $t = -\infty$ to $t = \infty$. However, analyzing the outgoing flux leads to the same condition (Eq. (1.10)). The *differential scattering cross section*

[1] For dipolar quantum gases this is not fulfilled anymore, [56]

σ which is a measure for the scattered particle flux into the solid angle $d\Omega$ per incoming particle flux is related to the scattering amplitude by

$$\frac{d\sigma}{d\Omega} = |f(\theta)|^2 \quad . \tag{1.11}$$

This relation allows for a probabilistic interpretation of the scattering amplitude. It can therefore be regarded as a regular observable.

A useful approximation to calculate scattering amplitudes is the zeroth-order term of the Born series [57]. In this approximation, the scattering amplitude becomes

$$f(\mathbf{q}) = -\frac{2m}{4\pi\hbar^2} \int d^3r \mathrm{e}^{\mathrm{i}\mathbf{q}\cdot\mathbf{r}} \quad . \tag{1.12}$$

Within zeroth-order Born approximation, the scattering amplitude is given by the Fourier transform with respect to the momentum transfer $\mathbf{q} = \mathbf{k} - \mathbf{k}'$ where $\mathbf{k}$ and $\mathbf{k}'$ are the momenta of the incoming and the outgoing waves. Because the scattering process is considered to be elastic the absolute values $|\mathbf{k}| = |\mathbf{k}'| = k$ are equal. Although the Born approximation is easy to use and offers a nice interpretation of the scattering amplitude, it is not exact and does not account for the effective range of the potential. The next method to calculate scattering amplitudes introduced is especially important for low-energy scattering of ultracold atoms. Terms like the scattering length are widely used and are introduced in the following.

The partial-wave expansion

In the case of a spherically symmetric potential the scattering amplitude depends on the angle $\theta \in [0, \pi]$ or $z = \cos\theta \in [-1, 1]$ and also on the energy $E = \frac{\hbar^2 k^2}{2m}$ of the colliding particles, where k denotes the absolute value of the wave vector. For fixed k the scattering amplitude is a non-singular square-integrable function. Hence, it can be expanded in spherical harmonics $Y_{lm}(\theta, \phi)$. Since the interaction is rotationally symmetric and therefore ϕ independent, also the scattering amplitude is independent on the azimuthal angle and only $m = 0$ terms are present in the expansion. The spherical harmonics with $m = 0$ are proportional to the Legendre polynomials $P_l(\cos\theta)$,

$$Y_{l0} = \sqrt{\frac{2l+1}{4\pi}} P_l(\cos\theta) \quad . \tag{1.13}$$

Thus, the scattering amplitude

$$f(\theta) = \sum_{l=0}^{\infty} (2l+1) f_l(k) P_l(\cos\theta). \tag{1.14}$$

can be written independent of ϕ including the *partial-wave amplitudes* $f_l(k)$. This series converges only if the amplitudes become sufficiently small for large values of l. This is fulfilled and becomes obvious when looking at the effective potential

$$U_{\text{eff}}(r) = \frac{\hbar^2 l(l+1)}{2mr^2} + U_{\text{int}}(r) \tag{1.15}$$

which arises when treating spherically symmetric problems and contains the centrifugal potential $\frac{\hbar^2 l(l+1)}{2mr^2}$. The effective potential is dominated by the centrifugal barrier for large l, and decreases quickly with increasing r. Therefore the amplitudes f_l become small for large l. The wavefunctions can be expanded into partial waves analogously to the scattering amplitude. Expressing the lth partial wave as $R_l(r)Y_{l0}(\theta) = \frac{u_l(r)}{r}Y_{l0}(\theta)$ with the scaled radial wavefunction $u_l(r) = rR_l(r)$ where R_l denotes the original unscaled radial wavefunction, the Schrödinger equation

$$\frac{d^2}{dr^2}u_l(r) - \left(\frac{2m}{\hbar^2}U_{\text{eff}}(r) - k^2\right)u_l(r) = 0 \tag{1.16}$$

for the radial wavefunctions becomes one-dimensional. In the asymptotic limit $r \to \infty$ the solutions of a free-particle

$$u_l(r) = C\sin(kr - l\frac{\pi}{2} + \delta_l(k)) \tag{1.17}$$

are obtained where $\delta_l(k)$ are the scattering phases for angular momentum quantum number l. The free particle solutions can be written as a superposition of spherical Bessel and spherical Neumann functions, j_l and n_l, with the asymptotic forms

$$\lim_{r\to\infty} j_l(kr) \propto \sin\left(kr - l\frac{\pi}{2}\right) \tag{1.18}$$

and

$$\lim_{r\to\infty} n_l(kr) \propto \cos\left(kr - l\frac{\pi}{2}\right) \quad , \tag{1.19}$$

respectively. Eq. (1.17), Eq. (1.18), and Eq. (1.19) together with the trigonometric addition formula lead to

$$u_l(r) = kr\ [\cos(\delta_l)j_l(kr) + \sin(\delta_l)n_l(kr)] \quad . \tag{1.20}$$

To relate the partial-wave amplitudes defined in Eq. (1.14) to the scattering phase, the Sommerfeld condition Eq. (1.10) is used to write the asymptotic scattering solutions in terms of Legendre polynomials [58]. Comparing the result with Eq. (1.20) leads to the amplitudes

$$f_l(k) = \frac{1}{k}\mathrm{e}^{\mathrm{i}\delta_l(k)}\sin\delta_l(k) \quad . \tag{1.21}$$

By plugging these amplitudes into Eq. (1.14), the total scattering cross section

$$\sigma = \int |f(\theta)|^2 d\Omega = 4\pi \sum_{l=0}^{\infty} (2l+1)|f_l(k)|^2 = \frac{4\pi}{k^2} \sum_{l=0}^{\infty} (2l+1) \sin^2 \delta_l(k) \tag{1.22}$$

is obtained.

A direct consequence is the *optical theorem* that relates the total scattering cross section σ via

$$\sigma = \frac{4\pi}{k} \mathrm{Im} f(0) \tag{1.23}$$

with the scattering amplitude at zero. This equation is remarkable because all the scattering information up to the differential one is already contained in the scattering amplitude for $\theta = 0$.

Low-energy scattering and the s-wave scattering length

After having introduced the general scattering case the low-energy scattering regime is considered which covers the case of ultracold collisions and is central to this thesis. As temperature approaches zero, the energy E as well as the wave number k approach zero. It is possible to show rigorously that in the limit of $k \to 0$ the amplitudes f_l behave like k^{2l} [58]. For the scattering phases this is equivalent to

$$\lim_{k\to 0} f_l = \lim_{k\to 0} \frac{1}{k} \mathrm{e}^{\mathrm{i}\delta_l(k)} \sin \delta_l(k) = \frac{1}{k} \delta_l \propto k^{2l} \quad . \tag{1.24}$$

Therefore, the scattering phases behave like $\delta_l \propto k^{2l+1}$ in the low-energy limit. To address this behavior the scattering length

$$a_l := \lim_{k\to 0} \frac{f_l}{k^{2l}} = \lim_{k\to 0} \frac{\delta_l}{k^{2l+1}}. \tag{1.25}$$

is introduced that has the dimension L^{2l+1} with a length L. a_l becomes constant at zero energy because of the mentioned behavior of f_l for $k \to 0$, Eq. (1.24). Expanding $k \cot \delta_l$ around $k = 0$ results in

$$k \cot \delta_l = -\frac{1}{a_l} + \frac{1}{2} r_0^{(l)} k^2 + O(k^3) \quad . \tag{1.26}$$

The second term contains the *effective range* r_0^l. For $l = 0$ special names are given, the *s-wave scattering length* a_0 and the *s-wave effective range* $r_0^{(0)}$. Substituting this into the total cross section Eq. (1.22) and noting that $\lim_{k\to 0} f_l = \delta_l/k$ (Eq. (1.24)), leads to

$$\sigma_{tot} = 4\pi a_0^2 + O(k^2) \quad . \tag{1.27}$$

Hence, the *low-energy cross section is dominated by the s-wave scattering length*. It should be mentioned that identical fermions do not interaction via s-wave scattering. Fermions in contrast to bosons have odd parity wavefunctions which only allow for the interaction in odd partial waves ($p, f, \dots$).

For interacting ultracold atoms that underlie a short-range interaction such as a Born-Oppenheimer potential, an alternative and perhaps more intuitive derivation for the dominance of the s-wave interaction can be given. By the definition of the interaction range r_0^{vdW} in Eq. (1.9), for $r > r_0^{\mathrm{vdW}}$ the interatomic interaction is negligible and only the centrifugal part $\hbar^2 l(l+1)/(2mr^2)$ of the effective potential U_{eff} of Eq. (1.15) has an effect. For $E = \hbar^2 k^2/(2m)$ the classical turning point is at $r_t = \sqrt{l(l+1)}/k$. Hence, for $r < r_t$ the wavefunction exponentially decays inside the centrifugal barrier for $l > 0$. Thus, for $r_t > r_0^{\mathrm{vdW}}$ the particles are not influenced by the interaction potential at all. Consequently, the particles are only scattered if $r_t < r_0^{\mathrm{vdW}}$ which is fulfilled for $\sqrt{l(l+1)} \approx l < k r_0^{\mathrm{vdW}}$. The thermal wavelength

$$\lambda_{\mathrm{th}} = \hbar \sqrt{\frac{2\pi}{m k_B T}} \tag{1.28}$$

of ultracold systems at typical temperatures of $T \approx 1\mu K$ is on the order of 10000 a.u. Hence, $k r_0^{\mathrm{vdW}} = 2\pi r_0^{\mathrm{vdW}}/\lambda_{\mathrm{th}} \ll 1$. Therefore, only s-wave interaction is present for ultracold temperatures. All other states with higher l contribution are blocked by the centrifugal barrier. In the following, the s-wave scattering length is simply denoted by a instead of a_0 (and is often simply called scattering length).

Since the scattering-length concept is central to the theoretical description of ultracold atoms, it is demonstrated how it manifests in the radial wavefunction. The value of a can directly be extracted from the behavior of the wavefunction outside the interatomic potential. This becomes obvious when applying $kr \ll 1$ to the asymptotic wavefunction. Using Eq. (1.20), rewriting it, and inserting the first-order term of the expansion of δ_l (Eq. (1.26)) leads to

$$u_0(r) \propto \left[-\frac{1}{ka} \sin(kr) + \cos(kr) \right] \propto \left(1 - \frac{r}{a} \right) \quad . \tag{1.29}$$

In the last step $kr \ll 1$ is used. This equation shows that the extrapolation of the scaled radial wavefunction intersects with the r axis at a. A graphical example is given in Figure 1.2 where the asymptotes of the scaled radial wavefunctions can be directly read out from the zero crossing.

The scattering cross section at ultracold temperatures only depends on the scattering length a which is implied by Eq. (1.27). Ultracold scattering is therefore *universal* in the sense that the interaction only depends on the asymptotic behavior

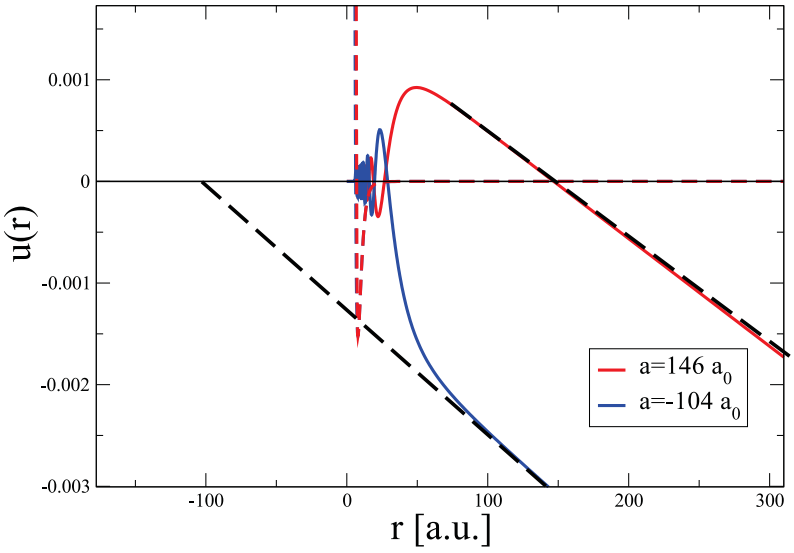

Figure 1.2: Born-Oppenheimer potentials (dashed red and dashed blue) that are manipulated by an inner-wall shift together with the corresponding scaled radial wavefunctions (solid red and solid blue). The intersection of the asymptotes (black dashed lines) with the r axis determine the value of the scattering length.

of the wavefunction. Therefore, details of the interatomic short-range potential do not affect ultracold collisions. This is the ideal starting point for the use of model potentials. The perhaps most widely used one is the δ pseudopotential.

1.3 The δ pseudopotential

The δ pseudopotential can be constructed from the asymptotic behavior of the wavefunction. Starting from the Schrödinger equation for $l = 0$,

$$\left(\Delta - \frac{2mV}{\hbar^2} + k^2\right)\psi(\mathbf{r}) = 0 \tag{1.30}$$

the asymptotic condition for the wavefunction

$$\psi(\mathbf{r}) = \frac{C}{r}\left(\sin(kr) + \tan(\delta_0)\cos(kr)\right) \tag{1.31}$$

is used. After applying the source equation $\Delta(1/r) = -4\pi\delta(\mathbf{r})$ and the relations $\frac{1}{k}\frac{\partial}{\partial r}[r\psi(\mathbf{r})]\Big|_{r\to 0} = C$ and $\tan\delta_0 = -ka$ a comparison with the Schrödinger equation

yields the Fermi-Huang δ pseudopotential [59, 60]

$$V(\mathbf{r}) = \frac{4\pi\hbar^2 a}{m}\delta(\mathbf{r})\frac{\partial}{\partial r}r \quad . \tag{1.32}$$

By construction, the solution fulfills the correct asymptotic boundary condition. Moreover, the solution provides a bound state. As will be seen, this bound state plays a crucial role in the theory of confinement-induced resonances but also for magnetic Feshbach resonances that are briefly introduced next.

1.4 Feshbach resonances

In a two-channel model, a Feshbach resonance occurs if the scattering energy of an incoming open channel coincides with the energy of a coupled closed-channel bound state [4]. The mixing of both states results in a change of the scattering length. Since the channel potentials are spin-dependent it is possible to use the Zeeman effect to change the relative energetic positions of the channels (Figure 1.3) and therefore to tune with magnetic fields the scattering length to arbitrary values. A manipulation of the scattering length is equivalent to a change in the cross-section (see Eq. (1.27)) which results in an effective change of the interaction of the trapped particles. This external tunability of the interaction offers great control of the system which is still one of the cornerstones of the field of ultracold atoms.

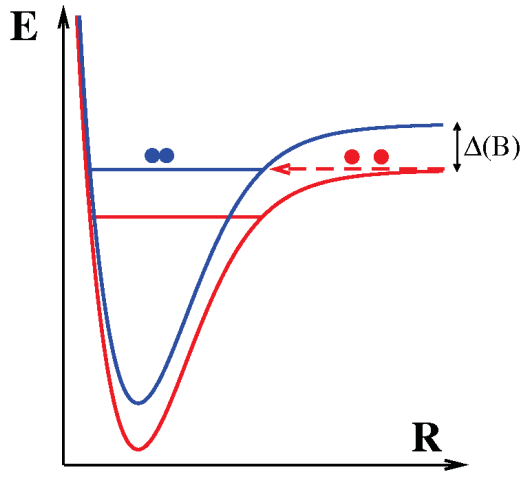

Figure 1.3: Illustration of the appearance of a magnetic Feshbach resonance. A Feshbach resonance occurs when the incoming channel (red) couples resonantly to the bound state of another channel (blue). The energy of the bound state can be varied relatively to the energy of the incoming channel by an external magnetic field B making use of the Zeeman effect.

In the present thesis energy spectra for a variation of the scattering length are analyzed in order to simulate the behavior around a Feshbach resonance in experiments. In general, the accurate calculation of magnetic Feshbach resonances involves the solution of complicated multi-channel problems. However, methods have been developed [61] to mimic the variation of the s-wave scattering length at a Feshbach resonance with single-channel approaches. The technique used in the present work is the variation of the inner wall of the potential curve which is the steep repulsive part of the used Born-Oppenheimer curve of the interaction potential. Modifying the inner wall continuously leads to a change in scattering length. In Figure 1.4 the ^{7}Li-^{7}Li Born-Oppenheimer potential curve of the $a^3\Sigma_g^+$ electronic state is illustrated with several inner-wall shifts and the resulting wavefunctions. As before, the scattering length can directly be read out of the asymptotic behavior of the scaled radial wavefunctions $u(r)$ determined by the intersection point with the $r = 0$ axes as indicated in Figure 1.4.

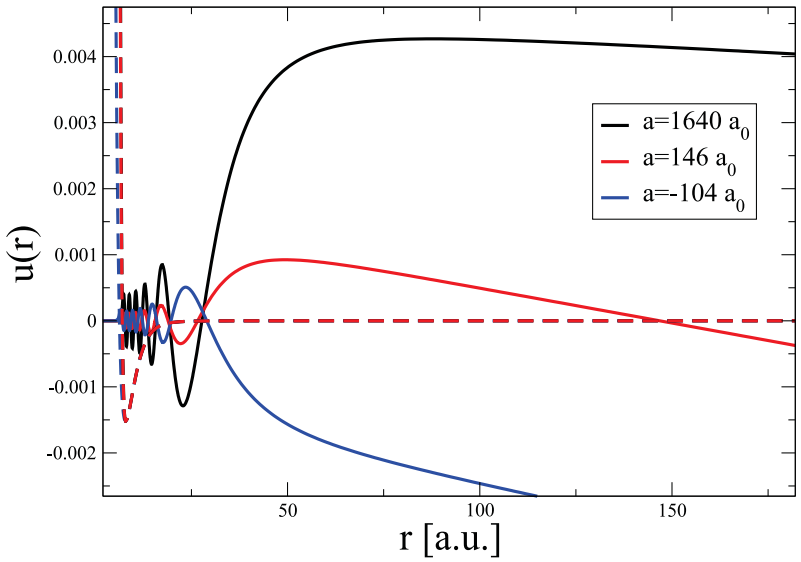

Figure 1.4: Inner-wall shifted Born-Oppenheimer curves (dashed lines) for the interaction of ^{7}Li in the $a^3\Sigma_g^+$ electronic state change the behavior of the scaled wavefunctions $u(r)$ (solid lines) and hence the scattering length.

The dominance of s-wave scattering in the ultracold limit is crucial. It allows to parametrize the interaction by a single parameter. This simplifies not only the theoretical description tremendously, but also allows to adopt Feshbach resonances experimentally. The second ingredient for the fast ascend of the field of ultracold atoms is the variability of the external potential that are fabricated by light sources.

1.5 Optical trap potentials

As mentioned earlier a fully controlled technique to spatially confine and manipulate ultracold atoms is the use of optical trapping potentials. Widely used are optical lattices [6]. They overcome the limitation of the typically used magnetic traps, in which only a small subset of the available atomic spin states can be trapped. Optical trap potentials rely on the interaction between an induced dipole moment in an atom and an external electric field. Such a field can be provided by the electric field of superimposed lasers which form a standing wave, see Figure 1.5. The laser light is usually tuned far away from an atomic resonance frequency, such that stimulated emissions from resonant excitations can be neglected. The dipole-induced atom-field interaction can be attractive for laser light with a frequency ω smaller than the atomic resonance frequency ω_0, or repulsive for a laser frequency larger than the atomic resonance frequency.

An optical lattice potential in one spatial direction can then be formed by overlapping two counter-propagating laser beams. The interference between the two laser beams forms an optical standing wave with period $\frac{\lambda}{2}$, which can trap the atoms. The electrical field components of a laser beam

$$\mathbf{E}(\mathbf{r}) = \sum_{j=x,y,z} E_{0,j} \sin(k_j j)\mathbf{e}_j \tag{1.33}$$

with the unit vectors $\mathbf{e}_j$ induce the electric dipole-moment

$$\mathbf{d} = \alpha(\mu)\mathbf{E} \quad . \tag{1.34}$$

At the same time, the field interacts with this dipole moment which effectively creates a trap potential for the atoms. In general, the polarizability α is frequency dependent, complex, and depends on the direction of the field. For lithium, however, that is considered in *ab initio* calculations, it is to good approximation 164.2 a.u. The expression for the optical lattice potential

$$V_{\mathrm{OL}} = -\frac{1}{2}\langle \mathbf{d} \cdot \mathbf{E} \rangle = -\frac{1}{2c\epsilon_0} \mathrm{Re}(\alpha) I(\mathbf{r}). \tag{1.35}$$

is obtained by averaging $\mathbf{d} \cdot \mathbf{E}$ over time. The intensity profile

$$I(\mathbf{r}) = \sum_{j=x,y,z} I_{0,j} \sin^2(k_j j) \tag{1.36}$$

contains $k_j = \frac{2\pi}{\lambda_j}$ where λ_j denotes the wavelength of the laser in direction j. The potential depth of the lattice is then given by $V_{0,j} = -\frac{1}{2c\epsilon_0} \mathrm{Re}(\alpha) I_{0,j}$ resulting in the

final expression

$$V_{\mathrm{OL}} = \sum_{j=x,y,z} V_j \sin^2(k_j j) \tag{1.37}$$

for the optical-lattice potential for a single particle.

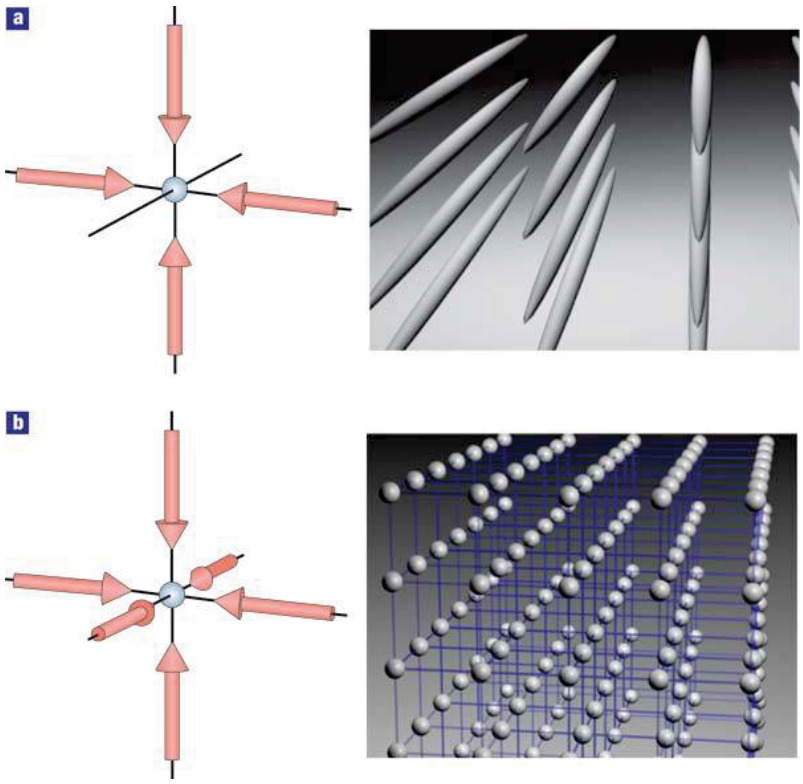

Figure 1.5: The creation of optical-lattice potentials by superimposing standing waves that are formed by counter-propagating laser beams. In (a), the confinement of two transversal directions leads to an array of cigar-shaped, quasi-1D tubes. In (b), a cubic optical lattice is obtained by superimposing lasers in three spatial directions. The figure is copied from [6].

The harmonic trap potential is fundamental to this thesis. It can be obtained by expanding the optical-lattice potential in a Taylor series. In order to demonstrate the important separability of relative (rel.) and center-of-mass (c.m.) degrees of freedom in a two-body system, the Taylor expansion up to the second order of the optical lattice potential of Eq. (1.37) for two particles ($i = \{1, 2\}$) is considered. A transformation to rel. and c.m. coordinates,

$$\mathbf{r} = \mathbf{r_1} - \mathbf{r_2} \quad , \tag{1.38}$$

$$\mathbf{R} = \frac{m_1\mathbf{r_1} + m_2\mathbf{r_2}}{m_1 + m_2} = \mu_1\mathbf{r_1} + \mu_2\mathbf{r_2} \quad , \tag{1.39}$$

respectively, where $\mu_{1,2} = \frac{m_{1,2}}{m_1+m_2} = \frac{\mu}{m_{2,1}}$ and μ denotes the reduced mass as in Eq. (1.8) leads to

$$V_{\text{rel.}}(\mathbf{r}) = \sum_{i=1,2} \sum_{j=x,y,z} V_j^{(i)} k_j^2 \mu_{\eta_i}^2 r_j^2 \tag{1.40}$$

$$V_{\text{c.m.}}(\mathbf{R}) = \sum_{i=1,2} \sum_{j=x,y,z} V_j^{(i)} k_j^2 R_j^2 \tag{1.41}$$

$$W(\mathbf{r},\mathbf{R}) = \frac{1}{2} \sum_{j=x,y,z} k_j^2 r_j R_j \left[V_j^{(1)} \mu_2 - V_j^{(2)} \mu_1 \right] \tag{1.42}$$

where $\eta_1 = 2$ and $\eta_2 = 1$. In Eqs. (1.40–1.42) , the harmonic potential is split in three terms, the relative motion part $V_{\text{rel.}}$, the c.m. part $V_{\text{c.m.}}$, and the coupling term W. It is crucial to recognize that the center-of-mass to relative motion (c.m.-rel.) coupling W vanishes if and only if the product $I_j^i \alpha_j^i \mu_i$ is equal for both particles $i = 1, 2$. Hence, *the coupling for two homonuclear particles in the same electronic state vanishes in a harmonic trap potential*. For heteronuclear systems or if two of the same atoms are in different electronic states the coupling does not vanish even in an harmonic trap potential.

It is convenient to introduce the harmonic oscillator frequencies ω and Ω for the rel. and c.m. motions, respectively. In the present thesis, only homonuclear systems are considered. Hence, it is sufficient to introduce the harmonic-oscillator frequencies

$$\omega^2 = \frac{k^2 V}{\mu} = \frac{2k^2 V}{m} \tag{1.43}$$

and

$$\Omega^2 = \frac{4k^2 V}{M} = \frac{2k^2 V}{m} \tag{1.44}$$

for the rel. and c.m. motions, respectively, for the special case of $\mu_1 = \mu_2 = \frac{1}{2}$, $\mu = \frac{m}{2}$, $M = 2m$, $V^{(1)} = V^{(2)} = V$.

It is highly important to this thesis that with optical trapping potentials, systems of reduced dimensionality can be realized. For instance, increasing the intensity of an optical-lattice potential in two transversal directions leads to the formation of a stack of cigar-shaped tubes, see Figure 1.5. Although such potentials are, of course, still 3D (as every realistic potential) their strong anisotropy leads to phenomena that can be described by pure 1D models. Hence, in the following such strongly anisotropic systems are denoted as *quasi-1D* (*quasi-2D*) systems in the case of two (one) strongly confined directions.

Part I

Inelastic resonances due to the coupling of center-of-mass and relative motion

Theoretical treatments of strongly-correlated ultracold atoms in single-well potentials routinely adopt the harmonic approximation to describe the trap potential. This is, of course, an idealization because every realistic trap potential is finite and thus anharmonic. A major benefit of the harmonic approximation is the decoupling of rel. and c.m. motion for identical[2] particles. Moreover, especially for deep potentials the harmonic confinement resulting from a second-order Taylor expansion of the potential in its minimum is a good approximation in most cases, because the c.m.-rel. coupling introduced by the anharmonicity of the trap potential is energetically negligible compared to the energy scale of the interatomic interaction. As a consequence, the theoretically predicted binding energy of two ultracold atoms confined in a harmonic trap [62] has been experimentally confirmed [30]. Moreover, the measurement [63] and calculation [64] of the influence of the anharmonicity on the energy of states in deep optical lattices has revealed that the deviation to the harmonic approximation for the lowest band is negligible in most cases. However, as will be worked out and analyzed in Part I, although the c.m.-rel. coupling is negligible in energy compared to the interaction, it can have a great impact on an ultracold atomic quantum gas even in rather deep potentials where the harmonic approximation is routinely adopted.

The presented exploration of anharmonicity-induced effects was initiated by the experiment described in [39] performed by Elmar Haller *et al.* in the group of Hanns-Christoph Nägerl at the University of Innsbruck (this experiment will sometimes simply be denoted as "Innsbruck experiment"). There, the measurement of losses and heating in a gas of ^{133}Cs for a variable interaction strength revealed resonant features. At first, as described in the original work [39], elastic confinement-induced resonances[3] (CIR) were believed to cause the losses. At the elastic CIR, the effective 1D interaction strength $g_{1\mathrm{D}}$ shows a divergent behavior. Also in 2D the elastic CIR exists, leading to a divergence in $g_{2\mathrm{D}}$ [65]. These divergences were confirmed in quasi-1D[4] by *ab initio* calculations of $g_{1\mathrm{D}}$ [36] and by experiments [30–34] that control $g_{1\mathrm{D}}$ by the scattering length a. In quasi-2D, the divergence of $g_{2\mathrm{D}}$ was observed adopting radio-frequency spectroscopy [66]. At the latest when the elastic CIR were experimentally confirmed in quasi-2D, the theory was considered well established in the community. The Innsbruck loss experiment [39] revealed a resonance close to the position predicted by the theory of elastic CIR in quasi-1D in the case of an isotropic confinement in the strongly confined (transversal) directions. This seemed

[2] In fact, as demonstrated in Section 1.5 for the decoupling of rel. and c.m. motion in a harmonic confinement, it is already sufficient that the particles have equal masses and equal polarizabilities.

[3] Noteworthy, in the original works on elastic CIR they were simply denoted as CIR. The term *elastic* CIR is introduced to distinguish them from the inelastic CIR studied in this thesis.

[4] For a definition of quasi-1D (quasi-2D) confinement, see Section 1.5.

to be yet another experimental evidence for the occurrence of elastic CIR. However, the experiment considered also an anisotropic transversal confinement and found a *splitting* of the resonance. Furthermore, in quasi-2D a loss resonance was observed at *positive* values of the scattering length [39], but *not* for negative values [67]. A detailed analysis [40, 41] proved formally that these two observations contradict the theory of elastic CIR that predicts a *single* resonance in quasi-1D (even for transversal anisotropy) and a resonance at *negative* scattering lengths in quasi-2D confinement.

The observations led to a controversial debate in the community. Especially since the elastic CIR have been confirmed experimentally in quasi-1D and quasi-2D confinement, researchers were doubtful about the discrepancies. Still, the Innsbruck experiment [39] raised important questions: What kind of resonances were truly observed? Are the elastic CIR modified due to the experimental setup, or are the losses of completely different origin? If so, why are the elastic CIR not seen in terms of losses? In Part I a complete explanation that addresses these questions is presented. It will be demonstrated that the origin of the losses are inelastic CIR due to the resonant coupling of c.m. and rel. motion. Also their emergence in multi-well systems is presented. Moreover, it will be shown that a molecule formation is responsible for their character and that the process of creating a molecule can be performed experimentally fully coherently. In fact, the molecule formation at the inelastic CIR can not only be tuned by changing the s-wave scattering length, but also by modifying the confinement geometry. This paves the way for a magnetic Feshbach-resonance-type molecule association of atomic species where magnetic Feshbach resonances cannot be used to vary the interaction behavior such as for earth-alkali atoms.

2 Elastic confinement-induced resonances

Elastic CIR are of great importance for ultracold-atom experiments in reduced dimensionality. They were introduced in the theoretical works [35, 36] and recently reviewed in [68]. They allow for a controlled manipulation of the effective quasi-1D interaction strength g_{1D} [30–34] that can be achieved by a variation of the 3D s-wave scattering length around a Feshbach resonance [4]. Elastic CIR are universal since the resonance position is determined by a single parameter $d_\perp/a$, i. e. the ratio of the transversal confinement length $d_\perp$ to the s-wave scattering length a. The resonance position can thus not only be reached by tuning the scattering length, but also by a variation of the confinement geometry[1]. By definition, at the elastic CIR g_{1D} diverges. This leads to the formation of a Tonks-Girardeau gas [37, 38] which was confirmed experimentally [27, 28, 32]. In the Tonks-Girardeau limit, a 1D gas impenetrable, strongly repulsively interacting bosons acquires fermionic properties[2] such that all local observables such as the energy or the square modulus of the wavefunction (as was explicitly confirmed experimentally [34]) will take the same value as in a 1D gas of non-interacting identical fermions. The divergence of g_{1D} in the theory of elastic CIR stems theoretically from a formal mapping of the scattering amplitude of a 1D system of two harmonically trapped bosonic atoms interacting via a 1D contact interaction on the corresponding scattering amplitude of bosonic atoms confined to a strongly anisotropic harmonic confinement[3] [35]. An analogous derivation also exists for quasi-2D confinement [65].

A derivation of elastic CIR in quasi-1D confinement is presented which differs from the original work [35] but delivers a deeper insight into the mechanism of elastic CIR

[1] This lead to the name *confinement-induced* resonances.

[2] The fermionization of 1D strongly repulsively interacting bosons follows from the existence of a mapping on a system of non-interacting fermions. The eigenfunctions of the interacting Bose system are exactly provided by the mapping

$$\psi_B(z_1, \ldots, z_n) = |\psi_F(z_1, \ldots, z_n)| \tag{2.1}$$

where ψ_F are the eigenstates of the ideal one-dimensional Fermi gas, i. e. Slater determinants. Hence, all local observables A_{local} will take the same value calculated with ψ_B or ψ_F,

$$\langle \phi_B | A_{\text{local}} | \phi_B \rangle = \langle \phi_F | A_{\text{local}} | \phi_F \rangle \,. \tag{2.2}$$

For further details see, e. g., [69].

[3] In the original work, in fact, the longitudinal direction is unbound, resulting in a transversally confined waveguide.

and why they are not suitable to describe molecule formation, losses and heating as previously assumed.

2.1 1D spectrum of two harmonically trapped ultracold atoms

For two harmonically trapped homonuclear atoms in the same electronic state the c.m. and rel. motions decouple and it suffices to consider the rel. motion Hamiltonian. The c.m. motion Hamiltonian is the well known harmonic oscillator. Approximating the short-range atomic interaction by the contact potential

$$V_{\mathrm{1D}} = g_{\mathrm{1D}}\delta(x) \quad , \tag{2.3}$$

the 1D Hamiltonian written in dimensionless units of energies in $\hbar\omega$ and lengths in d_{ho} given in Eq. (1.7) reads

$$H = -\frac{1}{2}\frac{d^2}{dx^2} + \frac{1}{2}x^2 + V_{\mathrm{1D}}(x) \quad . \tag{2.4}$$

In contrast to the 3D Fermi-Huang pseudopotential of Eq. (1.32), the pure 1D interaction strength[4]

$$g_{\mathrm{1D}} = -\frac{1}{a_{\mathrm{1D}}} \tag{2.5}$$

is inversely proportional to the pure 1D s-wave scattering length a_{1D} and a regularization of the potential is not necessary.

The solution for the energy spectrum of the Hamiltonian in Eq. (2.4) is, e. g., presented in [62, 70]. It is implicitly given in dependence of the scattering length by

$$a_{\mathrm{1D}} = \frac{\Gamma\left(-\frac{E}{2}+\frac{1}{4}\right)}{2\Gamma\left(-\frac{E}{2}+\frac{3}{4}\right)} \quad . \tag{2.6}$$

The resulting energy spectrum is shown in Figure 2.1 [5]. A property different to 3D is that the bound state only exists for negative values of the 1D interaction strength

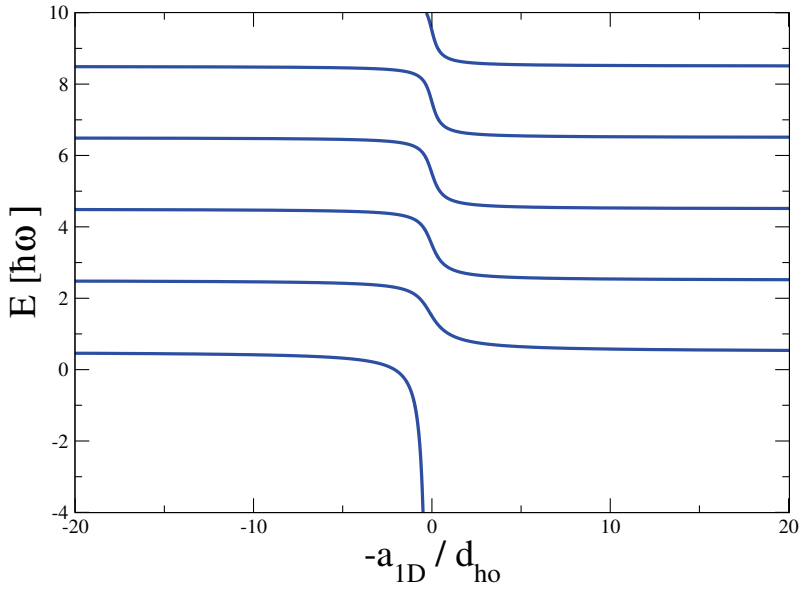

Figure 2.1: 1D eigenenergy spectrum of two atoms confined in a harmonic trap that are subject to s-wave interaction via a δ potential.

and reaches asymptotically the $a_{1\mathrm{D}} = 0$ axis. Formula Eq. (2.6) is only valid for the even eigenstates of the system. The odd ones vanish at zero and are therefore not affected by the delta potential because $\delta(x - x_0)f(x) = f(x_0)$ and $x_0 = 0$. This reflects the fact that identical fermions are not subject to s-wave interaction.

2.2 3D spectrum of two harmonically trapped ultracold atoms

An analytical description for an isotropic 3D system of two homonuclear atoms interacting via the Fermi-Huang δ-pseudopotential was first given in [62]. A treatment involving a confinement with a single anisotropy, i. e. the transversal frequencies $\omega_x = \omega_y$ differ from the longitudinal one ω_z, is found in [70]. For the following consideration the solutions of [70] are adopted.

[4] In physical units $g_{1\mathrm{D}} = -\hbar^2/(\mu a_{1\mathrm{D}})$.

[5] The relative motion energies of two non-interacting atoms are obtained for $g_{1\mathrm{D}} = 0$, i. e. for $a_{1\mathrm{D}} \to \infty$. They are given by $\Gamma(-\frac{E}{2} + \frac{1}{4}) = \infty$ which can be resolved to $E = 2n + 1/2,\ n \in \mathbb{N}^0$ using that the Γ function has no zeros for real arguments and has singularities of order one for the negative integers including zero. This directly follows from the product representation [71]

$$\frac{1}{\Gamma(z)} = \lim_{n\to\infty} \frac{n^{-z}}{n!} z(z+1)\cdots(z+n) \quad . \tag{2.7}$$

By an analogous argument, the eigenenergies at unitarity $g_{1\mathrm{D}} = \infty \Leftrightarrow a_{1\mathrm{D}} = 0$ are found to be $E = 2n + 3/2,\ n \in \mathbb{N}^0$.

The 3D rel. motion Hamiltonian

$$H = -\frac{1}{2}\nabla^2_{\mathbf{r}} + \frac{1}{2}\mu(\eta^2\rho^2 + z^2) + 2\pi a\delta(\vec{r})\frac{\partial}{\partial r}r \quad , \tag{2.8}$$

written in dimensionless units of energies in $\hbar\omega_z$ and lengths in $d_z = d_{\mathrm{ho},z} = \sqrt{\hbar/(\mu\omega_z)}$, contains $\rho^2 = x^2 + y^2$ and $\eta = \omega_\perp/\omega_z$. The quasi-1D regime is characterized by an elongated cigar-shape trap, i. e. $\eta \gg 1$. By expanding the wavefunctions in a basis of 2D harmonic-oscillator eigenfunctions the implicit energy equation

$$-\frac{\sqrt{\pi}}{a} = \mathcal{F}\left(-\frac{\epsilon}{2}\right) \tag{2.9}$$

for the energy spectrum in dependence of the 3D s-wave scattering length is found [70] with

$$\mathcal{F}(x) = \int_0^\infty dt\left(\frac{\eta e^{-xt}}{\sqrt{1-e^{-t}}(1-e^{-\eta t})} - \frac{1}{t^{\frac{3}{2}}}\right), \quad x > 0. \tag{2.10}$$

The energies ϵ are the eigenenergies of the system in units of $\hbar\omega_z$, shifted by the asymptotic ground state energy $E_0 = \frac{1}{2} + \eta$, $\epsilon = E - E_0$. The integral is valid for arbitrary values of η including isotropic ($\eta = 1$), quasi-1D ($\eta \gg 1$), and quasi-2D ($\eta \ll 1$) confinement geometries. The integral is only valid for positive values of x which corresponds to the bound state energies $\epsilon < 0$. To extend the result the recursion relation[6] given in [70]

$$\mathcal{F}(x) - \mathcal{F}(x+\eta) = \int_0^\infty dt\frac{\eta \mathrm{e}^{-xt}}{\sqrt{1-\mathrm{e}^{-t}}} = \eta\sqrt{\pi}\frac{\Gamma(x)}{\Gamma(x+\frac{1}{2})} \tag{2.11}$$

can be applied.

For the special case of an isotropic confinement ($\eta = 1$) [62, 70] the equations Eq. (2.9) and Eq. (2.10) reduce to

$$a = \frac{1}{\sqrt{2}}\frac{\Gamma\left(-\frac{E}{2}+\frac{1}{4}\right)}{\Gamma\left(-\frac{E}{2}+\frac{3}{4}\right)} \quad . \tag{2.12}$$

The analytical solutions of the isotropic 3D and pure 1D spectra have a similar form. This is an artifact of the consideration of s-wave scattering where the centrifugal part ($\propto l(l+1)$) of the radial Schrödinger equation vanishes. The resulting radial differential equation is an effective 1D harmonic oscillator. In order to derive the

[6] An integral equation similar to Eq. (2.10) exists also in the case of full anisotropy, $\omega_x \neq \omega_y \neq \omega_z$, see [72]. However, the validity of the formula reduces to the bound state because such a recursion relation is missing.

elastic CIR position, a connection between the 1D spectrum and the 3D spectrum in strongly anisotropic (quasi-1D) confinement needs to be established. This can be achieved by the *quasi-1D approximation*.

2.3 Quasi-1D approximation

As demonstrated in [70], in the quasi-1D regime the function $\mathcal{F}$ in Eq. (2.10) can be simplified to

$$\mathcal{F}(x) = \sqrt{\pi\,\eta}\,\zeta_H\left(\frac{1}{2}, \frac{x}{\eta}\right), \quad x \gtrsim \eta \tag{2.13}$$

using the fact that for $\eta \gg 1$, $\sqrt{1-\mathrm{e}^{-t}} \approx \sqrt{t}$. Here, ζ_H denotes the Hurwitz Zeta function $\zeta_H(a,b) = \sum_{k=0}^{\infty}(k+b)^{-a}$. Again, this formula is only valid for the bound state. To extend its validity to higher energies the recurrence formula Eq. (2.11) is applied once leading to

$$\mathcal{F}(x) = \sqrt{\pi\,\eta}\,\zeta_H\left(\frac{1}{2}, 1+\frac{x}{\eta}\right) + \frac{\eta\sqrt{\pi}\,\Gamma(x)}{\Gamma\left(x+\frac{1}{2}\right)} \quad . \tag{2.14}$$

This formula is now valid in the range $\frac{E_0-2\hbar\omega_\perp}{\hbar\omega_\perp} < \frac{E}{\hbar\omega_\perp} < \frac{E_0+2\hbar\omega_\perp}{\hbar\omega_\perp}$. Repeated application of the recurrence formula leads to the general expression

$$\mathcal{F}(x) = \sqrt{\pi\,\eta}\,\zeta\left(1/2, n+\frac{x}{\eta}\right) + n\frac{\eta\sqrt{\pi}\,\Gamma(x)}{\Gamma(x+1/2)}, \quad n \in \mathbb{N},\, n > 2 \tag{2.15}$$

which is valid for $\frac{E_0-2(n-1)\hbar\omega_\perp}{\hbar\omega_\perp} < \frac{E}{\hbar\omega_\perp} < \frac{E_0+2n\hbar\omega_\perp}{\hbar\omega_\perp}$. With these formulas the quasi-1D spectrum for all energies can be calculated. The quasi-1D approximation is already very well satisfied for $\eta = 10$, e. g., in the strongly correlated regime, at $d_\perp/a = 1.46$, the first 6 trap states and the bound state agree to at least five digits.

Having in mind that the equation for the bound state in quasi-1D is given by

$$-\frac{\sqrt{\pi}}{a} = \sqrt{\pi\,\eta}\,\zeta_H\left(\frac{1}{2}, -\frac{\epsilon}{2\eta}\right), \tag{2.16}$$

the function $\mathcal{F}_n^b(x)$

$$\mathcal{F}_n^b(x) = \sqrt{\pi\,\eta}\,\zeta_H\left(1/2, n+\frac{x}{\eta}\right) \tag{2.17}$$

contained in Eq. (2.15) represents the *bound state shifted by* $2n\hbar\omega_\perp$. Identifying,

moreover, the pure 1D scattering length $a_{1\mathrm{D}}$ in Eq. (2.15), it can be rewritten as

$$-\frac{\sqrt{\pi}}{a} = \mathcal{F}_n^b\left(-\frac{\epsilon}{2}\right) + 2n\eta\sqrt{\pi}\, a_{1\mathrm{D}}\left(-\frac{\epsilon}{2}\right) \quad n \in \mathbb{N} \quad . \tag{2.18}$$

This equation is central to understand remarkable properties of the quasi-1D spectrum and the key equation for identifying elastic CIR. First, the complete spectrum can be decomposed into a bound-state part and a part containing the 1D scattering length. It demonstrates that the spectrum is periodic with periodicity $2\hbar\omega_\perp$. Moreover, astonishingly, even far in the trap-state regime ($\epsilon \gg 0$) the information of the bound state is still contained in the spectrum. These properties become visible in the quasi-1D spectrum shown in Figure 2.2 where it can be seen how the inflection points, which are the points were the curvature of the energy branches change sign, of the trap states lie on the shifted bound part and that the spectrum is periodic. These properties are unique: Neither the isotropic 3D nor the pure 1D (see, Figure 2.1) spectra show such features. How these properties are responsible for the occurrence of elastic CIR will be demonstrated next.

2.4 Resonance position and mechanism

The elastic CIR is defined by a divergence of $g_{1\mathrm{D}}$ which is equivalent to $a_{1\mathrm{D}} = 0$. Staring from Eq. (2.15) for $n = 1$ and approximating that for a strongly anisotropic quasi-1D confinement $\epsilon \ll \eta$, the bound state part in Eq. (2.15) can be simplified [70] to

$$\begin{aligned}\mathcal{F}_1^b\left(\frac{-\epsilon}{2}\right) &= \sqrt{\pi\,\eta}\,\zeta_H\left(\frac{1}{2}, 1 - \frac{\epsilon}{2\eta}\right) \\ &\approx \sqrt{\pi\,\eta}\,\zeta_H\left(\frac{1}{2}, 1\right) \\ &= \sqrt{\pi\,\eta}\,\zeta\left(\frac{1}{2}\right) \quad .\end{aligned} \tag{2.19}$$

Substituting this into Eq. (2.15) and rewriting the expression leads to

$$a_{1\mathrm{D}} = -\frac{1}{2\eta a} - \frac{\zeta(\frac{1}{2})}{2\sqrt{\eta}} \tag{2.20}$$

or in terms of $g_{1\mathrm{D}}$ (in physical units)

$$g_{1\mathrm{D}} = \frac{2a\hbar^2}{\mu d_\perp^2}\frac{1}{1 - C\frac{a}{d_\perp}} \tag{2.21}$$

where $C = -\zeta(\frac{1}{2}) \approx 1.46$. This is the relation found in the original work [35]. Hence, in a quasi-1D confinement with no anisotropy in the transversal directions ($\omega_x = \omega_y$) the elastic CIR is at $d_\perp/a \approx 1.46$.

Using the property that the quasi-1D spectrum decomposes into shifted bound parts and a part containing the 1D scattering length, an interpretation of the Olshanii resonance can be given. Substituting the resonance position into Eq. (2.18) gives

$$\begin{aligned} -\zeta\left(\frac{1}{2}\right) &= -\frac{1}{\sqrt{\eta}\,\zeta(\frac{1}{2})\,\sqrt{\pi}}\,\mathcal{F}_n^b\left(-\frac{\epsilon}{2}\right) \\ &= -\zeta_H\left(\frac{1}{2}, n - \frac{\epsilon}{2\eta}\right) \end{aligned} \tag{2.22}$$

which determines the CIR position in terms of energies. From the connection between the Hurwitz Zeta and the Riemann Zeta function, $\zeta\left(\frac{1}{2}\right) = \zeta_H\left(\frac{1}{2}, 1\right)$, the resonance condition

$$n - \frac{\epsilon}{2\eta} = 1 \Rightarrow \epsilon = 2\eta(n-1) \tag{2.23}$$

follows. ϵ is just given as the energy of the system minus the asymptotic bound-state energy E_0 which is given in physical units as $E_0 = \hbar\omega_\perp + \frac{1}{2}\hbar\omega_z$. This directly leads to the expression for the resonance energies $E^{(\mathrm{R})}$ that are given in physical units as

$$E^{(\mathrm{R})} = 2\hbar\omega_\perp(n-1) + E_0 \quad . \tag{2.24}$$

Hence, the elastic CIR occurs at positions where the shifted bound-state energies coincide with the free energies of the ground trap states. This can be regarded as a mechanism for the elastic CIR. It is illustrated in Figure 2.2.

With Eq. (2.24) it is possible to draw similarities between the mechanism of elastic CIR and Feshbach resonances[7]. In a two channel picture, a Feshbach resonance occurs where the energy of a closed channel matches the continuum threshold of an open channel. In the case of the elastic CIR, the shifted bound part energy which is an implicit part of the spectrum matches the energy of the ground trap state. The connection gets even clearer when considering a perfect quasi-1D system where $\eta \to \infty$ which can be obtained by $\omega_z \to 0$. Then, the energy of the lowest trap state marks a continuum threshold and the elastic CIR occurs where the bound state in a closed channel becomes degenerate in energy with the continuum threshold of the open scattering channel.

The drawn connection of elastic CIR and Feshbach resonances had important

[7] An analogous picture can be deduced by an operator approach presented in [36].

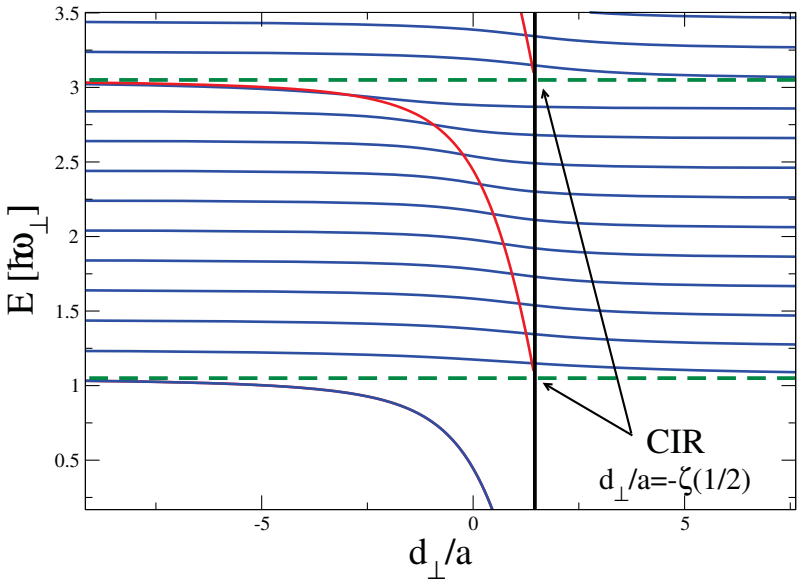

Figure 2.2: Eigenenergy spectrum of two ultracold atoms confined to a quasi-1D harmonic trap (blue curves). The bound state shifted (by hand) by $2n\hbar\omega$ is indicated in red. The elastic CIR occurs at the position (black vertical line) where the (n times shifted, $n > 0$) bound states (red) match the ($n-1$ times shifted) free ground-state energies (green dashed lines).

consequences. It lead to the erroneous assumption that similar to a Feshbach resonance, at an elastic CIR a bound state of the system couples to the state in the open channel. This is, however, *not* the case. In fact, the shifted bound part appearing in Eq. (2.18) is no eigenstate of the full rel. motion Hamiltonian. Moreover, there exists no coupling of the shifted bound part to the trap state. The appearance of this state as a part of the rel. motion Hamiltonian in quasi-1D is due to the mathematical fact that the 2D harmonic oscillator eigenfunctions all have the same absolute value at zero, which directly follows from the analogous property of the Legendre polynomials.

2.5 Experimental search for elastic confinement-induced resonances

A diverging parameter, like g_{1D} at the elastic CIR, makes always an interesting case for physicists as extraordinary behavior is expected. At the elastic CIR, the divergence of g_{1D} leads to a fermionization of a bosonic gas which can be described by a mapping of the strongly interacting bosons on a system of non-interacting fermions (see Section 2). Although the local behavior of an ultracold bosonic quantum gas at

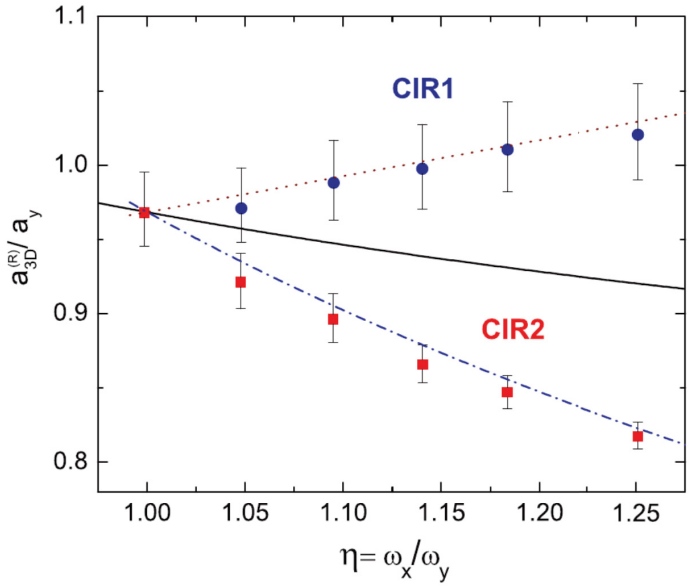

Figure 2.3: Plot copied from [40]. Resonance positions as a function of the transversal anisotropy $\eta = \frac{\omega_x}{\omega_y}$. The experimental results (symbols) are compared with the theory of elastic CIR (solid line). The experimental data are shifted by a constant offset such that the measured resonance position in the symmetric limit ($\eta = 1$) is equal to the known theoretical prediction.

the elastic CIR should be well described by the one of non-interacting fermions, i. e. a not very spectacularly behavior, the seeming Feshbach-type mechanism explained in the previous section led to the assumption that processes take place at the elastic CIR similar to those at a Feshbach resonance, e. g., particles losses and heating. In fact, the graphical illustrations of the CIR mechanisms in [36, 39] where the shifted bound state is drawn into the energy spectra "by hand" led to the erroneous assumption that this state is an transversally excited bound state of the quasi-1D system triggering a Feshbach resonance. This picture is, however, incorrect since this state is no eigenstate of the full Hamiltonian as can be easily seen from the quasi-1D spectrum shown in Figure 2.2. Therein, the shifted bound parts (red curves) are not contained in the eigenenergy spectrum (blue curves), i. e. the shifted bound parts are no eigenstates.

Nevertheless, in the Innsbruck experiment [39] losses and heating were measured in an ultracold gas of cesium atoms in the vicinity of the elastic CIR. The effective 1D interaction strength was tuned by a variation of an external magnetic field around a magnetic Feshbach resonance. In quasi-1D confinement, the experiment found a resonance at a position compatible with the prediction of the theory of elastic CIR, i. e. at $d_\perp/a \approx 1.46$ (see Eq. (2.21)), if isotropic transversal confine-

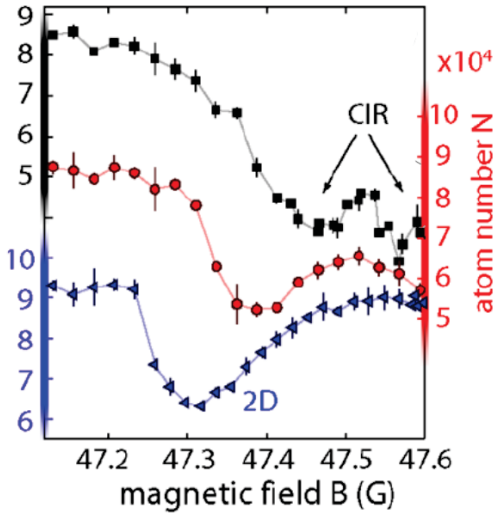

Figure 2.4: Plot copied from [39] and slightly modified. Measurement of the atom number in an ultracold gas of cesium atoms in the transition from quasi-1D to quasi-2D confinement. As the horizontal lattice is ramped down, CIR_2 shifts and persists, while CIR_1 disappears.

ment was adopted which, of course, seemed to verify the explanation in terms of an elastic CIR. However, two essential observations where made in disagreement to the expectation of the theory of elastic CIR. A key measurement of the experiment was the detection of loss features in quasi-1D confinement for different values of the transversal anisotropy. A *splitting* of the resonances was detected for an anisotropic transversal confinement. An analysis by Peng *et. al.* [40] demonstrated that there exists only a single CIR no matter whether the transversal confinement is isotropic or not.

In Figure 2.3 the position of the elastic CIR together with measured loss positions are visible showing the splitting of measured loss features and a single elastic CIR for variable transversal anisotropy[8]. The fact that there only exists a single elastic CIR can be understood on the basis of the CIR mechanism worked out in Section 2.4: The CIR occurs at a position where the shifted bound part crosses the trap state threshold. Independent of the transversal confinement there only exists a single bound state as a solution of the rel. motion Schrödinger equation, thus there exists only a single elastic CIR.

Another observation in the Innsbruck experiment that cannot be explained by the theory of elastic CIR is the behavior in the transition to a quasi 2D. When tuning the system from a quasi-1D to a quasi-2D confinement, in the experiment one of the

[8]Noteworthy, in the plot shown in Figure 2.3 (taken from [40]) the experimental data were adjusted by a constant offset to match the resonance position for the isotropic case. However, without this adjustment the position is still in good agreement as visible in [39].

two resonances sustains for the quasi-2D regime at *positive* values of the scattering length (Figure 2.4). The theory of elastic CIR, however, predicts one resonance for a wide range and then jumps to a resonance at *negative* scattering lengths for the quasi-2D regime [40].

At the latest when the theory of elastic CIR was experimentally directly confirmed in 2D by radio-frequency spectroscopy in [66], it was well established in the community. Consequently, the contradicting findings of the Innsbruck experiment created a great deal of attention and confusion. Based on the fact that the position of the loss resonance for an transversely isotropic quasi-1D confinement is accurate, most researchers in the field persisted on the theory of elastic CIR as an explanation for the losses [68]. At the same time, alternative explanations for the discrepancies were formulated. In [73] an explanation for the splitting loss resonances based on multichannel effects is presented. Also many-body and cesium specific effects were speculated on [40]. Finally, as will be demonstrated in the following sections, all the losses in [39] are caused by c.m.-rel. motion coupling of an unbound atom pair to a c.m. excited bound state at so-called *inelastic* CIR.

3 Inelastic confinement-induced resonances

Several excellent groups and researchers tried to find an explanation for the contradicting results of the theory of elastic CIR and the loss features found in the Innsbruck experiment [39]. Nevertheless, the origin of discrepancies remained mysterious. Looking back, this is not surprising, because the key to the solution is to abandon an absolute standard approximation in ultracold atomic gases – the harmonic approximation. If the external confinement is sufficiently deep, e. g., in case of an optical lattice $E_r/V \ll 1$ where $E_r = \frac{\hbar^2 k^2}{2m}$ is the recoil energy and V the potential depth, the trapping potential is routinely approximated by a harmonic potential. All proposals to explain the losses [39, 40, 68, 73] (as briefly described in the previous Section 2.5) were making use of the harmonic approximation. The consequence of a harmonic theory, the decoupling of c.m. and rel. motion was not questioned, since the c.m.-rel. coupling is negligible in energy compared to the interaction. Moreover, the first work [74] explicitly discussing a possible molecule formation due to the anharmonicity-induced c.m.-rel. coupling concludes that the dimer-production rate is too small to be significant in an experiment. This conclusion stems from the fact that model investigates the coupling of a trap state to a highly excited bound state. In the work a direct coupling to the continuum is investigated by describing the c.m. part of the bound-state wavefunction by a spherical wave, i. e. a continuum state. As will be demonstrated in Chapter 4, however, the coupling to highly excited bound states becomes very small which lead to the conclusion of negligible dimer-production rate in [74].

Although not further elaborated on in the present work, it should be mentioned that c.m.-rel. coupling is also present in the case of heteronuclear atoms [75, 76] even in a harmonic confinement. Moreover, the occurrence of Feshbach-type resonances due to the c.m.-rel. coupling was discussed in [77], their behavior in a superlattice was characterized in [78]. In mixed dimensions, the experiment performed in [79] also detected inelastic loss resonances for a variation of the scattering length. In fact, the experiment was performed prior to the Innsbruck experiment [39]. While at the time the experiment was performed, the origin of the losses was theoretically not completely comprehended, the explanation of the Innsbruck loss experiment in terms of c.m.-rel. coupling resonances that will be presented in Chapter 5 also

delivers the explanation for the losses in mixed dimensions in [79]. The behavior of resonances (including both CIR and inelastic CIR) within a quasi-1D lattice model was considered in [80].

The mechanism of inelastic CIR illustrated in the next section is on the first glance similar to the one promoted for elastic CIR, which lead to additional confusion. However, when analyzing the mechanism in more detail it turns out to be distinctively different.

3.1 Mechanism of inelastic confinement-induced resonances

In rel. and c.m. coordinates (see Eqs. (1.38) and (1.39)) the Hamiltonian of two identical particles in an external trap potential can be written as

$$H(\mathbf{r},\mathbf{R}) = H_{\text{rel.}}(\mathbf{r}) + H_{\text{c.m.}}(\mathbf{R}) + W(\mathbf{r},\mathbf{R}) \tag{3.1}$$

$$H_{\text{rel.}}(\mathbf{r}) = T_{\text{rel.}}(\mathbf{r}) + V_{\text{rel.}}(\mathbf{r}) + U_{\text{int}}(r) \tag{3.2}$$

$$H_{\text{c.m.}}(\mathbf{R}) = T_{\text{c.m.}}(\mathbf{R}) + V_{\text{c.m.}}(\mathbf{R}) \tag{3.3}$$

where $T_{\text{rel.}}$ and $T_{\text{c.m.}}$ denote the kinetic-energy operators of the rel. and c.m. motion, respectively, and $V_{\text{rel.}}$ and $V_{\text{c.m.}}$ are the separable parts of the potential energy. Thus, W contains only the non-separable terms of the potential energy. $U_{\text{int}}(r)$ is the interparticle interaction.

In Figure 3.1 the eigenenergy spectrum of the Hamiltonian Eq. (3.1) for two ultracold atoms interacting via the δ pseudopotential of Eq. (1.32) is shown. The atoms are confined to an isotropic, i. e. spherically symmetric, harmonic trap potential. The energies are plotted for a varying inverse scattering length d_{ho}/a. The spectrum of $H_{\text{rel.}}$ of Eq. (3.2) contains a bound state $|\psi_{\text{b}}\rangle$ bending down asymptotically to negative infinity for $1/a \to +\infty$ and trap states, the energetically lowest one denoted as $|\psi_1\rangle$. In case of a harmonic trap potential, the coupling W between the c.m. and the rel. motion vanishes. Hence, in order to obtain the spectrum of the full Hamiltonian Eq. (3.1) the c.m. energies are added to each state of the rel. spectrum, resulting in the right part of Figure 3.1. Each state of the rel. spectrum appears now with an infinite series of c.m. excitations. Crossings appear between c.m. excited bound states, e. g., $|\psi_{\text{b}}\Phi_{(2,0,0)}\rangle$, and trap states, e. g., the lowest trap state $|\psi_1\Phi_{(0,0,0)}\rangle$. For a vanishing c.m.-rel. coupling ($W = 0$) the states cross diabatically as indicated in the inset of Figure 3.1 and by black dashed lines in the lower part. A coupling $W \neq 0$, allows for an adiabatic transition (solid line in the lower part of Figure 3.1) of the trap state that is usually in the c.m. ground state into a

molecular state with c.m. excitation.

The c.m.-rel. coupling introduces a Feshbach-type resonance at the crossing position. The coherent occupation of the bound state at the resonance is only possible because the excess binding energy can be transferred into c.m. excitation energy mediated by the anharmonicity of the confining potential. This redistribution of binding energy to kinetic energy is an inelastic process. Hence, the c.m.-rel. coupling resonances are denoted as *inelastic* confinement-induced resonances.

The similarities and differences of inelastic and elastic CIR become clear now. The elastic CIR are based on the properties of the energy spectrum of a system of reduced dimensionality, see Section 2.4. The decomposition of the quasi-1D energy spectrum revealed that the elastic CIR occurs where the shifted bound part of the rel. motion Hamiltonian crosses the trap state threshold. Although this reminds on a Feshbach resonance, this bound part is no eigenstate of the full rel. motion Hamiltonian, does not couple, and does hence not lead to a true Feshbach resonance. In contrast, an inelastic CIR takes place where the bound state with a c.m. excitation crosses a trap state. The bound state is a true eigenstate of the system and a coupling exists due to the anharmonicity of the external confinement. Moreover, not only a single resonance, as in case of the elastic CIR, but a plethora of resonances occur, because there exists an infinite number of c.m. excitations.

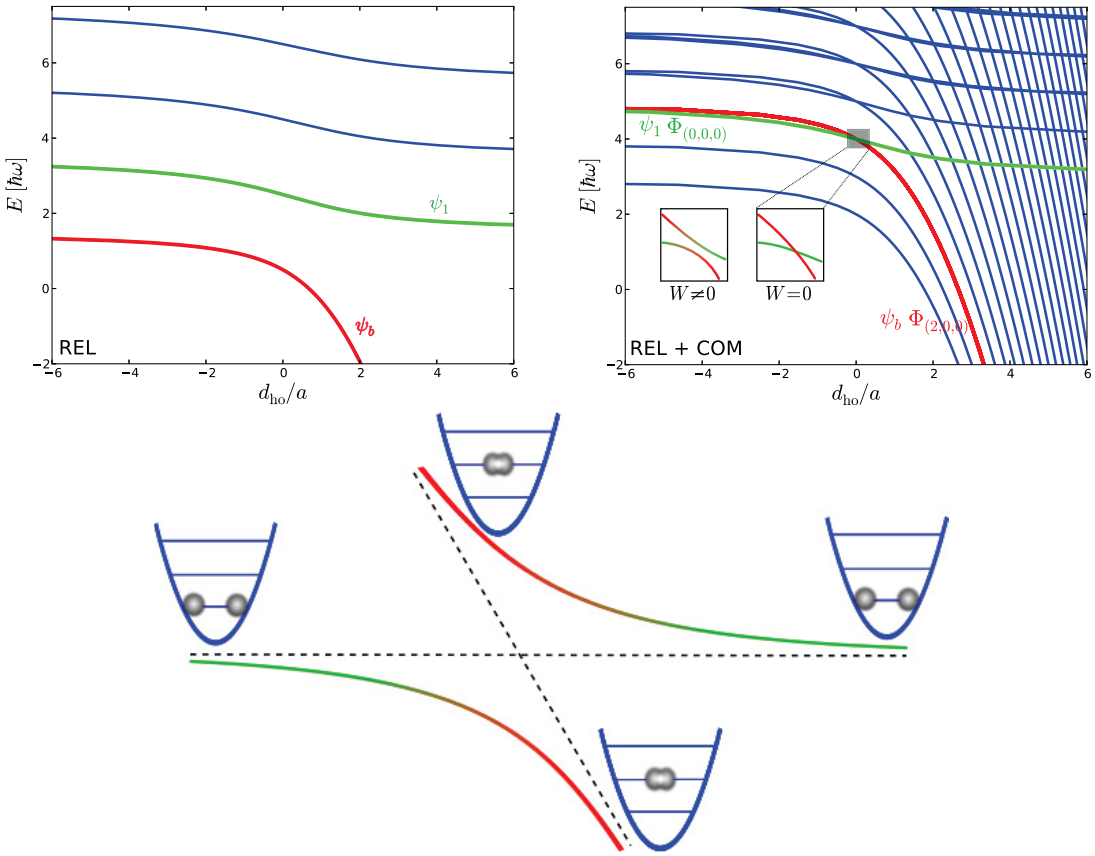

Figure 3.1: Eigenenergy spectrum of two ultracold atoms in an isotropic harmonic trap interacting via a δ pseudopotential [62, 70] for a varying s-wave scattering length a (upper part). The upper left panel shows the energy of the rel. motion Hamiltonian $H_{\mathrm{rel.}}$, the right one the energy of the rel. and c.m. motion Hamiltonian $H_{\mathrm{rel.}} + H_{\mathrm{c.m.}}$. Introducing a coupling between the rel. and c.m. motion makes the crossings become avoided as illustrated in the lower part as solid lines, the black dashed lines indicate the diabatic curves. Passing through the crossing adiabatically allows for a transformation of the bound state with c.m. excitation into a trap state in the c.m. ground state. The plot is also presented in [43].

3.2 C.m.-rel. coupling model – resonance positions

While a full six-dimensional treatment of the two-body problem involving a c.m.-rel. coupling is possible [81] and also performed for this thesis, it is numerically demanding. Hence, a perturbative model is introduced to predict the position and coupling strengths of inelastic CIR in single well potentials in closed-form expressions.

For c.m.-rel. coupling resonances to be present, of course, a c.m.-rel. coupling must be introduced. Therefore, the harmonic approximation has to be abandoned. Optical-lattice potentials [6] are widely used in ultracold experiments and offer a great degree of flexibility and control. In the case of an optical lattice in three spatial directions as given in Eq. (1.37) the potential separated in rel., c.m., and coupling term reads

$$V_{\mathrm{rel.}}(\mathbf{r}) = 2 \sum_{j=x,y,z} V_j \sin^2\left(\frac{1}{2} k_j r_j\right) \tag{3.4}$$

$$V_{\mathrm{c.m.}}(\mathbf{R}) = 2 \sum_{j=x,y,z} V_j \sin^2\left(k_j R_j\right) \tag{3.5}$$

$$W(\mathbf{r},\mathbf{R}) = -4 \sum_{j=x,y,z} V_j \sin^2\left(\frac{1}{2} k_j r_j\right) \sin^2\left(k_j R_j\right) \quad . \tag{3.6}$$

In a deep optical lattice, tunneling between neighboring wells is suppressed and the potential can be regarded as a stack of single-well potentials. Starting from a Taylor expansion of the optical lattice potential, a single-well potential including c.m.-rel. coupling can be obtained by an expansion up to the sixth degree. A separation of the expansion in rel., c.m., and coupling term

$$V_{\mathrm{rel.}}(\mathbf{r}) = \sum_{j=x,y,z} V_j \left[\frac{1}{2} k_j^2 r_j^2 - \frac{1}{24} k_j^4 r_j^4 + \frac{1}{720} k_j^6 r_j^6\right] \tag{3.7}$$

$$V_{\mathrm{c.m.}}(\mathbf{R}) = \sum_{j=x,y,z} V_j \left[2 k_j^2 R_j^2 - \frac{2}{3} k_j^4 R_j^4 + \frac{4}{45} k_j^6 R_j^6\right] \tag{3.8}$$

$$W(\mathbf{r},\mathbf{R}) = \sum_{j=x,y,z} V_j \left[-k_j^4 r_j^2 R_j^2 + \frac{1}{3} k_j^6 r_j^2 R_j^4 + \frac{1}{12} k_j^6 r_j^4 R_j^2\right], \tag{3.9}$$

respectively, shows that the quartic terms all have a negative sign which makes the expansion to the sextic terms necessary. Otherwise, (for an expansion to the 4th degree) an unphysical continuum occurs in the spectrum reaching in energy towards negative infinity.

In order to develop a formula for the resonance positions, it is first assumed that the (global) influence of the anharmonicity on the eigenenergies is negligible.

Hence, the harmonic approximation is used and the position of a c.m.-rel. coupling resonance is determined by the position of the energy crossing of the c.m. excited bound state $|\psi_\mathrm{b}\Phi_\mathbf{n}\rangle$, where $\mathbf{n} = (n_x, n_y, n_z)$ is the quantum number of the c.m. excitation, that separates spatially for an optical-lattice potential, and a trap state $|\psi_\mathrm{t}\Phi_\mathbf{m}\rangle$ as illustrated in Figure 3.1.

The energy $E_\mathrm{b}^\mathrm{rel.}$ of the bound state $|\psi_\mathrm{b}\rangle$ in a harmonic confinement of arbitrary anisotropy in terms of the scattering length a is given implicitly by [72]

$$\frac{\sqrt{\pi}d_y}{a} = -\int_0^\infty \left(\frac{\sqrt{\eta_x\eta_z}\mathrm{e}^{\frac{t\epsilon}{2}}}{\sqrt{(1-\mathrm{e}^{-t})\,(1-\mathrm{e}^{-\eta_x t})\,(1-\mathrm{e}^{-\eta_z t})}} - t^{-\frac{3}{2}} \right) dt \tag{3.10}$$

where $\epsilon = (E_\mathrm{b}^\mathrm{rel.} - E_0)/(\hbar\omega_y)$, $E_0 = \frac{\hbar}{2}(\omega_x + \omega_y + \omega_z)$, $\eta_x = \omega_x/\omega_y$, and $\eta_z = \omega_z/\omega_y$. The difference to other equations for the bound state, like e. g. in [62] (valid for a 3D isotropic confinement), in [70] (valid for a 3D harmonic confinement of single anisotropy) or in [40] (valid for only transversally trapped atoms), is that it is valid for an arbitrarily anisotropic 3D confinement.

A general expression for the eigenenergies of the trap states in an arbitrarily anisotropic confinement, i. e. states above $E_\mathrm{th} = \frac{\hbar}{2}(\omega_x + \omega_y + \omega_z)$, is not known yet. For ultracold temperatures the occupation of excited states is suppressed. Hence, in the following only crossings with the first trap state $|\psi_1\rangle$ are considered. Assuming without loss of generality that $\min(\omega_x, \omega_y, \omega_z) = \omega_z$ (unless stated differently), the eigenenergy $E_1^\mathrm{rel.}$ of $|\psi_1\rangle$ lies in the interval $[E_\mathrm{th}, E_\mathrm{th} + 2\hbar\omega_z)$. In the case of an isotropic harmonic confinement the crossing between a singly (evenly) excited bound state with the first trap state occurs at

$$E_1^\mathrm{rel} = E_\mathrm{th} + \hbar\omega_z \tag{3.11}$$

which is thus chosen for the model as an approximation of the energy of the first trap state. For crossings with higher trap states, the model can be extended by choosing the energy of such a trap state appropriately.

In the case of an external confinement that decouples spatially, e. g., expansions of an optical-lattice potential, the eigenstates of the c.m. Hamiltonian factorize as $\Phi_\mathbf{n}(\mathbf{R}) = \phi_{n_x}(X)\,\phi_{n_y}(Y)\,\phi_{n_z}(Z)$ with $\mathbf{n} = (n_x, n_y, n_z)$ and eigenenergies $E_\mathbf{n}^\mathrm{c.m.} = \sum_{j=x,y,z}\hbar\omega_j(n_j + \frac{1}{2})$. When combining rel. and c.m. motion, the energies of the bound states become $E_\mathrm{b}^\mathrm{rel.}(a) + E_\mathbf{n}^\mathrm{c.m.}$ while the energy of the lowest trap state is given by $E_1^\mathrm{rel.} + E_{(0,0,0)}^\mathrm{c.m.}$. Crossings between a c.m. excited bound state and the lowest trap state are determined by

$$E_\mathrm{b}^\mathrm{rel.} = E_1^\mathrm{rel.} - \Delta_\mathbf{n} \tag{3.12}$$

where

$$\Delta_{\mathbf{n}} = E^{\mathrm{cm}}_{\mathbf{n}} - E^{\mathrm{cm}}_{(0,0,0)} \tag{3.13}$$

is the c.m. excitation. The corresponding scattering length at the crossing is obtained from Eq. (3.10).

So far all energies were treated within the harmonic approximation. It will be demonstrated that this harmonic version of the model gives in some cases already good quantitative results. However, for the c.m. excitations $\Delta_{\mathbf{n}}$ higher c.m. states are involved. Additionally, for small $\Delta_{\mathbf{n}}$ the bound state crosses the trap state for small positive d_{ho}/a or even negative d_{ho}/a where the two states cross with a small difference in the slope, see Figure 3.1. For such crossings the position is very sensitive to the energies of the involved states. Hence, the energy of the first trap state as well as the c.m. excitation Δ must be corrected. Therefore, the anharmonicity is treated within first order perturbation theory. The unperturbed system is the 1D harmonic oscillator with corresponding wavefunctions given in Eq. (3.22). The anharmonic terms of the sextic potential,

$$V_j^{(\mathrm{a})}(R_j) = -\frac{1}{24}\frac{\hbar\omega_j}{V_j}R_j^4 + \frac{1}{720}\frac{\hbar^2\omega_j^2}{V_j^2}R_j^6 \quad , \tag{3.14}$$

are treated as a perturbation. Here, the potential is written in dimensionless units, i. e. energies in $\hbar\Omega_j$ (Ω given by Eq. (1.44)) and lengths in $\sqrt{\frac{\hbar}{M\Omega_j}}$, where $M = 2m$. For simplicity, only a single spatial direction is considered in the following and the subscript j is omitted. The first-order energy correction is determined by

$$E_n^{(\mathrm{a})} = \int_{-\infty}^{\infty} dR\, |\psi(R)|^2\, V^{(\mathrm{a})}(R) \quad . \tag{3.15}$$

An exact expression for the integral of a triple product of Hermite polynomials and a Gaussian is known [82] to be

$$\int_{-\infty}^{\infty} dx\, \mathrm{e}^{-x^2}\, \mathrm{H}_k(x)\, \mathrm{H}_n(x)\, \mathrm{H}_m(x) = \frac{2^{\frac{m+n+k}{2}}\sqrt{\pi}\, k!\, n!\, m!}{(s-k)!\,(s-n)!\,(s-m)!} \tag{3.16}$$

where $2s = n + k + m$ must be even for the equation to hold. To make use of this formula the R^4 and R^6 terms in $V^{(\mathrm{a})}$ need to be expressed in Hermite polynomials. For example,

$$R^4 = \frac{1}{16}\,\mathrm{H}_4(R) + \frac{3}{4}\,\mathrm{H}_2(R) + \frac{3}{4}\,\mathrm{H}_0(R). \tag{3.17}$$

Inserting the expressions for R^4 and R^6 into the integral Eq. (3.15), separating the integrals, and evaluating each of them with the aid of Eq. (3.16) leads to

$$E_n^{(\mathrm{a})} = -\frac{1}{1152\,V^2}\left[36\left(2\,n^2+2\,n+1\right)V\hbar^2\omega^2 - \left(4\,n^3+6\,n^2+8\,n+3\right)\hbar^3\omega^3\right] \quad . \tag{3.18}$$

To determine the 3D perturbative energies $E_n = \sum_{j=x,y,z} E_{n,j}^{(\mathrm{h})} + E_{n,j}^{(\mathrm{a})}$ of the sextic potential the anharmonic energy corrections $E_{n,j}^{(\mathrm{a})}$ of the three spatial directions and the corresponding harmonic-oscillator energies $E_n^{(\mathrm{h})} = \hbar\omega_j\,(n+\frac{1}{2})$ need to be added up.

With the corrected c.m. excitation

$$\Delta_{(n_x,n_y,n_z)} = \sum_{j=x,y,z} \hbar\omega_j\left[n_j - \frac{\hbar\omega_j}{16V_j}\left({n_j}^2+n_j\right) + \frac{\hbar^2\omega_j^2}{576V_j^2}\left(2\,{n_j}^3+3\,{n_j}^2+4\,n_j\right)\right] \tag{3.19}$$

and the energy of the first trap state

$$E_1^{\mathrm{rel.}} = \hbar\omega_z + \sum_{j=x,y,z}\frac{1}{2}\,\hbar\omega_j - \frac{{\hbar\omega_j}^2}{32\,V_j} + \frac{{\hbar\omega_j}^3}{384\,V_j^2} \tag{3.20}$$

the CIR positions for various excitations of the bound state can now be easily determined using Eq. (3.12).

As an alternative to the perturbative approach, the effective 1D c.m. problem can also be solved exactly numerically. It will be demonstrated that for the special case of negative values of the scattering length and a strongly anisotropic confinement, the effective 1D c.m. problem needs even to be solved exactly to obtain quantitatively accurate results. For the numerical evaluation of the stationary 1D Schrödinger equation, the approach described in [83] is used.

Therefore, three different versions of the model for the resonance position were introduced that differ by the treatment of the c.m. excitation Δ and by the energy of the first trap state E_1^{rel}. In the harmonic version, Δ and E_1^{rel} are given in the harmonic approximation by Eqs. (3.13) and (3.11), in the perturbative version, by Eqs. (3.19) and (3.20) within a perturbative corrections, respectively, and in the "exact" version, the c.m. energies are calculated numerical exact. For given Δ and E_1^{rel} within one version of the model, the inelastic CIR position for a c.m. excitation is then determined by Eq. (3.12).

3.3 C.m.-rel. coupling model – coupling strengths

After having introduced a straightforward to evaluate model for the resonance positions, the coupling strengths are considered. They are of particular interest for experiments, since they are necessary for a Landau-Zener evaluation of the resonances that allows to decide on diabatic and adiabatic transitions of the states. The matrix element defining the coupling strength $W_{\mathbf{n}}$ between a bound state $|\psi^{(b)}(\mathbf{r})\,\Phi_{\mathbf{n}}(\mathbf{R})\rangle$ with c.m. excitation $\Delta_{\mathbf{n}}$ and the lowest trap state $|\psi_1(\mathbf{r})\,\Phi_{(0,0,0)}(\mathbf{R})\rangle$ is

$$W_{\mathbf{n}} = \langle\psi^{(b)}(\mathbf{r})\,\Phi_{\mathbf{n}}(\mathbf{R})|W(\mathbf{r},\mathbf{R})|\psi_1(\mathbf{r})\,\Phi_{(0,0,0)}(\mathbf{R})\rangle \quad . \tag{3.21}$$

For the model the wavefunctions of a harmonic confinement are adopted. Hence, the c.m. wavefunction is the product of 1D harmonic oscillator wavefunctions (here written in dimensionless units of energies in $\hbar\Omega_j$ and lengths in $\sqrt{\frac{\hbar}{M\Omega_j}}$),

$$\Phi_n(R_j) = \pi^{-\frac{1}{4}}\sqrt{\frac{1}{2^n n!}}\,\mathrm{e}^{-\frac{1}{2}R_j^2}\,\mathrm{H}_n(R_j) \tag{3.22}$$

where $\mathrm{H_n}(R_j)$ denote the Hermite polynomials. The c.m. integral in Eq. (3.21) reduces to a sum of 1D integrals that can be calculated even analytically.

The 3D integral over the relative motion coordinate is more demanding. While an expression for the trap wavefunctions for an arbitrarily anisotropic harmonic confinement is so far (to the authors knowledge) not yet known, a general solution for the trap state in a harmonic potential with a single (but arbitrary) anisotropy, e. g. $\omega_x = \omega_y =: \omega_\perp \neq \omega_z$ is given in [70]. However, the numerical evaluation of Eq. (3.21) with the most general version of the relative motion wavefunction given in [70],

$$\psi_\epsilon(\rho,z) = \frac{\eta}{2\pi^{3/2}2^{\epsilon/2}}\,\mathrm{e}^{-\eta\rho^2/2}\sum_{m=0}^{\infty}2^{m\eta}\,\mathrm{L}_m(\eta\rho^2)\,\Gamma\left(\frac{2m\eta-\epsilon}{2}\right)\,\mathrm{D}_{\epsilon-2m\eta}\left(\sqrt{2}\,|z|\right) \tag{3.23}$$

has turned out prohibitively difficult. In the regime of a strongly elongated (quasi-1D) potential the expression greatly simplifies [70] to

$$\psi_1(\rho,z) = \frac{\eta}{2\pi^{3/2}2^{\epsilon/2}}\,\mathrm{e}^{-\eta\rho^2/2}\,\Gamma\left(-\frac{\epsilon}{2}\right)\,\mathrm{D}_\epsilon\left(\sqrt{2}|z|\right). \tag{3.24}$$

In above equations D_ν denotes the parabolic cylinder function, L_m the Laguerre polynomials, Γ the gamma function, and $\rho^2 = x^2 + y^2$. The wavefunctions are written in dimensionless units (energies in $\hbar\omega_z$ and lengths in d_z). $\eta = \frac{\omega_\perp}{\omega_z}$, and $\epsilon = E^{\mathrm{rel.}} - \frac{\hbar}{2}(\omega_x+\omega_y+\omega_z)$ are consistent with previous definitions. The energy at

the resonance is $\epsilon = \hbar\omega_z$ within the model (assuming that the elongation of the trap is along the z direction). It is important that for the wavefunction the energy is *not* corrected by the anharmonic terms, because this might result in a different energy branch of the spectrum. With $\epsilon = \hbar\omega_z$ at the resonance, Eq. (3.24) can be further simplified to

$$\psi_1(\rho, z) = \frac{\sqrt{2}\,\Gamma\left(-\frac{1}{2}\right)}{4\pi^{\frac{3}{2}} d_\perp^2 \sqrt{d_z}}\,|z|\,\exp\left(-\frac{\rho^2}{2d_\perp^2} - \frac{z^2}{2d_z^2}\right) \quad , \tag{3.25}$$

having in mind that for integer n,

$$\mathrm{D}_n(x) = 2^{-\frac{n}{2}} \mathrm{e}^{-\frac{x}{4}} H_n\left(\frac{x}{\sqrt{2}}\right), \quad n \in \mathbb{N}^0 \tag{3.26}$$

holds. Eq. (3.25) is written in physical units.

In quasi-2D, the general wavefunction can be simplified to [70]

$$\psi_1(\rho, z) = \frac{1}{2\pi^{\frac{3}{2}}} \mathrm{e}^{-\frac{\eta\rho^2 + z^2}{2}}\,\Gamma\left(-\frac{\epsilon}{2\eta}\right) \mathrm{U}\left(-\frac{\epsilon}{2\eta}, 1, \eta\rho^2\right) \tag{3.27}$$

where U denotes the confluent hypergeometric function. Again, dimensionless units are adopted where energies and lengths are expressed in $\hbar\omega_z$ and d_z, respectively.

The rel. motion bound-state wavefunction [70]

$$\psi_{\mathrm{b}}(\mathbf{r}) = \frac{\sqrt{d_z}}{{d_\perp}^2 (2\pi)^{3/2}} \int_0^\infty dt\, \frac{\exp\left(t\frac{E}{\hbar\omega_z} - \frac{z^2}{2t{d_z}^2} - \frac{\rho^2}{2d_\perp^2}\coth\left(\frac{t{d_z}^2}{{d_\perp}^2}\right)\right)}{\sqrt{t}\sinh\left(\frac{t{d_z}^2}{{d_\perp}^2}\right)}. \tag{3.28}$$

which is written here in physical units, is valid for an isotropic confinement as well as for a strongly anisotropic trap geometry. It should be mentioned that in the case that the energy of the excited bound state crosses the energy of the trap state for positive values of the scattering length $a \lesssim d_\perp$, the energy of the corresponding non-excited bound-state is sufficiently small at the crossing such that the bound state wavefunction can be described in good approximation by its expression

$$\psi_{\mathrm{free}}(r) = \frac{1}{\sqrt{2\pi a}} \frac{\mathrm{e}^{-\frac{r}{a}}}{r} \tag{3.29}$$

for the case of no trap potential. However, for crossings at negative scattering lengths, this approximation certainly fails, because in the free case the bound state only exists for $a > 0$. Hence in the following Eq. (3.28) is used for the bound-state wavefunction.

The wavefunctions of a harmonic confinement of *single* anisotropy are used. Therefore, the rel. motion integral is reduced to a two-dimensional one where the coupling term $W(\mathbf{r}, \mathbf{R})$ is averaged over the transversal direction, $\omega_\perp = \frac{1}{2}(\omega_x + \omega_y)$. The matrix element becomes

$$W_{\mathbf{n}} = 2\pi \int_0^\infty d\rho\ \rho \int_{-\infty}^\infty dz\, \psi_{\mathrm{b}}(\rho, z)\, \psi_1(\rho, z)\, \tilde{W}(\rho, z) \quad , \tag{3.30}$$

with

$$\tilde{W}(\rho, z) = \sum_{k=x,y} V_k \int_{-\infty}^\infty dR_k\, W_k(\rho, R_k)\, \Phi_{n_k}\, \Phi_{n_0} + V_z \int_{-\infty}^\infty dZ\, W_z(z, Z)\, \Phi_{n_z}\, \Phi_{n_0} \tag{3.31}$$

where $W(\mathbf{r}, \mathbf{R}) = \sum_{j=x,y,z} V_j\, W_j(r_j, R_j)$ and $\mathbf{n} = (n_x, n_y, n_z)$.

Hence, different to the resonance position where three types of models were introduced that differed in the treatment of the c.m. energies, two models for the coupling strength were introduced that differ in the way the rel.-motion wavefunction ψ_1 is treated. In isotropic and cigar-shaped potentials Eq. (3.25) is used for ψ_1. In pancake-shaped potentials Eq. (3.27) is adopted for ψ_1. The models solve the coupling matrix element of Eq. (3.21) for the exact coupling term of the sextic potential of Eq. (3.9) with wavefunctions in the harmonic approximation.

The introduced model delivers expressions for resonance positions and coupling strengths in anharmonic single-well potentials. In order to evaluate the model in a systematic way and to be able to go beyond single-well potentials, *ab initio* calculations of the stationary Schrödinger equation with the six-dimensional Hamiltonian Eq. (3.1) are performed. The numerical method is briefly summarized in the following section.

3.4 *Ab initio* calculations of inelastic confinement-induced resonances

The stationary Schrödinger equation with the six-dimensional Hamiltonian Eq. (3.1) can be tackled numerically from first principles via an exact diagonalization approach as described in [61, 84] [1]. The structure of the method is closely adapted to the one

[1] For the complex and hardware-demanding investigation of inelastic CIR, it was a major technical advance to develop a comprehensive interface which allows to produce energy spectra for a variety of parameters in an automated way.

of the Hamiltonian given in Eq. (3.1). In a first step, the *orbital* calculation [2], the solutions of the stationary Schrödinger equations of the uncoupled Hamiltonians of Eqs. (3.2) and (3.3) are calculated separately. The eigenfunctions $\psi_i(\mathrm{r})$ and $\phi_i(\mathbf{R})$ of the Hamiltonians $H_{\mathrm{rel.}}(\mathbf{r})$ and $H_{\mathrm{c.m.}}(\mathbf{R})$, respectively, are expanded in a basis of B splines and spherical harmonics. Adopting the Rayleigh-Ritz-Garlerkin variational principle, the stationary Schrödinger equations

$$H_{\mathrm{rel.}}(\mathbf{r})\,\psi_i(\mathbf{r}) = \epsilon_i\,\psi_i(\mathbf{r}) \tag{3.32}$$

$$H_{\mathrm{c.m.}}(\mathbf{R})\,\phi_i(\mathbf{R}) = \varepsilon_i\,\phi_i(\mathbf{R}) \tag{3.33}$$

transform into matrix eigenvalue problems.

In a second step, the exact diagonalization, the eigenvalue problem for the complete Hamiltonian is diagonalized including the c.m. and rel. Hamiltonians and the coupling term. Therefore, the solutions of the orbital calculations $\psi_i(\mathbf{r})$ and $\phi_i(\mathbf{R})$ are used to form configuration-state wavefunctions

$$\Phi_k(\mathbf{r},\mathbf{R}) = \psi_k(\mathbf{r})\phi_k(\mathbf{R}). \tag{3.34}$$

The time-independent Schrödinger equation of the full Hamiltonian Eq. (3.1)

$$H(\mathbf{r},\mathbf{R})\Psi_i(\mathbf{r},\mathbf{R}) = E_i\Psi_i(\mathbf{r},\mathbf{R}) \tag{3.35}$$

is then solved by expanding the eigenfunction in the configuration-state wavefunctions

$$\Psi(\mathbf{r},\mathbf{R}) = \sum_k \tilde{C}_k\Phi_k(\mathbf{r},\mathbf{R}) \tag{3.36}$$

and numerically diagonalizing the resulting Hamiltonian matrix to obtain the final eigenenergies and the eigenfunctions.

A very important feature of the code is that it exploits the symmetry properties of the Hamiltonian. The Hamiltonian Eq. (3.1) is for symmetric, separable external potentials invariant under the $\mathrm{D_{2h}}$ point group. $\mathrm{D_{2h}}$ is the orthorhombic symmetry group and consists of the identity, rotations by π around the three symmetry axis, reflections at the three symmetry planes, and inversion at the origin, see [61]. The introduction of symmetry-adapted basis functions allows to treat each of the eight irreducible representations of $D_{2\mathrm{h}}$ (A_g,B_{1g},B_{2g},B_{3g},A_u,B_{1u},B_{1u},B_{1u}) independently. Hence, the Hamiltonian matrix decomposes into an eight-fold block-diagonal matrix which can be diagonalized separately. Since matrix diagonalization scales with

[2] The nomenclature is adapted to electronic-structure calculations where orbitals denote effective single-particle wavefunctions. In the ultracold atom code, the basis vectors of the rel. and c.m. Hamiltonians are denoted orbitals.

$O(n^3)$, a $8^3/8 = 64$-fold efficiency increase is achieved in general. In particular, sometimes only a single symmetry is of interest which leads to an $8^3 = 512$-fold efficiency increase. Another main advantage of imposing symmetry is the possibility to directly construct bosonic and fermionic solutions. In the CI step, only basis functions which have the desired symmetry under particle exchange (+1 bosonic, −1 fermionic) are used. In the present thesis, only spectra of the A_g symmetry are shown without explicit mentioning. A thorough analysis has revealed that inelastic CIR involving the ground trap state are contained in the A_g spectrum. Moreover, it has been found that for the configuration-interaction calculation it is sufficient to adopt active orbitals with a_g symmetry [3] (see Section A in the appendix for specification the used basis sets).

In order to vary the scattering length simulating the behavior around a magnetic Feshbach resonance, the manipulation of the inner wall of the Born Oppenheimer potential is adopted as described in Section 1.4.

In order to extract from the *ab initio* calculations the position, coupling strength, and width of inelastic CIR, a two-channel model is introduced. It involves two diabatic states, the trap state $|t\rangle$ and the bound state $|b\rangle$ with diabatic energies E_t and E_b. Introducing a coupling W between these states results in the Hamiltonian matrix

$$H = \begin{pmatrix} E_\mathrm{t} & W \\ W & E_\mathrm{b} \end{pmatrix} \quad . \tag{3.37}$$

A diagonalization of this matrix by a linear transformation $H_\mathrm{d} = U^{-1}HU$, where U consists of the eigenvectors $|\psi_1\rangle$ and $|\psi_2\rangle$ of the diagonal matrix H_d, leads to the energies E_1 and E_2 of the adiabatic states which are known from the *ab initio* calculations. Assuming that the diabatic states are linear in the vicinity of the avoided crossing, i. e. $E_\mathrm{t} = ax + b$ and $E_\mathrm{b} = cx + d$ (where $x = \frac{d_y}{a}$), the coefficients a, b, c, d and the coupling W can be obtained by a numerical minimization of $\|U^{-1}HU - H_\mathrm{d}\|$, where $\|A\| = \sqrt{\sum_{i,j} |a_{ij}|^2}$ is defined as the norm of a matrix A with elements a_{ij}. The position of the resonance is then easily obtained from the crossing point of $E_\mathrm{t}(x)$ and $E_\mathrm{b}(x)$.

The resonance width is determined by the overlap O of the bound state and the trap state

$$O = \sum_{i=1,2} |\langle t|\psi_i\rangle|^2 \; |\langle \psi_i|b\rangle|^2 \quad . \tag{3.38}$$

For the two-channel Hamiltonian Eq. (3.37) the overlap can be calculated analyti-

[3] By convention, in case of orbital symmetry a lower-case letter is used, i. e. a_g instead of A_g.

cally. With $|t\rangle = (1,0)^T$ and $|b\rangle = (0,1)^T$ the overlap

$$O = \frac{1}{2}\,\frac{1}{1+\left(\frac{\Delta E}{2W}\right)^2} \tag{3.39}$$

has a Lorentz profile. At the crossing point, at $\Delta E = E_\mathrm{t} - E_\mathrm{b} = 0$, the states are equally admixed. In order to obtain the width of an avoided crossing from a set of *ab initio* calculations, the more flexible Lorentz

$$O(x) = O_0 + \frac{A}{4(x-x_0)^2+\gamma^2} \tag{3.40}$$

is fitted to the overlap for varying inverse scattering lengths. The width of the crossing is then just given by the full width at the half maximum (FWHM) γ of the Lorentz.

4 Systematic validation of the c.m.-rel. coupling model

After the introduction into the theory of inelastic CIR, the perturbative model is validated in comparison to *ab initio* calculations.

4.1 3D – 1D transition

In the following the behavior of inelastic CIR is investigated in the transition from a 3D to a quasi-1D confinement. Considered are two ^{7}Li atoms in the sextic potential given by Eqs. (3.7)-(3.9) with λ=1000 nm, $\omega_x/\omega_y = 1.1$, $V_y = 35.9\,E_r$. To obtain an elongation in the longitudinal z direction, the potential depth V_z is decreased. Hence, an almost spherical potential is deformed into an elongated, cigar-shaped one. It should be mentioned that a quasi-1D geometry can be achieved not only by decreasing the potential depth along the longitudinal direction, but also by increasing the potential depth in the transversal directions. It was found that both geometry variations lead to essentially equivalent results. Hence the behavior of the inelastic CIR is universal under this geometry variation because it solely depends on the anisotropy. In the following only the weakening in the longitudinal direction is considered.

For ultracold temperatures the system is initially in the lowest trap state. Hence, only crossings with this state are considered. Since the coupling potential Eq. (3.9) is symmetric only states of equal symmetry (n_j even) couple. In the following, the two lowest-order transversal resonances with $(2,0,0)$ and $(0,2,0)$ c.m. excitation and the first-order longitudinal resonance with $(0,0,4)$ c.m. excitation are investigated. These resonances are selected because they are the most pronounced ones. As a rule of thumb the coupling between a c.m. excited bound state and the ground trap state decreases with the order of the c.m. excitation. Hence, the lowest-order resonances with $n_i = 2, n_{j\neq i} = 0$ show the strongest coupling. The reason is that the stronger oscillations in higher excited c.m. bound states decrease the overlap to the trap state and hence also the coupling matrix element in Eq. (3.21). Numerically the rule can be verified by calculating the coupling matrix element for different c.m. excitations. In Table 4.1 resulting matrix elements are shown confirming that $W_{\mathbf{n}}$ decreases with an increasing order of the c.m. excitation. It can also be seen in

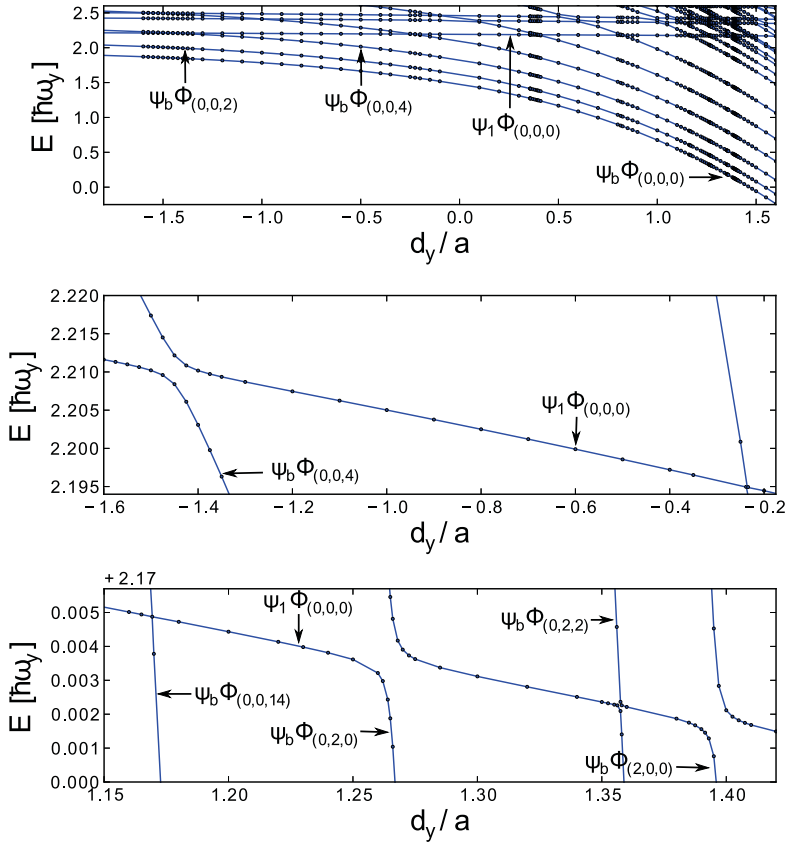

Figure 4.1: *Ab initio* energy spectrum of a ^{7}Li-^{7}Li system confined in a sextic trap potential with λ=1000 nm, $\omega_x/\omega_y = 1.1$, $\omega_y/\omega_z = 10$, $V_y = 35.9\,E_r$. The middle and bottom parts show excerpts of the top part with the avoided crossings relevant for the discussion. The labels of the energy branches denote the corresponding diabatic states. Converged results were obtained with the basis set specified in Table A.1. The plot is also presented in [43].

Figure 4.1 where high-order resonances show no avoided crossings[1]. In fact, it is now clear that states with a c.m. excitation that is such high that it reaches to the continuum, as considered in [74], lead to a negligible coupling. Therefore, [74] concluded that the dimer-production rate at such resonances is too low to be of significance in an experiment.

Although the lowest-order resonances are the most pronounced ones, the lowest-order longitudinal resonance with c.m. excitation $(0, 0, 2)$ (also simply denoted as $(0, 0, 2)$ resonance in the following) is not considered since its position fades away

[1]The reason why the $(0, 0, 4)$ resonance is much stronger than, e. g., the $(0, 2, 2)$ resonance in Figure 4.1 compared to the Table 4.1 is the different confinement geometry, strongly elongated against almost isotropic, respectively.

$\mathbf{n}$	$(0,2,0)$	$(0,2,2)$	$(0,4,0)$	$(0,6,0)$	$(0,8,0)$
$W_{\mathbf{n}}[10^{-3}\hbar\omega_y]$	3.19	1.46	0.795	0.50	0.31

Table 4.1: Coupling strengths $W_{\mathbf{n}}$ for $\omega_x/\omega_y = 1.1$, $\omega_y/\omega_z = 1$, $V_y = 35.9\,E_r$ of the first trap state with c.m. excited bound states for different c.m. excitations $\mathbf{n}$ obtained with the model with a perturbative correction of the c.m. energies.

to $d_y/a \ll -1$ with decreasing ω_z. There, the bound state crosses with the trap state with a tiny difference in slope and has lost its small characteristic interatomic distance. In the full spectrum the crossing can therefore not be easily resolved any more. This can be seen in Figure 4.1 in the most upper panel, where the energy of the $|\psi_b\Phi_{(0,0,2)}\rangle$ state asymptotically approaches $|\psi_1\Phi_{(0,0,0)}\rangle$ without a pronounced crossing.

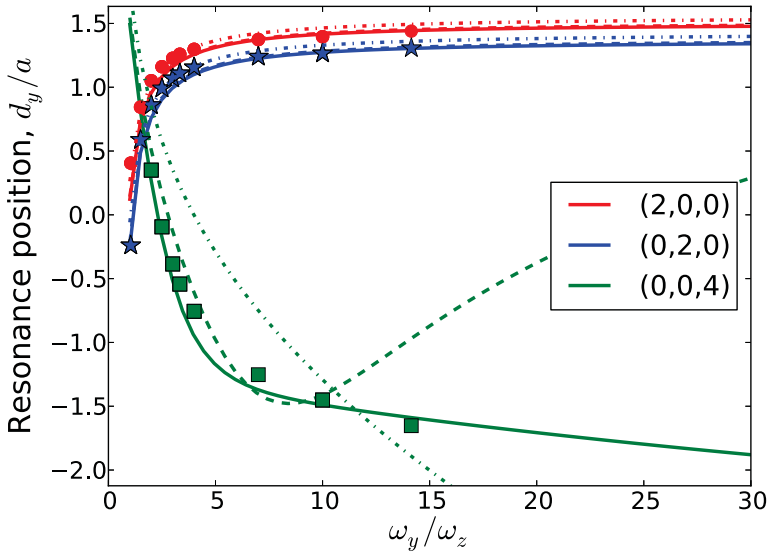

Figure 4.2: Resonance positions for different c.m. excitations obtained by full *ab initio* calculations (symbols) and the model (lines). The dashed-dotted lines correspond to the harmonic approximation of the model. The dashed lines are obtained by a perturbative correction of the energies, Eqs. (3.19) and (3.20). For the solid lines, the correction is done numerically exact. The plot is also presented in [43].

In Figure 4.2 the three considered resonance positions of the model with different degrees of correction together with *ab initio* results are shown. Converged *ab initio* calculations were obtained with the basis specified in Table A.1. Prior to a discussion of the validity of the model, the behavior of the resonances is analyzed. For small

anisotropies $\omega_y/\omega_z \lesssim 2$ the resonance with $(0,0,4)$ c.m. excitation lies at larger values of d_y/a compared to the resonances with transversal c.m. excitation (the green curve lies above the red and blue curves in Figure 4.2) simply because the c.m. excitation $\Delta_{(0,0,4)}$ is larger than $\Delta_{(0,2,0)}$ and $\Delta_{(2,0,0)}$. Therefore, the c.m. excited bound state $|\psi_b\Phi_{(0,0,4)}\rangle$ crosses at larger values of d_y/a than the ones with a single excitation. A decrease of $V_z \propto \omega_z^2$ decreases the spacings of the states that have a c.m. excitation in the z direction. Hence, for decreasing ω_z the $(0,0,4)$ resonance crosses constantly at smaller values of d_y/a which explains the monotonic decrease of the *ab initio* results in Figure 4.2 (green squares). On the other hand, the transversal c.m. excitations ($\Delta_{(0,2,0)}$ and $\Delta_{(2,0,0)}$) remain constant for a variation of ω_z. Yet, a decrease in ω_z also decreases the energy of the first trap state. Therefore, the transversally excited c.m. states $|\psi_b\Phi_{(2,0,0)}\rangle$ and $|\psi_b\Phi_{(0,2,0)}\rangle$ cross at larger values of d_y/a with decreasing ω_z converging to a finite value as $\omega_z \to 0$.

Next, the validity of the model is considered. For the transversal $(2,0,0)$ and $(0,2,0)$ resonances the perturbative corrections Eqs. (3.19) and (3.20) agree with the numerically exact corrections (the dashed and solid lines are indistinguishable). The resonance positions resulting from the harmonic approximation (dashed-dotted lines) show an almost constant offset towards larger values compared to the versions of the model were the anharmonicity in the c.m. motion has been taken into account. This small offset is due to the missing negative quartic term that is present for the sextic potential. Certainly, the model gives very good quantitative agreement with the *ab initio* calculations. For strong anisotropies the formulas where the anharmonicity is taken into account (dashed and solid lines) are in perfect quantitative agreement, e. g., at $\omega_y/\omega_z = 10$ the model gives $d_y/a = 1.397$ and the *ab initio* method results in $d_y/a = 1.396$ for the $(2,0,0)$ resonance.

The results for the longitudinal $(0,0,4)$ resonances are more sensitive. First, with a decreasing potential depth the anharmonicity is important already for low lying states. Second, for the $(0,0,4)$ resonance higher c.m. excitations are involved which enhances the influence of the anharmonicity. Moreover, for a decreasing resonance position the bound state crosses the trap state with an increasingly comparable slope which makes the position more sensitive to energy variations. Therefore, the model including uncorrected, harmonic c.m. excitation is inaccurate over the entire range of anisotropies. The perturbatively corrected model is acceptable for mild anisotropies ($\omega_y/\omega_z \lesssim 10$) but has a wrong behavior for $\omega_y/\omega_z \gtrsim 10$. Finally, the model which numerically corrects the c.m. excitations and the energy of the trap state exactly numerically is quantitatively accurate over the entire range of the scattering length, even in the limit $\omega_z \to 0$ (green solid line).

In Figure 4.3 the corresponding coupling strengths are shown. Again, the overall behavior is discussed prior to the validity of the model. The coupling strength of

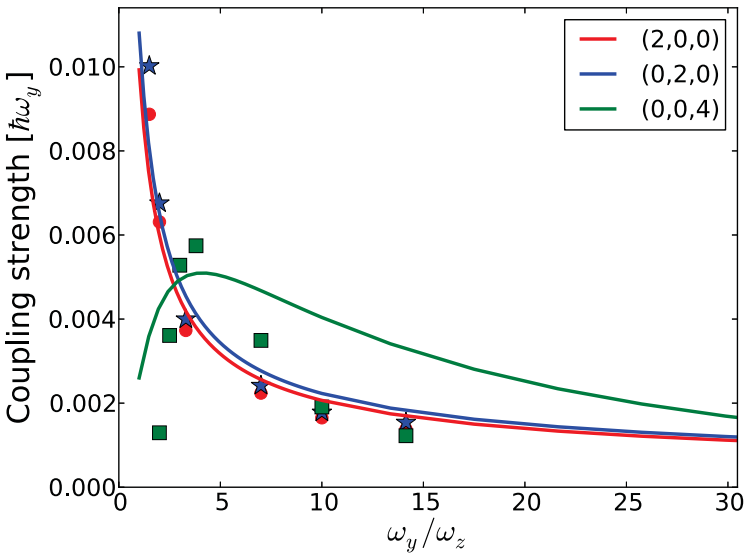

Figure 4.3: Coupling strength for different c.m. excitations obtained by full *ab initio* calculations (symbols) and the model (solid line). The plot is also presented in [43].

the transversal resonances with $(2,0,0)$ and $(0,2,0)$ c.m. excitations (red circles and blue stars, respectively) decreases monotonically with increasing anisotropy but approaches a constant value for $\omega_z \to \infty$. A simple argument for the monotonic decrease is that $W(\mathbf{r},\mathbf{R}) \propto V_k$.

For the resonance with longitudinal $(0,4,0)$ c.m. excitation, a non-monotonic behavior is visible. In the limit of $\omega_z \to 0$ which corresponds to a zero potential in the z-direction, the coupling of the resonances with a c.m. excitation in the longitudinal direction vanishes. This is intuitive, since without a confinement potential there exists no confinement-induced c.m.-rel. coupling. On the other hand, a decrease in the potential depth V_z leads to an enhancement of the anharmonicity-induced coupling, since the potential becomes more anharmonic (this will be discusses in more detail in Section 4.3). The result of these counter-acting effects is the non-monotonic curve with the local maximum for the $(0,0,4)$ resonance and a vanishing coupling for $\omega_z \to 0$.

Next, the validity of the model is considered. For the longitudinal resonance, the model provides the correct qualitative behavior and reproduces the local maximum accurate in position. In general, however, it does not provide highly accurate quantitative agreement. Especially for larger anisotropies ($\omega_y/\omega_z \gtrsim 7$), the model overestimates the coupling strengths. Again, this behavior is understandable since for the higher-order longitudinal resonances the anharmonicity becomes increasingly important, which cannot be modeled accurately with wavefunctions in the harmonic

approximation.

For the transversal resonances with $\Delta_{(0,2,0)}$ and $\Delta_{(2,0,0)}$ c.m. excitation, the coupling strengths predicted by the model agree quantitatively very well with the *ab initio* ones for $\omega_y/\omega_z \geq 2$. This agreement is remarkable, since no free parameters were used in the calculations of the matrix elements within the model.

4.2 3D – 2D transition

In the following, the transition from a 3D to a quasi-2D confinement is considered. Again two ^{7}Li atoms in a sextic confinement of λ=1000 nm and V_y=35.9E_r are chosen and the basis set specified in Table A.1 leads to converged results. To obtain a pancake-shaped trap, ω_x and ω_z are decreased keeping the ratio $\omega_x/\omega_z = 1.1$ constant. The lowest-order resonance with $(0, 2, 0)$ c.m. excitation and the next to leading order resonances with $\mathbf{n} = (4, 0, 0)$ and $\mathbf{n} = (0, 0, 4)$ are considered. Again, in analogy to the 1D case these resonances are the most pronounced ones, having in mind that the two lowest-order resonances with excitations in the weakly confined directions, i. e. with c.m. excitations $(2, 0, 0)$ and $(0, 0, 2)$, fade away towards large negative values of d_y/a, loosing their resonant character.

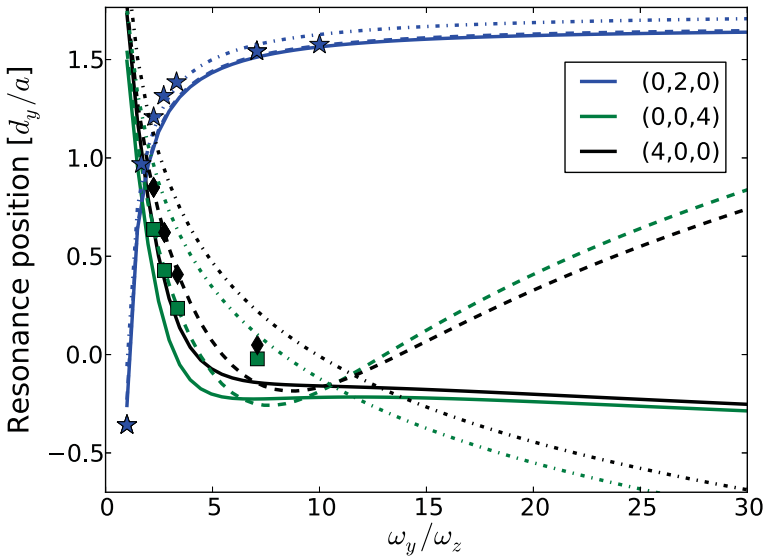

Figure 4.4: Resonance positions for different c.m. excitations obtained by full *ab initio* calculations (symbols) and the model (lines). The dashed lines are obtained by the perturbative correction of the energies given by Eqs. (3.19) and (3.20), the solid lines indicate the numerically exact c.m. correction and the dashed-dotted lines correspond the harmonic approximation. The plot is also presented in [43].

As before, the behavior of the resonance positions in Figure 4.4 is discussed first based on the *ab initio* results. A similar behavior as for the 1D case is visible. By the same arguments that hold in the 3D to 1D transition, the $(0, 2, 0)$ resonance with excitation in the strongly confined direction starts at negative values of d_y/a for small anisotropies and converges to an asymptotic value for strong anisotropies $(\omega_x, \omega_z \to 0)$. The higher order $(4, 0, 0)$ and $(0, 0, 4)$ resonances start at positive values of d_y/a at small anisotropies and do not converge to an asymptotic value for $\omega_x, \omega_z \to 0$.

For the $(0, 2, 0)$ resonance, the model without any energy corrections (harmonic approximation) is again shifted to slightly higher resonance positions due to the absence of a negative quartic term. While for intermediate anisotropies the harmonic theory gives slightly better quantitative agreement to the *ab initio* calculations, the asymptotic value is quantitatively reproduced to high accuracy within the corrected model, where a perturbative treatment of the energy corrections is sufficient.

For the higher order $(4, 0, 0)$ and $(0, 0, 4)$ resonances, the perturbative treatment of the corrections gives an almost perfect quantitative description of the resonance positions for mild anisotropies. However, for strong anisotropies it fails (shows a minimum in the resonance positions and then goes to positive values of d_y/a) and the exact treatment of the 1D c.m. excitation delivers the most accurate results.

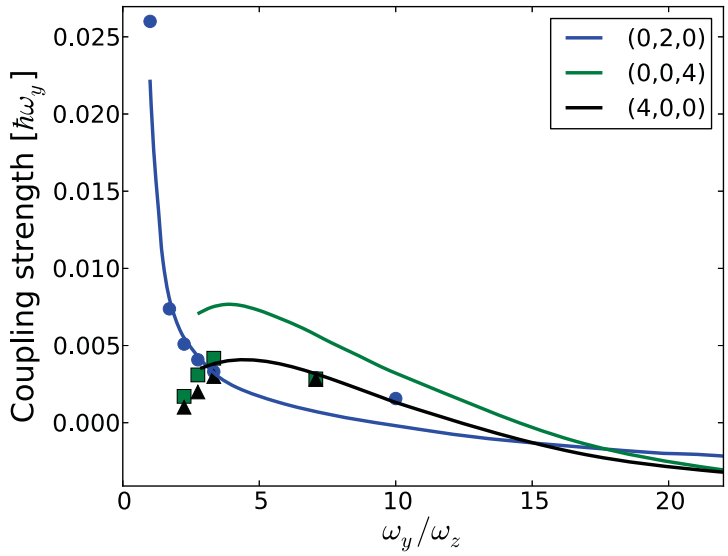

Figure 4.5: Coupling strength for different c.m. excitations obtained by full *ab initio* calculations (symbols) and the model (solid line). The plot is also presented in [43].

In Figure 4.5 the coupling strengths for the transition from a 3D to a quasi-2D confinement are shown. The *ab initio* results show a constant decrease for

the $(0, 2, 0)$ resonance. This in analogy to the resonances with excitations in the strongly confined direction in the transition to a cigar-shaped potential shown in Figure 4.3. Again, the decrease can be explained by the decrease of the coupling potential $W(\mathbf{r}, \mathbf{R}) \propto V_k$ when V_x and V_z are reduced in the transition to a pancake shaped confinement.

The behavior of the coupling strengths of the $(4, 0, 0)$ and $(0, 0, 4)$ resonances in a pancake-shaped confinement exhibit a similar behavior as the longitudinal $(0, 0, 4)$ resonance in a cigar-shaped confinement shown Figure 4.3. The *ab initio* results demonstrate that the coupling strength is close to zero for an almost isotropic confinement (that is why it cannot be resolved for $\omega_y/\omega_z \lesssim 2$), increases until it reaches a maximum and then falls off to zero as $\omega_x, \omega_z \to 0$. Again, its behavior is a result of the counter-acting effect that first, decreasing the potential depth increases the anharmonicity and hence the coupling strength, but second, $\omega_z \to 0$ corresponds to switching off the confinement leading to a zero confinement-induced coupling.

A breakdown of model 2 is detected for very large anisotropies ($\omega_y/\omega_z > 10$) where the model 2 predicts negative coupling strengths for all resonances. The reason why the coupling integral in Eq. (3.30) can result in negative values is the negative quartic term in Eq. (3.9). However, while negative coupling strengths for themselves are not a problem yet, an unphysical discontinuity is introduced when taking the absolute value. Hence, the sign change (or even vanishing value) of the coupling strength is unphysical. Since such a behavior is absent for the cigar-shaped regime, the used harmonic quasi-2D trap state wavefunction, Eq. (3.27) turns out to be inappropriate here.

Still, the model reproduces correctly the decreasing coupling strength for the $(0, 2, 0)$ resonance. For smaller anisotropies $\omega_y/\omega_z \lesssim 5$ even quantitatively accurate. For the $(4, 0, 0)$ and $(0, 0, 4)$ resonances, the non-monotonic behavior is reproduced qualitatively.

In general, for the positions as well as for the coupling strengths, the model shows a better quantitative agreement in quasi 1D than in quasi 2D, simply because for a single decreasing potential depth the anharmonicity effects are milder compared to two the pancake-shaped potential and can be reproduced by the model that is based on the harmonic approximation more accurately.

4.3 Simultaneous variation of the potential depths

It is an important question how the c.m.-rel. coupling can be optimized. As demonstrated above, the coupling at the lowest-order resonances, i. e. with c.m. excitations $n_i = 2, n_{j\neq i} = 0$, and with excitations in the tightly confined direction have a peak coupling strength for an isotropic trap and then monotonically decrease with the

anisotropy, i. e. with a decreasing potential depth in the weakly confined direction(s).

Higher-order resonances in the weakly confined direction(s) have a very small coupling for an isotropic confinement, peak at mild anisotropies and then decrease to zero for increasing anisotropies.

V_y/E_r	53.9	36.0	18.0	9.0	4.5
$W[10^{-3}\hbar\omega_y]$ (*ab initio*)	7.7	9.3	13.2	19.0	25.0
$W_{\text{model}}[10^{-3}\hbar\omega_y]$ (model)	5.2	5.9	6.7	6.3	2.6

Table 4.2: Coupling strengths $W_{\mathbf{n}}$ for $\omega_x/\omega_y = 1$, $\omega_y/\omega_z = 0.5$ of the $(0, 2, 0)$ resonance for different values of the potential depth.

In general, the coupling strength can also be modified by a simultaneous variation of the potential depth, i. e. by a variation of all potential depths and not only selected ones leading to a different (quasi-1D or quasi-2D) trap geometry. The *ab initio* results in Table 4.2 demonstrate that the coupling increases with a decrease of the potential depth V. This behavior can be understood intuitively: As the potential becomes deeper, the harmonic approximation becomes more accurate which has a zero c.m.-rel. coupling. While the model reproduces this behavior for a deep potential, it looses accuracy if the potential becomes too shallow and results in a decrease of the coupling. The reason is that the adopted harmonic wavefunctions become less accurate for a decreasing potential depth.

V_y/E_r	53.9	36.0	18.0	9.0	4.5
d_y/a (*ab initio*)	0.9	0.91	0.92	0.9	0.81
d_y/a (model)	0.82	0.8	0.77	0.72	0.66

Table 4.3: Resonance position for $\omega_x/\omega_y = 1$, $\omega_y/\omega_z = 2$ of the $(0, 2, 0)$ resonance for different values of the potential depth for *ab initio* calculations and the model with the perturbative energy correction. The harmonic approximation of the model predicts a resonance position of $d_y/a = 0.886$ independent of V.

With a decreasing potential depth the harmonic approximation of the potential becomes inaccurate and the limitations of the introduced model become visible. In Figure 4.2 a good agreement of the harmonic approximation was visible for the positions, especially for small anisotropies. In the harmonic approximation, i. e. without the energy corrections in Eqs. (3.19) and (3.20) the positions of the resonances are independent of the potential depth. However, with decreasing potential depth, the anharmonic terms in the sextic potential start to have a significant influence already

at energies of the lowest trap state and, hence, influence the resonance positions. In Table 4.3 the dependence of the position for a mild anisotropy is compared for the model and *ab initio* calculations. While the *ab initio* results are almost constant for a deep potential, the resonance position decreases when decreasing the potential depth to small values. While the energy-corrected model reflects this decrease, the model in the harmonic approximation is independent of the potential depth.

4.4 Wavefunction analysis – molecule formation at the (0,0,4) resonance

In the following, *ab initio* wavefunctions are analyzed for the system of two ^{7}Li atoms confined to a sextic potential with parameters λ=1000 nm, $\omega_x/\omega_y = 1.1$, $\omega_x/\omega_y = 10$, and $V_y = 35.9\,E_r$. The corresponding energy spectrum is shown in Figure 4.1. Considered are the densities of the bound and trap states involved in the transversally excited $(2,0,0)$ resonance and the longitudinally excited $(0,0,4)$ resonance. The positions where the wavefunctions are investigated are chosen such that the overlap of the involved trap and the bound states are still small in order to compare the characteristics of the states. Therefore, for the resonance with $(2,0,0)$ $[(0,0,4)]$ c.m. excitation, $d_y/a = 1.42$ $[d_y/a = -1.2]$ is chosen.

In Figure 4.6 cuts through the trap-state densities are shown. Since both states have the same diabatic state, i. e. $|\psi_1\Phi_{(0,0,0)}\rangle$, they have the same global nodal structure, i. e. two regions of large probability to find the particles separated from each other, away from the diagonal $z_1 = z_2$. This behavior is also reflected in the mean radial pair density

$$\rho(r) = r^2 \int \mathrm{d}V_{\mathbf{R}}\,\mathrm{d}\Omega_{\mathbf{r}}\,|\Psi(\mathbf{r},\mathbf{R})|^2 \tag{4.1}$$

that contains the complete six-dimensional wavefunction $\Psi(\mathbf{r},\mathbf{R})$, $\mathrm{d}V_{\mathbf{R}}$ denotes the c.m. volume element, and $\mathrm{d}\Omega_{\mathbf{r}}$ the angular one of the rel. motion. For the trap states of Figure 4.6 the radial pair density is shown in Figure 4.7. The large probability for the particles to be off-diagonal in Figure 4.6 is clearly reflected. This can be quantified by the mean radial distance

$$\overline{r} = \int_0^\infty \mathrm{d}r\, r\, \rho(r). \tag{4.2}$$

that is considered to characterize the crossing states. The mean radial distance is $\overline{r_t} = 3.95\,d_y = 1.25 d_z$ at $d_y/a = 1.42$ and $\overline{r_t} = 4.56\,d_y = 1.44\,d_z$ at $d_y/a = -1.2$. Hence, the mean distance of the trap state is of the order of the longitudinal trap

length $d_z = 291\,\mathrm{nm}$ which reflects the elongated shape of the confinement.

In the region of interaction a strong and small-scale nodal structure is visible close to the diagonal $z_1 = z_2$ where both particles are close to each other. The nodal structure is also visible in the inset of the radial pair density plot which shows $\rho(r)$ for small r. In this region, the Born-Oppenheimer interaction potential possesses a deep minimum (compared to the energy scale of the trapping potential) which supports many bound states leading to the rich nodal structure.

In Figure 4.9 cuts through the bound-state densities are shown. In both states, which differ by the c.m. part and the scattering length, the particles only occupy regions where they are very close to each other, i. e. close to the diagonal $z_1 = z_2$. The bound state at $d_y/a = 1.42$ (upper panel in Figure 4.9) has no c.m. excitation in the z direction. Hence, no zeros (nodes) are visible in the density (wavefunction). The bound state at $d_y/a = -1.2$ shows four nodes along the z direction which is due to the $(0, 0, 4)$ c.m. excitation of this bound state.

At the resonance involving c.m. excitation in the transversal direction, at $d_y/a = 1.42$, see Figure 4.1, the atoms in the bound state which can be approximated by $|\psi_{(b)}\,\Phi_{(2,0,0)}\rangle$ have a mean distance of $\overline{r_b} = 0.29\,d_y$, i. e. it is small compared to the confinement length in the tight y direction. This demonstrates the strong binding of the atoms. In the vicinity of the $(0, 0, 4)$ resonance (i. e. not directly at the resonance position, see Figure 4.1), at $d_y/a = -1.2$ the atoms in the bound state have a mean distance of $\overline{r_b} = 1.01\,d_y = 92.9\,\mathrm{nm}$, i. e. it is on the order of the trap length in the tightly confined direction.

It will be demonstrated in the following Chapters 5 and 6 that inelastic CIR are directly observed experimentally in a two-body system via a coherent molecule formation [42] and indirectly in a many-body system in terms of particle loss and heating [39, 46, 85]. The latter is also a consequence of the molecule formation at the resonance. It will be identified that the corresponding experiments observed the $(2, 0, 0)$ and $(0, 2, 0)$ resonances [39, 42] in quasi 1D, and the $(0, 2, 0)$ resonance [39] in quasi 2D. Due to the anisotropies of the adopted trap potentials, the resonance positions occur for positive values of the scattering length. Hence, it is an interesting question whether the state $|\psi_{(b)}\,\Phi_{(0,0,4)}\rangle$ which has mean particle distance on scales of the transversal trap length and appears at negative values of the scattering length has enough bound character to trigger a molecule formation and subsequent losses in a many-body system. As will be demonstrated, the atoms in the bound state in [42] that was experimentally identified as a molecule has a mean particle distance of $\overline{r_\mathrm{b}} = 140\,\mathrm{nm}$. This is even larger than the value of $\overline{r_\mathrm{b}} = 96.8\,\mathrm{nm}$ at the $(0, 0, 4)$ resonance. Hence, a molecule formation with subsequent losses is also expected at the $(0, 0, 4)$ resonance.

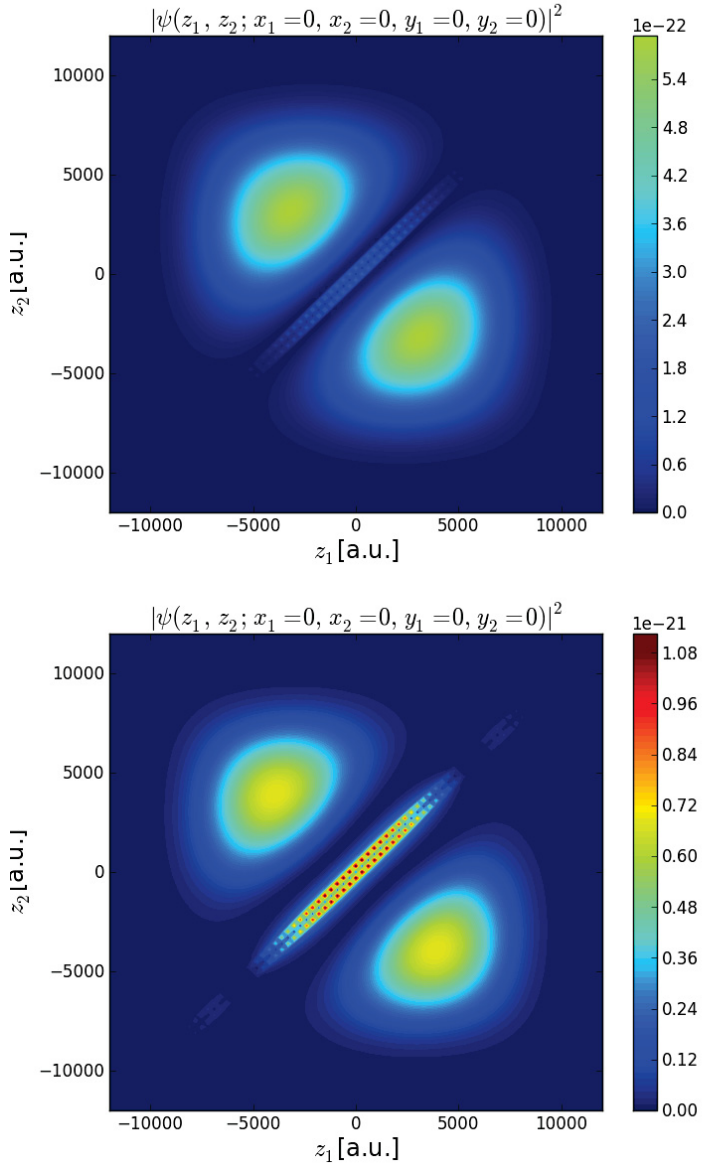

Figure 4.6: Cuts along the elongated z direction ($|\Psi(z_1, z_2; x_1 = x_2 = y_1 = y_2 = 0)|^2$) through the full six-dimensional *ab initio* wavefunction of the first trap state diabatically described by $|\psi_1 \Phi_{(0,0,0)}\rangle$ at $d_y/a = 1.42$ (upper part) and $d_y/a = -1.2$ (lower part). For both plots an identical color code has been used. The plot is also used in [43].

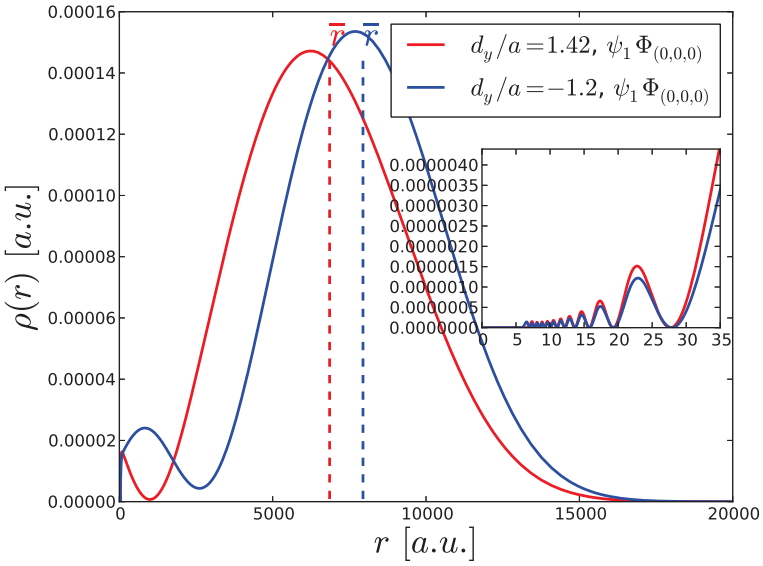

Figure 4.7: Radial pair density of the first trap state for different values of the scattering length. The plot is also presented in [43].

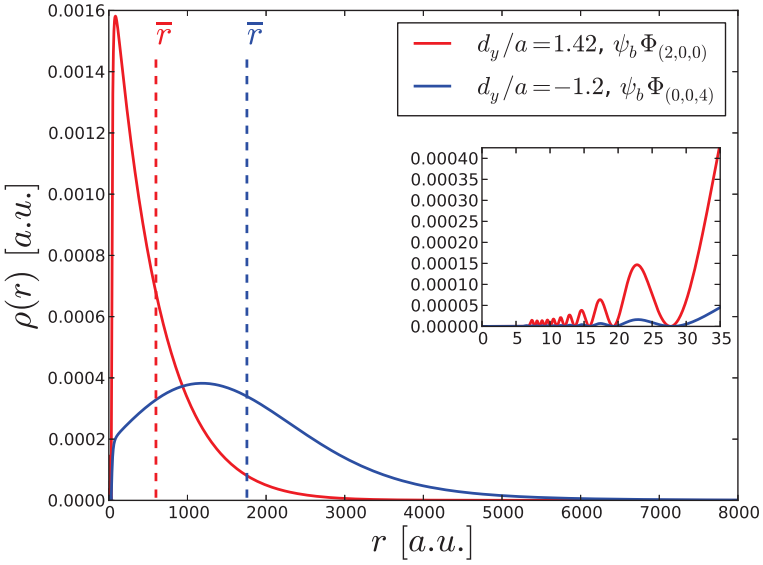

Figure 4.8: Radial density of the c.m. excited bound states for different values of the scattering length. The plot is also presented in [43].

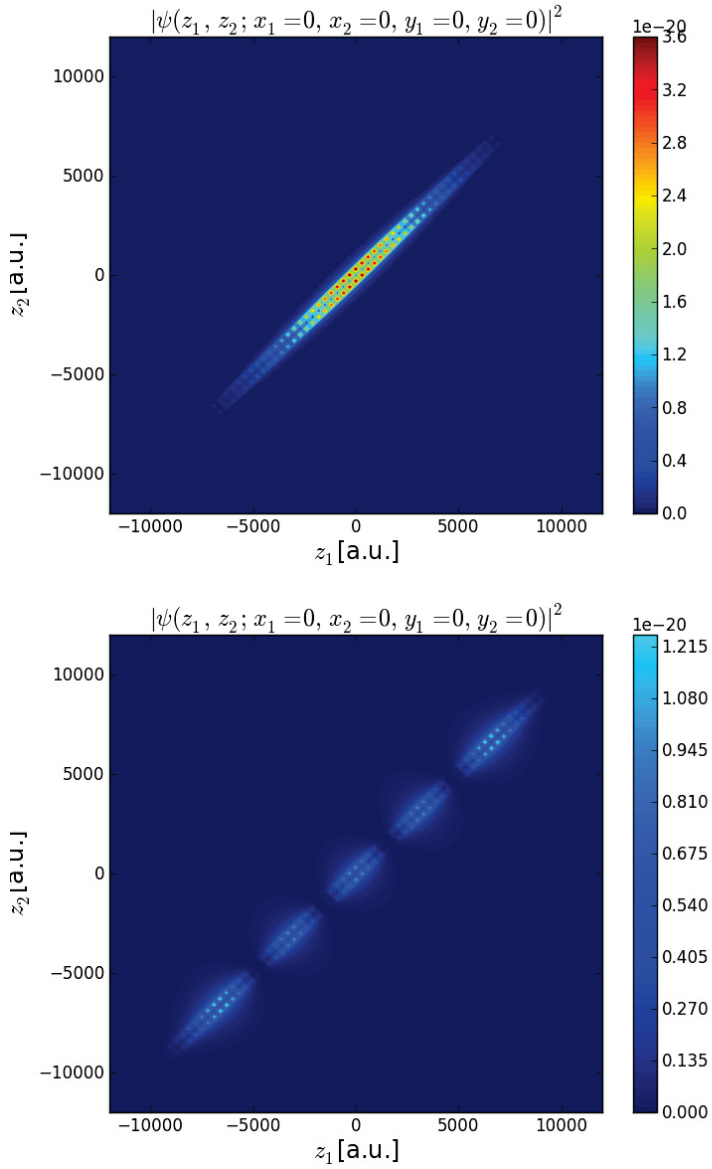

Figure 4.9: Cuts along the elongated z direction ($|\Psi(z_1, z_2; x_1 = x_2 = y_1 = y_2 = 0)|^2$) through the full six-dimensional *ab initio* wavefunction.
Upper part: The c.m. excited bound state diabatically described by $|\psi_{\mathrm{b}}\Phi_{(2,0,0)}\rangle$ at $d_y/a = 1.42$.
Lower part: The c.m. excited bound state diabatically described by $|\psi_{\mathrm{b}}\Phi_{(0,0,4)}\rangle$ at $d_y/a = -1.2$.
For both plots an identical color code has been used. The plots are also presented in [43].

5 Particle loss at inelastic confinement-induced resonances

Having introduced and validated the model that describes the positions and coupling strength of inelastic c.m.-rel. coupling resonances (inelastic CIR), the Innsbruck loss experiment [39] (see Section 2.5) is analyzed and newly explained.

The basic idea about how the atom losses in [39] can be triggered by inelastic CIR is the following: In the experiment the atom loss is measured for different values of the s-wave scattering length. Due to the ultracold temperatures, the system is initially prepared in the lowest trap state. If the scattering length is then ramped to a value which coincides with an inelastic CIR, the lowest trap state couples to a c.m. excited molecular bound state due to the anharmonicity in the trap potential. This molecule then collides either with another molecule or an unbound atom leading to a deexcitation of the molecule into a deeply bound state and subsequent loss of the involved particles from the trap.

5.1 Quasi-1D regime

First, the experimental finding that created major attention is considered, the splitting of the resonance positions for a variation of the transversal anisotropy. For the measurement of the splitting, the trap potential was adjusted to a strong anisotropy $\omega_y/\omega_z = 825$ leading to a quasi-1D confinement. The very weak longitudinal confinement leads to selection rules: Resonances involving bound states with excitations in the longitudinal direction can be neglected, because the bound state has an extension $d_\mathrm{b} \ll d_z$. Hence, $W(z, Z) \approx W(0, Z)$ holds within the extension of the bound state $|z| \leq d_\mathrm{b}$. Due to the orthogonality of the rel. eigenstates the longitudinal matrix element vanishes

$$\langle \Phi_\mathbf{n} \psi^{(b)} | W_z | \psi_1 \Phi_{(0,0,0)} \rangle \approx \langle \Phi_\mathbf{n} | W_z(z=0, Z) | \Phi_{(0,0,0)} \rangle \langle \psi^{(b)} | \psi_1 \rangle = 0 \quad . \tag{5.1}$$

This formal argument can also be understood intuitively (in agreement to the results of Section 4.1): In the limit of a vanishing confinement in a specific direction, the confinement-induced c.m.-rel. coupling vanishes in that direction. Without a c.m.-rel. coupling, no inelastic CIR occurs, i. e. the states cross non-avoided in the energy

spectrum which prohibits the transition of an unbound atom pair into a molecule.

Adopting the approximation in Eq. (5.1), the coupling matrix element of an c.m.-excited bound state to the lowest trap states simplifies to

$$W_{\mathbf{n}} \approx \delta_{n_z,0} \times \left[\delta_{n_y,0} \langle \phi_{n_x} \psi^{(b)} | W_x | \psi_1 \phi_0 \rangle + \delta_{n_x,0} \langle \phi_{n_y} \psi^{(b)} | W_y | \psi_1 \phi_0 \rangle \right] \quad . \tag{5.2}$$

Eq. (3.12) implies that the excitation of the bound state $\Delta_{\mathbf{n}}$ must be nonzero for crossings to exist. Following Eq. (5.2), in the limit of $\omega_z \to 0$ resonances can only occur for excitations of the bound state in a *single transversal* direction. The even symmetry of the c.m.-rel. coupling potential Eq. (3.6) (or equivalently Eq. (3.9)) couples only states of the same symmetry. Since only s-wave interacting atoms are considered, the excitations must be even. The couplings connected to the lowest transversal excitations are dominant, because for higher excitations the increasing oscillatory behavior of the wavefunctions reduces the values of the integrals in Eq. (5.2)[1]. Hence, the inelastic CIR for this quasi-1D confinement arises dominantly from the coupling matrix elements with quantum numbers $n = (2, 0, 0)$ and $n = (0, 2, 0)$.

In Figure 5.1 the CIR positions of the experiment are shown together with the positions of the elastic CIR and the inelastic CIR. For the evaluation of the model, the exact correction of the c.m. energies is used. It should be shortly mentioned that in [39] the "edges", i. e. the scattering length for which the atom loss starts to rise significantly, were chosen as resonances positions. Here, the more conventional positions of maximal particle loss are adopted[2]. The inelastic CIR positions agree with the experimental ones within the experimental accuracy. The splitting as well as the slopes of the branches is reproduced to high accuracy. A small, constant offset[3] is visible. The elastic CIR does not show a splitting as explained in Section 2.5.

While in the experiment a quasi-1D trap of large anisotropy with $\omega_y/\omega_z = 825$ is used, converged *ab initio* calculations with the numerical approach at hand (see Section 3.4) are impossible to achieve with the current implementation of the *ab*

[1] This behavior will be explicitly investigated in Chapter 4.

[2] The maximal loss positions are determined by shifting the known "edge" positions by a constant offset $\Delta a = 89\ a_0$ that is obtained from the isotropic case.

[3] In [46] this offset is actually not present. The reason is that in [46] a perturbative correction of the energies was used where only the quartic leading order term of the sextic potential Eq. (3.8) is taken into account. For smaller anisotropies the perturbative correction adopting the leading order term does not lead to significantly different results than the perturbative treatment using the sextic potential. However, the latter is more accurate for resonances involving higher c.m. excitation as will be demonstrated in Chapter 4.

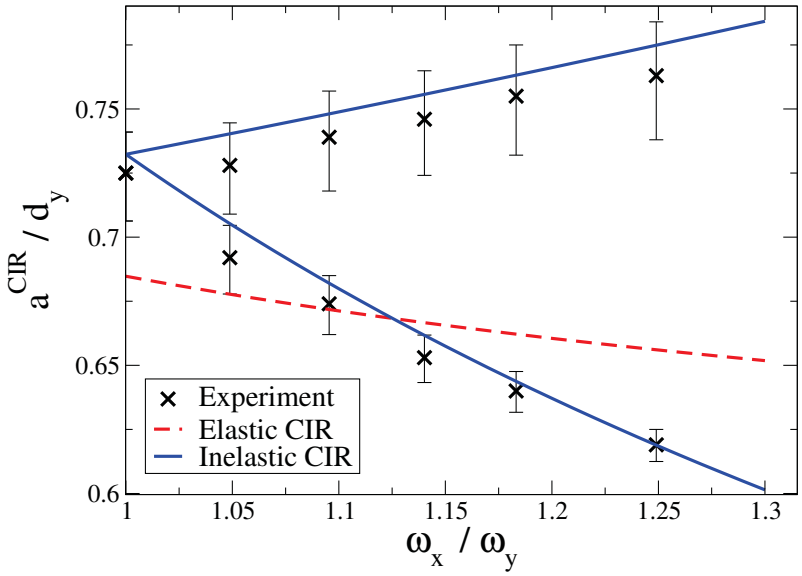

Figure 5.1: Positions of inelastic CIR in terms of the scattering lengths for different values of the transversal anisotropy in quasi 1D. The experimental positions of maximal particle loss, the elastic CIR positions and inelastic CIR positions using the experimental parameters (Cs atoms confined in a trap with $\omega_y/\omega_z = 825$, $V_y = 24.8E_r$ and $\lambda = 1064.49\,\mathrm{nm}$ are shown. The plot is not identical to the one in [46] since there a slightly different model was used.

initio method[4]. Hence, to verify the splitting of the resonances and the selection rules of Eq. (5.2) calculations are performed with $\omega_y/\omega_z = 10$ which is already well in the quasi-1D regime [70]. A fully coupled spectrum for transversal isotropy ($\omega_x = \omega_y$) is shown in Figure 5.2. The complex structure of the energy spectrum is highlighting the importance of the derived selection rules that specify which of the crossing states couple significantly. In accordance with the selection rules, Eq. (5.2), the dominant resonances arise from the lowest transversal c.m. excitations.

Another strong evidence that the measured loss resonances in [39] are the inelastic CIR and not the elastic ones can be derived from the resonance widths. The widths of the loss resonances are about 0.05 G [67] in agreement with the widths of the inelastic CIR calculated here. However, in the Innsbruck experiment [39], direct measurement of g_{1D} gives a width of the elastic CIR on the order of 0.5 G which stems from the width of the used Cs Feshbach resonance of 0.16 G [39] and Eq. (2.21).

On the first glance it might be surprising that in the case of a degeneracy in the c.m. excitation as is the case for transversal isotropy, i. e. $\omega_x = \omega_y$, the energy of one

[4]Very shortly before submitting this thesis, in fact, changes to the code that allow for a selection of the m-quantum numbers of the spherical harmonics used in the basis might allow in future for calculations in very strongly anisotropic external confinement.

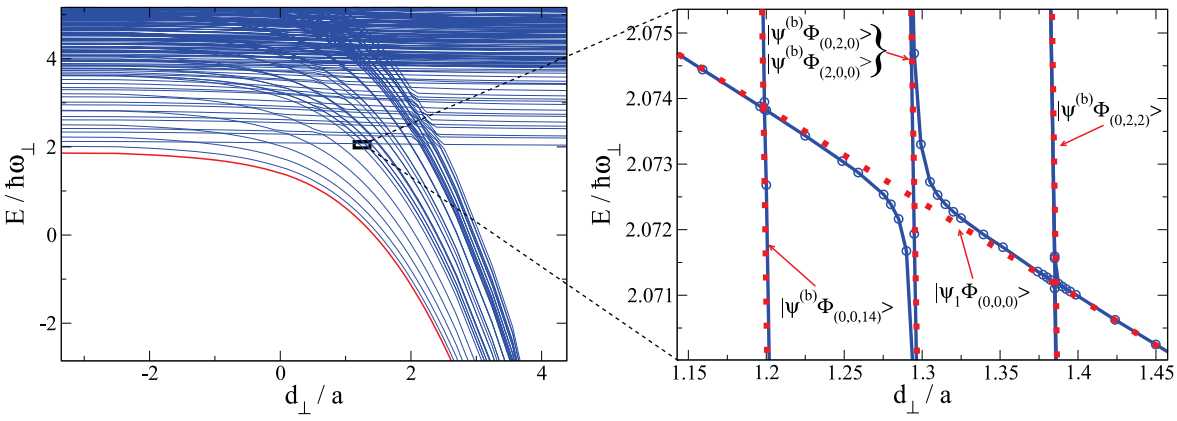

Figure 5.2: Adiabatic spectrum (blue) of the coupled Hamiltonian in Eq. (3.1) for ^{7}Li atoms confined in a sextic trap potential with $V_x = V_y = 35.9E_r$, $\omega_y/\omega_z = 10$, $\omega_x = \omega_y$ and $\lambda = 1000$ nm. The bound state in the c.m. ground state is marked red. The magnified part shows the avoided crossing responsible for the inelastic CIR which arises from the crossings of the transversally excited bound states with the ground trap state. The diabatic states are sketched with red dots and labeled by kets. Only transversally excited states couple strongly while for longitudinal excitation the coupling is very small resulting in almost non-avoided crossings. For isotropic transversal confinement only one CIR occurs due to the degeneracy of the transversal excitation. Converged results were obtained with the basis set specified in Table A.1. (This plot is (with a different arrangement) also presented in [46].)

of the degenerate bound states remains unaffected by the c.m.-rel. coupling. Hence, in the right part of Figure 5.2, the energy of one bound state passes through the avoided crossing as a (almost) vertical line unaffected by the c.m.-rel. coupling. This can be understood on the basis of a simple three-channel model: Let E_t denote the energy of the trap state and E_b the energy of the (degenerate) bound states which are each coupled with strength δ to the trap state. Then a diagonalization of the resulting Hamiltonian yields

$$\det\begin{pmatrix} E_\mathrm{b}-E & 0 & \delta \\ 0 & E_\mathrm{b}-E & \delta \\ \delta & \delta & E_\mathrm{t}-E \end{pmatrix} = (E_\mathrm{b}-E)^2(E_\mathrm{t}-E) - 2\delta^2(E_\mathrm{b}-E) = 0\,. \quad (5.3)$$

One of the solutions is $E = E_\mathrm{b}$ which corresponds to the almost vertical line in the magnified spectrum. Note that the corresponding eigenstate is an antisymmetric superposition of the bound states. The remaining equation (after dividing by $E_\mathrm{b} -$

E), i. e.

$$(E_\mathrm{b} - E)(E_\mathrm{t} - E) = 2\delta^2 \quad , \tag{5.4}$$

results in an avoided crossing of the trap state with a bound state, more precisely with the symmetric superposition of the originally degenerate bound states.

For an anisotropic confinement, $\omega_x \neq \omega_y$, the degeneracy of the c.m.-rel. excited bound states is broken. In accordance with the model for inelastic CIR a splitting of the resonance positions appears in Figure 5.3 where the degeneracy of the avoided crossings is lifted.

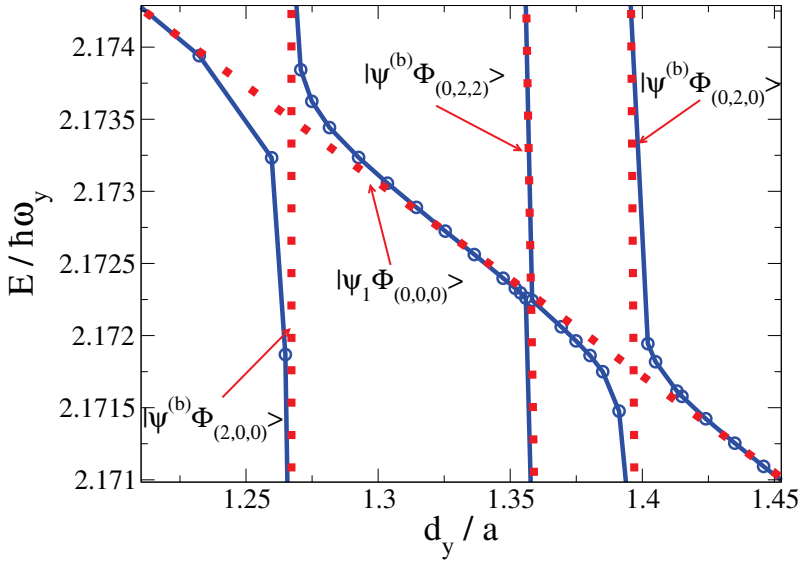

Figure 5.3: As Figure 5.2 but for ^{7}Li atoms confined in a sextic trap potential with $V_y = 35.9E_r$, $\omega_x/\omega_z = 11$, $\omega_y/\omega_z = 10$, and $\lambda = 1000$ nm. The bound state in the c.m. ground state is marked red. For anisotropic transversal confinement the inelastic CIR are non-degenerate. The distinct avoided crossings responsible for the inelastic CIR which arise from the crossings of the transversally excited bound states with the ground trap state are clearly visible. The diabatic states are sketched with red dots and labeled by kets. Only transversally excited states couple strongly while for longitudinal excitation the coupling is very small resulting in almost non-avoided crossings. Converged results were obtained with the basis set specified in Table A.1. The plot is reproduced from [46].

To validate the accuracy for the splitting of the resonance positions in the model of inelastic CIR, the model values are compared to *ab initio* calculations at an anisotropy of $\omega_y/\omega_z = 10$. Figure 5.4 shows a (very good) quantitative agreement.

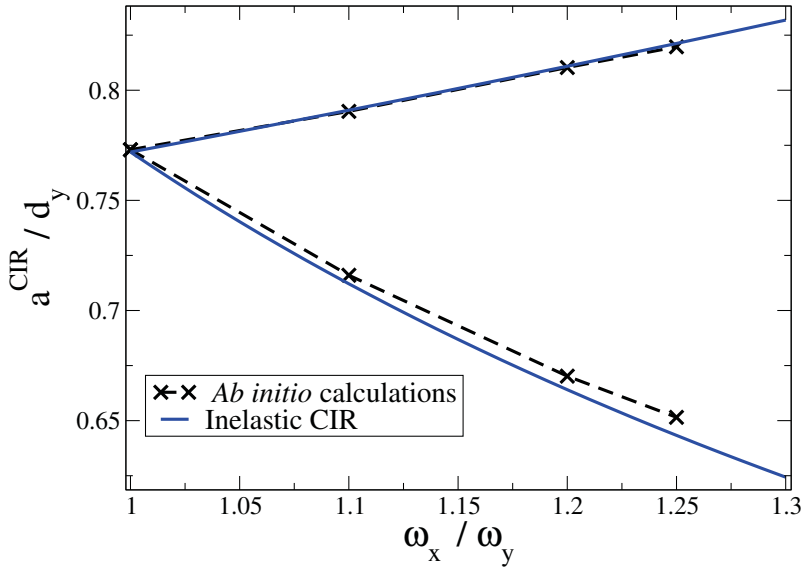

Figure 5.4: Positions of the inelastic CIR for different values of the transversal anisotropy. The results of the *ab initio* calculations are compared to the prediction of the model for inelastic CIR using the perturbative correction specified in Eqs. (3.19) and (3.20). The same parameters (^{7}Li atoms confined in a sextic trapping potential with $V_y = 35.9E_r$, $\eta_y = 10$ and $\lambda = 1000$ nm) are used for the *ab initio* calculation as well as for the model that, however, differ to the ones in Figure 5.1. Converged results were obtained with the basis set specified in Table A.1. The plot is not identical to the one in [46] due to the use of a slightly different model.

5.2 Quasi-2D regime

Next, the observations of the experiment for a quasi-2D confinement are considered. For a single very strong transversal anisotropy the c.m.-rel. coupling matrix element can be simplified to

$$W_{\mathbf{n}} \approx \delta_{n_y,0}\,\delta_{n_z,0}\,\langle\phi_{n_x}\psi^{(b)}|W_x|\psi_1\phi_0\rangle \quad . \tag{5.5}$$

This approximation is only valid for a very weak longitudinal confinement, such that the longitudinal c.m.-rel. coupling approaches zero. Then, only a transversally excited bound state with $n_y = 2, 4, \ldots$; $n_x = n_z = 0$ can lead to coupling. Again, the first excitation $\mathbf{n} = (0, 2, 0)$ is dominant. In the Innsbruck experiment [39] a *single* resonance is observed for quasi-2D confinement [67], indicated by maximal particle loss at $a/d_y = 0.593$. For the experimental trap parameters the model for inelastic CIR using the exact (non-perturbative) treatment of the c.m. corrections predicts

a resonance position at $a/d_y = 0.604$[5]. This is again in very good agreement with the experimental value. In complete contrast, the theory of elastic CIR predicts a resonance position at *negative* values of the scattering length in 2D confinement.

Similar to the quasi-1D case, the model can also be compared to ab initio calculations at smaller anisotropy. For $\omega_y/\omega_z = 10$ and $\omega_x = \omega_y$ both the *ab initio* calculation (with the basis specified in Table A.1.) and the model result in an inelastic CIR position of $a/d_y = 0.64$. In comparison with the experimental data it becomes obvious that the inelastic CIR position depends on the longitudinal confinement. This is another difference to the elastic CIR that is independent of the longitudinal confinement as long as this is sufficiently small such that the system can be treated in the quasi-1D approximation that was discussed in Section 2.3.

Despite the remarkable quantitative agreement of the theory of inelastic CIR with the experimental data, the opinion that the elastic CIR should nevertheless be responsible for the loss features in the Innsbruck experiment [39] persisted in large fractions of the community. The reason was that the diverging interaction strength at the elastic CIR was confirmed experimentally in 1D [30–34, 36] and in 2D [66]. Second, the simple Feshbach-type picture seemed intuitive and plausible on the first glance. And perhaps most importantly, the loss position in the isotropic case (i. e. the position of the inelastic CIR) almost coincides with the position of the elastic CIR. The fact, that the elastic CIR is not observable in terms of losses was not very clear within the community. Additionally, a number of optional explanations [40, 68, 73] were formulated that tried to explain the splitting of the loss features in the quasi-1D confinement. The results presented in next chapter finally provide unique evidence that the experimentally observed losses are caused by inelastic CIR.

[5] In [46] a resonance position at $a/d_y = 0.595$ is predicted using a model where only the leading quartic-order term is considered.

6 Coherent molecule formation at inelastic confinement-induced resonances

The introduced model for inelastic CIR reproduces the positions of the loss resonances in the Innsbruck experiment [39] to high accuracy. However, also other proposals were discussed in literature to explain the loss features. In [73], it is claimed that enhanced three-body effects occur in the vicinity of the elastic CIR due to multichannel effects. In [68], the validity of the known Feshbach-type mechanism for elastic CIR is persisted on. In [40], many-body or Cs-specific effects were speculated on. In fact, in a many-body system of Cs atoms as used in the Innsbruck experiment [39], different loss mechanisms are in principle possible and cannot strictly be distinguished by the experiment.

In order to resolve this issue, a measurement was suggested by the author which was then performed in the group of Selim Jochim from the University of Heidelberg. In their sophisticated experimental setup [8, 34] it is possible to prepare a quasi-1D few-fermion system in which the number of particles as well as the quantum state can be determined to high fidelity. By a tilt of the threshold of the trap potential atoms can tunnel out of the trap, the ones in the highest energy levels at first. By such a controlled spilling a defined number of trapped particles can prepared.

Within this setup, a measurement of the tunneling dynamics has lead to the observation of the fermionization of distinguishable fermions at the elastic CIR [34]. The fermionization was proved by measuring the tunneling time (defined as inverse of tunneling rate) of two distinguishable fermions for different values of the 1D effective interaction strength. The experiment revealed that the tunneling time decreases with increasing $-1/g_{1\mathrm{D}}$. The reason is that with increasing $-1/g_{1\mathrm{D}}$ the energy of the trapped distinguishable fermions increases, e. g., $-1/g_{1\mathrm{D}} = [-\infty, 0, +\infty]$ corresponds to the relative motion energy $E_{\mathrm{rel}} = [0.5, 1.5, 2.5]\hbar\omega$. An increasing energy leads to an increased tunneling rate because the effective tunneling barrier gets less high and less wide. For $-1/g_{1\mathrm{D}} \to 0$, i. e. at the elastic CIR, the tunneling rate of two distinguishable fermions equals the one of two identical fermions that is independent of $g_{1\mathrm{D}}$ because identical fermions are not subject to s-wave interaction and hence their energy $E_{\mathrm{rel}} = 1.5\hbar\omega$ and their tunneling time is independent of

the applied external magnetic field (that is used to tune g_{1D}). Hence, at the elastic CIR the tunneling energy of two distinguishable fermions (the same applies for bosons) is equal to the one of two identical fermions. At this energy ($E_{rel} = 1.5\hbar\omega$), only a unique square modulus of the wavefunction is allowed which is then identical for the distinguishable and identical fermions. This manifests a Tonks-Girardeau ($g_{1D} \to +\infty$) and super-Tonks-Girardeau ($g_{1D} \to -\infty$) system of two distinguishable fermions.

For the identification of inelastic CIR, the experimental setup thus allows on the one hand for the exclusion of three-body effects by investigating a pure 2-body system. Additionally, for the first time the inelastic CIR can be experimentally characterized not only by the position but also by the width and coupling strength which will be shown to agree quantitatively to theory. Finally, it is possible to uniquely identify inelastic CIR because the c.m.-rel. coupling induced molecule formation can be directly observed and distinguished from the elastic CIR.

6.1 Experimental setup

The experimental setup [8, 34] allows for an extreme control over the quantum system which is obtained by a remarkably clever preparation procedure. While details of the preparation scheme can be found in [86] (and references therein), here only the steps are mentioned that are of direct relevance for the thesis (also in view of the experimental realization of a quantum simulator for attosecond science that will be introduced and discussed in detail in Part III of this thesis.).

First, ^{6}Li atoms of two hyperfine states are trapped and cooled in a magneto-optical trap (MOT) by standard techniques. The MOT provides a cooling down to the Doppler temperature of a few hundred μK. In order to further cool the atoms, they are transferred into an optical dipole trap. By evaporative cooling a degenerate Fermi gas of about 4×10^4 atoms can be reached with temperatures down to 250 nK [86]. In order to create a highly degenerate Fermi gas, where the occupation probability of the ground state is close to unity, a trap of very small volume compared to the dipole trap, the "dimple", is superimposed. To control the number of particles in the dimple, a linear potential is switched on in form of a magnetic-field gradient that tilts the potential threshold and allows to spill atoms out of the trap in a controlled way, see Figure 6.1, until the desired number of particles are left.

In an idealized case, the optical dipole trap has the profile of a Gaussian-beam

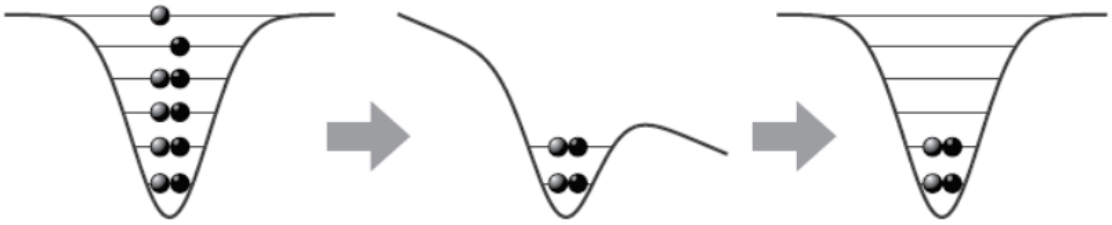

Figure 6.1: Finite optical trap potential and the application of a magnetic-field gradient. By tilting the threshold of the trap potential by superimposing a magnetic-field gradient, atoms can tunnel out of the potential until the desired number of atoms are left in the trap.

potential

$$V_{\text{Gauss}}(\mathbf{r}) = V_0 \left(\frac{w_0}{w(z)} \right)^2 \exp\left(\frac{-2(x^2+y^2)}{w^2(z)} \right) \tag{6.1}$$

where $w(z) = w_0 \sqrt{1 + \left(\frac{z}{z_\text{R}}\right)^2}$ and $w_0 = w(0)$ is the waist size of the beam and $z_\text{R} = \frac{\pi w_0^2}{\lambda}$ is the Rayleigh range and $\lambda = 1064\,\text{nm}$ is the wavelength of the used laser.

To characterize the optical dipole trap, transition frequencies for the excitation of a single atom were precisely measured [42, 86]. The transition frequencies in Table 6.1 as well as additional information on the measurement that was performed

h.o. number (n_x,n_y,n_z)	frequency $\omega/2\pi$ [kHz]
(0,0,1)	1.486(0.011)
(0,0,2)	2.985(0.010)
(0,0,4)	2.897(0.020)
(1,0,0)	13.96(0.08)
(0,1,0)	14.82(0.09)
(2,0,0)	26.43(0.27)
(0,2,0)	28.26(0.25)

Table 6.1: Transition frequencies of atoms excited in the trap. The transitions are labeled by the corresponding quantum number of a harmonic oscillator. The table is identical to the one in [42].

in order to more exactly characterize inelastic CIR can be found in the supplemental material of the corresponding publication [42]. The transition frequencies reveal that the trap potential has an anisotropic, cigar-shaped form with an aspect ratio of $\omega_z/\omega_{x,y} \approx 1/10$. At this anisotropy the quasi-1D approximation is valid, see

Section 2.3. Hence, the system is sufficiently in the quasi-1D regime such that elastic CIR occur which was experimentally confirmed in [34] by the observation of a fermionization of distinguishable fermions at the elastic CIR (see above).

The theoretical treatment of the Gaussian beam potential is challenging because it couples all spatial coordinates. Moreover, the measurement of the excitation frequencies in Table 6.1 uncovers an anisotropy of $\omega_{x\,2-0}/\omega_{y\,2-0} = 1.07$ in the transversal direction that cannot be described by the ideal Gaussian beam potential in Eq. (6.1). In fact, a complete characterization of the experimental confinement is not available. Therefore, the Gaussian beam potential in Eq. (6.1) is expanded in a Taylor series around the origin up to second order leading to a harmonic potential

$$V(\mathbf{r}) = \frac{\hbar}{2} \sum_{j=x,y,z} \omega_j^2 \, j^2 \quad . \tag{6.2}$$

To address the transversal anisotropy different harmonic frequencies ω_j are chosen. Now, higher-order terms must be included to address the c.m.-rel. coupling. Since sextic potentials have already proven to appropriately describe anharmonicity induced c.m.-rel. coupling, the potential described in Eqs. (3.7-3.9) is adopted. Minimizing the differences of the measured transition frequencies in Table 6.1 and excitation energies (in terms of frequencies) in the eigenenergy spectrum of the one-particle Schrödinger equation in a sextic potential with respect to the potential parameters leads to the parameters (in a.u.) $(k_x, k_y, k_z) = (9.23, 8.77, 1.58) \cdot 10^{-5}$ and $(V_x, V_y, V_z) = (6.82, 6.58, 2.33) \cdot 10^{-12}$.

6.2 *Ab initio* calculation

Solving the stationary Schrödinger equation for two ^{6}Li atoms in the sextic potential with the *ab initio* method described in Section 3.4 results in the full spectrum shown in Figure 6.2. As discussed before, e. g., in Section 3.1, inelastic c.m.-rel. coupling resonances appear where the c.m. excited molecular states cross the lowest trap state. For the quasi-1D confinement, the dominant resonances are the lowest-order transversal resonances as described by the selection rules given by Eq. (5.2).

Shortly before the resonance, at $d_y/a = 1.38$, the bound state has a mean radial distance (defined in Eq. (4.2)) of $\overline{r} = 0.29\, d_\perp$ which is small compared to the mean transversal confinement length, but not as small as the orders of magnitude for the case of deeply bound molecular states of the Born-Oppenheimer interaction potential. The small mean interatomic distance is the most significant characteristic of the bound state and reflects the tight binding of the atoms. Differently, the atoms possess a mean distance of $\overline{r} = 1.19\, d_z = 3.06\, d_\perp$ in the trap state which is on the

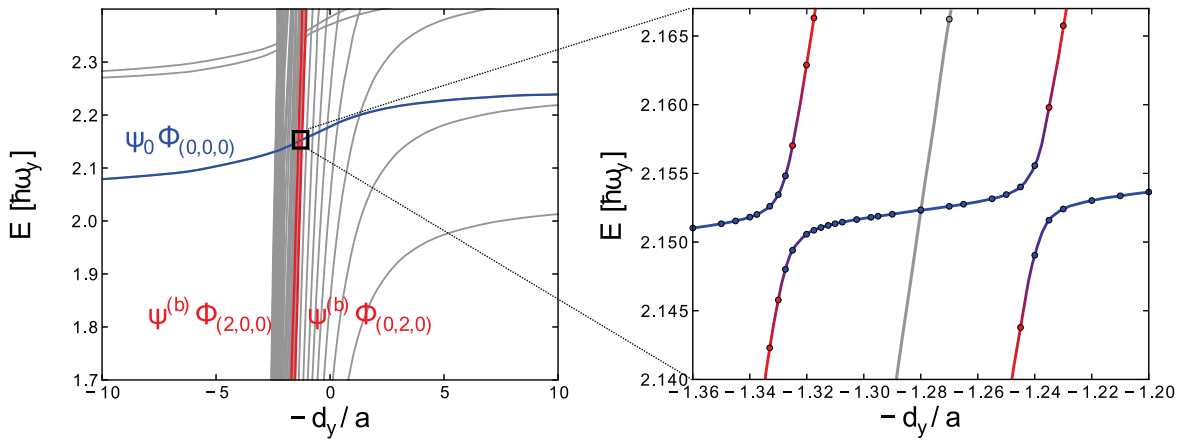

Figure 6.2: Eigenenergy spectrum of the Hamiltonian of Eq. (3.1) for two ^{6}Li atoms confined in a sextic trap potential adjusted to the parameters of the experimental confinement. The two bound states marked in red are the ones which have a dominant coupling to the lowest trap state (blue). For the other states (gray) the coupling is negligible. The magnified part shows the avoided crossings responsible for the c.m.-rel. coupling resonances. Converged results were obtained with the basis set specified in Table A.2. (The plots are also presented in [42].)

order of the longitudinal trap length $d_z = 1.25\,\mu$m and reflects the elongation of the trap.

6.3 Coherent molecule formation

Close to the c.m.-rel. coupling resonance, states other than the crossing ones are energetically nearly inaccessible and the system can be in good approximation described as a two-level system. A coherent superposition of the c.m. excited bound state $|\psi^{(b)}\,\Phi_{\mathbf{n}}\rangle$ and the lowest trap state $|\psi_0\,\Phi_{(0,0,0)}\rangle$ can be created by non-adiabatically ramping the magnetic field (and hence the scattering length) in the gap region of the avoided crossing. A Rabi-oscillation between the states sets in as both states dynamically evolve with different phases. The Rabi-frequency

$$\Omega = \frac{1}{\hbar}\sqrt{W_{\mathbf{n}}^2 + \delta^2} \tag{6.3}$$

becomes a measure of the c.m.-rel. coupling strength for the detuning $\delta = (E_\mathrm{b} - E_\mathrm{t})/2 = 0$. To remind, E_b and E_t denote the energies of the diabatic bound and trap states, respectively, and $W_{\mathbf{n}}$ refers to the c.m.-rel. coupling matrix element given in Eq. (3.21).

The following quoted section describes the experimental measurement performed in the group of Selim Jochim and is extracted from [42] (with references adjusted to the numbering used here).

> "Experimentally this coherent superposition is realized by first preparing two ^{6}Li atoms in the ground state of the potential and then increasing the scattering length a by ramping up the magnetic offset field non-adiabatically with a speed of 20 G/ms [1]. To locate the molecule formation resonances the ramp is suddenly stopped at different values of the magnetic offset field. The population is expected to oscillate between the unbound and the c.m.-excited molecular state as a function of the Rabi frequency Ω which depends on the magnetic field.
>
> In a first experiment we wait for a fixed hold time of 12.5 ms after stopping the ramp at different magnetic field values between 779 G and 788 G [2]. We then measure the number of free atoms remaining in the ground state of the trap by ramping to a magnetic field of 523 G where the molecules are deeply bound and therefore not observed with our detection scheme. Thus, the mean number of molecules is given by $N_{\mathrm{mol}} = (N_0 - N_{\mathrm{GS}})/N_0$, where N_0 is the mean number of atoms in the initial system and N_{GS} is the mean number of particles detected in the non-molecular ground state at the end of the experiment. To check whether the missing atoms indeed end up in the molecular state we repeated the experiment but ramped the magnetic field to a value of 900 G before measuring the number of particles. At this magnetic field we are far above the elastic CIR so that the molecules become weakly bound and the constituent particles of the molecules can be detected with our detection scheme. We found that there is no measurable change compared to the initial particle number when measuring above the elastic CIR, which excludes the presence of any significant loss channels in our system. Figure 6.3 shows the detected number of particles in the repulsive state depending on the magnetic offset field. As expected from numerics, two peaks are observable which are identified as the c.m.-rel. motion coupling resonances created by the two molecular states excited in x- and y- direction of the anisotropic confinement.
>
> To analyze the dynamics of the coupling we ramped to different values of the magnetic offset field around the features shown in Figure 6.3 and

[1] Instead of tuning the scattering length a to ramp into the resonance, alternatively, the transversal confinement length $d_\perp$ could be varied.

[2] The duration of the hold time is such that it corresponds to a half-cycle (i. e. a π-pulse) of an expected Rabi-Frequency of $\Omega_0 = 2\pi \cdot 80\,\mathrm{Hz}$.

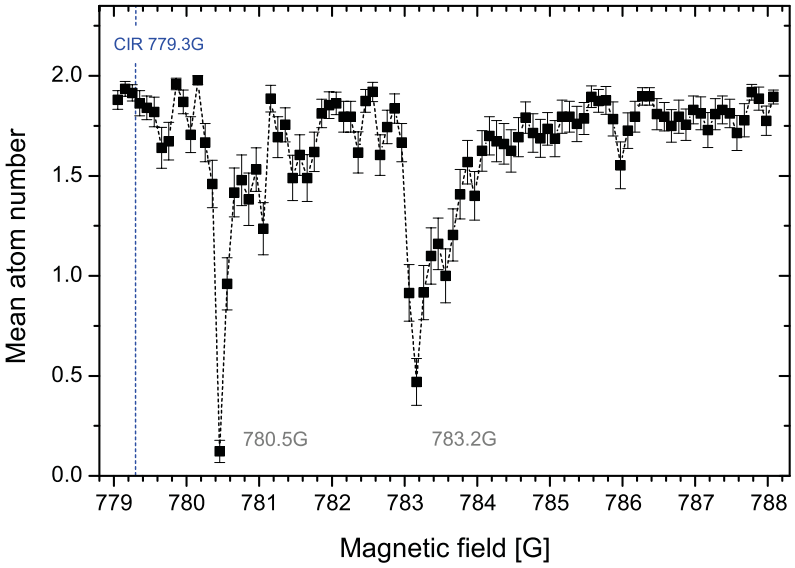

Figure 6.3: Disappearance of particles in the repulsive non-bound state. Due to the c.m.-rel. motion coupling the particles in the non-bound state couple into a molecule and disappear when detecting the number of particles in the non-bound state. One observes two peaks indicating c.m.-rel. motion coupling resonances involving two excited molecular states in x- and y-direction of the confinement. Each data point is the average of about 50 individual measurements with discrete atom number. The blue dashed line indicates the position of the elastic CIR at $779.3 \pm 0.5\,\mathrm{G}$ calculated using the transversal confinement length $d_\perp$ and the calibration of the scattering length $a(B)$ of [87] as inputs for the theory of [36]. (The plot is also presented in [42].)

held the system for different hold times. With less than 10% probability we detect only a single atom in the trap, i. e. with more than 90% probability the two atoms are either free (two atoms detected) or bound to a molecule (no atoms detected). The few realizations with just a single atom detected are not considered in the analysis. Figure 6.4 a) shows the result of one of these measurements. The oscillation of the fraction of molecules shows that we have created a coherent superposition of the molecular and the repulsive state. By performing a sinusoidal fit to the data we can extract the Rabi frequency Ω of the oscillation. The maximum amplitudes of the oscillation for different magnetic fields are shown in Figure 6.4 b). From a Lorentzian fit to the amplitude we can extract the width (FWHM) of the coupling in terms of the magnetic offset field. Table 6.2 shows the width of the coupling resonances determined from the measurement."

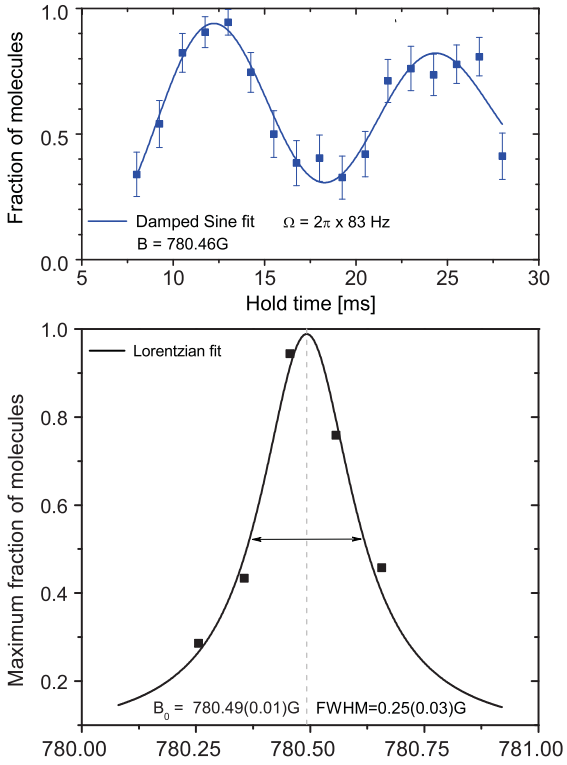

Figure 6.4: Coherent dynamic of the c.m.-rel. motion coupling. (a) Oscillation between the non-bound and the c.m. excited molecular state. From a sinusoidal fit we deduce the Rabi-frequency Ω. (b) Maximum amplitude of the oscillation. The data points are extracted from measurements analog to figure a) at different magnetic offset fields. The plot is also presented in [42].

c.m.	Position [G]		FWHM[G]		$\Omega_0/2\pi$ [Hz]	
excitation	exp.	num.	exp.	num.	exp.	num.
$(0,2,0)$	780.5	776.01	0.25(0.03)	0.35	83(2)	69
$(2,0,0)$	783.2	779.02	0.42(0.06)$^{(*)}$	0.35	75(1) $^{(*)}$	64

Table 6.2: Comparison between experiment and numerical calculation. $^{(*)}$ See the supplemental material of [42] for these measurements. It should be mentioned here, that the numerically calculated widths have been accidentally swapped in the paper [42]. Here the values are corrected. (Converged results for the *ab initio* calculations were obtained with the basis set specified in Table A.2)

In order to compare the results of the measurements with the *ab initio* calculations, the two-channel model introduced in Section 6.2 is applied to obtain the resonance positions, widths and coupling strengths.

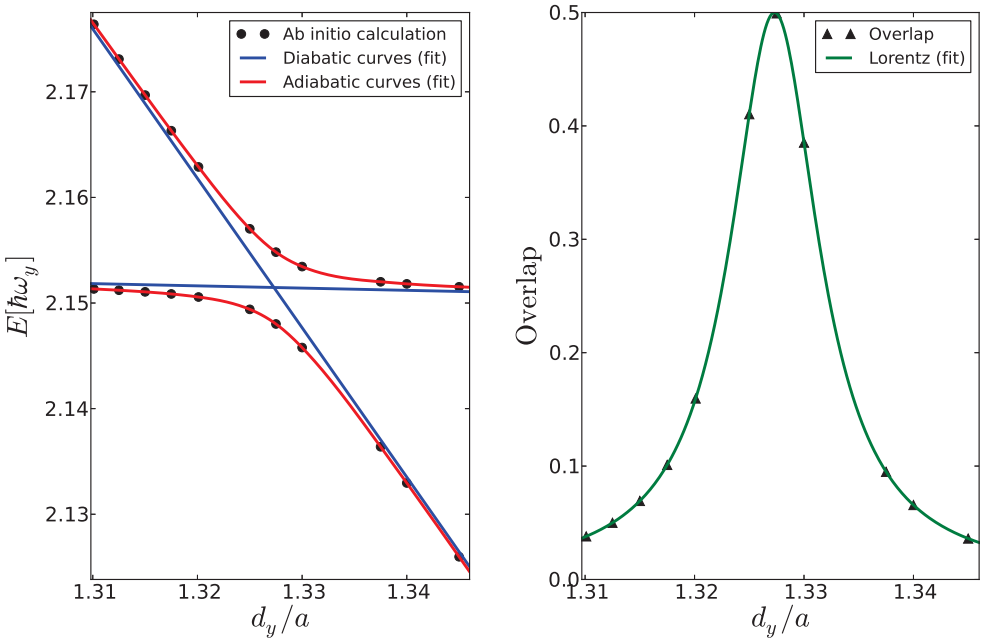

Figure 6.5: Graphical representation of the two-channel fit for the inelastic CIR with $(0, 2, 0)$ c.m. excitation. The position of the avoided crossing is $1.327 d_y/a$, the width $0.00987 d_y/a$ and the coupling $0.00344 \hbar\omega_y$.

In Figure 6.5 the results of the two-channel fit described in Section 3.4 for the resonance of the $(0, 2, 0)$ c.m. excited state is graphically represented. The translation of scattering lengths to values of the external magnetic field around the Feshbach resonance is performed with data provided by Gerhard Zürn (private communication). The data contains the latest and most accurate values [87] for the used magnetic Feshbach resonance.

A comparison of the numerical and experimental resonance parameters can be found in Table 6.2. The spacing of the two resonances is in agreement up to 0.3 G, the absolute positions are shifted by about 4.3 G between the numerical calculation and the measurement. The accuracy is remarkable having in mind that the width of the used Feshbach resonance is about 262 G [87].

The agreement of the *ab initio* calculations and the experiment provides a direct quantitative confirmation of the theory of inelastic CIR. Moreover, in the experiment no molecule formation was found over the whole width of the elastic CIR [42]. This confirms experimentally the theoretical fact that the shifted bound part in the Feshbach-type mechanism of the elastic CIR is no eigenstate of the full Hamiltonian and does not couple to the trap state, see Section 2.4 and Section 2.5. This observation finally proves that the losses in the Innsbruck experiment are caused by inelastic CIR because the fermionized system at the elastic CIR does not give rise

to losses nor heating. Additionally, it demonstrates that the losses caused by the c.m.-rel. coupling resonances in [39] are initiated by a multi-step processes. This is in contrast to earlier assumptions. In [74] it was supposed that the trap state couples to continuum bound states which would lead to a direct loss of the molecule. As demonstrated here, this is not the case. This implies that in a many-body experiment like the one in [39], first a molecule is coherently created. The losses are then caused by collisions of the molecule with other atoms or molecules which leads to a deexcitation into a deeply bound state with subsequent losses of the collision partners.

7 Inelastic confinement-induced resonances in multi-well potentials

So far, only single-well potentials have been considered. However, the c.m.-rel. coupling becomes even more pronounced in systems containing more wells. This can be understood intuitively. In a harmonic trap the c.m.-rel. coupling of identical particles vanishes and the physics can be described by separately solving the rel. and c.m. motion Hamiltonians. Hence, the rel. motion spectrum contains already all interesting physics. For multi-well systems this is not the case because the rel. motion strongly depends on the c.m. coordinate. For example, the rel. motion differs, if the center of mass is located in the classically forbidden barrier region or inside a well minimum. In the following, the occurrence of inelastic CIR in multi-well potentials is investigated [44] together with a very recent measurement of loss features in a shallow 3D optical lattice.

7.1 The experiment

Similar to the Innsbruck loss experiment considered previously (see Section 2.5 and Chapter 5), Manfred Mark and co-workers in the group of Hanns-Christoph Nägerl at the University of Innsbruck have very recently performed loss measurements in an ultracold gas of ^{133}Cs atoms around a broad Feshbach resonance in the presence of a shallow 3D optical lattice. The experiment revealed a rich structure of resonances.

For the measurement, a Bose-Einstein condensate of about 10^5 Cs atoms in the lowest hyperfine state in an optical dipole trap is produced. The preparation procedure basically follows the one described in [88]. The BEC is loaded into a cubic optical lattice potential created by three counter-propagating laser beams with a wavelength of $\lambda = 1064.5\,\mathrm{nm}$ and a lattice depth of $V_{x,y,z} = 20\,E_R$. For the analysis of the experiment, it is important to mention that the lattice depth can vary by up to 5% in each direction due to the experimental setup. A Mott-insulating state with single filling is prepared by suppressing doubly occupied sites by controlling the external confinement strength during the loading process as described in [89]. Loss structures around the Feshbach resonance at a position of 48 G and a width of 160 mG are investigated. The parameters of this Feshbach resonance have been determined with high accuracy [90]. Since gravity is not compensated by an external

magnetic-field gradient, a tilt along the vertical lattice axis [89] is present.

In order to detect loss features, the procedure described in [44] is applied: The external magnetic field B is ramped to different values between $B = 0\,\mathrm{G}$ and $B = 250\,G$ with a resolution of about 8 mG. After a hold time of $t_H = 50\,\mathrm{ms}$ B is ramped to its final value of about 18.5 G where the gas is weakly repulsively interacting ($a = 82\,\mathrm{a.u.}$)[1], the lattice beams and remaining dipole traps are switched off and an absorption picture of the atomic cloud is taken to determine the number of atoms n_A.

The resulting atom number n_A is shown in Figure 7.1(a) as a function of B around the pole of the Feshbach resonance at 47.78 G. The measurement reveals several distinct loss features, the majority located on the repulsive branch of the Feshbach resonance. In Figure 7.1(b) the calculated s-wave scattering length as a function of the magnetic field B is shown and the position and width of the measured loss resonances are indicated as gray-shaded areas.

For the applied range of magnetic field values, the mapping of scattering lengths to magnetic field values is obtained by [91]

$$a_s = a_{\mathrm{bg}} \prod_{i=1}^{N} \frac{B - B_i^*}{B - B_{0,i}} \tag{7.1}$$

which allows for the calculation of the scattering length of N overlapping Feshbach resonances and was introduced in [90]. For a single resonance, this formula reduces to the standard one given in [4]. In Eq. (7.1) a_{bg} is the background scattering length, $B_{0,i}$ is the pole, and B_i^* is the zero crossing for the ith Feshbach resonance. The applied parameters are extracted from the supplementary material of [91].

7.2 Interpretation and comparison to theory

The loss features need to be explained by the identification of the dominant loss channels. As the initial state is a Mott-insulator state with single filling, losses can primarily[2] occur at locations where atoms are allowed to tunnel. On-site three-body recombination for $n_i > 2$, or off-resonant three-body recombination for $n_i = 2$ lead to increased atom losses. Such a tunneling can happen at the zero crossing

[1] The zero crossing of the scattering length is at 17.1 G. However, a small positive value is chosen for the expansion because at $a = 0$ the magnetic field varies more strongly throughout the sample because of the applied gradient.

[2] Secondary processes such as one-body loss due to background atom collisions, off-resonant light scattering, and off-resonant three-body recombination [92] can also occur. However, if only such processes are involved, the lifetimes of the Mott insulating state can reach times above 10 s [93] and can therefore be neglected in the present consideration.

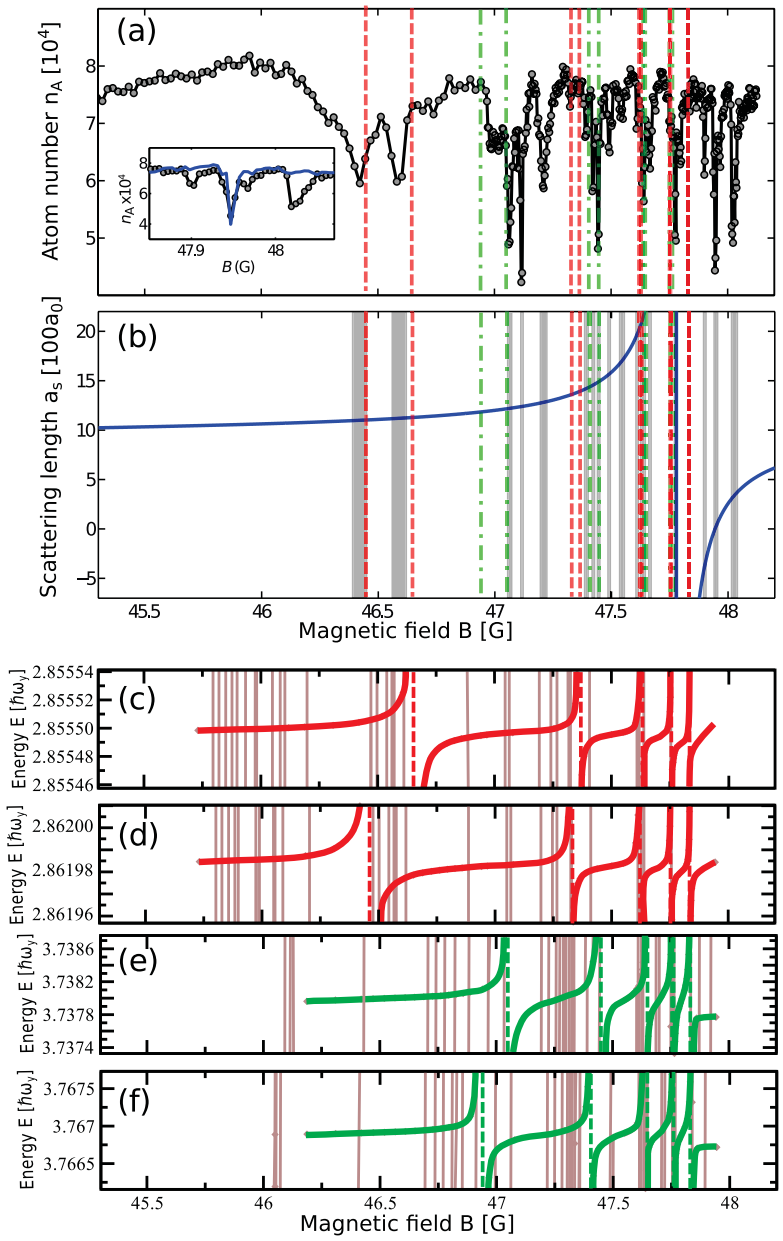

Figure 7.1: (a) Number of remaining atoms n_A in a singly occupied 3D Mott-insulator state for $t_H = 50\,\text{ms}$ and $V_{x,y,z} = 20\,E_R$ as a function of B around 48 G. A complex structure of narrow loss features around the Feshbach resonance pole at 47.78 G is visible. The inset shows an expanded view around the Feshbach resonance zero crossing at 47.944 G with the same data (black circles) and data taken at $V_z = 30\,E_R$ (blue squares). The solid lines simply connect the data points. (b) Solid blue line: Calculated a_S for the same magnetic field region as shown in (a). The shaded areas denote the positions of the loss features shown in (a). The red dashed (green dashed-dotted) lines in (a) and (b) indicate the calculated positions of inelastic CIR resulting from the lowest (first) Bloch band. (c)-(f) show the inelastic CIR as avoided crossings in the energy spectrum of the *ab initio* calculation where the basis set specified in Table A.3 was adopted. The plot is also presented in [44].

of the scattering length where the system becomes superfluid. Moreover, in the situation where the system exhibits a tilt along one lattice direction due to gravity, it has been demonstrated [89] that tunneling is also allowed at positions where the absolute value of the on-site interaction $|U|$ equals the inter-site energy difference caused by the tilt. All three resonances are visible as distinct atom-loss features in Figure 7.1(a): The zero crossing of the Feshbach resonance at 47.944 G and the two resonances left and right from the zero crossing. The latter ones correspond to values of the scattering length of $a_S = -347(17)\,a_0$ and $a_S = +334(16)\,a_0$. A calculation of the positions where the on-site interaction equals the energy gap created by the vertical tilt, leads to positions of $a_S = -371\,a_0$ and $a_S = +335\,a_0$ which is very close to the measured values [44]. Moreover, the assumption that these two loss features are caused by pronounced tunneling in the z direction (the tilted direction) is strengthened by a measurement with a slowing down of tunneling processes along the z direction by increasing the lattice depth V_z to $30\,E_R$. The inset of Figure 7.1(a) shows the measured loss where only the zero-crossing loss survives. This underlines the origin of these loss features to be the tilt.

The other main loss mechanism is the one of inelastic CIR. In a multi-well system, the coupling to a molecule at an inelastic CIR goes along with a tunneling process. Such a tunneling is necessary because, in the Mott-insulating state the particles reside in different wells, while in the molecular state the particles share the same wells (see also Figure 1). Subsequent atom-molecule collisions lead then to enhanced three-body losses.

In Figures 7.1(c)-(f) excerpts of the energy spectrum of *ab initio* calculations that were performed with the approach described in Section 3.4 are shown. The optical-lattice potential of the experiment has to be truncated in order to be computable with the *ab initio* approach. Certainly, a cubic 8-fold degenerate primitive lattice cell is the most natural choice. However, it has turned out that such a potential leads to hardware requirements that are (at the time the calculations were performed)[3] hardly possible. As the computational effort reduces with a decrease in the number of wells, a four-fold degenerate (quadruple well) potential is adopted. This potential results from a Taylor expansion of a $\cos^2$ lattice potential up to order 12 (double well) in the y and z direction and an expansion to the order 6 (sextic single well) in the z direction. In order to reflect the experimental uncertainty of 5% in the potential depths, they are chosen as $(V_x, V_y, V_z) = (19, 20, 21)E_\mathrm{r}$ for the calculation. Since the calculations are already at the edge of computational feasibility, instead of the interaction potential of ^{133}Cs the one of ^{7}Li atoms in the electronic state

[3] Very recent improvements in the code might allow in future to calculate even such complicated structures due to the reduction in the maximal m quantum numbers of the spherical harmonic in the basis.

$a^3\sum_u^+$ [53] is chosen, because it requires less B splines as it supports less number of vibrational bound states than the cesium potential. Although the energies of the highest bound state at low energies might differ slightly for the two interaction potentials, the trap state energies are due to the universality of s-wave interaction almost identical. Hence, the change of the interaction potential might only have a small effect on the resonance positions.

In the experiment, the system is initially prepared in the lowest band. A measurement of the extension of the lowest band shows that it extends from $1.4087\,\hbar\omega_y$ to $1.4120\,\hbar\omega_y$. The two lowest unbound discretized energies for a single-particle solution of the quadruple well are at $1.4275\,\hbar\omega_y$ and $1.431\,\hbar\omega_y$. The energies in the quadruple well are expected to be slightly higher because unlike the optical-lattice potential the quadruple well is infinite and represents a stronger confinement. It is, however, important that the width of the lowest band of $0.0033\,\hbar\omega_y$ for the experiment is in quantitative agreement with the theoretical value of $0.0035\,\hbar\omega_y$ for the quadruple well.

As visible in Figures 7.1(c)-(f), only a few excited bound states show a significant coupling because of symmetry. Considering only resonances with the lowest band (indicated by red dashed lines in Figure 7.1), the structure of the measured and calculated resonances is comparable which is remarkable having in mind the complexity of the system and the fact that a many-body system in a tilted optical lattice is approximated by a two-body calculation in a quadruple well. However, a too small number of resonances are reproduced by the calculation which can be explained by several reasons. First, the linear gradient present in the measurement leads to additional structure in the experimental data as can be seen by the inset of Figure 7.1(a). This gradient cannot be incorporated in the calculation as it breaks the D_2h symmetry which leads to prohibitive computational effort. Moreover, it is possible that the coupling to higher bands leads to resonances with higher states. Resonances with the next band are indicated as green dashed-dotted lines in Figure 7.1. Also, an extension of the external potential to an 8-fold degenerate potential would lead to additional couplings of states that cross non-avoidedly in Figure 7.1(a)-(f). In order to back up the latter reasoning, Figure 7.2 shows the energy spectra of a (sextic) single well, a double well, and a quadruple (four-fold degenerate) well. Clearly, with increasing degeneracy in the wells, the crossing structure becomes more complex leading to an increasing number of. While in the sextic potential only a single clearly distinct resonance position is present at $d_y/a \approx 0$ (where the bound state with com excitations $(2,0,0)$, $(0,2,0)$, and $(0,0,2)$ form avoided crossings with the trap state), for the double well four (one resonance is located at $d_y/a \approx 2$), and for the quadruple well five distinct resonances are visible.

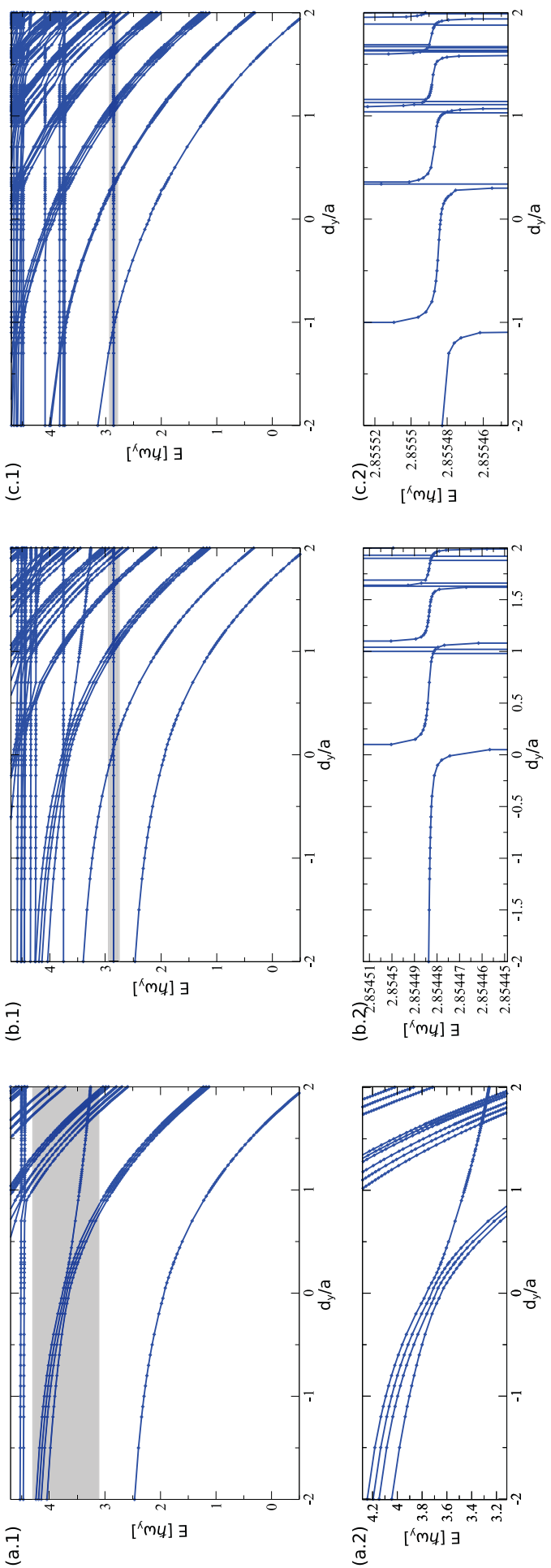

Figure 7.2: From a single well to a quadruple well. The energy spectrum of two Li^7 atoms for the anisotropic trap of the experiment of Innsbruck. (a) single well of sextic form, (b) double well, (c) quadruple well. The plots in the lower row show the zoomed excerpts indicated by gray boxes of the corresponding plots in the first row. With increasing number of wells, the number of resonances with the ground trap state increases. The basis set for the single, double, quadruple well are given in Table A.5, Table A.4, and Table A.3, respectively.

Finally, the wavefunctions are considered. In Figure 7.3 cuts along the z direction (which has a double-well profile) are shown. The bound state of Figure 7.3(a) is a deeply bound rovibrational state of the Born-Oppenheimer potential. The particles in this molecular state share almost the same position which is displayed by the fact that only the diagonal, where the two atoms are at the same position ($z_1 = z_2$; $x_1 = x_2 = y_1 = y_2 = 0$), is populated. Figure 7.3(b) shows a bound state close to a resonance (avoided crossing) where the trap state of Figure 7.3(c) is already admixed. Hence, the population of the diagonal is weakened (compared to the pure bound state without trap state admixture) but still predominantly present. It is important to note that the double-well structure along the z direction is reflected in the two distinct maxima that correspond to the two potential minima in the z direction. Figure 7.3(c) and Figure 7.3(d) are two discretized states of the lowest band at $a \approx 0$. Both states show the feature that the atoms are separated. Figure 7.3(d) is the typical Mott-insulator state with unit filling where both atoms reside exclusively in different wells. This is displayed in the occupation of the anti-diagonal wells (on the anti-diagonal the positions satisfy $z_1 = -z_2$, $x_1 = x_2 = y_1 = y_2 = 0$). Remarkably, the ground state is not the Mott-insulator state of Figure 7.3(d) but the state shown in Figure 7.3(c) that has a slightly smaller energy. While the emergence of this unconventional ground state is not directly related to the occurrence of inelastic CIR and hence beyond the scope of this thesis, its occurrence is surprising and will be subject to further research.

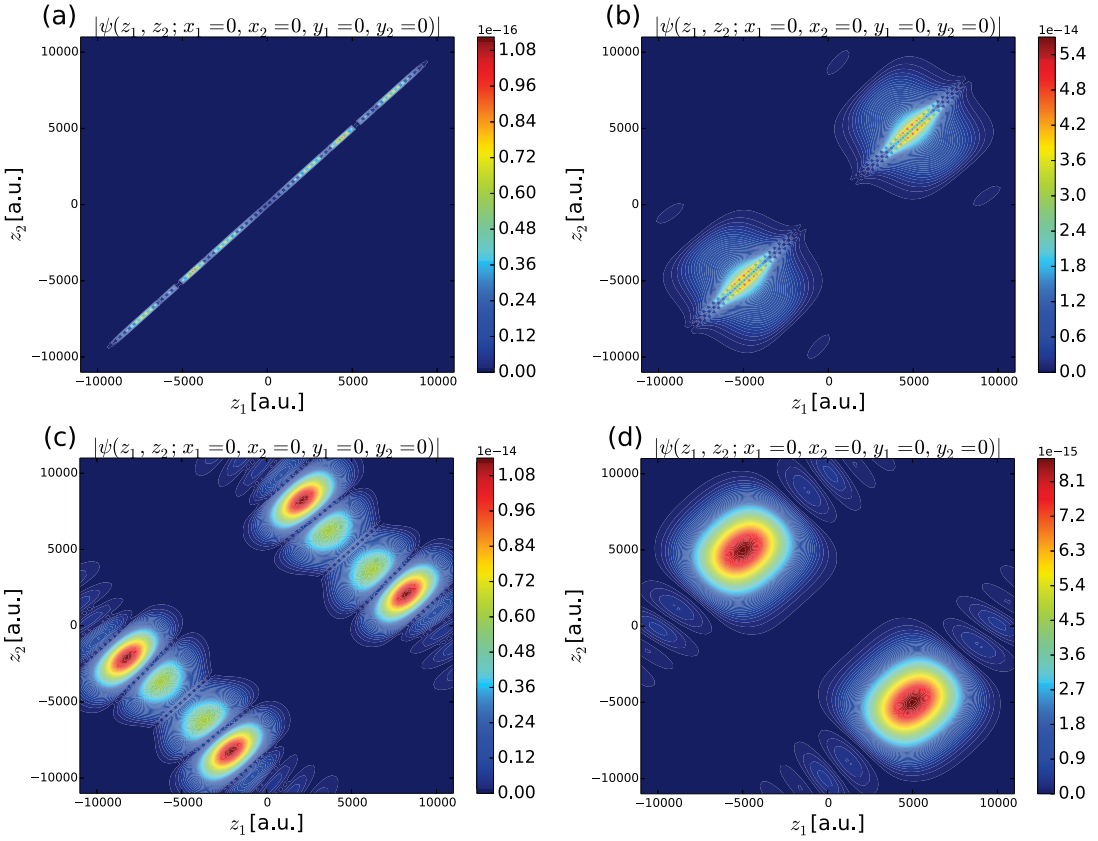

Figure 7.3: Cuts along the z-direction (direction of the elongated double well) ($|\Psi(z_1, z_2; x_1 = x_2 = y_1 = y_2 = 0)|^2$) through the full six-dimensional *ab initio* wavefunction. (a) Wavefunction of a deeply bound state at $d_y/a = -2$ with an energy of $E = -56855\hbar\omega_y$. (b) Bound state close to a resonance that has already significant admixture of the trap state at $d_y/a = -2$ with an energy of $E = 2.836\hbar\omega_y$. (c) Cut through a wavefunction of a trap state at $a \approx 0$ ($d_y/a = -10000$) with an energy of $E = 2.855\hbar\omega_y$. (d) Cut through a wavefunction of a trap state at $a \approx 0$ ($d_y/a = -10000$) with an energy of $E = 2.862\hbar\omega_y$. The basis set used is the one of Table A.3.

8 Conclusion of Part I

In Part I, it was shown that the originally unexpected behavior of loss resonances in an ultracold atomic gas of cesium atoms [39], i. e. a splitting of the resonance position for a transversal anisotropic quasi-1D confinement and a resonance position for a negative value of the s-wave scattering length, cannot be described by elastic CIR as first persistently presumed. It was worked out, by an alternative formulation of the mechanism of elastic CIR in quasi 1D, that the resonance occurs where the shifted bound part of the energy spectrum crosses the trap-state threshold. Thus, there exists only a single resonance in quasi 1D, regardless of the transversal anisotropy of the external confinement, because only a single rel. motion bound state exists. Moreover, the shifted bound part of the rel. motion Hamiltonian which is one part of the decomposition of the energy spectrum is no eigenstate of the full rel. motion Hamiltonian. Therefore, no coupling of this state to the trap state is present which could allow for a molecule formation with subsequent losses. Hence, in the Innsbruck loss experiment [39] no loss feature at the elastic CIR is observed (although it first seemed so due to the within their widths overlapping positions of the inelastic and elastic CIR). In contrast, at the elastic CIR the diverging effective 1D interaction strength $g_{1\mathrm{D}}$ leads to a local behavior of the quantum gas equivalent to the one of non-interacting identical fermions – a system where it is intuitive that no losses and heating occurs.

It was demonstrated that the theory of inelastic CIR, in which resonances occur due to the c.m.-rel. motion coupling of c.m. excited bound states with trap states, is capable of describing quantitatively the diverse loss features of the experiments in [39, 42, 44]. In order to indisputably confirm that the observed losses in the Innsbruck experiment are caused by inelastic CIR and not by other proposed mechanisms such as elastic CIR, multichannel, many-body, or cesium-specific effects, an experiment was suggested and then performed that, by design, allows for an exclusion of other mechanisms: the observation of a coherent molecule formation at inelastic CIR in a two-body system of lithium atoms initially prepared in the lowest trap state [42]. Quantitative agreement of the resonance positions, widths and coupling strengths confirms uniquely the introduced theory of inelastic CIR.

In order to provide easy-to-access formulas for the calculation of the inelastic CIR positions and coupling strengths in single-well potentials, the c.m.-rel. motion coupling model was introduced. A comparison to *ab initio* calculations demonstrated

that the model accurately describes the behavior of inelastic CIR. The analysis, however, also revealed the limitations of the model which is only capable to describe qualitatively the coupling strengths for resonances involving higher-order longitudinally excited c.m. states in the quasi-1D limit and leads to unphysical behavior for the coupling strengths in the quasi-2D limit. However, in comparison to the experiment described in [42] it has lead to the insight that inelastic CIR can also be present for negative values of the s-wave scattering length. Moreover, resonances with c.m. excitations in the weakly confined direction can lead to molecule formation, especially for mild anisotropies where the coupling strength has a maximum. Hence, also these resonances are expected to have a direct impact on the stability of ultracold quantum gases.

Finally, the investigation of inelastic CIR in multi-well systems has lead to the finding that the complex structure of loss features very recently observed in a shallow 3D optical lattice are caused by anharmonicity-induced c.m.-rel. motion coupling resonances. Starting in a Mott-insulator state the coupling to a molecule with subsequent losses at the inelastic CIR goes along with a tunneling process.

It is remarkable that the mechanism of inelastic CIR is of very universal nature. Recently, it was found that in ultracold dipolar [94] systems these resonances are also present as well as in excitons and quantum dots underlying the Coulomb interaction [95]. For the latter they are proposed for a novel kind of single-photon source.

The performed studies have not only impressively demonstrated that one of the most fundamental and routinely adopted approximations in ultracold atomic quantum gases – the harmonic approximation – has to be abandoned in order to describe particle loss, heating, and molecule formation in a variety of experiments. But also pave the way for novel methods in ultracold atom experiments to alter the interaction behavior. Especially in cases where the standard technique of using magnetic Feshbach resonances is blocked, such as for earth-alkali atoms, it seems to be possible to tune the effective interaction of the system by a variation of the external confinement in the vicinity of an inelastic CIR. Similar to a magnetic Feshbach resonance this enables the coherent association of molecules.

Part II

Theoretical approach for ultracold few-body systems beyond the harmonic approximation

Part I focused on two-body resonances induced by the coupling of c.m. and rel. motion. Such inelastic CIR occur when c.m. excited bound states cross with trap states and couple via an anharmonicity in the external potential. On the other hand, it is known that the Efimov effect [96–98], which has established itself as a flagship of few-body physics and has been extensively investigated theoretically [45, 99–101] and experimentally [102–109], leads to three-body bound states. Moreover, it has been found that bound states involving more than three atoms [105, 106, 110, 111] exist. It is possible that c.m. excited few-body bound states couple to a state of unbound atoms via c.m.-rel. coupling due to the anharmonicity of the external confinement and lead to *inelastic few-body CIR*.

In order to investigate the influence of an anharmonic confinement on ultracold few-body systems, many computational methods (such as those working in hyperspherical coordinates, see e. g. [45] and references therein) are not suitable because most are based on a harmonic approximation of the trap potential. In order to perform calculations of ultracold few-body systems beyond the harmonic harmonic approximation, Part II describes the development of a theoretical method for solving the stationary non-relativistic Schrödinger equation for a variable number of ultracold atoms in a variable external confinement.

The approach builds on well established computational methods of electronic-structure theory, i. e. Hartree-Fock and configuration interaction. In order to adapt these methods to the computation of ultracold atomic systems, the electrons are formally replaced by ultracold atoms and the potential of the nuclei is exchanged by an external trap potential.

In electronic-structure calculations the use of Gaussian basis functions has a long tradition and is even more widespread than the use of Slater-type orbitals. Although the Gaussian basis functions consisting of the product of a Gaussian exponent an a polynomial describe the wavefunctions of the Coulomb potential less accurately than Slater-type orbitals, they are numerically much more efficient. The main reason is that the multi-center two-electron integrals can be calculated more rapidly because the product of two Gaussians at two distinct locations is equal to one Gaussian at a third location. Different to the Coulomb potential, the wells in an optical potential can be approximated by an harmonic potential. Since the Gaussian basis functions resemble the eigenfunctions of a harmonic oscillator they are the natural choice for this type potentials. This makes the approach of describing few-body systems of ultracold atoms in a finite multi-well potential very promising from a computational perspective.

In principle also other approaches to describe few-body systems can be chosen. For example, the structure of an optical lattice is equivalent to the periodic structure of a solid state where basis sets resembling the band structure more appropriately

such as plane waves are favorable. However, since ultracold few-body experiments adopting only a small number of wells even in low dimensionality are very topical nowadays, the Gaussian basis is preferred due to its flexibility. Of course, also different approaches such as density-functional theory could be adopted. The main reason that at first the Hartree-Fock with subsequent CI based approach is chosen relies on the fact that for a realistic potential the variational principle is valid and convergence is expected to be achievable in a systematic way.

Different to the numerical method used in Part I to calculate interacting two-body systems, the developed approach is formulated in cartesian coordinates instead of spherical ones. This has the advantage that the external potential can be treated in a simple way. However, different to the spherical approach where the calculation of the interaction integral reduced to an effective single-particle one, the treatment of the interaction becomes the most demanding step.

Due to the origin of electronic-structure calculations the present implementation is so far restricted to fermionic atoms. Yet, a future extension to bosons seems straightforward.

Before describing the details of the implementation, the basics of the theory of electronic-structure calculations are reviewed. The description is reduced to a brief summary of important concepts with direct relevance to the presented approach.

9 Basics of electronic-structure theory

The gross of electronic-structure theory literature uses first quantization notation in which observables are represented by operators and wavefunctions by functions, i. e. electronic spin orbitals in terms of *Slater determinants*. In the description presented here, the formalism of *second quantization* is adopted such as presented, e. g. in [112], where the wavefunctions are represented by operators, i. e. by creation and annihilation operators acting on the vacuum. One advantage of second quantization is that the formulation becomes independent of the particle number. In fact, the very heart of the presented approach, the full configuration-interaction (FCI) code (introduced in Section 10.3) explicitly uses excitation operators consisting of combinations of creation and annihilation operators which leads to an enormous simplification of the resulting code.

9.1 Fock space

An *orbital* is defined as a single-particle wavefunction, i. e. in electronic-structure theory it is the wavefunction of a single electron. A *spin orbital* $\phi_P(\mathbf{x})$ depends on the collection of coordinates $(\mathbf{r}, \sigma)$, where $\mathbf{r}$ is the spatial coordinate and σ the spin coordinate. A wavefunction of N fermions has to be antisymmetric under particle exchange (Pauli exclusion principle) and is conveniently represented by a normalized *Slater determinant*

$$|\phi_{P_1}\phi_{P_2}\cdots\phi_{P_N}| = \frac{1}{\sqrt{N!}} \begin{vmatrix} \phi_{P_1}(\mathbf{x_1}) & \phi_{P_2}(\mathbf{x_1}) & \cdots & \phi_{P_N}(\mathbf{x_1}) \\ \phi_{P_1}(\mathbf{x_2}) & \phi_{P_2}(\mathbf{x_2}) & \cdots & \phi_{P_N}(\mathbf{x_2}) \\ \vdots & \vdots & \ddots & \vdots \\ \phi_{P_1}(\mathbf{x_N}) & \phi_{P_2}(\mathbf{x_N}) & \cdots & \phi_{P_N}(\mathbf{x_N}) \end{vmatrix} . \tag{9.1}$$

In *Fock space*, each determinant is represented by an *occupation number* vector

$$|\mathbf{k}\rangle = |k_1, k_2, \ldots, k_M\rangle , \quad k_P = \begin{cases} 1, & \text{if } \phi_P \text{ occupied} \\ 0, & \text{if } \phi_P \text{ unoccupied} \end{cases} \tag{9.2}$$

where M is the number of considered spin orbitals. Note, for fermions the occupation number can only take the values $\{0, 1\}$ which reflects the fact that only a single

electron can occupy one spin orbital due to the Pauli exclusion principle. In case of bosons, the occupation number can take all integer values.

For an orthonormal set of spin orbitals the inner product of occupation-number vectors is given by

$$\langle \mathbf{k}|\mathbf{m}\rangle = \delta_{\mathbf{k},\mathbf{m}} = \prod_{P=1}^{M} \delta_{k_P,m_P}. \tag{9.3}$$

Operators and states can be expressed in second quantization by *creation* operators $a_P^\dagger$ and *annihilation* operators a_P that are defined by

$$a_P^\dagger \left|k_1, k_2, \ldots, 0_P, \ldots, k_M\right\rangle = \Gamma_P^{\mathbf{k}} \left|k_1, k_2, \ldots, 1_P, \ldots, k_M\right\rangle \tag{9.4}$$
$$a_P^\dagger \left|k_1, k_2, \ldots, 1_P, \ldots, k_M\right\rangle = 0 \tag{9.5}$$

and

$$a_P \left|k_1, k_2, \ldots, 1_P, \ldots, k_M\right\rangle = \Gamma_P^{\mathbf{k}} \left|k_1, k_2, \ldots, 0_P, \ldots, k_M\right\rangle \tag{9.6}$$
$$a_P \left|k_1, k_2, \ldots, 0_P, \ldots, k_M\right\rangle = 0 \tag{9.7}$$

where the phase factor

$$\Gamma_P^{\mathbf{k}} = \prod_{Q=1}^{P-1} (-1)^{k_Q} \tag{9.8}$$

is necessary to conform with the definition of wavefunctions and operators in first quantization. The creation and annihilation operators fulfill the anti-commutation relation

$$[a_P^\dagger, a_Q^\dagger]_+ = 0 \tag{9.9}$$
$$[a_P, a_Q]_+ = 0 \tag{9.10}$$
$$[a_P^\dagger, a_Q]_+ = \delta_{PQ} \tag{9.11}$$

where the anti-commutator bracket

$$[X, Y]_+ = XY + YX \tag{9.12}$$

reflects the fermionic properties under particle exchange. Another operator that will be of crucial importance in the FCI code is the excitation operator

$$X_Q^P = a_P^\dagger a_Q \tag{9.13}$$

that annihilates a particle in orbital Q and creates one in orbital P. X_Q^P conserves the total number of particles given as the expectation value of the particle number operator

$$N = \sum_{P=1}^{M} N_P = \sum_{P=1}^{M} a_P^\dagger a_P \quad . \tag{9.14}$$

It is important to note that every occupation-number vector can be presented as the action of creation operators on the vacuum state $|\text{vac}\rangle$.

9.2 Electronic Hamiltonian in second quantization

The electronic Hamiltonian in Born-Oppenheimer approximation describing N electrons in the Coulomb potential of M nuclei reads in second quantization

$$H = \sum_{PQ} h_{PQ}\, a_P^\dagger a_Q + \frac{1}{2} \sum_{PQRS} g_{PQRS}\, a_P^\dagger a_R^\dagger a_S a_Q + h_{\text{nuc}} \tag{9.15}$$

with

$$h_{PQ} = \int d\mathbf{x}\, \phi_P^*(\mathbf{x}) \left(-\frac{1}{2}\nabla^2 - \sum_A \frac{Z_A}{|\mathbf{r} - \mathbf{r}_A|} \right) \phi_Q(\mathbf{x}) \tag{9.16}$$

$$g_{PQRS} = \int\int d\mathbf{x}_1 d\mathbf{x}_2\, \phi_P^*(\mathbf{x}_1)\phi_R^*(\mathbf{x}_2)\, \frac{1}{|\mathbf{r}_1 - \mathbf{r}_2|}\, \phi_Q(\mathbf{x}_1)\phi_S(\mathbf{x}_2) \tag{9.17}$$

$$h_{\text{nuc}} = \frac{1}{2} \sum_{A \neq B} \frac{Z_A Z_B}{|\mathbf{r}_A - \mathbf{r}_B|} \tag{9.18}$$

where Z_A is the charge of the nucleus at position $\mathbf{r}_A$. Note, the nuclear repulsion term h_{nuc} reduces to a constant for the solution of the electronic Schrödinger equation in Born-Oppenheimer approximation. Hence, the operators in first quantization enter in the amplitudes h_{PQ} and g_{PQRS}. These amplitudes can be interpreted respectively as a measure of probability of the occurrence of the corresponding single and double excitations. An important difference between the first and second quantized representation is that while in first quantization the exact operators enter directly the Hamiltonian that is dependent on the number of electrons but independent on the spin-orbital basis, the Hamiltonian in second quantization contains only projections of the exact operators in the amplitudes h_{PQ} and g_{PQRS}, and the operators are independent of the number of electrons but explicitly dependent on the spin-orbital basis.

The Hamiltonian in Eq. (9.15) explicitly contains spin coordinates through the

creation and annihilation operators of spin orbitals and the integrals over spin coordinates in h_{PQ} and g_{PQRS}. Since the Hamiltonian commutes with the total and the projected angular momentum operators,

$$[H, L_z] = 0 \quad \text{and} \quad [H, L^2] = 0, \tag{9.19}$$

respectively, it can be written in a spin-free form. Because of the orthonormality of spin functions

$$\int dm_s \, \sigma^*(m_s) \, \tau(m_s) = \delta_{\sigma\tau} \quad , \tag{9.20}$$

integrals containing opposite spin parts over a spin-free operator vanish. Therefore, the spin-free one-electron operator f in spin-orbital basis can be expressed directly in a spatial orbital basis

$$f = \sum_{PQ} f_{PQ} a_P^\dagger a_Q = \sum_{p\sigma q\tau} f_{p\sigma q\tau} a_{p\sigma}^\dagger a_{q\tau} = \sum_{pq} f_{pq} E_{pq} \tag{9.21}$$

where

$$f_{p\sigma q\tau} = \delta_{\sigma\tau} \int d\mathbf{r} \, \phi_p^*(\mathbf{r}) f(\mathbf{r}) \phi_q(\mathbf{r}) = f_{pq} \delta_{\sigma\tau} \tag{9.22}$$

was used and the *singlet excitation operator*

$$E_{pq} = a_{p\alpha}^\dagger a_{q\alpha} + a_{p\beta}^\dagger a_{q\beta} \tag{9.23}$$

is introduced. Here, the creation operator $a_{p\sigma}^\dagger$ is meant to create an occupation of the spin orbital

$$\phi_{p\sigma}(\mathbf{r}, m_s) = \phi_p(\mathbf{r}) \, \sigma(m_s) \tag{9.24}$$

that consists of a spatial orbital part ϕ_p multiplied by a spin eigenfunction σ which can take as spin coordinate $m_s \in \{-1/2, 1/2\}$. α and β denote the eigenfunctions of the projected angular-momentum spin operator S_z. The singlet excitation operator E_{pq} will play a crucial role in the FCI code. An analogous derivation [112] can be performed for two-electron operators which leads to

$$g = \frac{1}{2} \sum_{pqrs} g_{pqrs} \, (E_{pq} E_{rs} - \delta_{qr} E_{ps}) \quad . \tag{9.25}$$

where

$$g_{pqrs} = \int\int d\mathbf{r}_1 d\mathbf{r}_2 \, \phi_p^*(\mathbf{r}_1)\phi_r^*(\mathbf{r}_2) \, g(\mathbf{r}_1, \mathbf{r}_2) \, \phi_q(\mathbf{r}_1)\phi_s(\mathbf{r}_2) \tag{9.26}$$

is the matrix element of spatial orbitals over the two-electron operator in first quantization. Finally, the second-quantization representation of the non-relativistic spin-free electronic Hamiltonian in spatial orbital basis is given by

$$H = \sum_{pq} h_{pq} \, E_{pq} + \frac{1}{2} \sum_{pqrs} g_{pqrs} \;\; (E_{pq}E_{rs} - \delta_{qr}E_{ps}) + h_{\text{nuc}} \tag{9.27}$$

with

$$h_{pq} = \int d\mathbf{r} \, \phi_p^*(\mathbf{r}) \left(-\frac{1}{2}\nabla^2 - \sum_A \frac{Z_A}{|\mathbf{r} - \mathbf{r}_A|} \right) \phi_q(\mathbf{r}) \tag{9.28}$$

$$g_{pqrs} = \int\int d\mathbf{r}_1 d\mathbf{r}_2 \, \phi_p^*(\mathbf{r}_1)\phi_r^*(\mathbf{r}_2) \, \frac{1}{|\mathbf{r}_1 - \mathbf{r}_2|} \, \phi_q(\mathbf{r}_1)\phi_s(\mathbf{r}_2) \quad . \tag{9.29}$$

The Hamiltonian Eq. (9.27) quickly becomes computationally intractable for many-body systems of interest and therefore approximations have been developed. One of the most basic ones is the Hartree-Fock approximation.

9.3 The Hartree-Fock approximation

The Hartree-Fock approximation is central to electronic-structure theory. Many advanced methods, so called post-Hartree-Fock methods, use it as a starting point. The Hartree-Fock approximation is a single-determinant model, i. e. the Hartree-Fock approximation delivers a set of spin orbitals such that the determinant formed from it results in the lowest possible ground-state energy. In view of ultracold atomic gases it should be noted that the Hartree-Fock approximation leads to a mean-field theory, i. e. the influence of interparticle interaction on a single particle is treated as field created by all other particles. Due to this ansatz Hartree-Fock does not take fully into account electron correlation. In fact, due to the anti-symmetrized determinant wavefunction, the exchange correlation that describes the correlation of electrons with parallel spins is included in the Hartree-Fock approximation, but not the interaction correlation (because of the mean-field ansatz) or the correlation associated with the total spin or the overall symmetry of the system. The sum of correlation energy not included in the Hartree-Fock energy can be defined by the difference of the exact non-relativistic ground-state energy of the system and the Hartree-Fock limit, i. e. the (converged) ground-state energy of the Hartree-Fock

approximation in the limit of an infinite basis.

Especially for the description of BECs the Hartree-Fock approximation has gained major popularity in ultracold gases in terms of the Gross Gross-Pitaevski equation [69, 113, 114]. It can be derived by applying the Hartree-Fock approximation to a system of Bosons interacting via the δ pseudopotential.

9.3.1 The Fock operator

A Hartree-Fock state represents a variationally optimized Slater determinant and can thus be interpreted as a wavefunction where each particle behaves independently. Such a wavefunction is the solution of an effective one-electron Schrödinger equation, the effective Hamiltonian being the Fock operator $\mathcal{F}$. For convenience, the theoretical introduction (but not the implemented numerical method) presented here is restricted to closed-shell systems, i. e. each occupied orbital contains both spin components (α and β).

The Fock operator in second quantization must have a one-electron representation that is Hermitian and totally symmetric in spin space. It can hence be given as

$$\mathcal{F} = \sum_{pq} f_{pq} E_{pq} \tag{9.30}$$

with the symmetric *Fock matrix* f_{pq}. By the construction with the operators E_{pq} (that includes both spin components), the energy levels of the Fock operator are doubly degenerate, occupied by one eigenfunction with α and one with β spin. The eigenfunctions of the Hartree-Fock equation

$$\mathcal{F} a^\dagger_{p\sigma} |\mathrm{vac}\rangle = \varepsilon_p a^\dagger_{p\sigma} |\mathrm{vac}\rangle \tag{9.31}$$

are the canonical spin-orbitals with orbital energy ε_p. The total energy of the closed-shell Hartree-Fock wavefunction

$$|\mathrm{cs}\rangle = \left(\prod_p a^\dagger_{p\alpha} a^\dagger_{p\beta} \right) |\mathrm{vac}\rangle \tag{9.32}$$

is obtained from the expectation value with the total Hamiltonian

$$E_0^{\mathrm{HF}} = \langle \mathrm{cs}|H|\mathrm{cs}\rangle \quad . \tag{9.33}$$

Optimizing variationally $|\mathrm{cs}\rangle$ and requiring that $\mathcal{F}$ becomes the exact Hamilitonian in the limit of no electron correlation, the Fock operator is determined by the matrix

[112]

$$f_{pq} = \frac{1}{2}\sum_{\sigma} \langle \mathrm{cs}|[a^{\dagger}_{q\sigma}, [a_{p\sigma}, H]]_{+}|\mathrm{cs}\rangle \tag{9.34}$$

which can be shown to evaluate to

$$f_{pq} = h_{pq} + \sum_{i}(2g_{pqii} - g_{piiq}) \quad . \tag{9.35}$$

It should be noted the Fock matrix takes this form only in a canonical basis where the Fock operator is diagonal. Based on this representation and noting that for a closed-shell Hartree-Fock ground state the only non-zero density matrix elements are those with all indices inactive

$$D_{pq} = \langle \mathrm{cs}|E_{pq}|\mathrm{cs}\rangle = 2\delta_{pq} \tag{9.36}$$

$$d_{pqrs} = \langle \mathrm{cs}|E_{pq}E_{rs} - \delta_{qr}E_{ps}|\mathrm{cs}\rangle = 4\delta_{pq}\delta_{rs} - 2\delta_{ps}\delta_{qr} \quad , \tag{9.37}$$

the Hartree-Fock ground state energy for a closed shell system

$$E_0^{\mathrm{HF}} = 2\sum_{i} h_{ii} + \sum_{ij}(2g_{iijj} - g_{ijji}) + h_{\mathrm{nuc}} \tag{9.38}$$

resembles the mean-field character of Hartree-Fock theory. The first term reflects the kinetic energy and the interaction of the electrons with the static nuclei. The second term reflects averaged repulsive interactions between the electrons, that contains exchange and Coulomb contributions.

The diagonalization of the Fock matrix yields a set of canonical orbitals from which the Hartree-Fock ground state is constructed. However, the matrix itself consists of contributions of the orbitals. This makes the problem nonlinear and not directly solvable. Hence, the solution of the Hartree-Fock equations must be found iteratively which results in a self-consistent wavefunction. Such a non-linear fixed-point iteration is, of course, not guaranteed to converge and can be highly complex. Such an iteration scheme for a non-orthonormal basis set is described next.

9.3.2 Roothaan-Hall equations and SCF procedure

In the approach presented here, the molecular orbitals ϕ_p are expanded as

$$\phi_p = \sum_{\mu} C_{p\mu}\chi_{\mu} \tag{9.39}$$

in terms of atomic orbitals χ_μ that are given as a set of contracted Gaussian basis functions (CGBF). Using the expansion coefficients $C_{p\mu}$ as variational parameters to minimize the Hartree-Fock ground-state energy (which can be performed by introducing Lagrangian multipliers, see [112, 115]) leads to the Roothaan-Hall equations [115] that can compactly be written in matrix form as

$$\mathbf{F}^{\mathrm{AO}}\mathbf{C} = \mathbf{S}\mathbf{C}\varepsilon \tag{9.40}$$

where $\mathbf{S}$ is the overlap matrix and $\mathbf{F}^{\mathrm{AO}}$ is the Fock matrix in the atomic-orbital basis

$$f_{\mu\nu}^{\mathrm{AO}} = h_{\mu\nu} + \tilde{g}_{\mu\nu} \tag{9.41}$$

$$\tilde{g}_{\mu\nu} = \sum_{\rho\sigma} D_{\rho\sigma}^{\mathrm{AO}} (g_{\mu\nu\rho\sigma} - \frac{1}{2} g_{\mu\sigma\rho\nu}) \quad . \tag{9.42}$$

Here,

$$D_{\rho\sigma}^{\mathrm{AO}} = \mathbf{C}\mathbf{D}\mathbf{C}^T = 2\sum_i C_{\rho i} C_{\sigma i} \tag{9.43}$$

is the matrix representation of the one-electron density matrix in the atomic-orbital basis that can be obtained by a linear transformation of the representation in the molecular-orbital basis. The Roothaan-Hall equations transform the Hartree-Fock equations that are a coupled system of integro-differential equations into a pseudo-eigenvalue equation involving matrices that can be diagonalized efficiently using standard numerical analysis techniques.

An iterative procedure [115] to solve self-consistently the Roothaan-Hall equation can now schematically be drawn as follows.

1. Specify the molecule (system of trapped ultracold atoms): a configuration of nuclei (external trap potential), a number of electrons (ultracold atoms) and a basis set.
2. Calculate all necessary integrals needed for $h_{\mu\nu}$ and $g_{\mu\nu\rho\sigma}$, i. e. overlap $S_{\mu\nu}$, kinetic energy, potential energy and interaction integrals.
3. Diagonalize the overlap matrix $\mathbf{S}$ to obtain a transformation matrix $\mathbf{X}$ to orthogonalize the basis set.
4. Make an initial guess for density matrix $\mathbf{D}$, in the present case the one for the non-interacting system is chosen.
5. Build the Fock matrix $f_{\mu\nu}^{\mathrm{AO}} = h_{\mu\nu} + \tilde{g}_{\mu\nu}$.
6. Transform the Fock matrix to the orthonormal basis via $\mathbf{f}' = \mathbf{X}^\dagger \mathbf{f}^{\mathrm{AO}} \mathbf{X}$.
7. Diagonalize $\mathbf{f}'$ to obtain the C' and the orbital energies.

8. Transform back to get $\mathbf{C} = \mathbf{X}\mathbf{C}'$
9. Form a new density $D_{\mu,\nu} = \sum_\sigma C_{\mu\sigma} C_{\nu\sigma}$.
10. Is density converged? $\begin{cases} \text{Yes: Finish} \\ \text{No: Rebuild Fock matrix with new density, go to 5.} \end{cases}$

9.3.3 Unrestricted, open-shell Hartree-Fock

So far, the special case of restricted closed-shell Hartee-Fock theory has been considered. However, not all physical situations can be described by restricted closed-shell calculations. In electronic structure theory, for instance, the dissociation of molecules like H_2 at long bond lengths into open-shell systems cannot be described accurately by restricted closed-shell calculations [115].

In the case of restricted calculations, a set of K spatial orbitals ϕ_p leads to a set of $2K$ spin orbitals $\{\phi_{2P-1}\alpha_{2P-1}, \phi_{2P}\beta_{2P}\}$. In a closed-shell case all spin orbitals are doubly occupied. In contrast, in the unrestricted case, the spatial orbitals for different spin orbitals can differ which leads to a spin-dependent set represented by $\{\phi^\alpha_{2P-1}\alpha_{2P-1}, \phi^\beta_{2P}\beta_{2P}\}$. In the unrestricted case, the Pople-Nesbet [115] equations

$$\mathbf{F}^\alpha \mathbf{C}^\alpha = \mathbf{S}\mathbf{C}^\alpha \varepsilon^\alpha \tag{9.44}$$

$$\mathbf{F}^\beta \mathbf{C}^\beta = \mathbf{S}\mathbf{C}^\beta \varepsilon^\beta \tag{9.45}$$

build the analog to the Roothaan-Hall equations of the restricted case, which are coupled since the Fock matrices $\mathbf{F}^\alpha$ and $\mathbf{F}^\beta$ each depend on both $\mathbf{C}^\alpha$ and $\mathbf{C}^\beta$. The two eigenvalue problems can be solved simultaneously in a similar fashion as the Roothaan-Hall equations involving unrestricted density matrices. For a more detailed description, the reader is referred to literature, e. g. [115, 116].

9.4 Configuration interaction

Configuration interaction (CI) is conceptually (but by far not computationally) perhaps the simplest post-Hartree-Fock method. Before in Section 10.3 a detailed description of the implementation of a determinant-based direct FCI algorithm will be described, in the present section the basic principle of configuration interaction is briefly outlined.

As a post-Hartree-Fock method, CI starts from the Hartree-Fock ground state determinant $|\mathrm{HF}\rangle$. Applying singly, doubly, ..., N-tuply excitation operators to $|\mathrm{HF}\rangle$ leads to a set of many-electron wavefunctions which can be used as a basis to represent the complete wavefunction of the system. If all excitations up to the

particle number N are incorporated, full CI (FCI) is achieved. The FCI wavefunction

$$|\mathrm{FCI}\rangle = \left(c_0 + c_I^A \sum_{AI} X_I^A + c_{IJ}^{AB} \sum_{A>B,I>J} X_{IJ}^{AB} + \cdots \right) |\mathrm{HF}\rangle \tag{9.46}$$

is the best approximation to the exact wavefunction that is achievable with a given basis set of atomic orbitals. Hence, FCI serves as a basis-set benchmark to other post-Hartree-Fock methods that incorporate electron correlation. In Eq. (9.46), the excitation operators are given as

$$X_I^A = a_A^\dagger a_I \tag{9.47}$$

$$X_{IJ}^{AB} = a_A^\dagger a_B^\dagger a_I a_J \tag{9.48}$$

$$\vdots \quad .$$

The procedure for obtaining the FCI energies and wavefunctions is to represent the Hamiltonian matrix in the basis of the excited determinants followed by a diagonalization of the resulting FCI matrix. It is important to mention that the number of FCI n-tuply excited determinants scales very inconveniently. A treatment of $N = 4$ electrons with $K = 1000$ spatial orbitals results in $\binom{2K}{N} \approx 6.6 \cdot 10^{11}$ configurations. Although it is neither possible to store such a matrix nor to diagonalize it, there are possibilities to compute iteratively eigenenergies and eigenfunctions of a very large number of configurations as will be described in Section 10.3.

10 Numerical implementation

The implementation of a collection of quantum-chemistry methods is time consuming. There are estimates [116] that large, highly optimized, versatile quantum-chemistry packages require roughly about 25 man-years to be developed from scratch. Although the complexity of a Hartree-Fock with subsequent CI calculation falls below the one of large quantum-chemistry packages, the implementation and testing is still very time consuming. Especially, since the chosen ansatz of a basis consisting of contracted Gaussian basis functions is widely used, the author decided to use an open-source quantum chemistry program package that uses Gaussians as a starting point. This saved a huge amount of developing time that is needed to write and structure and test a large number of low-level routines.

On the other hand, the manipulation of large quantum-chemistry programs is an adventurous task because they are (usually) written in different programing languages, have been grown and optimized over decades and are even to the developers hard to maintain. Especially since the transition from an electronic systems to ultracold atoms requires substantial changes to the code the author decided to choose the comparably transparently structured open-source quantum-chemistry package PyQuante [117] at version 1.64. The most parts of the codes, especially administrative ones, are written in the Python programing language, the numerically demanding parts are implemented in C. Python is a high-level object-oriented programming language that is widely considered to result well-structured codes. As an interpreted language it is slower compared to compiled low-level languages. However, there are several possibilities to easily optimize time consuming parts of the code by wrapping low-level code such as Fortran [118] and C [119]. Perhaps the most elegant way to speed up code (at least at the time when the author was working on the code) is the use of Cython, which is "an optimising static compiler for both the Python programming language and the extended Cython programming language" [119, 120].

10.1 Basic structure of PyQuante

In the following, the basic structure of the PyQuante code and the changes that were necessary in order to compute N ultracold fermionic atoms in a versatile external trap potential are explained.

Every calculation starts with the definition of a system, that is represented by the `Molecule` object that contains information on the molecule, i. e. a generic name, information on the atom numbers and their positions, the molecular charge, and the multiplicity. For example, a H_2 molecule with internuclear distance of $1.4\,a_0$ can be specified[1] by

```
from Molecule import Molecule
h2 = Molecule('h2',[(1,(0,0,0)),(1,(1.4,0,0))], charge=0,
              multiplicity=1)
```

where each element in the list of nuclei `[(1,(0,0,0)),(1,(1.4,0,0))]` consists of the nuclear charge and the position in cartesian coordinates. Next, a basis set must be specified which is constructed from contracted Gaussian basis functions (CGBF)

$$\mathrm{CGBF}(\mathbf{r}) = \sum_j c_j \eta_j(\mathbf{r}) \tag{10.1}$$

that in turn consist of primitive Gaussian basis functions (PGBF)

$$\eta_j(\mathbf{r}) = N_j \,(x - x_{A_j})^{l_j} (y - y_{A_j})^{m_j} (z - z_{A_j})^{n_j} \,\exp(\alpha_j (\mathbf{r} - \mathbf{A}_j)^2) \tag{10.2}$$

centered at $\mathbf{A}_j$ where

$$N_j = \left(\frac{2^{2(l_j+m_j+n_j)+3/2}\, \alpha_j^{l_j+m_j+n_j+3/2}}{\pi^{3/2}\,(2l_j-1)!!\,(2m_j-1)!!\,(2n_j-1)!!} \right)^{\frac{1}{2}} \tag{10.3}$$

is the normalization constant with the double factorial $i!! = 1 \cdot 3 \cdot 5 \cdots i$. The objects `CGBF` and `PGBF` store the information on the parameters but also contain numerous useful routines such as different types of integrals with other Gaussians, gradients, Laplacians, etc. The code allows to specify a custom basis set (e. g. only a couple of s-Gaussians) but also contains a variety of standard basis sets, such as the Pople STO-3G or the Dunning cc-pVTZ basis sets. The basis is then constructed (and stored in the `BasisSet` object) such that the CGFBs are located at the position of the nuclei. While virtual centers of the Gaussians are not possible in PyQuante 1.6.4, the code has been changed to allow for arbitrary Gaussian centers for the ultracold-atom implementation.

Next, a solver is specified, e. g., restricted closed-shell Hartree-Fock, and the computation can be performed via

```
from PyQuante import SCF
```

[1] Please see also the online documentation of PyQuante at the address given in [117] for examples, also including this one.

```
Solver = SCF(h2, method = "HF")
Solver.iterate()
```

After iteration, all the output is stored in variables of the `Solver` instance, such as, e. g., the Hartree-Fock energy in `Solver.energy` or the electron repulsion integrals in `Solver.ERI`. With these quantities post-Hartree-Fock methods can be performed.

10.2 From electronic structure to ultracold trapped atoms

After having introduced the very basic structure of the PyQuante code, the main parts that were necessary to change in order to perform calculations on ultracold trapped atoms are outlined.

(i) trap potential. The Coulomb potential that in the electronic-structure case is created by M nuclei has to be replaced by a non-Coulombic external trap potential. In the most simple case such a trap potential is a harmonic oscillator potential, but in view of the versatile possibilities to create optical trap potentials today [6], a very flexible ansatz should be chosen. A convenient and flexible one is to define the trap potential as a set of CGBFs. By setting the exponent α to zero[2], the polynomial ring $K[\mathbb{R}]$ is available. Noting the theorem of Weierstrass of approximation theory, i. e. for every $\epsilon > 0$ and for every continuous real function f on a compact interval there exists a polynomial p such that $\|f - p\| < \epsilon$, this ring is already complete which means that in principle any real continuous function can be adopted as trap potential.

A convenient advantage of representing the trap as a set of CGBFs allows for the direct use of already implemented overlap and three-center integrals for the one-atom trap integrals entering the Hamiltonian matrix and the Fock matrix. This can be directly seen as follows. The one-atom integrals over the one-atom Hamiltonian

$$h_{pq} = \int d\mathbf{r}\, \phi_p^*(\mathbf{r}) \left(-\frac{1}{2}\nabla^2 - V_{\text{trap}} \right) \phi_q(\mathbf{r}) \tag{10.4}$$

in the Gaussian-type orbital basis reduces to integrals of the type

$$t_{pq} = -\frac{1}{2} \langle \eta_p | \nabla^2 | \eta_q \rangle \tag{10.5}$$

[2] In practice, it has to be set to a tiny positive value in order to not break integral formulas where otherwise division by zero errors occur.

for the kinetic term and

$$v_{pq} = \langle \eta_p | V_{\text{trap}} | \eta_q \rangle \tag{10.6}$$

for the trap-potential term. Since the trap is given as a set of CGBFs, which can be written as a sum of PGBFs

$$V_{\text{trap}}(\mathbf{r}) = \sum_j c_j \eta_j(\mathbf{r}) \quad , \tag{10.7}$$

the trap-potential part reduces to

$$v_{pq} = \sum_j c_j \, \langle \eta_p | \eta_j | \eta_q \rangle \quad . \tag{10.8}$$

Central to the evaluation of these type of integrals is the *Gaussian product rule*, i. e. the product of two Gaussians η_1 and η_2 positioned at $\mathbf{A}_1$ and $\mathbf{A}_2$ is equal to a Gaussian centered around a position $\mathbf{P}$,

$$\begin{aligned} \eta_1(\mathbf{r})\, \eta_2(\mathbf{r}) =& N_1 N_2 \, \exp(\frac{-\alpha\beta|\mathbf{A}_1\mathbf{A}_2|^2}{\gamma}) \\ & \times \sum_{i=0}^{l_1+l_2} f_i(l_1, l_2, (\mathbf{PA}_1)_x, (\mathbf{PA}_2)_x) x_P^i \exp(-\gamma x_P^2) \\ & \times \sum_{j=0}^{m_1+m_2} f_j(m_1, m_2, (\mathbf{PA}_1)_y, (\mathbf{PA}_2)_y) y_P^j \exp(-\gamma y_P^2) \\ & \times \sum_{k=0}^{n_1+n_2} f_k(n_1, n_2, (\mathbf{PA}_1)_z, (\mathbf{PA}_2)_z) z_P^k \exp(-\gamma z_P^2) \end{aligned} \tag{10.9}$$

with

$$\gamma = \alpha + \beta \quad , \tag{10.10}$$

$$f_j(l, m, a, b) = \sum_{k=\max(0, j-m)}^{\min(j,l)} \binom{l}{k} \binom{m}{j-k} a^{l-k} b^{m+k-j} \tag{10.11}$$

and

$$\mathbf{P} = \frac{\alpha\mathbf{A} + \beta\mathbf{B}}{\gamma} \quad . \tag{10.12}$$

Together with the intergral formula

$$\int_{-\infty}^{\infty} dt\ t^j \exp(-\alpha t^2) = \frac{\Gamma((j+1)/2)}{\alpha^{(j+1)/2}} \tag{10.13}$$

the integrals for the kinetic term and the three-point Gaussian products for the trap integrals follow straightforwardly.

A more technical detail of the implementation of the trap is that in the construction of CGBFs and PGBFs for the trap potential the normalization of the basis functions that is done automatically in PyQuante had to be changed into an optional flag which is turned off for the creation of trap potentials that are, of course, in general not normalized. These changes are directly made in the objects `CGBF` and `PGBF`.

(ii) Molecule. Major changes are, of course, needed for the system definition, that is in PyQuante encoded in the `Molecule` object. The charge, that together with the atom numbers leads to the number of electrons loses its meaning for a number of neutral atoms. Hence, the charge is taken out and the number of atoms (in the code `nel`) is to be passed directly to the `Molecule` instance. Moreover, different to the interaction of electrons, the strength of interaction can be varied for ultracold atoms by making use of Feshbach resonances. Hence, the type of interaction and its strength have to be passed to the `Molecule` instance explicitly. Additionally, trap specifications in form of a list of CGBFs have to be passed directly.

(iii) Atom. The `Molecule` object contains a set of `Atom` objects. In PyQuante an "atom" consists basically of an atom number and a position. Since the atoms in the molecule are for ultracold calculations replaced by the external trap potential this object changes significantly to hold the information on the CGBFs the trap potential is formed of.

(iv) Interparticle interaction. The repulsive Coulomb interaction potential of electrons has to be exchanged by the interaction potential of ultracold atoms. In the present work a δ-contact interaction as well as a Gaussian-type interaction potential is considered. Both have the advantage that the explicit two-atom integrals remain analytically solvable. The exact expressions and applicability of the two types of interaction are discussed in Chapter 11.

(v) Integrals. Significant changes had to be performed on the `Ints` module that manages most integral calculations.

(vi) Interface. The calculation interface is contained in the `PyQuante2` module. Some flags were added to control the convergence criteria for the iterative procedures and a criterion was implemented that uses the density instead of energies.

(vii) Basis set. Although the basis remains in principle the same, the way how it is constructed has to be adapted. While in PyQuante, the Gaussians are automatically centered at the position of the nuclei, for an external trap potential the local potential well minima are not accessible without a calculation. Hence, in the construction of the basis, the positions where the Gaussians are centered at have to be specified explicitly. This made some crucial changes in the `BasisSet` object necessary to adapt to the new conventions. Convenience functions were developed for the purpose of constructing a basis bundled in the `BasisCreator` object.

10.3 Development of a post-Hartree-Fock method

In PyQuante only CI with single excitations is implemented. However, it is known from Brillouin's theorem that the singles do not interact with the ground state. In ultracold atoms, bound states of the interatomic interaction potential are strongly correlated because the strong spatial confinement of two atoms can not be described accurately by a mean-field interaction. Therefore, at large scattering lengths, where the bound state plays a crucial role, post-Hartree-Fock methods are needed. It has been reported in [121] that the Hartree-Fock CI method results in divergence when the δ pseudopotential is used as an interaction potential. Yet, numerous works [122–127] reported on renormalization schemes to cure the divergence in the approach. Since it is hence not clear how appropriate the method works, it is necessary to have a benchmark, without the uncertainty to have a lack of precision due to a truncation of the FCI terms. Hence, FCI is desired in this case.

As described in Section 9.4 the number of determinants scales inconveniently with the number of particles and orbitals. A diagonalization scheme of the Hamiltonian matrix is hence needed that does not require to store the Hamiltonian matrix. Lanczos, Arnoldi, or Davidson algorithms can be used to iteratively solve for eigenvalues and eigenvectors of large matrices or linear operators. These methods do not require the full matrix, but only an input function that calculates matrix-vector products. Hence, for a FCI algorithm it suffices to be able to efficiently calculate contractions of the form

$$\sigma = \mathbf{HC} \tag{10.14}$$

of the Hamiltonian matrix and a reduced number of coefficient vectors.

10.3.1 Spin strings

Another crucial ingredient of a FCI code besides the iterative diagonalization is a compact scheme of storing, addressing, and ordering information on the occupation of Slater determinants. This is especially helpful when certain types of configurations are to be dropped compared to the FCI expansion as is the case for, e. g., *restricted active space* (RAS) [112] or *complete active space* (CAS) [112] CI. In the present work, the scheme introduced in [112, 128] is adopted that uses alpha and beta *strings* to represent determinants consisting of alpha and beta spin particles, respectively. Writing in an ordered way alpha-spin orbitals before beta-spin orbitals, each Slater determinant can be written in second quantization as

$$|I_\alpha I_\beta\rangle = \alpha_{I_\alpha}\beta_{I_\beta}\,|\mathrm{vac}\rangle \tag{10.15}$$

where the alpha and beta spin strings

$$\alpha_{I_\alpha} = \prod_{i=1}^{N} a_{i\alpha}^\dagger \tag{10.16}$$

$$\beta_{I_\beta} = \prod_{i=1}^{N} a_{i\beta}^\dagger \tag{10.17}$$

are given as products of creation operators, respectively. By convention, in a given spin string the orbitals are written in ascending order.

In order to build an FCI wavefunction, all possible alpha and beta strings need to be generated by distributing

$$N_\alpha = \frac{N}{2} + \tilde{M} \tag{10.18}$$

alpha particles and

$$N_\beta = \frac{N}{2} - \tilde{M} \tag{10.19}$$

beta particles on n orbitals. Here N is the total number of particles and $\tilde{M} = \sum m_s$ the sum of the projectional spin quantum numbers. All possible products of alpha and beta strings need to be included in the FCI expansion. The determinants are compactly written as a matrix where the rows (columns) refer to the alpha (beta) strings. Equivalently, the coefficients in the FCI expansion can be written in matrix form $C_{I_\alpha I_\beta}$.

For the implementation of the FCI procedure, a scheme needs to be introduced that allows for ordering and addressing of spin strings. The approach described in

[112] is adopted (with slight modifications) and in the following briefly summarized. The idea is to represent strings as *paths* in a diagram and to introduce an ordering of these paths. For N particles and n orbitals a path is a vector of n *vertices*, i. e. n ordered pairs of (k, m) in an $n \times N$ diagram connected by *arcs*, k being the orbital index and m the number of particles in the orbitals up to k. In *reverse lexical order*, string A has a smaller order than string B, if A has a lower orbital number in the last occupation where they differ. For example, $a_1^\dagger a_2^\dagger a_4^\dagger$ has a smaller order than $a_1^\dagger a_3^\dagger a_5^\dagger$ because $4 < 5$. To obtain an address (ordering number) of a string, each vertex (k, m) is associated with a vertex weight $W_{k,m}$ that is equal to the number of (different) paths the vertex can be reached from. Since a vertex (k, m) can only be reached from either $(k-1, m-1)$ (in the case that orbital k is occupied) or $(k-1, m)$ (meaning that orbital k is unoccupied) the recurrence relation

$$W_{k,m} = W_{k-1,m} + W_{k-1,m-1} \tag{10.20}$$

for the vertex weights holds. The vertex weights of the forbidden vertices, i. e. vertices that are not connected by a path, are set to zero. The vertex weight $W_{0,0}$ is set to 1. Next, *arc weigths* $Y_{k,m}^j$ are introduced such that the *address*

$$I_{m_0,\ldots,m_{n-1}} = \sum_{k=0}^{n-1} Y_{k,m_k}^{m_k - m_{k-1}} \tag{10.21}$$

of a path is just given as the sum over its arc weights. Only diagonal (with weight $Y_{k,m}^1$) and vertical (with weights $Y_{k,m}^0 = 0$) arcs occur, the weight of vertical ones is set to zero. Finally, the diagonal arc weights

$$Y_{k+1,m+1}^1 = W_{k,m+1} \tag{10.22}$$

can be directly related to the vertex weights. In the appendix, the code of the `Graph` object can be found that implements the scheme above.

In summary, after determining the arc weights, the path addresses which establish a one-to-one mapping of spin strings to integers, are obtained. This addressing scheme is very efficient, since the address of a string is calculated as a simple sum of arc weights which can be efficiently extracted from a small matrix.

10.3.2 The FCI algorithm

After having introduced a compact and efficient to evaluate addressing scheme for spin strings, the procedure of the FCI calculation can be described [3]. With the string notation, the products of the Hamiltonian matrix with coefficient matrices that are needed for an iterative diagonalization in the FCI basis can be written [112] as

$$\sigma_{I_\alpha I_\beta} = \sum_{J_\alpha J_\beta} \langle I_\alpha I_\beta | H | J_\alpha J_\beta \rangle \, C_{J_\alpha J_\beta} \quad . \tag{10.23}$$

For a direct FCI scheme [129], where the contraction of operators in determinantal representation is directly obtained from the representation of the operators in second-quantization, it is convenient to rewrite the Hamiltonian of Eq. (9.15) as

$$\begin{aligned} H &= \sum_{pq} h_{pq} \, E_{pq} + \frac{1}{2} \sum_{pqrs} g_{pqrs} \;\; (E_{pq} E_{rs} - \delta_{qr} E_{ps}) \\ &= \sum_{pq} k_{pq} \, E_{pq} + \frac{1}{2} \sum_{pqrs} g_{pqrs} \, E_{pq} E_{rs} \end{aligned} \tag{10.24}$$

with the effective one-particle integrals

$$k_{pq} = h_{pq} - \frac{1}{2} \sum_{r} g_{prrq} \quad . \tag{10.25}$$

In Eq. (10.24) the nuclear repulsion h_{nuc} is omitted as it simply adds a constant offset that is zero for ultracold atoms because an optical trap potential does not interact with itself.

The FCI procedure in [130] is implemented that is denoted as *minimal operator-count method* in [112] since it leads to an operator count that is equal to the theoretical minimum, i. e. only non-zero matrix elements of the sparse Hamiltonian matrix are processed. First, the sigma matrix of Eq. (10.23) can be separated

$$\sigma_{I_\alpha I_\beta} = \sigma^{(1)}_{I_\alpha I_\beta} + \sigma^{(2)}_{I_\alpha I_\beta} \tag{10.26}$$

into a one-particle part

$$\sigma^{(1)}_{I_\alpha I_\beta} = \sum_{pq} \sum_{J_\alpha J_\beta} k_{pq} \, \langle I_\alpha I_\beta | E_{pq} | J_\alpha J_\beta \rangle \, C_{J_\alpha J_\beta} \tag{10.27}$$

[3] The author has sent the founder of the PyQuante code, Rick Muller, the implemented FCI code in order to include it to the PyQuante program package. It is also accessible at *https://github.com/simsta/pyquante-fullci*.

and a two-particle part

$$\sigma^{(2)}_{I_\alpha I_\beta} = \sum_{pqrs} \sum_{J_\alpha J_\beta} g_{pqrs} \langle I_\alpha I_\beta | E_{pq} E_{rs} | J_\alpha J_\beta \rangle C_{J_\alpha J_\beta} \quad . \tag{10.28}$$

Introducing, moreover, the spin-separated singlet-excitations operators

$$E^\alpha_{pq} = a^\dagger_{p\alpha} a_{q\alpha} \tag{10.29}$$

$$E^\beta_{pq} = a^\dagger_{p\beta} a_{q\beta} \quad , \tag{10.30}$$

the one- and two-particle parts of the sigma matrix can further be partitioned into different spin components. For the one-particle part the separation

$$\sigma^{(1)}_{I_\alpha I_\beta} = \sigma^\alpha_{I_\alpha I_\beta} + \sigma^\beta_{I_\alpha I_\beta} \tag{10.31}$$

consists of the two terms

$$\sigma^\alpha_{I_\alpha I_\beta} = \sum_{J_\alpha} k^\alpha_{I_\alpha J_\alpha} C_{J_\alpha I_\beta} \tag{10.32}$$

$$\sigma^\beta_{I_\alpha I_\beta} = \sum_{J_\beta} k^\beta_{I_\beta J_\beta} C_{I_\alpha J_\beta} \tag{10.33}$$

with the matrices ($\gamma \in \alpha, \beta$)

$$k^\gamma_{I_\gamma J_\gamma} = \sum_{pq} k_{pq} \langle I_\gamma | E^\gamma_{pq} | J_\gamma \rangle \quad . \tag{10.34}$$

The two-particle term

$$\sigma^{(2)}_{I_\alpha I_\beta} = \sigma^{\alpha\alpha}_{I_\alpha I_\beta} + \sigma^{\beta\beta}_{I_\alpha I_\beta} + \sigma^{\alpha\beta}_{I_\alpha I_\beta} \tag{10.35}$$

can be written in three parts that can be presented as

$$\sigma^{\alpha\alpha}_{I_\alpha I_\beta} = \sum_{J_\alpha} G^\alpha_{I_\alpha J_\alpha} C_{J_\alpha I_\beta} \tag{10.36}$$

$$\sigma^{\beta\beta}_{I_\alpha I_\beta} = \sum_{J_\beta} G^\beta_{I_\beta J_\beta} C_{I_\alpha J_\beta} \tag{10.37}$$

$$\sigma^{\alpha\beta}_{I_\alpha I_\beta} = \sum_{pq} \sigma^{\alpha\beta}_{I_\alpha I_\beta}(pq) \tag{10.38}$$

with the matrices ($\gamma \in \alpha, \beta$)

$$G^{\gamma}_{I_\gamma J_\gamma} = \frac{1}{2} \sum_{pqrs} g_{pqrs} \langle I_\gamma | E^{\gamma}_{pq} E^{\gamma}_{rs} | J_\gamma \rangle \quad . \tag{10.39}$$

The mixed-spin term $\sigma^{\alpha\beta}_{I_\alpha I_\beta}$ has a more complicated representation given by

$$\sigma^{\alpha\beta}_{I_\alpha I_\beta}(pq) = \sum_{J_\beta} D^{\alpha}_{I_\alpha J_\beta}(pq)\, G^{\beta}_{I_\beta J_\beta}(pq) \tag{10.40}$$

where

$$D^{\alpha}_{I_\alpha J_\beta}(pq) = \sum_{J_\alpha} \langle I_\alpha | E^{\alpha}_{pq} | J_\alpha \rangle\, C_{J_\alpha J_\beta} \tag{10.41}$$

and

$$G^{\beta}_{I_\beta J_\beta}(pq) = \sum_{rs} g_{pqrs} \langle I_\beta | E^{\beta}_{rs} | J_\beta \rangle \quad . \tag{10.42}$$

With the FCI equations at hand, the FCI calculation can now be described by its implementation. In the code, there exists a class object `Sigma` that performs the contraction of the Hamiltonian matrix with the coefficient matrix C of Eq. (10.23). The coefficient matrix is indexed with the addressing scheme of alpha and beta strings in the diagrammatic representation described in Section 10.3.1. First, by creating an instance of the class `Sigma`, all the necessary matrices $k^{\alpha}_{I_\alpha J_\alpha}$, $k^{\beta}_{I_\beta J_\beta}$, $G^{\alpha}_{I_\alpha J_\alpha}$, $G^{\beta}_{I_\beta J_\beta}$ and $D^{\alpha}_{I_\alpha J_\beta}(pq)$, and $G^{\beta}_{I_\beta J_\beta}(pq)$ as list of matrices are constructed as sparse matrices. The format is chosen as CSR (compressed sparse row matrix) as it supports very efficient matrix-matrix and vector-matrix multiplications. For example, to create the matrix $k^{\alpha}_{I_\alpha J_\alpha}$, a loop over all pairs of strings $(I_\alpha J_\alpha)$ (obtained from the class variable `Graph.occupations`) is performed. A string is just given by its ordered list of occupation numbers. The row and column indices are obtained as the address of the string pair (obtained from the class method `Graph.address()`). If the strings are identical (have the same address), the matrix element is zero (since $\langle I | E_{pq} | I \rangle = 0$) and the next string pair is considered. If the strings are not identical, the action of E^{α}_{pq} on J_α is performed for all possible combinations of (p, q). Each time the strings do not differ by more than the pair (p, q) the matrix element k_{pq} is added with the correct phase factor given in Eq. (9.8). The second-quantized operator E^{γ}_{pq} is implemented in the function `e_pq_on_string` and takes as arguments p, q, and the string and returns the phase factor and the final string. It returns $(0, 0)$ if q is unoccupied (annihilation of the vacuum) or if $p \neq q$ is already occupied (double

occupation is not possible for fermions). Otherwise it annihilates q, creates p, sorts again, and returns. Finally, the matrix is stored as a sparse CSR matrix.

The generation of the other matrices is in principle analogous to the description above, with the difference that for $G^{\gamma}_{I_\gamma J_\gamma}$ matrices the excitation operators have to act two times, one time to the right and one time as an adjoint to the left.

The creation of the spin-mixed matrix $\sigma^{\alpha\beta}_{I_\alpha I_\beta}$ is more demanding. First, the lists of matrices $D^{\alpha}_{I_\alpha J_\beta}(pq)$ and $G^{\beta}_{I_\beta J_\beta}(pq)$ have to be created that are added up in the end.

After all sparse matrices have been calculated and stored (in main memory), the contractions that are needed by the iterative diagonalization routine can be performed efficiently. Therefore, the wrapper `scipy.sparse.linalg.eigsh` to the `ARPACK` package [131] functions `SSEUPD` and `DSEUPD` is used which are implementations of the implicitly restarted Arnoldi method to find eigenvalues and eigenvectors.

A copy of the source code of parts of the code can be found in the appendix in Section B.2. The entire FCI source code (unoptimized Python version) is accessible online at `https://github.com/simsta/pyquante-fullci`. However, since this version of the code is rather slow, also a highly-optimized Cython [119] version that compiles time-critical parts of the code to native C binaries has been developed. The speedup is two to three orders of magnitude, depending on the problem.

10.3.3 Validation of the code

Of course, a complex implementation such as the FCI code as well as critical changes to the core of a quantum-chemistry implementation require careful tests. Besides steady tests of the correctness of subroutines and functions, as a first test of the complete code, a Hartree-Fock with subsequent FCI calculation is performed to evaluate the correctness of the FCI implementation. By design of the code structures, the FCI code does, in fact, not change for the ultracold atoms compared to the electronic-structure case besides the constant term $V_{\mathrm{nuc,nuc}}$ that is set to zero for ultracold atoms because all necessary changes already enter in the Hartree-Fock step. Hence, a test of the correctness of the FCI code in the electronic-structure case also evaluates its correctness for the ultracold case.

Examples of FCI calculations on H_2 can be found in [115]. Therein, the correlation energy

$$E_{\mathrm{corr}} = E_0^{\mathrm{FCI}} - E_0^{\mathrm{HF}} \tag{10.43}$$

that is the energy difference between the ground-state energy of the FCI calculation and the Hartree-Fock calculation is compared for an internuclear separation of $R = 1.4\,\mathrm{a.u.}$ and different basis sets.

Basis set	E_{corr} (literature [115])	E_{corr} (FCI)
STO-3G	-0.02056	-0.0205616192
6-31G**	-0.03387	-0.0338691025

Table 10.1: Comparison of the correlation energy of FCI calculations from literature with the present implementation for different basis sets for the H_2 molecule at $R = 1.4$ a.u..

Table 10.1 shows the comparison for of the calculation of the literature values with the values obtained with the present code. The results are identical in the provided digits of the literature values which delivers strong evidence for the correctness of the FCI implementation.

While the FCI calculation can be tested in comparison to electronic structure calculations, the transformation of the PyQuante code to the ultracold calculations have to be tested, of course, with an ultracold calculation. Therefore, the harmonic-oscillator potential

$$V_{\text{ho}} = \frac{1}{2}(x^2 + y^2 + z^2) \tag{10.44}$$

in natural units (lengths in d_{ho} and energies in $\hbar\omega$) is chosen. The calculation of two non-interacting atoms with a natural basis of S, P, and D Gaussians, all with exponents of 0.5, (which just give the eigenfunctions of the harmonic oscillator) result in the correct eigenenergies of a 6D harmonic oscillator ($E_0/\hbar\omega = 3.0$ (non-degenerate), $E_0/\hbar\omega = 4.0$ (6-fold degenerate), $E_0/\hbar\omega = 5.0$ (21-fold degenerate), etc.) and correct wavefunctions (product wavefunctions of two harmonic-oscillator eigenfunctions).

11 Interaction potentials and applicability to the ultracold regime

Finally, the crucial question is discussed how the interaction potentials can be treated in order to reproduce the s-wave scattering physics of the ultracold regime. In the following, two types of interaction potentials are investigated, a zero-range δ contact interaction potential, and a Gaussian-type potential. First, the matrix elements

$$g_{pqrs} = \int\int d\mathbf{r}_1 d\mathbf{r}_2 \, \eta_p^*(\mathbf{r}_1)\eta_r^*(\mathbf{r}_2) \, V_{\text{int}}(\mathbf{r}_1, \mathbf{r}_2) \, \eta_q(\mathbf{r}_1)\eta_s(\mathbf{r}_2) \tag{11.1}$$

are calculated. In both cases this can be performed analytically. Then the applicability is discussed by comparing the eigenenergy spectra for a varying scattering length of the Hartree-Fock CI calculation for two particles in a spin singlet state with the analytical solution of the eigenenergy spectrum of two atoms interacting via the δ pseudopotential, Eq. (1.32). As a trap potential an isotropic harmonic confinement is considered.

Prior to the evaluation of the computational method, the accuracy of the analytical δ pseudopotential has to be validated. In [30] the validity was confirmed especially for the trap-state regime. For the present study, the complete spectrum including bound states is of interest and it is thus insightful to first compare the solution of the δ pseudopotential to the one of a realistic numerically given Born-Oppenheimer interatomic potential. In Figure 11.1 the corresponding two-body spectra of the numerical method described in Section 3.4 together with the analytical solution for the δ pseudopotential are shown for the case of an isotropic harmonic confinement. Since only the A_g part of the numerically obtained spectrum is displayed, odd c.m. excitations are not included in the spectrum. Hence, only every second excited bound state is reproduced by the numerical calculation in Figure 11.1. Moreover, only a few c.m. states are included in the calculation which leads to the absence of higher excited c.m. excitations. While the energies of the pseudopotential and the lithium interaction potential for the trap state and the lowest bound state above $1\hbar\omega$ are in perfect quantitative agreement, for smaller energies (or excited bound states) the lithium bound states lie energetically lower than the pseudopotential energies which is especially visible in the magnified (right) part of Figure 11.1. The pseudopotential can hence be regarded as “too soft” in

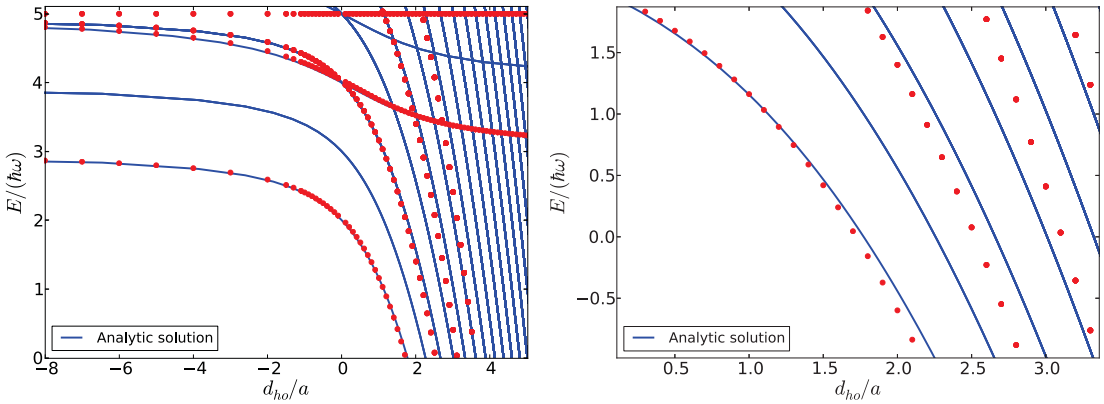

Figure 11.1: A_g part of the two-body eigenenergy spectrum of a ^{7}Li-^{7}Li interaction potential in comparison to the analytical solution of a δ-pseudopotential interaction.

comparison to a realistic potential.

11.1 δ contact interaction potential

In Section 1.3, the Fermi-Huang δ pseudopotential was derived. In natural units of energies in $\hbar\omega$ and lengths in d_{ho} it has the form

$$V_\delta(\mathbf{r}_1, \mathbf{r}_2) = 2\pi a \delta(r) \frac{\partial}{\partial r} r \tag{11.2}$$

where $\mathbf{r} = \mathbf{r}_1 - \mathbf{r}_2$ and $r = |\mathbf{r}_{12}|$. The regularization term $\frac{\partial}{\partial r} r$ is crucial for the analytical treatment of the δ potential but can be omitted in case of well-behaved Gaussian basis functions where it has no effect. Therefore, the two-atom matrix element reduces to

$$\begin{aligned} g_{pqrs} &= g \int\int d\mathbf{r}_1 d\mathbf{r}_2 \, \eta_p^*(\mathbf{r}_1)\eta_r^*(\mathbf{r}_2) \, \delta(\mathbf{r}_1 - \mathbf{r}_2) \, \eta_q(\mathbf{r}_1)\eta_s(\mathbf{r}_2) \\ &= g \int d\mathbf{r} \, \eta_p^*(\mathbf{r})\eta_r^*(\mathbf{r}) \, \eta_q(\mathbf{r})\eta_s(\mathbf{r}) \\ &= \langle \eta_p \eta_r | \eta_q \eta_s \rangle \end{aligned} \tag{11.3}$$

and contains the bare interaction strength

$$g(a) = 2\pi a \quad . \tag{11.4}$$

Following the Gaussian product rule Eq. (10.9) and performing some laborious algebra, the four-point integral can be reduced to regular overlap integrals that are know analytically as specified in Eq. (10.13).

It is known that due to the singularity of the pseudopotential a direct CI evaluation fails [121] and renormalization is necessary. A general discussion of renormalization in a quantum-field theoretical framework applied to ultracold scattering can be found in [132]. Using methods from effective-field theory [123] and a no-core shell model [124], δ-potential renormalizations for harmonically trapped ultracold Fermi gases were performed. A renormalization procedure has also helped to apply the δ-contact potential to a four-fermion system within a configuration-interaction calculation [122]. Similarly, a renormalization of the δ-potential in 2D can be found in [125]. The procedure was adopted to study effects of pairing and Hund's rule in a few-body system of 2D fermions [126].

Motivated by the renormalization of contact-interacting fermionic systems in [122, 124, 125], in the present approach the most direct renormalization procedure is applied which basically consists of introducing a basis-dependent (or in the words of quantum-field theory momentum-cutoff dependent) coupling constant $g(a, \Lambda)$ that is chosen such that the two-body ground state energies of the analytical pseudopo-

tential solution in an isotropic harmonic trap are recovered. The renormalization of the coupling constant is performed in a two-step process. First, the Hartree-Fock and CI calculations are performed for the bare coupling constant of Eq. (11.4) in an isotropic harmonic trap potential which results in a set of eigenenergies $E^{(\Lambda)}$, that are of course dependent on the basis set Λ. Since in a harmonic trap the rel. and c.m. motion decouple, the ground-state energy of the rel. motion Hamiltonian $E_0^{(\Lambda,\mathrm{rel})}$ can be obtained by subtracting $3/2\hbar\omega$ from the ground state of the CI calculation. Then, the renormalized coupling constant $g(a,\Lambda)$ is obtained by evaluating the implicit energy equation Eq. (2.9) for a 3D isotropic harmonic potential with $E_0^{(\Lambda,\mathrm{rel})}$ as input to obtain the bare scattering length which is translated into a coupling constant via Eq. (11.4). If a calculation is performed with more than 2 particles, $g(a,\Lambda)$ has first to be determined for the used basis set by the procedure just described. Finally it has to be confirmed that the result becomes basis-set (cutoff) independent.

In Figure 11.2 the bare and renormalized spectra, respectively, for the calculation of two fermionic atoms in a spin-singlet state trapped in an isotropic harmonic potential with the basis set specified in Table B.2 for CIS and FCI calculations are shown. First, the CIS calculation is considered shown in Figure 11.2(a) for the bare and (b) for the renormalized case. The calculations are very unstable for small negative scattering lengths resulting in the lack of data points in the interval $d_{\mathrm{ho}}/a \in (-3,0)$. The lowest states decrease in energy, resembling the bound states, but fall even below these. This is possible because for the δ potential the variational principle is not valid anymore because even for an infinite basis set, the exact (analytically given) wavefunctions cannot be reconstructed since they are singular at $r=0$ which is not the case for Gaussian basis functions or in general single-particle basis functions. For positive scattering lengths, the trap states are resembled but not the excited bound states, approaching accurate results in the mean-field limit but leading to too large values for large positive scattering lengths. In the renormalization (Figure 11.2(b)), effectively, the energetically too low lying states for bare negative scattering lengths are mapped towards larger inverse scattering lengths. The too highly lying values for positive bare scattering lengths are mapped towards smaller inverse scattering lengths. The bare negative values build the bound state, the bare positive values the trap states. The first trap state is accurately described up to about $d_{\mathrm{ho}}/a = -1.5$. For smaller d_{ho}/a the branch is, in fact, the bound state with double c.m. excitation resulting from negative bare scattering lengths. The spectrum demonstrates that it is in principle possible to construct the complete energy spectrum by renormalization.

In comparison to the bare CIS spectrum, the energies in the bare FCI spectrum shown in Figure 11.2(c) have lower energy values. The most significant difference is certainly that the energies for large positive scattering lengths do not exceed the

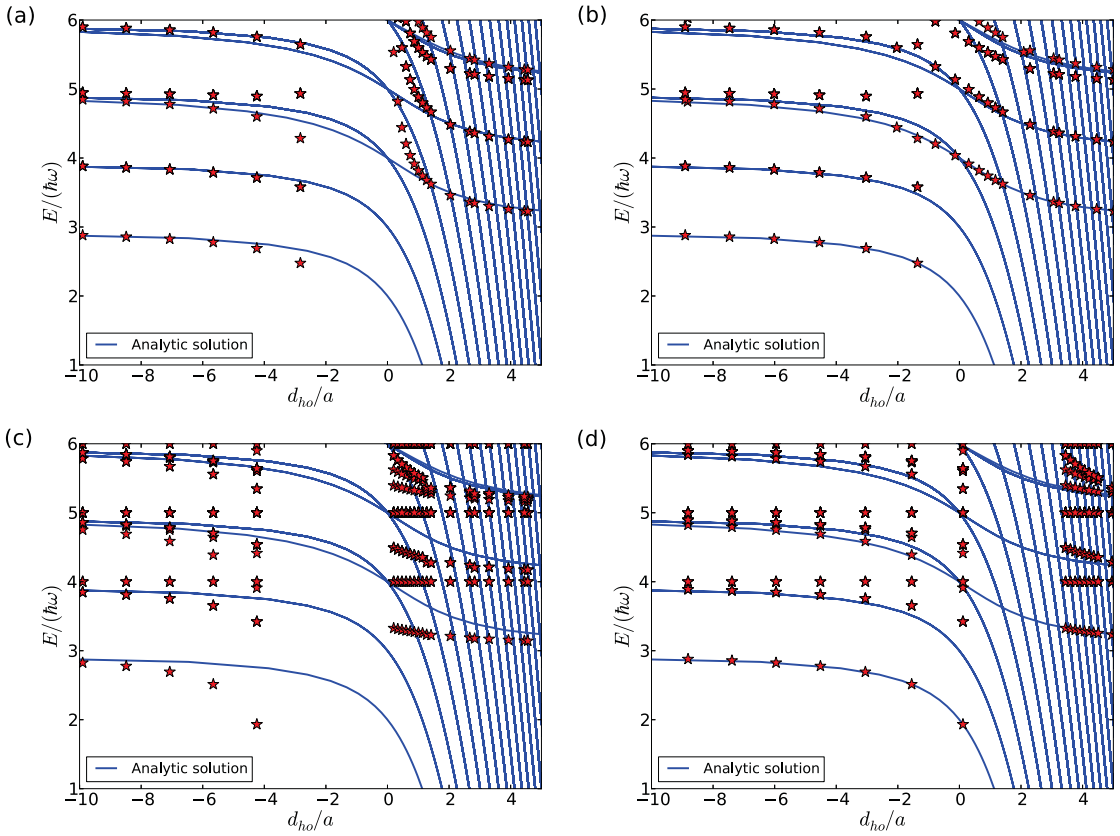

Figure 11.2: Two-body eigenenergy spectrum of two atoms interacting via a δ-contact potential in comparison to the analytical solution of the δ-pseudopotential interaction. (a) shows the solution of the CIS calculation for a bare contact potential, (b) shows the renormalized CIS results. In (c) the bare FCI solution is displayed, in (d) the renormalized FCI solutions.

analytical ones as in the case of the CIS calculation. In the renormalization step, these energies are hence not mapped towards smaller inverse scattering lengths but to larger values. This leads to the counter-intuitive result that the in principle less accurate CIS calculations lead to better results for the trap state energies after renormalization than a FCI calculation.

As will be shown in the next Section 11.2, the appearance of many molecular states for $d_{\mathrm{ho}}/a \gtrsim 1.0$ makes the Hartree-Fock FCI approach unstable for non-zero-range potentials. This makes it particularly hard to perform calculations for positive scattering lengths. This is understandable as the (lowest) bound state lies at very small energies and is subject to a strong confinement that is not easily resolvable with Gaussian basis functions centered at the origin. Moreover, many c.m. excitations of the bound state have to be resolved where the Hartree-Fock method is not well

suited. Hence, the perhaps most valuable property of the zero-range δ-potential interaction approach is that it allows for the accurate calculation in the mean-field regime of positive scattering lengths.

11.2 Gaussian interaction potential

For the choice of an interaction potential with non-zero range, the choice of the Gaussian interaction potential

$$V_{\mathrm{g}}(\mathbf{r}_1, \mathbf{r}_2) = V_0 \, \mathrm{e}^{-\xi_0 r^2} \tag{11.5}$$

where $\xi_0 = 2r_0^{-2}$ and r_0 is the range of the Gaussian and $r = |\mathbf{r}| = |\mathbf{r}_1 - \mathbf{r}_2|$ is the relative distance between two interacting particles, is particularly convenient from a computational point of view, since it allows for an analytical evaluation of the two-atom integrals. After several pages of algebra, and repeated application of Eq. (10.9), the two-atom matrix element of Eq. (11.1) over the Gaussian interaction potential V_{g} can compactly be written as

$$\begin{aligned} g_{pqrs} =& V_0 \, N_p N_q N_r N_s \left(\frac{\pi}{\gamma}\right)^{\frac{3}{2}} \left(\frac{\pi}{\kappa+\tau}\right)^{\frac{3}{2}} \exp\left(-\frac{\alpha_p \alpha_q |\mathbf{A}_p \mathbf{A}_q|^2}{\gamma}\right) \exp\left(-\frac{\kappa\tau |\mathbf{CP}|^2}{\kappa+\tau}\right) \\ & \times \exp\left(-\frac{\alpha_r \alpha_s |\mathbf{A}_r \mathbf{A}_s|^2}{\kappa}\right) \prod_{c=x,y,z} \sum_{i_c=0}^{{\epsilon^{(c)}}_r + {\epsilon^{(c)}}_s} \sum_{h_c=0}^{{\epsilon^{(c)}}_p + {\epsilon^{(c)}}_q} \sum_{j_c=0}^{h_c/2} \sum_{k_c=0}^{(i_c+h_c-2j_c)/2} \left\{ \binom{h_c}{2j_c} \right. \\ & \times \left(\frac{\xi_0}{\delta}\right)^{m-2j_c} \frac{(2j_c-1)!!}{(2\delta)^{j_c}} \frac{(2k_c-1)!!}{(2(\kappa+\tau))^{k_c}} f_{i_c}({\epsilon^{(c)}}_r, {\epsilon^{(c)}}_s, (\mathbf{CA}_r)_c, (\mathbf{CA}_s)_c) \\ & \left. \times f_{h_c}({\epsilon^{(c)}}_p, {\epsilon^{(c)}}_q, (\mathbf{PA}_p)_c, (\mathbf{PA}_q)_c) \, f_{2k_c}(i_c, h_c - 2j_c, (\mathbf{SC})_c, (\mathbf{SP})_c) \right\} \end{aligned} \tag{11.6}$$

where the N_i are the normalization factors of the primitive Gaussian basis functions given by Eq. (10.3), $(\mathbf{XY})$ is used as a short-hand notation for $(\mathbf{X} - \mathbf{Y})$, $(\mathbf{XY})_c$ denotes the c'th component and $|\mathbf{XY}|$ the absolute value of $(\mathbf{X} - \mathbf{Y})$, respectively, $\gamma = \alpha_p + \alpha_q$, $\kappa = \alpha_r + \alpha_s$, $\delta = \gamma + \xi_0$, $\mathbf{P} = (\alpha_p \mathbf{A}_p + \alpha_q \mathbf{A}_q)/\gamma$, $\mathbf{C} = (\alpha_r \mathbf{A}_r + \alpha_s \mathbf{A}_s)/\kappa$, $\tau = \gamma\xi_0/\delta$, $\mathbf{S} = (\tau\mathbf{P} + \kappa\mathbf{C})/(\kappa+\tau)$, and $(\epsilon^{(x)}, \epsilon^{(y)}, \epsilon^{(z)}) = (l, m, n)$.

In order to calculate the s-wave scattering length for the Gaussian interaction potential V_{g}, the radial Schrödinger equation of Eq. (1.16) is solved (in natural units) for zero collision energy

$$-\frac{d^2}{dr^2} u_0(r) + V_{\mathrm{g}}(r) u_0(r) = 0 \tag{11.7}$$

with the boundary condition $u_0(0) = 0$, where the angular-momentum dependent term $l(l+1)/r^2$ originally present in the radial equation vanishes since only s-wave scattering is considered. As mentioned in Section 1.2, in the asymptotic regime, the wavefunction then behaves as $u_0(r) \propto (1 - r/a) \propto (r - a)$ where a is the s-wave scattering length for potentials that fulfill $\lim_{r\to\infty} r^n U(r) = 0, n > 3$, i. e. potentials that decrease asymptotically faster than r^{-3}. The scattering length for V_g is obtained by rewriting the second-order equation into two first-order equations

$$\frac{d}{dr}\begin{pmatrix} y_0 \\ y_1 \end{pmatrix} = \begin{pmatrix} 0 & 2(V_\mathrm{g}(r) - E) \\ 1 & 0 \end{pmatrix}\begin{pmatrix} y_0 \\ y_1 \end{pmatrix} \tag{11.8}$$

with

$$y_0 = \frac{d}{dr}u_0(r); \quad y_1 = u_0(r) \quad . \tag{11.9}$$

and $E = 0$. This system of first-order ordinary differential equations is then solved by using of a standard solver, here `lsoda` from the FORTRAN library `odepack` is used through `scipy.integrate.odeint`. From the wavefunction u_0 at two asymptotic points $r_1, r_2 \gg r_0$, the scattering length

$$a = -(r_2 - r_1)\frac{u_0(r_1)}{u_0(r_2) - u_0(r_1)} + r_1 \tag{11.10}$$

can be extracted. Figure 11.3 shows the scattering length in dependence of the potential depth V_0. The scattering length vanishes for $V_0 = 0$ and decreases with the potential depth. The poles in the scattering length mark the position of bound states that become degenerate in energy with the potential threshold. For example, the Gaussian potential with $\xi_0 = 10\, d_\mathrm{ho}^{-2}$ supports a single bound state for $178.8 < V_0/(\hbar\omega) < 26.0$.

For the validation of the Gaussian potential, a range ξ_0 has to be chosen such that the properties in the ultracold regime are reflected. As derived in Section 1.2, this is the case for $kr_0 = \frac{2\pi}{\lambda} r_0 \ll 1$ with thermal wavelengths λ typically in the range of 10^4 a.u. Hence, with a typical trap length of about 10^3 a.u., the range $r_0/d_\mathrm{ho} = 0.1$ which is equivalent to $\xi_0 = 50\, d_\mathrm{ho}^{-2}$ results in $kr_0 \approx 0.05$ and is hence a good starting point to test the Gaussian potential. In Figure 11.4 the eigenenergy spectrum is shown for a calculation with the basis set specified in Section B.1 consisting of 108 basis functions which results in a total number of determinants for the FCI calculation of 11664. Obviously, the agreement of the numerical calculation to the analytical pseudopotential solution is poor for $d_\mathrm{ho}/a > -10$, e. g., the lowest bound-state energy is too large, especially for positive scattering lengths.

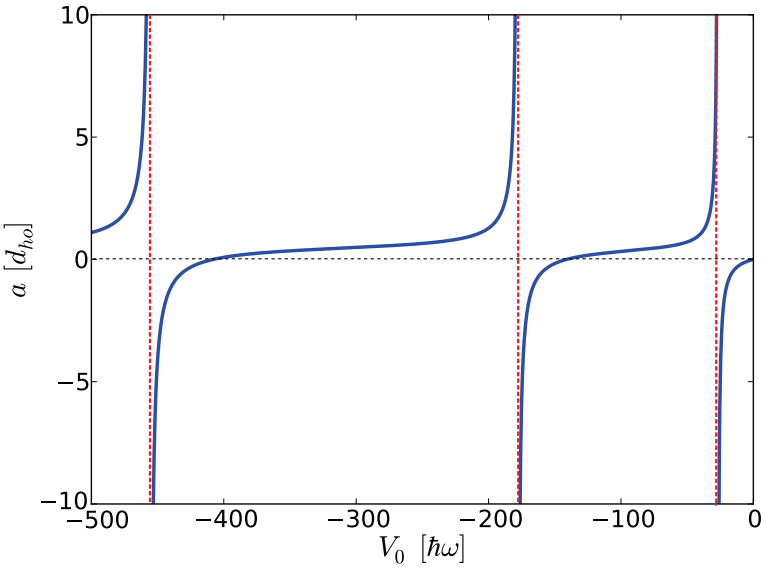

Figure 11.3: Scattering length for a Gaussian potential with $\xi_0 = 10\, d_{\mathrm{ho}}^{-2}$ for a varying potential depth.

It is important to note, that the shown FCI results are not yet converged. However, a variation of the basis size has shown that the calculations converge slowly for this Gaussian interaction potential such that even for very large basis sets the results are only slightly better (smaller). The reason is that the small-scale structures around $|\mathbf{r}_1 - \mathbf{r}_2| = 0$ introduced by the small finite range of the interaction potential, (that can, e. g., be seen in Figure 4.6 for the lithium potential involving many bound states) cannot easily be resolved with Gaussian basis functions in the potential minimum. Despite the fact that for the calculations at positive scattering lengths the depth of the Gaussian potential is chosen such that only a single bound state is supported (and none for negative scattering lengths).

Moreover, while it might be expected that convergence can be increased monotonically by increasing the number of basis function, for the Hartree-Fock calculation, however, this might rather result in divergences or periodic cycles of the SCF procedure that then fails to terminate. Additionally, the initial density is a sensitive parameter for convergence. As a consequence, in practice, the Hartree-Fock followed by CI calculations require a careful and experienced selection of basis functions and initial density.

Yet, it is possible to improve the convergence behavior by choosing a wider potential. This enlarges the interaction regime and range of the bound states which makes the Gaussian basis functions better resolve the small-scale structures. Of course, by such a procedure it has to be ensured that the ultracold regime, i. e. where s-wave

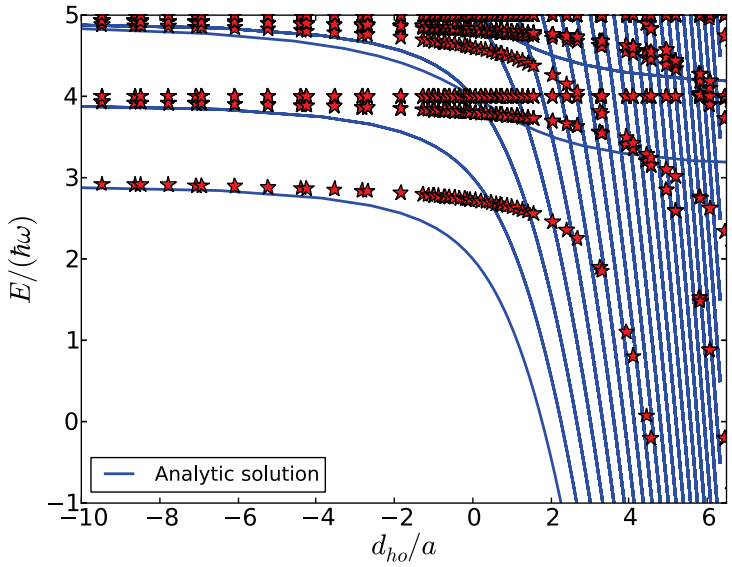

Figure 11.4: Two-body eigenenergy spectrum of the Gaussian potential with $\xi_0 = 50\, d_{\mathrm{ho}}^{-2}$ obtained by FCI calculations for a varying potential depth which is equivalent to a change of the scattering in comparison to the analytical solution of a δ-pseudopotential interaction.

scattering is dominant, is preserved.

First, it is interesting to consider the results of a CIS calculations. As a consequence of the Brillouin theorem the ground state of the CIS calculation is identical to the Hartree-Fock ground state because it is unaffected by CIS. In Figure 11.5 the CIS energy spectrum is displayed for the Gaussian potential with $\xi_0 = 5\, d_{\mathrm{ho}}^{-2}$ with the basis set given in Table A.1. For a temperature of $T = 1\,\mu\mathrm{K}$, kr_0 is given by ≈ 0.4. However, in nowadays experiments temperatures routinely reach the nK regime where $kr_0 \ll 1$ (which is the criterion for dominant s-wave scattering) is well satisfied again. Clearly the ground state, which is the Hartree-Fock ground state, is only appropriate in the regime of smaller interactions $d_{\mathrm{ho}}/a < -4$. As soon as the spectrum involves states with molecular character, i. e. for $d_{\mathrm{ho}}/a \gtrsim -1$, the Hartree-Fock (and CIS) calculation states become inappropriate. The reason is that for the molecular state the strong binding of the particles leads to a small mean interparticle distance with strong spatial correlation. Such correlation effects are, however, not fully accounted for in the Hartree-Fock approximation. On that basis it is remarkable that the Hartree-Fock ground state reproduces the bound state still qualitatively. The energies drop towards large negative values. Even more surprising is the behavior of the trap state energies in the mean-field description: Passing unitary ($d_{\mathrm{ho}}/a = 0$) the energies of the trap states increase with increasing inverse scattering length, which is completely inaccurate. Hence, even in the trap

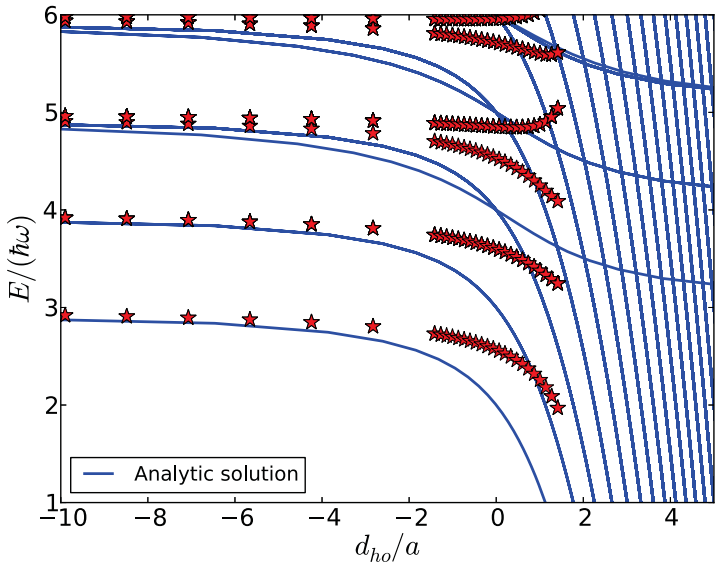

Figure 11.5: Two-body eigenenergy spectrum of the Gaussian potential with $\xi_0 = 5\,d_{\mathrm{ho}}^{-2}$ for a varying potential depth obtained by CIS calculations in comparison to the analytical solution of the δ pseudopotential.

state, were the particles are not strongly bound, correlations are highly important, especially for large positive scattering lengths.

Especially the behavior of the trap state close to unitary makes the need for post-Hartree-Fock calculations obvious. The FCI eigenenergy spectrum for the Gaussian potential with $\xi_0 = 5\,d_{\mathrm{ho}}^{-2}$ is shown in Figure 11.6. Clearly, the same basis (given in Table B.1) leads to much better agreement of the FCI energies with the analytical pseudopotential ones than the corresponding potential with $\xi_0 = 50 d_{\mathrm{ho}}^{-2}$ shown in Figure 11.4. The bound state energies are much closer to the pseudopotential energies compared to the potential with $\xi_0 = 50 d_{\mathrm{ho}}^{-2}$. In fact, for the bound state the energies fall below the energies of the pseudopotential for increasing inverse scattering length. This is not a violation of the variational principle but is in accordance with realistic interaction potentials as shown in Figure 11.1 for ^{7}Li. There it was revealed that the δ pseudopotential is too "soft".

As visible in Figure 11.6 as well as in Figure 11.4 more states appear in the FCI calculation than in the analytical solution. This can be best understood considering the energy of two non-interacting particles confined to an isotropic harmonic potential in c.m. and rel. motion coordinates, $E/\hbar\omega = 2k_{\mathrm{rel}} + l_{\mathrm{rel}} + 2k_{\mathrm{cm}} + l_{\mathrm{cm}} + 3$. In case of the analytical pseudopotential solution [62] the relative-motion solutions are restricted to s-wave scattering, i. e. $l_{\mathrm{rel}} = 0$. In the numerical calculations, however, states with $l_{\mathrm{rel}} > 0$ are included in the spectrum and cause the interaction-independent horizontal lines at $E/(\hbar\omega) = 4, 5, 6, \ldots$. These states are multiply

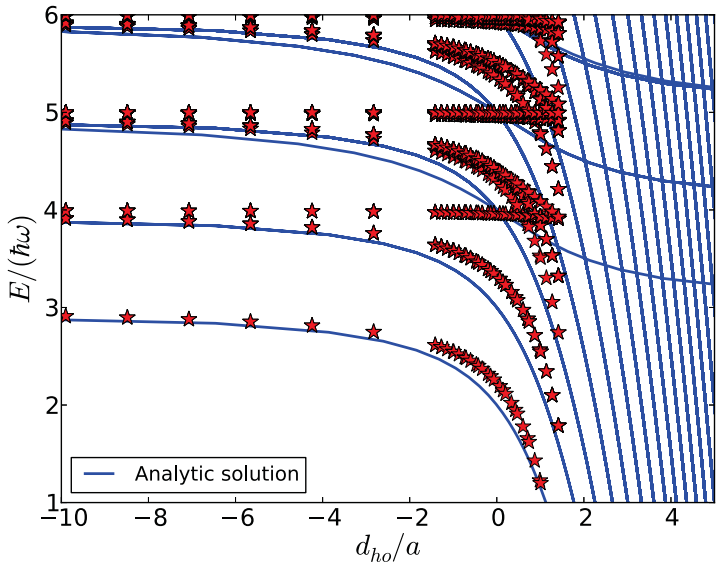

Figure 11.6: Two-body eigenenergy spectrum of the Gaussian potential with $\xi_0 = 5\,d_{\mathrm{ho}}^{-2}$ obtained by FCI calculations for a varying potential depth which is equivalent to a change in of the scattering in comparison to the analytical solution of a δ-pseudopotential interaction.

degenerate, since for each l there exist $2l+1$ states with different m quantum numbers. For example, the interaction independent state at $E/\hbar\omega = 4$ has quantum numbers $(k_{\mathrm{rel}}, l_{\mathrm{rel}}, k_{\mathrm{cm}}, l_{\mathrm{cm}}) = (0, 1, 0, 0)$ and has a 3-fold degeneracy which is correctly reproduced by the calculations. In a similar vein, the first excited bound state that has also an energy of $E/\hbar\omega = 3$ for $d_{\mathrm{ho}}/a \to -\infty$ is also 3-fold degenerate and corresponds to the quantum numbers $(k_{\mathrm{rel}}, l_{\mathrm{rel}}, k_{\mathrm{cm}}, l_{\mathrm{cm}}) = (0, 0, 0, 1)$.

The fact that the $l_{\mathrm{rel}} > 0$ states are non-interacting for s-wave scattering, can be used to validate whether the extended range of the potential of $\xi_0 = 5d_{\mathrm{ho}}^{-2}$ given in the calculations presented in Figure 11.6 is still acceptable. In the ultracold regime s-wave scattering is dominant because the centrifugal barrier blocks states with $l_{\mathrm{rel}} > 0$ to result in a strongly suppressed amplitude in the interaction regime. By widening the potential, the centrifugal barrier effectively decreases which leads to the interaction of states beyond s-wave scattering. This behavior can be identified by comparing the energy of the $l_{\mathrm{rel}} = 1$ state of the potentials with $\xi_0 = 50\,d_{\mathrm{ho}}^{-2}$ and $\xi_0 = 5\,d_{\mathrm{ho}}^{-2}$ in Figure 11.7 (which show enlargements of Figure 11.4 and Figure 11.6, respectively). Clearly, the $l_{\mathrm{rel}} = 1$ states are hardly affected by the change of the potential depth for the $\xi_0 = 50\,d_{\mathrm{ho}}^{-2}$ potential where they are constant at $4\,\hbar\omega$ up to 4 digits over the entire range of scattering lengths. For the wide (but much easier to converge) potential with $\xi_0 = 5\,d_{\mathrm{ho}}^{-2}$ the energies are much more affected by the interaction potential and decrease with increasing inverse scattering length. This is a

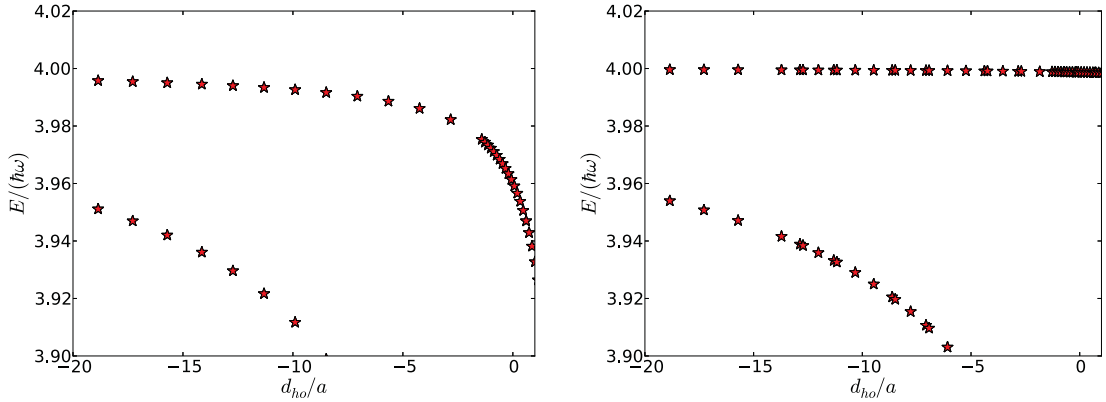

Figure 11.7: Two-body eigenenergy spectrum of the Gaussian potential with $\xi_0 = 5\,d_{\mathrm{ho}}^{-2}$ and $\xi_0 = 50\,d_{\mathrm{ho}}^{-2}$ obtained by FCI calculations for a varying potential depth enlarged around the energy of the $l_{\mathrm{rel}} = 1$ states.

direct evidence of p-wave interactions, that are, however, still small compared to the energy variations introduced by the s-wave scattering, i. e. the p-wave contributions are still at least about an order of magnitude smaller than $\hbar\omega$.

Although higher-order partial-wave interactions are introduced by adopting a potential with a wider range, the basic structure of the s-wave spectrum is very well fulfilled for $\xi_0 = 5\,d_{\mathrm{ho}}^{-2}$. To recognize this, consider the spectrum enlarged in the unitary regime (around $d_{\mathrm{ho}}/a = 0$) in Figure 11.8. The bending down of the $l_{\mathrm{rel}} = 1$ state at $E/(\hbar\omega) \approx 4$ is the just mentioned effect of the p-wave interaction introduced by the wide Gaussian potential. The focus is now put on the structure of the trap states (marked $|t^{\delta}\rangle$ and $|t^{(\mathrm{FCI})}\rangle$) and the bound states (marked $|b^{\delta}\rangle$ and $|b^{(\mathrm{FCI})}\rangle$).

The trap states ($|t^{\delta}\rangle$ and $|t^{(\mathrm{FCI})}\rangle$) are non-degenerate states with quantum numbers given in the non-interacting limit $d_{\mathrm{ho}}/a \to -\infty$ by $(k_{\mathrm{rel}}, l_{\mathrm{rel}}, k_{\mathrm{cm}}, l_{\mathrm{cm}}) = (1, 0, 0, 0)$. $|b_2^{(\mathrm{FCI})}\rangle$ is a non-degenerate excited bound state in the non-interacting limit described by the quantum numbers $(k_{\mathrm{rel}}, l_{\mathrm{rel}}, k_{\mathrm{cm}}, l_{\mathrm{cm}}) = (0, 0, 1, 0)$. $|b_1^{(\mathrm{FCI})}\rangle$ is a 5-fold degenerate excited bound state with quantum numbers $(k_{\mathrm{rel}}, l_{\mathrm{rel}}, k_{\mathrm{cm}}, l_{\mathrm{cm}}) = (0, 0, 2, 0)$ in the non-interacting limit. The missing full convergence of the FCI calculations makes $|b_2^{(\mathrm{FCI})}\rangle$ and $|b_1^{(\mathrm{FCI})}\rangle$ become non-degenerate. These states have to be degenerate in a converged calculation, as it is the case for the analytical spectrum where only the single 6-fold degenerate bound state $|b^{\delta}\rangle$ is visible. Considering the adopted basis set specified in Table B.1 it is understandable that $|b_2^{(\mathrm{FCI})}\rangle$ is better converged than $|b_1^{(\mathrm{FCI})}\rangle$, because in the used basis there are more s and p states than d functions. Hence, it is not surprising that the isotropic bound state with just a single radial c.m. excitation is better converged than the degenerate bound states with d-like c.m. excitation. In general, higher excited states are expected to be converged worse because of their more complex spatial (nodal) structure. This convergence behavior

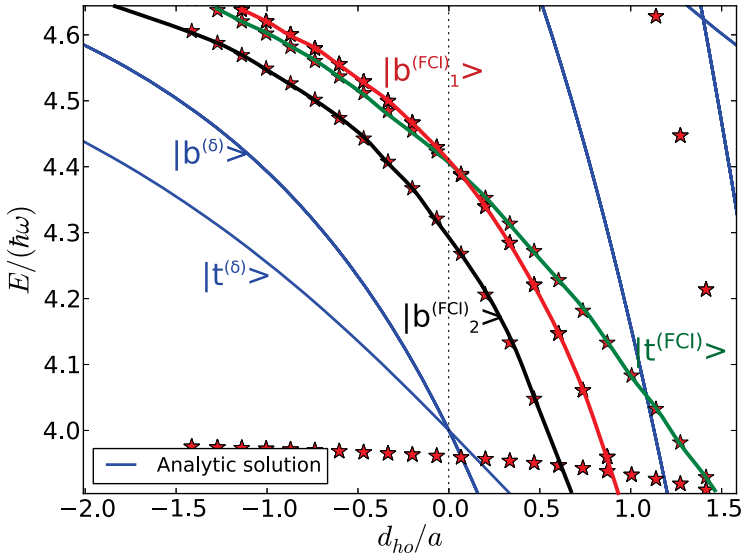

Figure 11.8: Two-body eigenenergy spectrum of the Gaussian potential with $\xi_0 = 5\,d_{\mathrm{ho}}^{-2}$ obtained by FCI calculations for a varying potential depth enlarged with focus on the unitary regime in comparison to the analytical solution of the δ pseudopotential. Unitary is marked by the vertical black dashed line. Explicitly denoted are the energies of the analytically calculated trap and bound states, $|t^{\delta}\rangle$ and $|b^{\delta}\rangle$, respectively, and the numerically obtained trap and bound states $|t^{(\mathrm{FCI})}\rangle$, $|b_1^{(\mathrm{FCI})}\rangle$, and $|b_2^{(\mathrm{FCI})}\rangle$, respectively. Due to missing full convergence, the bound states of the FCI calculation are not degenerate as it is the case for the analytical evaluation of the δ pseudopotential.

can also be observed at $d_{\mathrm{ho}}/a \ll -1$: the 5-fold degenerate states with quantum numbers $(0,2,0,0)$ are the energetically highest lying ones, followed (in this order) by the 9-fold degenerate $(0,1,0,1)$ states, the 5-fold degenerate $(0,0,0,2)$ states, the $(1,0,0,0)$ state and the energetically lowest lying $(0,0,1,0)$ state.

However, besides convergence effects it is important that the structure of the spectrum, especially the not only for the description of CIR important crossing of the bound and trap state is reproduced by the FCI calculation. In an isotropic harmonic trap the first excited bound state crosses with the trap state at $1/a = 0$ as can be seen from $|b^{\delta}\rangle$ and $|t^{\delta}\rangle$ in Figure 11.8. This crossing is also reproduced in position surprisingly accurately by $|b_1^{(\mathrm{FCI})}\rangle$ and $|t^{(\mathrm{FCI})}\rangle$. Certainly, this accuracy should not be over-interpreted, since full convergence is not yet achieved. Still, in summary, the basic structure of bound and trap states, their degeneracy, and the crossings are all reproduced by the FCI calculation.

12 Conclusion of Part II

A theoretical approach was developed that allows for the computational treatment of a variable number of particles in a trap potential that can, in principle, be part of the entire space of real continuous functions. Hence, in contrast to many other methods a treatment of few-body systems beyond the harmonic approximation becomes feasible that was shown in Part I to be necessary in order to describe instabilities and molecule formation in recent experiments of ultracold atomic gases.

The computational approach uses concepts of traditional electronic-structure theory, such as Hartree-Fock and configuration interaction. In order to save precious development time the implementation is based on modification and extension of the existing open-source quantum-chemistry package PyQuante. The code is designed such that a set of contracted Gaussian basis functions can be distributed arbitrarily in space. In order to be able to describe the strong correlation present for large scattering lengths, a crucial step was the development of a post-Hartree-Fock method, i. e. the FCI algorithm. In the implementation, the second-quantized excitation operators are translated into functions that reflect the action on spin strings. The usage of spin strings as a representation of the determinants pays off as it allows for a compact and easy-to-access addressing and ordering scheme.

The investigation of a system of two spin-singlet fermionic atoms interacting via a zero-range δ potential turns out to be inappropriate in the case of a bare coupling constant. A renormalization scheme is developed that allows in principle to reconstruct the entire analytically given spectrum of two harmonically trapped ultracold atoms interacting via the δ pseudopotential. In practice, this has not been achieved so far, since the numerical calculations for the δ potential turned out to be nonconvergent for large negative scattering lengths. Differently, the energies of the low lying trap states for positive scattering lengths are quantitatively reproduced.

The analysis of a finite-range Gaussian interaction potential revealed that the Hartree-Fock treatment is unstable for positive scattering lengths beyond the strongly correlated regime $d_{\mathrm{ho}}/a \gg 1$. The reason is that the rich bound-state structure cannot be resolved appropriately. For the FCI calculation, in order to obtain results close to the analytical results of the δ pseudopotential of two atoms in an isotropic harmonic trap, it is necessary to widen the effective range of the Gaussian interaction potential. This introduces mild effects of higher-order partial wave interactions, such as p-wave and d-wave interactions. However, the higher-order interactions are

still negligible in energy compared to the s-wave contribution. With such a potential the essential spectral structure of the analytical pseudopotential is replicated. Deviations in the eigenenergies of the molecular bound states are shown to be partly an effect of the δ pseudopotential that turns out to be "too soft" in comparison to a realistic interaction potential of ^{7}Li atoms: the δ pseudopotential results in too large energies with increasing inverse scattering length compared to the realistic interaction. The trap and bound states of the FCI calculation show the correct degeneracy and crossing behavior.

For both, the finite-range and the renormalized δ potential further optimization of the code, possibly including a truncation of the CI space are expected to give further flexibility in the basis set. Moreover, further investigations of the behavior of different basis sets and initial conditions are expected to stabilize the Hartree-Fock calculations and lead to a better convergence.

Most importantly, however, the here developed approach paves the way for the treatment of a variety of few-body systems beyond the harmonic approximation. In fact, the approach can directly be applied to few-fermion systems in the mean-field regime. Here, studies of the influence of multi-well potentials are interesting. Moreover, ultracold few-fermion systems in multi-well potentials exposed to a magnetic-field gradient which is currently experimentally studied in the group of Selim Jochim at the University of Heidelberg can now be investigated computationally.

Part III

Quantum simulation of attosecond physics with ultracold atoms

Ultracold atoms have introduced an entirely novel degree of experimental control and flexibility. Moreover, the accessibility of extreme parameter regimes and novel, sophisticated preparation and detection schemes paved the way for ultracold atoms to first pioneer and nowadays being a working horse for an exciting research area: quantum simulation.

The original idea of quantum simulation goes back to the renowned lecture "Simulating physics with computers" [133] of Richard P. Feynman. There he suggested to use a precisely controllable quantum system to investigate the behavior of other quantum systems that cannot be examined by calculations on classical computers due to their complexity even in principle due to the exponentially growing Hilbert space. Hence, measurements on a highly controllable simulator system replace unfeasible calculations on a classical computer. Feynman had in mind an *universal* quantum simulator, i. e. a specific, extremely controllable quantum system which can be manipulated by a variation of parameters such that its effective Hamiltonian corresponds to *any* quantum system under investigation.

Different to Feynman's universal quantum simulator, nowadays quantum simulations usually aim for single, specific effects where the experimental realization in the native research area fails. The perhaps most renowned example is the Mott-insulator to superfluid phase transition. It was first described for condensed-matter systems [134]. After no experimental realization of the phase transition could be achieved within condensed-matter systems, it was predicted [48] and then observed [49, 135] with ultracold atoms in an optical lattice. Similarly, the Fulde-Ferrell-Larkina-Ovchinnikov (FFLO) phase [136, 137] has not been verified indisputably in superconducting materials, but was successfully simulated within ultracold gases [21, 23]. Also other phenomena have been studied using quantum simulation like the Higgs mechanism [26], high-temperature superconductivity [22], or *Zitterbewegung* [24]. Also the quantum simulation of electrons in crystalline solids that are exposed to laser fields has been proposed [138]. While there exist numerous quantum simulations with ultracold atoms [139], they have been realized also in other research fields. For example, quantum simulations were performed with trapped ions [140] or photons [141], and there are even quantum simulators with superconducting circuits on a chip in progress [142]. Different to the mentioned quantum simulations that aim for a specific effect the here proposed one is of more general nature. Its goal is to deepen the understanding of various fundamental questions in one of today's most topical research areas: attosecond science.

Attosecond science, i. e. the research field of atoms, ions, molecules, and even solids and crystals exposed to short, high intense laser fields has deepened the understanding of the interaction of light and matter. Nowadays, the duration of the light pulses has reached the few femtosecond to attosecond timescale [143]. More-

over, novel experimental techniques lead to exciting progresses like the imaging of molecular processes [144] in real time ("molecular movie") and orbital tomography [145].

Although nowadays strong-field experiments investigate the field response of higher elements and complex molecules, the theoretical description of the dynamical field response of such systems is extremely challenging. The state of the art for an exact non-relativistic treatment on a classical computer beyond the single-active electron approximation is, in fact, the description of two-electron systems like He or H_2 [146–149]. The reason is that the solution of the time-dependent electronic many-body Schrödinger equation for N electrons and M nuclei (with atomic numbers Z_A, fixed in space at r_{Aj} within Born-Oppenheimer approximation)

$$\left[-i\frac{\partial}{\partial t} - \frac{1}{2}\sum_{i=1}^{N}\nabla_i^2 + \frac{1}{2}\sum_{i\neq j}\frac{1}{|\mathbf{r}_i - \mathbf{r}_j|} - \sum_{i=1}^{N}\sum_{j=1}^{M}\frac{Z_A}{|\mathbf{r}_i - \mathbf{r}_{Aj}|} + \sum_{i=1}^{N}\mathbf{r}_i \cdot \mathbf{E}(\mathbf{r},t)\right]\psi(\mathbf{r},t) = 0 \tag{12.1}$$

here written down in atomic units for an electric-field component $\mathbf{E}(\mathbf{r},t)$ of the laser in length gauge, is by far too challenging for an exact solution for many electrons. In particular, because the time-dependent perturbation of such a system couples all states including continuum states. This is the essential difference to the stationary eigenvalue problems often present in quantum mechanics that can be solved for selected states even for very complex systems within, e. g., quantum-chemistry calculations. As a consequence, simplified, often semiclassical models have been developed to interpret modern attosecond-science experiments involving many-body systems. The systematic validation of these (often controversial) models is, however, in most cases impossible for several reasons.

First, the laser pulses underlie restrictions: Only limited wavelengths are accessible, nowadays Ti:sapphire lasers are widely used. Although the intensity of the lasers pulses is already very high (typically about $10^{14}\,\mathrm{W/cm^2}$ and higher), and the timescales have already reached the femtosecond (in case of Ti:sapphire lasers) to attosecond domain, further improvements seem extremely hard and perhaps require eminent technical improvements or even principle developments in how the pulses are generated. Another drawback for a systematic investigation is that pulse shapes are in general not known to high accuracy and, additionally, cannot exactly be reproduced.

Second, atoms and molecules are complicated many-body systems which do not allow for a simple manipulation. For example, the molecular geometry is well defined and cannot simply be altered. Additionally, the atomic core potential depends on the used element. Replacing the molecule or the element changes also charac-

teristic parameters such as the ionization energy, polarizability, or electron affinity. Additionally, a variation of the number of protons or electrons is constrained by electroneutrality. A systematic investigation where a single parameter is varied to find out about its influence (as theoretical works usually approach such questions) becomes impossible.

Third, the correlation of electronic and nuclear motion influences the strong-field behavior [150, 151]. However, due to its complexity, it must be neglected in most studies. This can be done theoretically in different approaches, the most common one is to simply spatially fix the nuclei and only consider the electronic response.

The dilemma that interesting (many-body) strong-field systems cannot be described exactly within non-relativistic quantum mechanics but only by simplified models, that often cannot be validated systematically due to experimental limitations, can be overcome by introducing a versatile quantum simulator that gathers the response of a confined many-body system to a time-dependent linear perturbation.

13 Atoms and molecules in strong laser fields

Before introducing the quantum simulator, a brief overview on strong-field physics needs to be presented in order to obtain a basic overview of the research field that is to be investigated by quantum simulation.

13.1 A brief strong-field physics survey

The interaction of a strong laser field with an atom or molecule can lead to excitation or ionization. These processes are typically described within two regimes depending whether a *field* or a *photon*[1] picture is more adequate. Both regimes can roughly be separated by the Keldysh adiabaticity parameter

$$\gamma := \omega_\mathrm{e} \frac{\sqrt{2 m_\mathrm{e} I_p}}{e E_0} \tag{13.1}$$

where ω_e is the field frequency, E_0 the peak electric field component of the laser, I_p the ionization potential of the field-free Hamiltonian (in analogy to the binding energy E_b of a trapped ultracold atom), e and m_e the electron charge and mass, respectively. In case of a slowly-varying field ($\gamma \ll 1$), the field picture is used to describe the ionization process where the system follows adiabatically the changes in the field such that the potential barrier formed by the positively charged nuclei is distorted and the electron can escape over the barrier or can tunnel through it, see Figures 13.1(d) and (e). The tunneling ionization rate for the hydrogen atom in the ground state in case of a weak static electric field was derived by Landau and Lifshitz [152] and was generalized to slowly varying alternating fields by Perelomov, Popov, and Terent'ev [153–155] (PPT rate). Further approximations by Ammosov, Delone, and Krainov [156] (ADK rate) lead to the description of arbitrary atoms.

In the case that the oscillating frequency of the field is too fast for the system to follow adiabatically the changes of electric field component ($\gamma \gg 1$), the photon picture is more adequate. Ionization in the photon picture occurs when an electron

[1] Although the term "photon" picture is widely used, it might be misleading, since the field is not treated in second quantization but classically as an oscillating electric field.

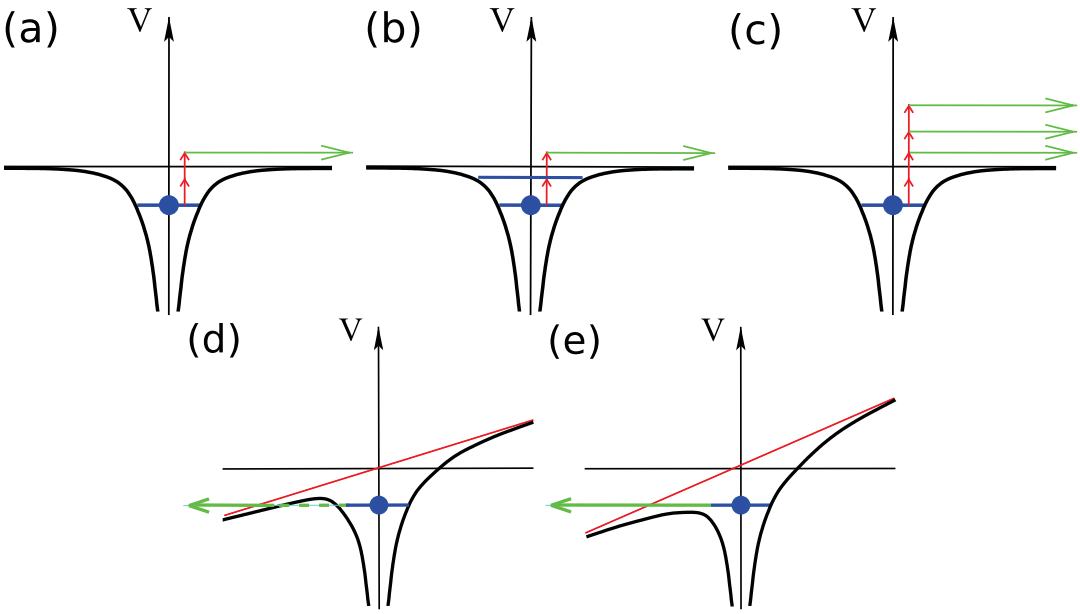

Figure 13.1: Strong-field ionization mechanisms. (a)-(c), multiphoton regime. In case of multiphoton ionization (a) the electron absorbs multiple photons to reach the continuum. For resonantly enhanced multiphoton ionization (b) an intermediate bound state is resonantly populated. Above threshold ionization (c) is characterized by the absorption of multiple photons that are visible as multiphoton peaks in photoelectron spectra. (d)-(e), adiabatic regime. The external field distorts the continuum threshold of the binding potential such that the electron can tunnel out (d) or escape over the barrier (e).

absorbs one or more photons to reach the continuum. Depending on the system as well as on the frequency and intensity of the used laser, photoionization can be described by different mechanisms. At first, the photoelectric effect was encountered [157, 158], that formed a cornerstone in the rise of quantum theory. Here, a bound electron is ionized by absorbing a single photon. This is possible if $\hbar\omega$ is larger than the binding energy I_p. Then, the energy difference $(\hbar\omega - I_p)$ is transferred into kinetic energy of the ionized electron. The onset of lasers triggered new capabilities in strong-field experiments. This lead to the observation of ionization processes where multiple photons are absorbed simultaneously, the so called *multiphoton ionization*, see Figure 13.1(a), predicted already in 1931 by Maria Göppert-Mayer [159]. The ionization rate in the photoelectric effect is proportional to the light source intensity I [158], $\Gamma \propto \sigma I$, σ being the total photoionization cross section. For a multiphoton process lowest-order perturbation theory (LOPT) [160, 161] results in $\Gamma \propto \sigma_N I^N$ where N is the minimum number of photons required for ionization. LOPT needs to be adjusted in the case that intermediate bound states are populated by the

photoabsorption. Such a scenario is called *resonantly enhanced multiphoton ionization* (REMPI), see Figure 13.1 (b). A groundbreaking experimental advancement was the detection of energy-resolved photoelectron spectra that lead to the observation of photoelectrons with kinetic energies larger than the photon energy [162], the so called *above-threshold ionization* (ATI) [163, 164], see Figure 13.1(c). ATI spectra may consists of peaks were the peak spacing corresponds to the photon energy. Such spectra reveal the non-perturbative character of ATI, since depending on the laser intensity higher-order peaks become dominant over the first one [165]. Another strong-field feature is the disappearance of leading peaks with increasing intensity. This observation was a direct evidence that the electron requires additional energy compared to the binding energy to escape the binding potential, i. e. the ponderomotive energy

$$U_p = \frac{I}{4\omega^2} \tag{13.2}$$

of an electron in a laser field.

Adopting a low-frequency laser [166] it was demonstrated experimentally that a *plateau* in the ATI spectra occurred. Theoretical investigations have revealed that the plateau is caused by the rescattering of the liberated electron with the parent ion. Closely connected to rescattering is the generation of high harmonic radiation that was explained theoretically within a semiclassical model describing a recollision scenario [167–170]. Here, an electron tunnels through the field-distorted potential barrier, accelerates in the laser field, reverses it's direction and recombines radiatively with the parent ion leading to the generation of high-harmonic radiation.

This brief introduction is, of course, by far not exhaustive. Especially for the ionization behavior of molecules there occur further fascinating phenomena like sequential and non-sequential multiple ionization, alignment-dependent effects, etc. However, since in the present study the quantum simulator is validated in correspondence to a hydrogen atom, only aspects of strong-field ionization which are directly relevant for the thesis are explicitly mentioned.

A fundamental aspect of electrodynamics is its gauge freedom. For a treatment of the light-matter interaction, of course, the role of gauges must be taken into account. In fact, it will turn out that aspects of gauges have exciting consequences for the quantum simulator.

13.2 Gauges, gauge transformations, and gauge invariance

The interaction of a strong laser field with matter is usually treated semiclassically in attosecond science, i. e. the structure of atoms and molecules is treated quantum mechanically while the field is described classically. The classical description of the field is justified, since the very high intensity leads to a very high photon density such that the quantum mechanical behavior of single photons can be neglected. The classical description of light, i. e. classical electrodynamics, is based on the Maxwell equations. They can either be formulated in terms of magnetic and electric fields $\mathbf{B}(\mathbf{r},t)$ and $\mathbf{E}(\mathbf{r},t)$, respectively, or by two potentials, the vectorpotential $\mathbf{A}(\mathbf{r},t)$ and the scalar potential $\Phi(\mathbf{r},t)$. These quantities are related to each other via

$$\mathbf{E}(\mathbf{r},t) = -\nabla\Phi_{\mathrm{g}}(\mathbf{r},t) - \frac{\partial}{\partial t}\mathbf{A}_{\mathrm{g}}(\mathbf{r},t) \tag{13.3}$$

$$\mathbf{B}(\mathbf{r},t) = \nabla \times \mathbf{A}_{\mathrm{g}}(\mathbf{r},t) \quad . \tag{13.4}$$

The subscript G is introduced here, since the electrodynamical potentials are not unique but differ within different *gauges*.

The interaction of a classical field with an electron bound to a electrostatic potential $U(\mathbf{r})$ is governed by the minimal coupling Hamiltonian satisfying the TDSE

$$i\frac{\partial}{\partial t}\psi_{\mathrm{g}}(\mathbf{r},t) = \left[\frac{1}{2}\left(-i\nabla + \mathbf{A}_{\mathrm{g}}(\mathbf{r},t)\right)^2 - \Phi_{\mathrm{g}}(\mathbf{r},t) + U(\mathbf{r})\right]\psi_{\mathrm{g}}(\mathbf{r},t) \tag{13.5}$$

in coordinate representation. *Local gauge invariance* means that Eq. (13.5) obtains the same form under simultaneous gauge transformations

$$\psi_{\mathrm{g}'}(\mathbf{r},t) = \psi_{\mathrm{g}'}(\mathbf{r},t)\exp[iT_{\mathrm{g}\to\mathrm{g}'}(\mathbf{r},t)] \tag{13.6}$$

$$\mathbf{A}_{\mathrm{g}'}(\mathbf{r},t) = \mathbf{A}_{\mathrm{g}}(\mathbf{r},t) - \nabla T_{\mathrm{g}\to\mathrm{g}'}(\mathbf{r},t) \tag{13.7}$$

$$\Phi_{\mathrm{g}'}(\mathbf{r},t) = \Phi_{\mathrm{g}}(\mathbf{r},t) - \frac{\partial}{\partial t}T_{\mathrm{g}\to\mathrm{g}'}(\mathbf{r},t) \tag{13.8}$$

of the electrodynamical potentials and the wavefunction with a transformation function $T_{\mathrm{g}\to\mathrm{g}'}(\mathbf{r},t)$ that satisfies

$$T_{\mathrm{g}\to\mathrm{g}'} = -T_{\mathrm{g}'\to\mathrm{g}}, \quad T_{\mathrm{g}\to\mathrm{g}'} + T_{\mathrm{g}'\to\mathrm{g}''} = T_{\mathrm{g}\to\mathrm{g}''} \quad . \tag{13.9}$$

The gauge transformation preserves physical quantities such as the fields or the absolute square of the wavefunction, i. e. these observables are identical in either gauge.

Although there exists, in principle, an infinite number of gauges, three are introduced in the following that are commonly (as well as in the present thesis) used. In *velocity gauge* the electrodynamical potentials are determined by

$$\nabla \cdot \mathbf{A}_{\mathrm{VG}} = 0, \quad \Phi_{\mathrm{VG}} = 0 \quad . \tag{13.10}$$

The total Hamiltonian

$$H_{\mathrm{VG}} = \frac{\mathrm{p}^2}{2} + \mathbf{A}_{\mathrm{VG}} \cdot \mathrm{p} + \frac{\mathbf{A}_{\mathrm{VG}}^2}{2} + U \tag{13.11}$$

contains a quadratic term in the vectorpotential. $\mathbf{p}$ is given in coordinate representation as $i\nabla$ and is independent of the gauge. The fields are given in velocity gauge as

$$\mathbf{E}(\mathbf{r},t) = -\frac{\partial}{\partial t}\mathbf{A}_{\mathrm{g}}(\mathbf{r},t), \quad \mathbf{B}(\mathbf{r},t) = \nabla \times \mathbf{A}_{\mathrm{g}}(\mathbf{r},t) \quad . \tag{13.12}$$

Throughout the present work, the dipole approximation will be adopted, which is well satisfied if the wavelength is sufficiently large such that a spatial dependence of the radiation can be neglected for length scales of the considered systems, i. e. $\mathbf{A}(\mathbf{r},t) \approx \mathbf{A}(t)$. Then, the fields become

$$\mathbf{E}(t) = -\frac{d}{dt}\mathbf{A}_{\mathrm{VG}}(t), \quad \mathbf{B}(\mathbf{r},t) = 0 \quad . \tag{13.13}$$

In the following the subscript VG is dropped for the vectorpotential, such that $\mathbf{A}_{\mathrm{VG}}(\mathbf{r},t) \equiv \mathbf{A}(\mathbf{r},t)$.

It is worth mentioning that, unfortunately, the term *velocity gauge* is not used consistently in literature. Sometimes the velocity gauge introduced above is considered as *radiation gauge* and a gauge where the quadratic term in the vectorpotential is removed by the transformation function

$$T_{\mathrm{VG}\to\mathrm{rVG}}(\mathbf{r}) = \frac{1}{2}\int dt \mathbf{A}_{\mathrm{VG}}(\mathbf{r},t) =: \beta(\mathbf{r}) \tag{13.14}$$

is then referred to as velocity gauge. In this gauge which will be denoted as *reduced velocity gauge* (since the $\mathbf{A}^2$ term is removed), the electrodynamical potentials

$$\mathbf{A}_{\mathrm{rVG}} = \mathbf{A} - \nabla\beta, \quad \Phi_{\mathrm{rVG}} = \frac{\mathbf{A}^2}{2} \tag{13.15}$$

simplify in dipole approximation since $\nabla\beta = 0$, to result in the final Hamiltonian

$$H_{\mathrm{rVG}} = \frac{\mathrm{p}^2}{2} + \mathbf{A}_{\mathrm{rVG}} \cdot \mathrm{p} + U \tag{13.16}$$

which is identical to the velocity gauge Hamiltonian except for the quadratic part in the vectorpotential. The possibility to drop the $\mathbf{A}^2$ term in dipole approximations may be regarded as a major reason for the dominance of the dipole approximation in literature.

Length gauge is obtained from the velocity gauge by the transformation

$$T_{\mathrm{VG}\to\mathrm{LG}}(\mathbf{r}, t) = \mathbf{A}(\mathbf{r}, t) \cdot \mathbf{r} \quad . \tag{13.17}$$

The electrodynamical potentials in length gauge are given by

$$\mathbf{A}_{\mathrm{LG}} = \mathbf{A} - \nabla(\mathbf{A} \cdot \mathbf{r}) = -i\mathbf{L} \times \mathbf{A}, \quad \Phi_{\mathrm{LG}} = -\mathbf{E} \cdot \mathbf{r} \tag{13.18}$$

where $\mathbf{L} = \mathbf{r} \times \mathbf{p}$ is the canonical angular momentum operator. In dipole approximation $\mathbf{A}_{\mathrm{LG}}$ vanish. Thus, the length-gauge Hamiltonian in dipole approximation

$$H_{\mathrm{LG}} = \frac{\mathrm{p}^2}{2} + \mathbf{E}(t) \cdot \mathbf{r} + U \tag{13.19}$$

does not contain the vectorpotential.

It should be noted that measurable quantities extracted from converged solutions of a TDSE calculation are (and of course have to be) independent of the used gauge. When approximations are introduced, the gauge independence might break down (depending on the approximation). For example, the SFA leads to different results in different gauges.

14 The attoscience quantum simulator

After having introduced briefly strong-field physics and the concept of gauges, the novel concept of an ultracold-atom quantum simulator is presented including the mapping of the strong-field and simulator Hamiltonians.

14.1 Basic concept

The basic idea of the attoscience quantum simulator is schematically reflected in Figure 14.1, where a simulator system (right) of trapped atoms is compared to a corresponding strong-field system of electrons in the Coulomb potential of a nucleus (left). Hence, the electrons of an atom or molecule are in the quantum simulator

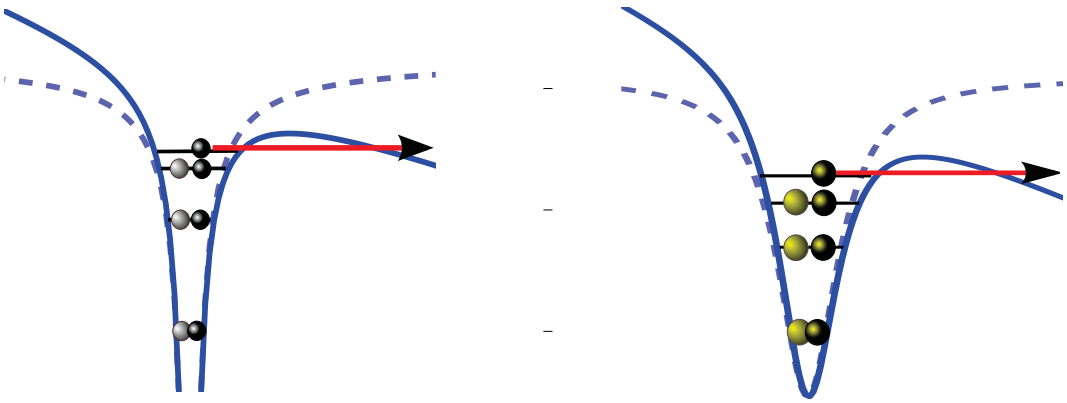

Figure 14.1: Comparison of the behavior of electrons in an atom exposed to a strong electric field (left) and atoms in an optical trap exposed to a magnetic-field gradient (right). The different shadings of the electrons and atoms, respectively, reflect their different spin states. For the atoms different spin states can be achieved by loading the trap with atoms in two Zeeman substates. The dashed curves indicate the potentials in absence of an external field. An external electric field (left) or magnetic-field gradient (right) effectively tilts the continuum threshold and the electrons (left) or atoms (right) can escape the binding potential by tunneling.

replaced by ultracold fermionic atoms. The two spin components m_s of the electron can be modeled by two hyperfine states of the fermionic atoms. The Coulomb

potential created by the nuclei that spatially confines the electrons is replaced by an external, optical trap potential in the quantum simulator. The laser-field that distorts the continuum threshold in the strong-field system is replaced by a magnetic-field gradient that distorts the continuum threshold of the trap potential. Hence, the pendant of the charge of the electrons is the magnetic moment of the ultracold atoms.

The investigation of strong-field physics by ultracold trapped atoms opens possibilities not available in attosecond science: While the electron-electron repulsion in atoms and molecules cannot be manipulated, the effective interatomic interaction can be tuned for ultracold atoms by Feshbach resonances [4]. While the core potential and molecular geometry of atoms and molecules, respectively, cannot be manipulated in a systematic fashion, the external, optical trap potential can be manufactured in a plethora of shapes. In fact, the control of the interatomic interaction as well as the external potential can be controlled in real time during an experiment. Periodic structures similar to the one of solids, few-well systems like in molecules, or single wells like in atoms, even exotic systems of reduced dimensionality are nowadays accessible. The high-intense laser pulse with all its restrictions (mentioned above) is replaced by a periodically driven magnetic-field gradient. Since the gradient is generated by current-carrying coils, it offers complete control over the created pulses.

The exceptional control and variability of the interaction, of the external potential as well as of the pulses build the basis of a versatile quantum simulator, that can help to deepen the understanding of attosecond many-body physics where the validity of simplified models is unknown and computations on a classical computer fail.

14.2 Simulator mapping

The simulator mapping builds the heart of the quantum simulator as it delivers the formal equivalence of the quantum simulator Hamiltonian to the electronic strong-field Hamiltonian at a fixed nuclear configuration. As already mentioned in Section 13.2, the high intense laser field can be treated classically. Adopting the dipole approximation and length gauge, the electronic strong-field Hamiltonian reads

$$H^{\mathrm{LG}}(t) = H_0 + \sum_{i=1}^{N} \mathbf{r}_i \cdot e\mathbf{E}(t) \quad , \tag{14.1}$$

where the field-free Hamiltonian

$$H_0 = \sum_{i=1}^{N} \frac{\mathbf{p}_i^2}{2m_\mathrm{e}} + V_\mathrm{ee} + V_\mathrm{e,nuc} \tag{14.2}$$

consists of the kinetic energy of N electrons, the electronic repulsion potential

$$V_\mathrm{ee} = \frac{1}{2} \sum_{i \neq j} \frac{1}{|\mathbf{r}_i - \mathbf{r}_j|} \tag{14.3}$$

and the electron-nucleus interaction potential

$$V_\mathrm{e,nuc} = -\sum_{i=1}^{N} \sum_{j=1}^{M} \frac{Z_A}{|\mathbf{r}_i - \mathbf{r}_{Aj}|} \tag{14.4}$$

of N electrons with M nuclei that are fixed at the positions $\mathbf{r}_A$ within the Born-Oppenheimer approximation (see also Section 1.1).

On the other hand, the Hamiltonian of N ultracold trapped atoms which are exposed to a time-dependent magnetic-field gradient $\boldsymbol{\mathcal{B}}'(t)$ (which is tilted in one spatial direction, e. g., $\boldsymbol{\mathcal{B}}'(t) = \partial \boldsymbol{\mathcal{B}}(t)/\partial x$) reads

$$\mathcal{H}^\mathrm{LG}(t) = \mathcal{H}_0 + \sum_{i=1}^{N} \mathbf{r}_i \cdot \mu \boldsymbol{\mathcal{B}}'(t) \quad , \tag{14.5}$$

where the gradient-free Hamiltonian

$$\mathcal{H}_0 = \sum_{i=1}^{N} \frac{\mathbf{p}_i^2}{2m_\mathrm{a}} + \mathcal{V}_\mathrm{aa} + \mathcal{V}_\mathrm{a,tr} \tag{14.6}$$

contains the kinetic energy of N atoms, the optical trap potential $\mathcal{V}_\mathrm{a,tr}$, and the interatomic interaction potential $\mathcal{V}_\mathrm{aa}$ which is given by a Born-Oppenheimer potential curve or can be approximated for ultracold atoms by the Fermi-Huang δ pseudopotential,

$$\mathcal{V}_\mathrm{aa} = \frac{1}{2} \sum_{i \neq j} \frac{4\pi\hbar^2 a_\mathrm{sc}}{m_\mathrm{a}} \delta(\mathbf{r}_{ij}) \frac{\partial}{\partial r_{ij}} r_{ij} \tag{14.7}$$

(in analogy to the potential given for two atoms in Section 1.3).

The Hamiltonians in Eq. (14.1) and Eq. (14.5) are *formally* equivalent under the

mapping

$$e\,\mathbf{E} \mapsto \mu\,\boldsymbol{\mathcal{B}}', \quad H_0 \mapsto \mathcal{H}_0 \quad . \tag{14.8}$$

This mapping builds the foundation of the here proposed versatile quantum simulator for the strong-field Hamiltonian Eq. (14.1). It allows for a systematic investigation of a many-body system that is confined to a finite potential and exposed to a linear, time-dependent perturbation.

The electrodynamical potentials introduced in Section 13.2 map accordingly to the fields. For instance, the electrodynamical vector potential $-\frac{\partial \mathbf{A}(t)}{\partial t} = \mathbf{E}$ is mapped to the "vector potential" in the simulator system by

$$-\frac{\partial \boldsymbol{\mathcal{A}}(t)}{\partial t} = \boldsymbol{\mathcal{B}}' \quad . \tag{14.9}$$

Of course, the potential $\boldsymbol{\mathcal{A}}$ differs from the physical vector potential $\tilde{\mathbf{A}}$ that generates the magnetic field $\boldsymbol{\mathcal{B}}$ and its gradient $\boldsymbol{\mathcal{B}}'$ via $\boldsymbol{\mathcal{B}} = \nabla \times \tilde{\mathbf{A}}$. Yet, Eq. (14.9) is the formal consequence of the simulator mapping in Eq. (14.8).

While the simulator mapping of Eq. (14.8) is intrinsically bound to length gauge, it is useful to consider the analog of the velocity-gauge formulation, too. A gauge transformation of the strong-field Hamiltonian in Eq. (14.1) leads to the velocity-gauge form[1]

$$H^{\mathrm{VG}}(t) = H_0 + \sum_{i=1}^{N} \frac{e}{m_{\mathrm{e}}}\,\mathbf{A}(t)\cdot\mathbf{p}_i + \frac{e^2}{2m_{\mathrm{e}}}\,\mathbf{A}(t)^2 \tag{14.10}$$

In analogy, a "gauge" transformation of the simulator Hamiltonian of Eq. (14.5) leads to the corresponding simulator Hamiltonian in "velocity gauge",

$$\mathcal{H}^{\mathrm{VG}}(t) = \mathcal{H}_0 + \sum_{i=1}^{N} \frac{\mu}{m_{\mathrm{a}}}\,\boldsymbol{\mathcal{A}}(t)\cdot\mathbf{p}_i + \frac{\mu^2}{2m_{\mathrm{a}}}\,\boldsymbol{\mathcal{A}}(t)^2 \quad . \tag{14.11}$$

Again, the Hamiltonians are *formally* equivalent. The vector potential $\boldsymbol{\mathcal{A}}(t)$ is the one resulting from the simulator mappings of Eq. (14.8) and Eq. (14.9). It is remarkable, that such an artificial gauge transformation can be performed and that, as the TDSE results will show, both formulations are equivalent, i. e. the physics is gauge invariant. In fact, the artificial "velocity gauge" for the simulator has important consequences. For example, the TDSE can be treated more efficiently. Without the

[1] Noteworthy, the $\mathbf{A}^2(t)$ term is spatially independent in dipole approximation and leads to a global, time-dependent phase in the wavefunction. Therefore it does not influence measurable quantities such as the photoelectron spectrum.

simulator mapping such an artificial gauge transformation to describe the ultracold trapped atoms exposed to a dynamically varying magnetic-field gradient, which is an interesting system to investigate even without the connection to strong-field systems, would have most likely remained hidden. Moreover, as will be demonstrated in Section 17.3, the (artificial) velocity-gauge formulation of the SFA allows to derive an imaging scheme for ultracold atoms.

14.3 Natural units and parameter mapping

In theory, strong-field systems are treated usually in atomic units. Atomic units are defined by setting the following four fundamental physical constants to unity: the electron mass m_e, the elementary charge e, the reduced Planck constant $\hbar$, and the Coulomb's constant $1/4\pi\epsilon_0$. All other physical quantities can be expressed in terms of these. For instance, the resulting measure for lengths is the Bohr radius a_0 which is the most probable distance between the electron and the proton of an hydrogen atom in the ground state (not to be confused with the expected value which is about 1.5 a_0). In contrast to strong-field systems, where atomic units are a natural choice, the traps in quantum-simulator realizations may be of very different shape. Therefore, for the simulator natural units (n.u.) are introduced, that are unique for each external trap potential (that is adapted to the simulated strong-field system). The natural units are defined by setting to unity $\hbar$, the magnetic moment μ, the atomic mass m_a, and the trap length d, which is defined by the extension of the ground-state wave function which, again, is defined as the distance where the ground-state wavefunction has decreased to 1/e of its maximum value. It is worth mentioning that having defined a complete basis (four linear independent unit quantities), the transformation of quantities between two unit systems boils down to a matrix inversion of a 4×4 matrix and a matrix-vector multiplication, see, e. g., [171].

For a given quantum simulator system the pulse parameters of the laser pulse are mapped onto the corresponding parameters for the magnetic-field gradient pulse by the following rule which is denoted as *parameter mapping*. The frequencies ω_e and ω as well as the peak vector potentials $|\mathbf{A}_0|$ and $\mathcal{A}_0$ for the strong-field and the simulator system, respectively, are determined by enforcing equal Keldysh parameters

$$\gamma_\mathrm{e} := \omega_\mathrm{e}\frac{\sqrt{2m_\mathrm{e}I_p}}{eE_0} = \omega\frac{\sqrt{2m_\mathrm{a}E_\mathrm{b}}}{\mu\mathcal{B}_0'} =: \gamma_\mathrm{a} \tag{14.12}$$

and an equal number of quanta to reach the continuum, which is expressed by equal

parameters

$$\beta_{\mathrm{e}} := \frac{I_p}{\hbar\omega_{\mathrm{e}}} = \frac{E_{\mathrm{b}}}{\hbar\omega} =: \beta_{\mathrm{a}} \quad . \tag{14.13}$$

The parameter mapping thus allows to "translate" strong-field into ultracold-atom systems and vice versa.

14.4 Experimental realizability and applicability

The most elaborate quantum simulator proposal is useless if it is impossible to be realized experimentally. Hence the experimental realizability has to be confirmed, i. e. it has to be shown that a realistic experimental setup is achievable. Second, the experimental applicability has to be verified, i. e. it has to be shown that characteristic effects in the regimes of strong-field physics can be realized within experimentally accessible parameters.

A sophisticated experimental realization of the attoscience quantum simulator is, of course, designed such that the symmetry properties of the atom or molecule under consideration are reflected appropriately. For example, in order to simulate the strong-field response of a single atom, an isotropic trap potential is chosen filled with the same number of atoms as electrons in the simulated atom. In order to simulate a molecule, a multi-well potential needs to be created in accordance with the alignment of the nuclei in the molecule relative to the laser polarization.

In order to deliver the proof-of-principle of the experimental realizability and applicability, it is convenient to extend an already existing experiment. The exceptional experimental setup described in Section 6.1 comprises all the basic ingredients needed for a first realization of the attoscience quantum simulator. In the experiment, a static magnetic-field gradient that tilts the threshold of the trap potential is applied to spill out of the trap a desired number of atoms (see Figure 6.1) to obtain a well defined, deterministically adjustable quantum system of fermionic ^{6}Li atoms in two hyperfine states. In Section 6.1 it was moreover deduced that the experiment has an anisotropy of about 1:10 and can be approximately described by a 1D system. Hence, it suffices to consider for the here presented evaluation the decoupled axial profile of the Gaussian beam of Eq. (6.1) which is given by the 1D Lorentz potential

$$U(z) = pU_0 \left[1 - \frac{1}{(1 + (z/z_r)^2}\right] \quad . \tag{14.14}$$

Here, p is introduced to accord with the experiment where it allows to effectively vary the trap depth $V_0 = pU_0$. In the experiment, the value of the waist w_0 (see

Eq. (6.1)) has been varied around 1.8 μm. Achieving values lower than this is challenging but in principle possible. A value of at least $w_0 = 0.7$ μm could be realized with a new experimental setup [172, 173]. The trap depth can at least be varied from $U_0 = 5.8\,\mathrm{k_b}\,\mu$K down to $U_0 = 3.3\,\mathrm{k_b}\,\mu$K with a p parameter in the range of 1 down to 0.01 [173].

Of course, with the chosen Lorentz potential the long-range Coulomb interaction of the nuclei and the electrons cannot be reproduced exactly. However, the choice of the parameters can be adjusted such that the energetic distribution of the low-lying bound-states resemble as accurately as possible the one of the simulated system. While for a quantum simulation of atoms an isotropic 3D potential would certainly be better suited, aspect ratios as in the present case can be found in molecular systems in, e. g., polymer chains or orbitals of delocalized linear π-electrons in carbon systems.

The attosecond-science quantum simulator based on the described experimental setup is realized by replacing the *static* magnetic-field gradient that tilts potentials continuum threshold to spill the atoms in a controlled way, see Figure 6.1, by a *periodically driven* one. Motivated by the quantum simulator proposal, the experimentalists have, in fact, build a device to dynamically vary the magnetic-field gradient [173]. This device allows for the generation of frequencies of the magnetic-field gradient in the range of about 0.01 - 500 kHz. With the realistic values of the potential specified in Table C.8, one cycle of a 450 kHz pulse has a corresponding cycle duration of a laser pulse applied to the ground-state hydrogen atom of about $0.65 \cdot 10^{-18}$ s. Hence, already a full cycle of the pulse is in the sub-attosecond regime. In fact, the ionization dynamics takes place around the pulse maximum. The effective timescales are far in the sub-attosecond regime. Such timescales are yet out of reach for attosecond science experiments. Therefore, the simulator allows for the investigation of strong-field effects beyond the possibilities in attosecond science.

14.5 Description of the pulse shapes

While the specification of a (generic) experimental realization demonstrates the experimental realizability, it has still to be demonstrated that strong-field physics is obtainable within such a setup. In order to demonstrate this applicability, the behavior of the simulator under experimentally realistic conditions is simulated by solving the time-dependent Schrödinger equation (TDSE) [2]. The adopted pulses are

[2] A comparison of the results of the TDSE solution of the 1D system also delivers a test for the assumption that the trap potential separates in the radial and the axial component as

$$U(r, z) = U(r) + U(z) \quad . \tag{14.15}$$

described in the following.

A laser pulse must fulfill the zero net-force condition, i. e. the time integral over the field strength must vanish. A magnetic field gradient pulse does not need to satisfy this condition which allows for more flexible pulse shapes, e. g., half-cycle pulses. However, in the present work, pulses are chosen that fulfill the zero net-force condition because a main goal is to validate the simulator proposal in comparison to a realistic strong-field system. For this reason, it is convenient to define the gradient pulse similar to strong-field systems via its mapped "vector potential" given in Eq. (14.9). The zero net-force condition is then satisfied by choosing a pulse for which $\boldsymbol{\mathcal{A}}(t=0) = \boldsymbol{\mathcal{A}}(t_{\mathrm{final}}) = 0$. The pulse shape is chosen as

$$\boldsymbol{\mathcal{A}}(t) = \boldsymbol{\mathcal{A}}_0 \sin\left(\frac{\omega t}{2n_{\mathrm{c}}}\right)^2 \sin(\omega t + \varphi) \tag{14.17}$$

where n_{c} is the number of cycles, φ is the carrier-envelope phase that is set to zero throughout the present work, ω the angular frequency, and $\boldsymbol{\mathcal{A}}_0$ the peak "vector potential" strength. In most situations, the experimental temporal pulse shape is not known exactly and thus has to be modeled in theory. While a $\sin^2$-pulse envelope drops to zero rapidly, a slower decrease such as for a Gaussian envelope is more realistic. For the here discussed phenomena these tail effects can, however, be neglected. Applying Eq. (14.9) leads to the expression for the magnetic-field gradient

$$\boldsymbol{\mathcal{B}}' = \boldsymbol{\mathcal{A}}_0\omega \sin\left(\frac{\omega t}{2n_{\mathrm{c}}}\right)^2 \cos(\omega t + \varphi) + \boldsymbol{\mathcal{A}}_0\omega \sin(\omega t + \varphi) \sin\left(\frac{\omega t}{2n_{\mathrm{c}}}\right) \cos\left(\frac{\omega t}{2n_{\mathrm{c}}}\right) / n_{\mathrm{c}} \quad . \tag{14.18}$$

Figure 14.2 shows the "vector potential" and the resulting gradient strength for such a pulse. The corresponding parameters for a strong-field system pulse are obtained by the parameter mapping (Section 14.3).

If the assumption is fulfilled, the 1D treatment is sufficient because the gradient is applied in the z direction and the separating potential does not couple the radial and axial motions. A system initially in an eigenstate of the potential will then stay radially in the eigenstate, the dynamics influences then only the z direction.

If, however, the trap potential supports a coupling between r and z, as is the case for a general Gaussian beam potential

$$U_{\mathrm{Gauss}} \propto \frac{1}{1 + (z/z_{\mathrm{r}})^2} \exp\left(\frac{-2r^2}{w_0^2(1 + (z/z_{\mathrm{r}})^2)}\right) \tag{14.16}$$

the time-dependent perturbation in z direction triggers also dynamics in the radial direction.

Hence, the measurement with a dynamical gradient in axial direction is also a measure for the coupling of axial and radial degrees of freedom.

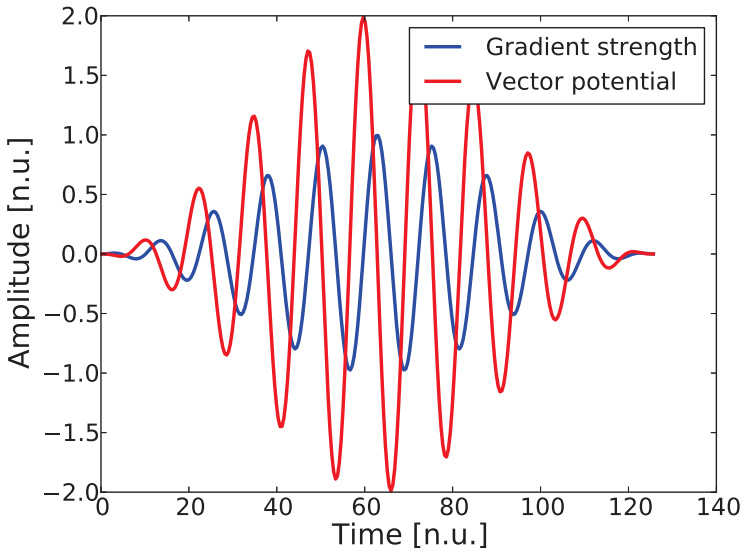

Figure 14.2: Vectorpotential and corresponding magnetic-field gradient defined by Eq. (14.17) and Eq. (14.18), respectively, for a 10-cycle pulse with $\mathcal{A}_0 = 2\,\text{n.u.}$ and $\omega = 0.5\,\text{n.u.}$

14.6 Application suggestions and limitations of the quantum simulator

After having introduced the concept of the attosecond-science quantum simulator, in the following a number of possible applications are described that can exclusively be performed with the simulator but not within strong-field experiments.

- Magnetic-field-gradient pulses, different to laser pulses do neither have to fulfill the zero-net force condition nor underlie their technical restrictions. Hence, the simulator offers complete freedom (within the validity of electromagnetism) over the pulse shapes including exotic ones like sub-cycle pulses. Noteworthy, in many theoretical works in strong-field physics an analysis is performed using artificial pulse shapes in order to obtain a better understanding. For THz radiation, a so called half-cycle pulse consists of a strongly asymmetric full-cycle pulse. With the simulator such exotic pulses can now be realized experimentally. Moreover, the pulses that can be generated with magnetic-field gradients even extend the limits of today's attosecond science experiments. As explicitly discussed in Section 14.4, pulses can be generated that formally correspond to sub-attosecond pulses.

- Studies of the influence of the interaction strength can be performed solely with

the simulator due to the possibility to tune the interaction strength between ultracold atoms.

- Only the simulator allows for experimental studies of models that otherwise were purely theoretical simplifications. For example, the experimental realization of a short-range potential becomes feasible which is the basic assumption of the widely used strong-field approximation (SFA).

- The possibility to implement various arrangements of the potential wells can be used to study the influence of the nuclear geometry on the ionization behavior [174] of molecules.

- In theoretical treatments of strong-field systems, the fixed-nuclei approximation is routinely adopted. Only with the simulator this approximation can be tested experimentally, since in a molecule the nuclei can never be fixed due to the Heisenberg uncertainty principle. Moreover, by dynamically varying the well positions in an experimental study, the differences of the quantum-mechanical nature of the vibronic states of a molecule and the simulation of a mechanical vibration of the nuclei can be performed.

- In theoretical works, models of reduced dimensionality (1D, 2D) are often adopted to reduce the complexity. These approximation can be tested experimentally with the simulator by adopting strongly anisotropic trap potentials that lead to quasi-1D and quasi-2D physics.

- The experimental control over ultracold quantum systems has reached a level where single atoms can be detected and manipulated [7, 8]. In contrast, electroneutrality restricts the arbitrary variation of number of electrons in atoms and molecules. This offers the unique opportunity to experimentally validate the widely used single-active-electron approximation by adding single atoms on demand. Moreover, the increase of correlations under the variation of the particle number and its influence on the ionization dynamics can be investigated in a fully controlled way.

On the first glance, it seems to be a major limitation that charged particles like electrons are simulated with neutral atoms. However, although the effective ranges of the interactions differ, an equivalent physics is obtainable. This was demonstrated in other quantum simulations, e. g., the famous superfluid to Mott-insulator phase transition [48]. In analogy to the Hubbard model (which is able to describe this quantum phase transition) where the tight-binding approximation limits the range of the interaction, an agreement between the ultracold-atom quantum simulator

and the atom or molecule in a laser field can be expected. At least on the level of the strong-field approximation (SFA) agreement is anticipated as the SFA is an effective short-range approximation, since the interaction of the liberated electron with the remaining system is practically neglected. Hence, short-range potentials as occurring in the simulator system, are thus even closer to this model situation than a long-range potential. The importance of the SFA for strong-field physics can hardly be overestimated. It is hence incredibly valuable to be able to validate the SFA by experimental means by, e. g., studying the influence of the effective range of the potential in the quantum simulator. Especially for many-body systems and molecular multi-center problems the validity of the SFA is completely unclear. The proposed quantum simulator paves the way to answer this and other urgent open questions.

Although the "worst-case" perspective of a SFA simulator is still delicate, the quantum simulator is expected to go beyond that which is explicitly demonstrated in this thesis for the hydrogen atom. However, also for many-electron systems the quantum simulator is expected to give accurate descriptions. While the long-range interatomic interaction scales like $1/r^6$ for neutral atoms (see Section 1.1), and with $1/r^3$ for dipolar atoms, it scales like $1/r^4$ for the atom-ion interaction, which is in functional agreement with the asymptotic interaction of an emitted electron with the remaining neutral atom. Hence, a system of trapped atoms and ions is expected to give accurate results for the strong-field quantum simulation of anions.

15 Solution of the TDSE

While a validation of the quantum simulator for a many-body system within an exact quantum-mechanical treatment is not feasible, a TDSE treatment for an effective single-particle system can be performed. For this purpose, the TDSE

$$i\frac{\partial}{\partial t}\left|\psi(t)\right\rangle = \mathcal{H}\left|\psi(t)\right\rangle \tag{15.1}$$

for the Hamiltonian $\mathcal{H}$ of Eq. (14.5) is solved by expanding the wavefunction $|\psi(t)\rangle$ in eigenstates $|\phi\rangle$ of the gradient-free Hamiltonian $\mathcal{H}_0$ of Eq. (14.6)[1].

15.1 Computation of gradient-free eigenstates

To compute the gradient-free eigenspectrum the matrix algorithm, described in [83], is adopted which is outstanding due to its extraordinary simplicity, flexibility and accuracy. As worked out in [83], the algorithm is based on a discrimination of the Hamiltonian in position and momentum space via a discrete Fourier transform. First, a one-dimensional position-space lattice is introduced consisting of an odd number of points N that are spaced equidistantly (with lattice spacing a) around the origin on an interval with length L,

$$x_k = ka, \quad k = -M, \ldots, M, \quad N = 2M + 1 \quad . \tag{15.2}$$

Spatial operators (such as the potential energy operator) become diagonal matrices, i. e. the position operator $\hat{\mathrm{x}}$ is represented as a diagonal matrix

$$\hat{\mathrm{x}}_{kl} = x_k \delta_{kl} \quad . \tag{15.3}$$

To express also the canonical conjugate momentum $\hat{\mathrm{p}}$, periodic boundary conditions, $\psi(x_k) = \psi(x_k + L)$, are introduced and a discrete Fourier transformation is

[1] While the solution for, e. g., an electron in a 1D soft-Coulomb potential exposed to a strong alternating electric field is in complete analogy, the formalism is introduced here in the notation of the simulator.

used to find that $\hat{\mathrm{p}}$ is represented by

$$\hat{\mathrm{p}}_{kl} = \frac{1}{N} \sum_p p e^{ip(x_k - x_l)} \quad . \tag{15.4}$$

where the p sum runs over the values

$$\left\{ -M\frac{2\pi}{L}, (-M-1)\frac{2\pi}{L}, \ldots, M\frac{2\pi}{L} \right\} \quad . \tag{15.5}$$

Hence the momentum operator is non-local and couples all lattice sites. For an efficient numerical treatment it is important to exploit that the sum over p can be further simplified (setting $j = i - k$) [83] to

$$(\hat{\mathrm{p}})_{ik} = \begin{cases} 0 & \text{for} \quad j = 0 \bmod N \\ \frac{\pi}{iL} \frac{(-1)^j}{\sin(\pi j/N)} & \text{else} \end{cases} , \tag{15.6}$$

$$(\hat{\mathrm{p}}^2)_{ik} = \begin{cases} \frac{\pi^2}{3a^2}(1 - a^2/L^2) & \text{for} \quad j = 0 \bmod N \\ \frac{2\pi^2}{L^2} \frac{(-1)^j \cos(\pi j/N)}{\sin^2(\pi j/N)} & \text{else} \end{cases} . \tag{15.7}$$

After having expressed the Hamiltonian in matrix form, a diagonalization leads to the eigenenergies and eigenstates of the Hamiltonian. Since the Hamiltonian matrix is hermitian and in the present case even real and symmetric the Scipy routine `scipy.linalg.eigh` was used to diagonalize the Hamiltonian matrix, which under the hood uses the Lapack routine `syerv` for real symmetric matrices or `heerv` for complex hermitian matrices.

15.2 Aspects of a discretized spectrum

The spectrum of a finite potential like, e. g., the 1D Lorentz potential studied here, in general consists of a set of discretized bound states and continuum states. Although the diagonalization procedure of the matrix algorithm only yields a discrete set of continuum states, these states can be adopted to describe the continuum accurately within the applied box-discretization. The range and distribution of energies in the continuum are determined by the box size and the number of points. An increasing point density leads to a larger maximum energy and momentum. An increasing box size increases the density of states,

$$\rho(E) = \frac{\partial N}{\partial E} \tag{15.8}$$

that is defined by the number of states per unit energy. For sufficiently dense lying continuum states the density of states can be approximated by expanding $E(N')$ in a Taylor series around $N = N'$, resulting in [175]

$$\rho(E_N) \approx \frac{2}{E_{N+1} - E_{N-1}} \quad . \tag{15.9}$$

The density of states of the continuum states is shown in Figure 15.1. Since the

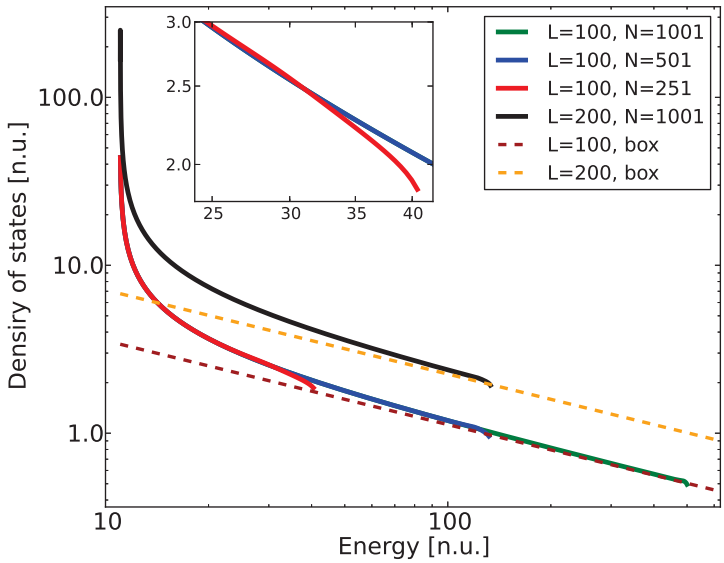

Figure 15.1: Density of states of the even continuum states of one ^{6}Li atom in the 1D Lorentz potential of Eq. (14.14) with the experimentally realizable parameters given in Table C.9. The brown and orange dashed curves correspond to a density of a box-potential discretization.

Lorentz potential is symmetric with respect to $x = 0$, the spectrum only contains states with even or odd symmetry. In Figure 15.1 the density for the even continuum states is shown. It decreases monotonically with the energy. This behavior can be understood considering a box quantization where the eigenenergies

$$E_n = \frac{\pi^2 n^2}{2L^2} \tag{15.10}$$

increase quadratically with the state index n. Applying Eq. (15.8), the density of states,

$$\rho(E) = \frac{L}{\pi\sqrt{2E}} \quad , \tag{15.11}$$

shows a monotonically decreasing behavior of the density of states with the energy as represented in Figure 15.1 by the dashed lines.

While for very large energies, the density of states of the Lorentz potential approaches the one of an atom in a box, the density has a different behavior for continuum states closer to the threshold. This can be understood intuitively since the low-energy continuum states are more affected by the underlying Lorentz potential. This also reflects in the shape of the wavefunction. For instance, the 25th

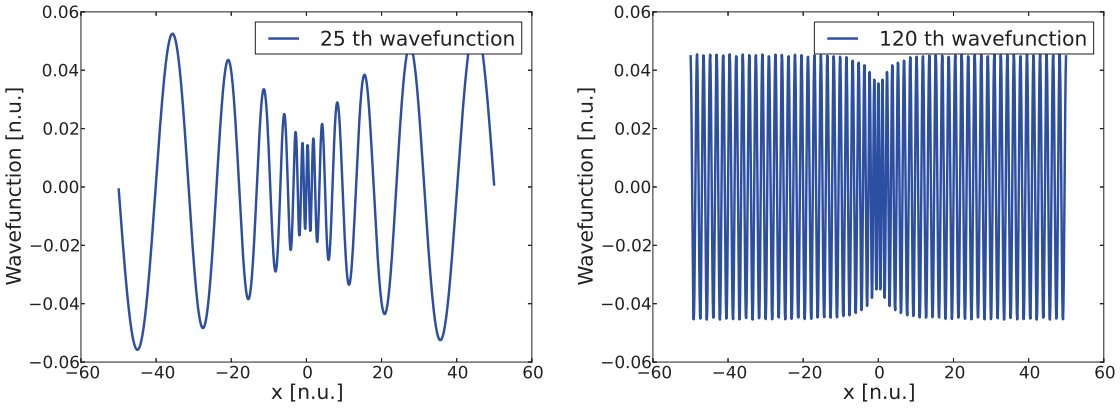

Figure 15.2: The 25th and 120th wavefunction of the Lorentz potential specified in Figure 15.1. While the 25th state is a continuum state just above the continuum threshold with $E = 11.08\,\text{n.u.}$, the 120th state has an energy of $E = 17.54\,\text{n.u.}$

wavefunction that lies just above the continuum threshold shown in Figure 15.2 is strongly affected by the underlying Lorentz potential. In the box potential, the stationary wavefunctions are given inside the box by

$$\phi_n^{(\text{box})}(x) = \sqrt{\frac{2}{L}} \sin\left(n\frac{\pi}{L}x\right) \tag{15.12}$$

and zero outside. The higher the energy, the closer the wavefunction approaches the "flat" continuum of the box as can be seen from the 120th wavefunction in Figure 15.2.

For a given continuum energy, the density of states increases with the box size in analogy to the particle in the box where $\rho(E) \propto L$. This is visible by a comparison of the blue and black lines in Figure 15.1. As visible from Figure 15.1, especially from the inset, there exists a critical energy where the density of states becomes inaccurate. This behavior is present for all basis sets. The critical energy for a given box size L can be increased by increasing the number of grid points as seen in Figure 15.1 comparing the red, blue and green curve that all have an equal box size

L. It is important that only states below the critical energy are used in the time propagation step of the solution of the TDSE.

There arises another issue when discretizing the continuum states, the so called *normalization problem* [175]. While continuum states are normalized with respect to the continuous energy and thus satisfy

$$\langle \phi_E | \phi_{E'} \rangle = \delta(E - E') \quad , \tag{15.13}$$

the discretized states stemming from a numerical diagonalization are normalized via the Kronecker delta,

$$\langle \phi_N | \phi_{N'} \rangle = \delta_{NN'} \quad . \tag{15.14}$$

Hence, if a measurable quantity is determined computationally that involves continuum states (e. g. tunneling yield, cross section, etc.) a renormalization of the final state has to be performed in order to obtain results that are comparable with an experiment. Such a renormalization can be performed using the density of states [175]. In the limit of an infinitely large box size, the discretized projection operator

$$\lim_{L\to\infty} \sum_N |\phi_N\rangle \langle \phi_N| = \int dE \, |\phi_E\rangle \langle \phi_E| \tag{15.15}$$

equals the continuous projection operator. Expanding the differential dE in the same limit leads to

$$\begin{aligned} \int dE \, |\phi_E\rangle \langle \phi_E| &= \int \frac{\partial E}{\partial N} dN \, |\phi_{E_N}\rangle \langle \phi_{E_N}| \\ &= \int \frac{1}{\rho(E_N)} dN \, |\phi_{E_N}\rangle \langle \phi_{E_N}| \\ &= \lim_{L\to\infty} \sum_{E_N} \frac{1}{\rho(E_N)} |\phi_{E_N}\rangle \langle \phi_{E_N}| \quad . \end{aligned} \tag{15.16}$$

Comparing Eq. (15.15) and Eq. (15.16) leads the renormalization description

$$|\phi_{E_N}\rangle = \sqrt{\rho_{E_N}} \, |\phi_N\rangle \tag{15.17}$$

for a conversion of a discretized state $|\phi_N\rangle$ into an energy-normalized state $|\phi_{E_N}\rangle$ with the density of states given by Eq. (15.9).

15.3 Time propagation

After the gradient-free states and a renormalization procedure for the continuum states have been introduced, it is described how the time-dependent problem can be solved using a spectral approach.

The TDSE is solved by expanding the time-dependent wavefunction $\psi(x,t)$

$$\psi(x,t) = \sum_n c_n(t)\phi_n(x) \tag{15.18}$$

in gradient-free eigenstates $\phi_n(x)$ that are obtained with the matrix algorithm. The time dependence is then solely contained in the coefficients $c_n(t)$. Substituting the expansion of Eq. (15.18) in the TDSE of Eq. (16.5), multiplying by ϕ_m^* from the right, performing an integration, and using the orthonormality of the gradient-free eigenstates $\langle\phi_n|\phi_m\rangle = \delta_{nm}$ leads to the equation

$$i\frac{\partial}{\partial t}c_m(t) = E_m c_m + \sum_n D_{m,n}c_n(t) \tag{15.19}$$

for the coefficients where $D_{m,n} = \langle\phi_m|\hat{\mathrm{D}}(x,t)|\phi_n\rangle$ is the matrix representation of the gradient operator $\hat{\mathrm{D}}(x,t) = \mu\mathcal{B}'(t)x$ of the Hamiltonian (in length gauge)[2] in the basis of gradient-free eigenstates.

Eq. (15.19) is a system of coupled first-order ordinary differential equations with complex functions $c_m(t)$. While there exist many solvers that can treat complex functions, the most efficient one for the current type of problem was found to be the routine `D02CJF` of the Numerical Algorithm Group (NAG) Fortran package. The Fortran routine was wrapped into the Python implementation of the TDSE code by the help of `F2PY`, a "Fortran to Python interface generator" [118]. To be able to use `D02CJF` which is based on a variable-order, variable-step Adams solver, the coefficient equation has to be brought into real form by splitting $c_n(t) = a_n(t) + ib_n(t)$ into its real and imaginary parts. Such a separation leads to the real coupled differential equations

$$\frac{\partial}{\partial t}a_m(t) = E_m b_m + \sum_n D_{m,n}b_n(t) \tag{15.20}$$

$$\frac{\partial}{\partial t}b_m(t) = -E_m a_m - \sum_n D_{m,n}a_n(t) \tag{15.21}$$

[2]Eq. (15.19) and its solution can be derived also in velocity gauge containing matrix elements of the momentum operator. Since the derivation is completely analogous to the one in length gauge, solely the procedure for the length gauge is presented.

that can be solved numerically using `D02CJF`.

The efficiency of the TDSE solution can be increased by taking into account the symmetry of the gradient-free eigenstates. Since the gradient-free potential is symmetric the eigenstates have either *gerade* or *ungerade* symmetry. Hence, the gradient matrix $D_{m,n} = \langle\phi_m|\hat{\mathrm{D}}(x,t)|\phi_n\rangle = \mu\mathcal{B}'(t)\,\langle\phi_m|\hat{\mathrm{x}}|\phi_n\rangle$ is only 50% filled, since $\langle\phi_m|\hat{\mathrm{x}}|\phi_n\rangle = 0$ if ϕ_n and ϕ_m have the same symmetry[3]. The sparsity of the gradient matrix can either be exploited directly in the matrix-vector-multiplication step of the TDSE propagation or, alternatively, the dipole matrix can be converted to a sparse matrix and efficient sparse linear-algebra algorithms can be used for the matrix-vector step. It has been tested that both methods are about equally efficient. Since the code with the sparse dipole matrix is more compact this version is preferred. For the sparse matrix the `scipy.sparse.csr_matrix` format is adopted, that is a standard compressed sparse row format. It has the particular advantage of efficient matrix-matrix and matrix-vector multiplication.

A quite trivial but yet crucial detail for the implementation is to exploit the dipole approximation. It offers the crucial advantage that the gradient operator $\langle\phi_m|\hat{\mathrm{D}}(x,t)|\phi_n\rangle = \mu\mathcal{B}'(t)\,\langle\phi_m|\hat{\mathrm{x}}|\phi_n\rangle$ can be obtained for each time step by multiplying the gradient for the time t with the dipole matrix $\langle\phi_m|\hat{\mathrm{x}}|\phi_n\rangle$ that has to be calculated only once.

One advantage of the spectral approach to other methods of solving the TDSE is that differential yield spectra can be obtained directly. They are very important for analyzing the tunneling behavior and can be directly extracted from the final wavefunction.

15.4 Differential yields

Besides the total ionization yield, in nowadays strong-field experiments, also differential ion yields can be measured. In general, diverse differential yields such as angle-resolved ones can be considered. In 1D, especially the energy-differential yield offers deep insides into the ionization mechanisms and, moreover, a direct comparison with the ionization amplitude of the SFA. It is thus considered for an evaluation of the quantum simulator.

To extract the tunneling amplitudes $M_{fi}(E_N)$ that provide the energy distribution of the atoms after the pulse at the final time t_f, the final state $\psi_f = \sum_{N'} c_{N'}(t_f)\phi_{N'}$

[3]The quantum mechanical rule that for a symmetric potential even and odd solutions alternate, i. e. if ϕ_n is even ϕ_{n+1} is odd, is not strictly fulfilled for numerical solutions where highly excited states are usually not fully converged. Hence, the symmetry of the basis functions must be determined "by hand". A procedure on how this is achieved is explained in Section 15.4.

must be projected on the energy renormalized basis states ϕ_{E_N}

$$\begin{aligned} M_{E_N} &= |\langle \phi_{E_N} | \psi_f \rangle|^2 \\ &= \left| \langle \sqrt{\rho(E_N)}\, \phi_N | \sum_{N'} c_{N'}(t_f)\, \phi_{N'} \rangle \right|^2 \\ &= \left| \sum_{N'} c_{N'}(t_f)\, \sqrt{\rho(E_N)}\, \langle \phi_N | \phi_{N'} \rangle \right|^2 \\ &= |c_N(t_f)|^2\, \rho(E_N) \quad . \end{aligned} \tag{15.22}$$

Hence, the amplitude for E_N is just given by the square of the coefficient c_N obtained from the TDSE solution times the density of states given by Eq. (15.9). In order to obtain a differential atom-yield spectrum, i. e. a spectrum of the kinetic energy distribution of the escaped atoms, first all amplitudes have to be calculated for each symmetry separately. After that, the amplitudes for the even and odd symmetry must be interpolated to obtain a function of energy. Then these functions can be added to give the final spectrum. The density of states is in most cases such high that a simple linear interpolation is sufficient. Otherwise best results were achieved using piecewise cubic Hermite interpolating polynomials via the `PCHIP` algorithm [176].

To be able to process the symmetries separately, each eigenstate has to be classified by its symmetry. Odd eigenfunctions fulfill $\phi_k^{\mathrm{odd}}(-x) = -\phi_k^{\mathrm{odd}}(x)$. To prevent that accidentally a zero of the wavefunction ϕ_l is used for the symmetry check, the value $x_{\max} > 0$ where $|\phi_l|$ has its maximum is chosen to evaluate the wavefunction. Then the sign of the product $\phi_l(-x_{\max})\phi_l(x_{\max})$ reflects whether ϕ_l is even or odd.

Based on the differential yield spectra it was confirmed for a selected number of pulse parameters that converged results of the TDSE solution in length and velocity gauge are in total agreement. However, it was found that convergence in velocity gauge can be achieved with significantly smaller box sizes and consequently with a smaller number of grid points. Hence, the TDSE solution in velocity gauge including the "artificial" vectorpotential of Eq. (14.9) is favorable.

16 Solution of the SFA

The impact of the SFA [177–179] on the advancement of strong-field physics is enormous. It is nowadays considered the most successful approximation to non-perturbatively treat strong-field ionization of atoms and molecules. The basic concept of the SFA is to ignore bound states of the potential other than the initial state and to replace the final continuum state by a Volkov state, i. e. the solution of a free electron in a laser field. Therefore, the interaction of the electron with the remaining ion is ignored in the final state. This principle is shared between all formulations of the SFA that exist in length gauge [177], velocity gauge [178, 179] or even generalized gauges [180]. The transition amplitudes can differ in different gauges and no arguments from first principles exist so far under which conditions which gauge is superior, known as the *gauge problem*. The SFA can be derived by a truncation of the infinite expansion of the S matrix that exactly describes the interaction of an atom or molecule with a laser pulse. The S-matrix description is exact and hence gauge independent. The gauge dependence is introduced by the truncation that leads to the SFA. Additionally to the different gauge versions of the SFA, further approximations are commonly used that lead to (in some cases only minor) differences in the result even in the same gauge, such as the method of steepest descent or infinite-pulse approximations. Since the SFA is an effective short-range approximation (the interaction of the escaped electron with the remaining ion is ignored) the assumptions of the SFA are better fulfilled for the simulator system. Moreover, also the number of trap states can be varied which allows for an experimental test of the assumption of the SFA to exclude bound states other than the initial state. Before the SFA is evaluated for the quantum-simulator system, it is introduced first.

16.1 Derivation of the SFA

The SFA is an approximation to evaluate the amplitude

$$M_{\mathbf{p}} = \lim_{t\to\infty} \lim_{t'\to-\infty} \langle \phi_{\mathbf{p}}(t)|U(t,t')|\phi_{\mathrm{b}}(t')\rangle \tag{16.1}$$

of the transition of an initial bound state $|\phi_{\mathrm{b}}(t)\rangle$ of the binding potential that evolves in time in the presence of a laser field, the propagation being described by the time-

evolution operator $U(t,t')$, into a final continuum state $|\phi_{\mathbf{p}}(t)\rangle$ with momentum $\mathbf{p}$. The initial and final states $|\phi_{\mathrm{b}}(t)\rangle$ and $|\phi_{\mathbf{p}}(t)\rangle$, respectively, are eigenstates of the gradient-free Hamiltonian H_0 which together with the potential V that describes the interaction with the laser field build the total Hamiltonian $H(t) = H_0 + V$ as given in Eq. (14.1). The time-evolution operator $U(t,t')$ of the total Hamiltonian H and $U_0(t,t')$ for the field-free Hamiltonian H_0 are defined by

$$\left[i\frac{\partial}{\partial t} - H\right] U(t,t') = 0, \quad U(t,t) = \mathbb{1} \tag{16.2}$$

$$\left[i\frac{\partial}{\partial t} - H_0\right] U_0(t,t') = 0, \quad U_0(t,t) = \mathbb{1} \quad . \tag{16.3}$$

Hence, $U(t,t')$ and $U_0(t,t')$ describe the time evolution

$$|\psi(t)\rangle = U(t,t')\,|\psi(t')\rangle\,, \quad |\phi(t)\rangle = U_0(t,t')\,|\phi(t')\rangle \tag{16.4}$$

of a perturbed and unperturbed wavefunction $\psi(t')$ and $\phi(t')$ at t', respectively, determined by the TDSE

$$i\frac{\partial}{\partial t}\,|\psi(t)\rangle = H(t)\,|\psi(t)\rangle \quad . \tag{16.5}$$

Of course, the time evolution of field-free eigenstates is given by

$$\phi_n(t) = \phi_n(t')\exp(iE_n/\hbar(t-t')) \quad . \tag{16.6}$$

Making use of the Dyson equation [181]

$$U(t,t') = U_0(t,t') - i\int_{t'}^{t} d\tau U(t,\tau)V(\tau)U_0(\tau,t') \tag{16.7}$$

and the assumption that the pulse vanishes ($V(t) = 0$) for $t \to -\infty$ such that $\psi(-\infty) = \phi(-\infty)$ the time evolved state

$$|\psi(t)\rangle = |\phi(t)\rangle - i\int_{-\infty}^{t} d\tau U(t,\tau)V(\tau)\,|\phi(\tau)\rangle \tag{16.8}$$

can be used to rewrite the transition amplitude

$$M_{\mathbf{p}} = -i\lim_{t\to\infty}\int_{-\infty}^{t} d\tau\,\langle\phi_{\mathbf{p}}(t)|U(t,\tau)V(\tau)|\phi_{\mathrm{b}}(\tau)\rangle \quad . \tag{16.9}$$

Until now, no approximations were performed such that Eq. (16.9) is exact within non-relativistic quantum mechanics. The approximations that lead to Keldysh's result are nowadays known as strong-field approximation and summarized in, e. g., [182]. First, the full propagator $U(t,t')$ is replaced by the one of a free particle in a laser field (magnetic-field gradient) $U_{\mathrm{V}}(t,t')$, known as the Volkov propagator, satisfying

$$\left[i\frac{\partial}{\partial t} - H_{\mathrm{V}}(t)\right] U_{\mathrm{V}}(t,t') = 0, \quad H_{\mathrm{V}}(t) = -\frac{1}{2}\nabla^2 + V(t) \quad . \tag{16.10}$$

The Volkov propagator

$$U_{\mathrm{V}}(t,t') = \int d^3\mathbf{k}\, |\chi_{\mathrm{V},\mathbf{k}}(t)\rangle \langle\chi_{\mathrm{V},\mathbf{k}}(t')| \tag{16.11}$$

can be decomposed in Volkov states $|\chi_{\mathrm{V},\mathbf{k}}(t)\rangle$ that are solutions of the TDSE with the Hamiltonian $H_{\mathrm{V}}(t)$ from Eq. (16.10). Moreover, the final continuum state $|\phi_{\mathbf{p}}\rangle$ which is a solution of the field-free Hamiltonian H_0 and hence represents a "non-flat" continuum state that is influenced by the binding potential, is replaced by a plane wave $|\phi_{\mathbf{p}}(t)\rangle$ with momentum $\mathbf{p}$ such that

$$\langle\psi_{\mathbf{p}}(t)|\, U_{\mathrm{V}}(t,\tau) \approx \langle\phi_{\mathbf{p}}(t)|\, U_{\mathrm{V}}(t,\tau) = \langle\chi_{\mathrm{V},\mathbf{p}}(t)| \quad . \tag{16.12}$$

Hence, in the SFA bound states of the potential other than the initial state are ignored, and the influence of the binding potential as well as the one of other electrons on the final continuum state is neglected. The SFA transition amplitude becomes

$$M_{\mathbf{p}} = -i\int_{-\infty}^{\infty} d\tau\, \langle\chi_{\mathrm{V},\mathbf{p}}(\tau)|V(\tau)|\phi_{\mathrm{b}}(\tau)\rangle \quad . \tag{16.13}$$

For a finite pulse, that starts at $t = 0$ and ends at $t = t_f$, the final expression for the transition amplitude in SFA becomes

$$M_{\mathbf{p}} = -i\int_{0}^{t_f} d\tau\, \langle\chi_{\mathrm{V},\tilde{\mathbf{p}}}(\tau)|V(\tau)|\phi_{\mathrm{b}}(\tau)\rangle \tag{16.14}$$

where the Volkov wavefunction has the momentum [164]

$$\tilde{\mathbf{p}} = \mathbf{p} - \mathbf{A}(t_f) \tag{16.15}$$

which is a result of the orthogonality of plane waves and the fact that the vectorpotential $\mathbf{A}$ is not necessarily zero after the pulse. In the present work, however, the SFA is only evaluated in situations where the vectorpotential is zero at the beginning

and end of the pulse as described in Section 14.5.

16.2 Introduction of the gauge

The SFA transition amplitude Eq. (16.14) is still general and valid for any gauge. However, depending on choosing a certain gauge the amplitude takes different specific forms. As demonstrated in Section 13.2, the interaction potential V describing the laser-matter interaction depends on the gauge and so does the form of the Volkov state. The Volkov wavefunction in length gauge (and dipole approximation)

$$\chi^{\mathrm{LG}}_{\mathrm{V},\mathbf{p}}(\mathbf{r},t) = \exp\left(i\mathbf{r}\cdot\boldsymbol{\pi}(t) - iS(t)\right) \tag{16.16}$$

satisfies the TDSE of Eq. (16.10) with the radiation interaction potential $V(\mathbf{r},t) = \mathbf{E}(t)\cdot\mathbf{r}$ in length gauge. In Eq. (16.16)

$$\boldsymbol{\pi}(t) = \mathbf{p} + \mathbf{A}(t) \tag{16.17}$$

is the mechanical momentum and

$$S_{\mathbf{p}}(t) = \frac{1}{2}\int_0^t dt' \boldsymbol{\pi}(t')^2 \tag{16.18}$$

is the classical action. Inserting these expressions in the amplitude Eq. (16.14) leads to

$$\begin{aligned} M^{\mathrm{LG}}_{\mathbf{p}} &= -i\int_0^{t_f} dt\ \langle\chi^{\mathrm{LG}}_{\mathrm{V},\mathbf{p}}(\mathbf{r},t)|\mathbf{r}\cdot\mathbf{E}(t)|\phi_b(\mathbf{r},t)\rangle \\ &= -i\int_0^{t_f} dt\ \int d^3r\ \chi^{\mathrm{LG}}_{\mathrm{V},\mathbf{p}}(\mathbf{r},t)\,\mathbf{r}\cdot\mathbf{E}(t)\,\phi_b(\mathbf{r})\mathrm{e}^{iE_bt} \\ &= -i\int_0^{t_f} dt\ e^{i(S_{\mathbf{p}}(t)+E_bt)}\int d^3r\mathrm{e}^{-i\boldsymbol{\pi}\cdot\mathbf{r}}\mathbf{E}(t)\cdot\mathbf{r}\phi_b(\mathbf{r}) \\ &= \int_0^{t_f} dt\ e^{i(S_{\mathbf{p}}(t)+E_bt)}\,\mathbf{E}(t)\cdot\nabla_{\boldsymbol{\pi}(t)}\tilde{\phi}_b(\boldsymbol{\pi}(t)) \end{aligned} \tag{16.19}$$

with the Fourier transform of the initial state $\tilde{\phi}_b$ and the binding energy E_b of the initial bound state ϕ_b. While Eq. (16.19) is already suitable to perform numerical calculations, it can be further simplified to [164]

$$M^{\mathrm{LG}}_{\mathbf{p}} = i\int_0^{t_f} dt\ e^{i(S_{\mathbf{p}}(t)+E_bt)}\left(\frac{dS_{\mathbf{p}}}{dt}+E_b\right)\tilde{\phi}_b(\boldsymbol{\pi}(t)) - \left[\tilde{\phi}_b(\boldsymbol{\pi}(t))e^{i(S_{\mathbf{p}}(t)+E_bt}\right]_0^{t_f} \tag{16.20}$$

by assuming that the vector potential before and after the pulse is equal, $\mathbf{A}(0) = \mathbf{A}(t_f)$. In order to obtain Eq. (16.20) an integration by parts has to be performed and the equation

$$\left(\mathbf{r}\cdot\mathbf{E}(t) + i\frac{\partial}{\partial t}\right)\mathrm{e}^{-i\boldsymbol{\pi}(t)\cdot\mathbf{r}} = 0 \tag{16.21}$$

needs to be adopted. Of course, the derivative of the action is given by $dS_{\mathbf{p}}/dt = \boldsymbol{\pi}(t)^2$. Eq. (16.20) is the one that can be implemented numerically most efficiently, since different to Eq. (16.19) the Fourier transform is used and the derivative has not to be computed.

In velocity gauge, the Volkov wavefunction

$$\chi^{\mathrm{VG}}_{\mathrm{V},\mathbf{p}}(\mathbf{r},t) = \exp\left(i\mathbf{r}\cdot\mathbf{p} - iS_{\mathbf{p}}(t)\right) \tag{16.22}$$

is a solution of the TDSE of Eq. (16.10) with the radiation interaction potential $V(\mathbf{r},t) = \mathbf{p}\cdot\mathbf{A}(t) + \frac{1}{2}\mathbf{A}(t)^2$ in velocity gauge. Inserting these expressions in the amplitude Eq. (16.14) leads to

$$\begin{aligned} M^{\mathrm{VG}}_{\mathbf{p}} &= -i\int_0^{t_f} dt\ \langle\chi^{\mathrm{VG}}_{\mathrm{V},\mathbf{p}}(\mathbf{r},t)|\mathbf{p}\cdot\mathbf{A}(t) + \frac{1}{2}\mathbf{A}(t)^2|\phi_b(\mathbf{r},t)\rangle \\ &= -i\int_0^{t_f} dt\ \int d^3r\ \chi^{\mathrm{VG}}_{\mathrm{V},\mathbf{p}}(\mathbf{r},t)\ \left[\mathbf{p}\cdot\mathbf{A}(t) + \frac{1}{2}\mathbf{A}(t)^2\right]\ \phi_b(\mathbf{r})\mathrm{e}^{iE_bt} \\ &= -i\tilde{\phi}_b(\mathbf{p})\int_0^{t_f} dt\ e^{i(S_{\mathbf{p}}(t)+E_bt)}\ \left[\mathbf{p}\cdot\mathbf{A}(t) + \frac{1}{2}\mathbf{A}(t)^2\right] \quad . \end{aligned} \tag{16.23}$$

For both gauges, the computational difficulty of calculating SFA amplitudes is the integration of the term $\exp\{i(S_{\mathbf{p}}(t) + E_bt)\}$. The action itself contains an integral and since the mechanical momentum and the binding energy are real quantities, this term is an extremely oscillatory function in time. The numerical integration of such functions is very challenging and it has been found that standard quadrature routines such as contained in the Fortran package `QUADPACK` can quickly loose precision and give erroneous results. To solve the issue several numerical approaches have been tested such as an adapted quadrature scheme proposed by Evans and Webster [183]. Finally, the most reliable integrator was found to be the `D01AKF` routine of the NAG FORTRAN package. It is an adaptive integrator, especially suited for highly oscillatory, though non-singular integrands, such as $\exp i(S_{\mathbf{p}}(t) + E_bt)$. It is based on the `QUADPACK` routine `QAG` and uses the high order Gauss 30-point and Kronrod 61-point rules. Despite the suitability for strongly oscillatory functions, as will be seen, even this method can loose accuracy in some cases and has hence to be handled with care.

Finally, the SFA expressions in natural units for the quantum simulator are obtained from the given expressions in atomic units for strong-field systems by simply exchanging the field-related quantities as prescribed by the simulator mapping Eq. (14.8), i. e. the simulator expressions can be obtained by replacing $\mathbf{E}$ by $\mathcal{B}'$ and $\mathbf{A}$ by $\mathcal{A}$. Of course, the initial-state wavefunctions must be adapted for the simulator potential.

16.3 Method of steepest descend

An approximate approach to tackle strongly oscillatory integrands is the application of the *method of steepest descent*. It will turn out that the application of this method is in the adiabatic regime essential to obtain accurate SFA results for the simulator. Application of this method on the SFA transition amplitude in length gauge, Eq. (16.19), leads to the saddle-point formula [184]

$$M_{\mathbf{p}}^{\mathrm{SPLG}} = -i \sum_s \sqrt{\left[\frac{2\pi i}{\mathbf{E}(t_s)\cdot\boldsymbol{\pi}(t_s)}\right]} \langle \boldsymbol{\pi}(t_s)|\mathbf{r}\cdot\mathbf{E}(t_s)|\phi_b(\mathbf{r})\rangle \, e^{i(S_{\mathbf{p}}(t_s)+E_b t_s)} \tag{16.24}$$

where the summation runs over the saddle points $t = t_s$ with $0 < \mathrm{Re}\, t_s < t_f$ and $\mathrm{Im}\, t_s > 0$ that fulfill [184]

$$\frac{\partial(S_{\mathbf{p}} + E_b t)}{\partial t} = E_b + \frac{1}{2}\boldsymbol{\pi}(t)^2 = 0 \quad . \tag{16.25}$$

The saddle points t_s are in general complex, such that also the field $\mathbf{A}(t_s)$ and the mechanical momentum $\boldsymbol{\pi}(t_s)$ become complex. Separating the mechanical momentum in its real and imaginary parts $\boldsymbol{\pi} = \mathrm{Re}\,\boldsymbol{\pi} + i\mathrm{Im}\,\boldsymbol{\pi}$ leads to

$$\begin{aligned} M_{\mathbf{p}}^{\mathrm{SPLG}} = -i \sum_s \sqrt{\left[\frac{2\pi i}{\mathbf{E}(t_s)\cdot\boldsymbol{\pi}(t_s)}\right]} e^{i(S_{\mathbf{p}}(t_s)+E_b t_s)} \, \mathbf{E}(t_s)\cdot \\ \int d^3r \, \mathbf{r} \, \mathrm{e}^{\mathrm{Im}\,\boldsymbol{\pi}(t_s)\cdot\mathbf{r}} \, \phi_b(\mathbf{r}) \, [\cos(\mathrm{Re}\,\boldsymbol{\pi}\cdot\mathbf{r}) - i\sin(\mathrm{Re}\,\boldsymbol{\pi}\cdot\mathbf{r})] \quad . \end{aligned} \tag{16.26}$$

Eq. (16.26) involves the evaluation of the action

$$\tilde{S}_{\mathbf{p}}(t_s) = \int_0^{t_s} dt \, \tilde{S}'_{\mathbf{p}}(t) = \int_0^{t_s} dt \, \frac{1}{2}\boldsymbol{\pi}(t)^2 + E_b \tag{16.27}$$

in the complex plane. A contour C from 0 to t_s that is split in two contours $C = C_1 + C_2$ is adopted where C_1 is parametrized as

$$\begin{aligned} \alpha_1 : [0, \operatorname{Re} t_s] &\to \mathbb{C} \\ t &\mapsto t + 0i \end{aligned} \tag{16.28}$$

and C_2 is parametrized as

$$\begin{aligned} \alpha_2 : [0, \operatorname{Im} t_s] &\to \mathbb{C} \\ t &\mapsto \operatorname{Re} t_s + it \quad . \end{aligned} \tag{16.29}$$

The action is then evaluated as

$$\int_0^{t_s} dt\, \tilde{S}'_{\mathbf{p}}(t) = \int_0^{\operatorname{Re} t_s} dt\, \tilde{S}'_{\mathbf{p}}(\alpha_1(t)) + i \int_0^{\operatorname{Im} t_s} dt\, \tilde{S}'_{\mathbf{p}}(\alpha_2(t)) \tag{16.30}$$

The saddle points for the simulator potential are not known analytically. Hence, a numerical root finding of the saddle points in the complex plane has to be performed. Root finding in higher dimensions is in general numerically very challenging. It is highly non-trivial to find all the roots of a function or resolve closely spaced ones. In the present situation it is crucial to exploit the constraint given in [164] which states that for linear polarized light $2(n_\mathrm{c} + 1)$ and for circular polarized radiation $(n_\mathrm{c} + 1)$ saddle points t_s exist that fulfill $0 < \operatorname{Re} t_s < t_f$ and $\operatorname{Im} t_s > 0$ where n_c is the number of optical cycles of the pulse. The algorithm developed to find all saddle points is the following: MINPACK's `HYBRD` root finding algorithm via `scipy.optimize.fsolve` is adopted that uses a modification of the Powell hybrid method to find a zero of a system of N non-linear functions in N variables given an initial value $t_0 \in \mathbb{C}$. In order to use `HYBRD`, the left hand side of the complex equation given in Eq. (16.25) has to be rewritten as a function that maps from $\mathbb{R}^2$ to $\mathbb{R}^2$. Since the algorithm produces only a single root per initial value, the initial values are sampled randomly over the region $0 < \operatorname{Re} t_s < t_f$ and $\operatorname{Im} t_s > 0$ where $t_f \in \mathbb{R}$ is the real final time of the pulse. Since this region is not bounded, the sampling is done in cycles. In each cycle $c \in \mathbb{N}$, $c > 0$ a number of b^c initial points t_0 are seeded that are distributed randomly in the region $0 < \operatorname{Re} t_0 < t_f$ and $0 < \operatorname{Im} t_0 < c t_f$. This sampling ensures that the total number of initial points increases in density for small $\operatorname{Im} t_0$ and that $\max(\operatorname{Im} t_0)$ gets larger with each cycle. The sampling is performed until all saddle points are found. For a value of $b = 100$, the algorithm typically requires only a few (most of the time one or two) cycles.

16.4 SFA for the hydrogen atom

In order to verify the correctness of the implementation, tests have been performed. For example, the SFA results were compared to the one in [181] adopting a zero-range potential and to [185] in case of a hydrogen atom. Since the SFA for the hydrogen atom will be considered in detail, it is briefly outlined. The Fourier transform

$$\tilde{\phi}_{\mathrm{b,H}}(\mathbf{p}) = \frac{8\sqrt{\pi}}{\kappa^{3/2}} \sum_{k=0}^{n-1} (-1)^k \, 2^{2k} \, C_{2k+1}^{n+k} \left(\frac{\kappa^2}{\mathbf{p}^2 + \kappa^2} \right)^{k+2} \tag{16.31}$$

of the nS state of the hydrogen atom with principle quantum number n is known [185] analytically. In Eq. (16.31), C_k^n are binomial coefficients, $\kappa = \sqrt{2E_\mathrm{b}}$ where E_b is the binding energy.

For an *infinite* pulse the integrated term of the integration by parts in Eq. (16.20) can be neglected. Assuming the radiation is described by $\mathbf{E}(t) = \mathbf{E}_0 \cos(\omega t)$ the amplitude Eq. (16.20) simplifies to [181]

$$-\frac{1}{T} \int_0^T dt \; e^{i(S_\mathbf{p}(t) + E_b t)} \left(\frac{dS_\mathbf{p}}{dt} + E_b \right) \tilde{\phi}_b(\boldsymbol{\pi}(t)) \tag{16.32}$$

where $T = 2\pi/\omega$. It should be emphasized that the total ionization rate Γ, i. e. the absolute square of the momentum integral over all amplitudes $M_\mathbf{p}$, simplifies for an infinite pulse to the sum [185]

$$\Gamma = \frac{1}{(2\pi)^2} \pi \int d^3p \, |M_\mathbf{p}|^2 \sum_{n \geq n_0} \delta(E_\mathrm{b} + \frac{p^2}{2} + U_p - n\omega) \tag{16.33}$$

over n-photon processes, i. e. over all n-photon processes where n_0 is the minimum number of photons required to reach the continuum. In Table 16.1 the results of

n	SFA amplitude A_ex, Eq. (8) of [185]	SFA amplitude of Eq. (16.20)
1	$(-1.406 + 3.368i) \cdot 10^{-8}$	$(-1.406106 + 3.367756i) \cdot 10^{-8}$
2	$(1.429 - 3.423i) \cdot 10^{-7}$	$(1.429131 - 3.422904i) \cdot 10^{-7}$
3	$(-1.039 + 2.489i) \cdot 10^{-6}$	$(-1.039151 + 2.488866i) \cdot 10^{-6}$

Table 16.1: Comparison of the length gauge SFA amplitude of [185] with the implementation used in the present thesis for a hydrogen atom in the nS state for $|\mathbf{E}| = 0.02$ a.u., $\omega = 0.01$ a.u., $\mathbf{E} \cdot \mathbf{p} = 0.9$ and $n_\mathrm{ph} = 161$. The results agree quantitatively.

the length-gauge SFA implementation of Eq. (16.20) are compared with the values

provided in [185]. Perfect quantitative agreement is obtained[1]. Note, the absolute value of the momentum $\mathbf{p}$ is obtained from n_{ph} by the conservation of energy

$$|\mathbf{p}| = \sqrt{2\left(n_{\mathrm{ph}}\omega - E_{\mathrm{b}} - U_p\right)} \tag{16.34}$$

where U_p is the ponderomotive energy. It has been confirmed that also the results for $n = 4$ and $n = 5$ agree.

After having introduced the method to solve the TDSE in the previous chapter and the one for the SFA in this chapter, all the tools are introduced that allow for a thorough validation of the quantum simulator.

[1]Note, in [185] the real part of the amplitude has the opposite sign than specified in Table 16.1. However, in [185] this results from a definition of the sign of the charge that is inconsistent with the definition of the mechanical momentum and is hence incorrect. Yet, considering the absolute square of the transition amplitude which is relevant for, e. g., photo-electron spectra, cancels the opposite sign.

17 Validation of the quantum simulator

In Chapter 17, the quantum simulator is validated in terms of differential yields. It is demonstrated that strong-field physics in different regimes of the laser-matter interaction is reproduced within experimentally accessible parameters. For the direct comparison, a strong-field system has to be taken into account that can be handled numerically. Here, the theoretically perhaps most studied system is consulted, the hydrogen atom. Moreover, it will be investigated how the SFA behaves in the simulator system. All the TDSE and SFA calculations presented in this thesis were performed by the author except for the 3D TDSE calculations of the hydrogen atom that were all performed by Johann Förster with an by him optimized implementation that was initially developed by Yulian Vanne.

For the following considerations, a simulator setup is chosen with trap parameters (and conversion constants) specified in the appendix in Table C.7. As pointed out in Section 14.4, these parameters are experimentally accessible.

In the experiment the quantum simulator proposal is based on [8] (see also Section 6.1), the number of trapped atoms can be measured to high precision. Hence, also the atom loss can be measured indirectly with high precision which corresponds to a measurement of the total ion or electron yield in strong-field experiments. While in the early years of strong-field experiments, only total yields could be extracted, experimental and technical progress allows nowadays also for a measurement of differential, energy-resolved yields. Although the measurement of differential yields requires still further developments, these spectra are considered for evaluating the simulator since they deliver detailed information on the underlying physics.

17.1 Multiphoton regime

First, the multiphoton regime is considered that was briefly described in Section 13.1. In Figure 17.1 the energy-resolved spectra resulting from converged TDSE solutions for the 3D hydrogen atom and the simulator system are shown. For the given pulse parameters, the Keldysh parameter is $\gamma = 2.02$ and in order to reach the continuum two quanta of the field need to be absorbed ($\beta = 1.77$). In comparison to the frequency of the laser light ($\nu = 1.17 \cdot 10^{16}\,\mathrm{Hz}$), the frequency of the magnetic-field gradient ($\nu = 413\,\mathrm{Hz}$) is 14(!) orders of magnitude lower. For a gradient with such a slow frequency a photon picture is certainly not usual. However, on

the time scale of the system the gradient changes are still as fast as indicated by $\gamma = 2.02$. This demonstrates nicely that a periodic driving of the system is sufficient to obtain a spectrum usually explained in terms of a photon absorption picture. In fact, the explanation in strong-field system does also not require quantized fields because the number of photons is such high that the absorption and emission of single photons is negligible. Figure 17.1 shows indisputably that the simulator reproduces

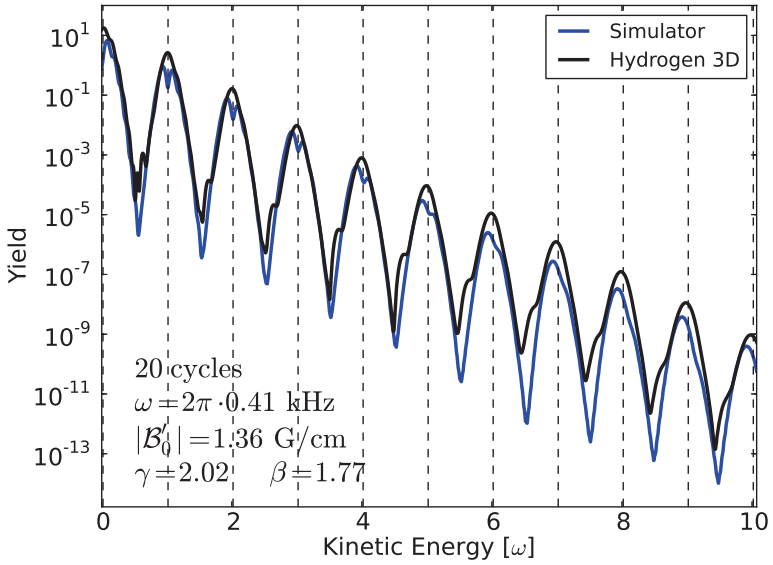

Figure 17.1: Energy-resolved spectra for the simulator and the 3D hydrogen atom from TDSE calculations in the multiphoton regime. The dashed vertical lines indicate the positions of the multiphoton peaks for an infinitely long pulse as expected from the subsequent absorption of field quanta. The magnetic-field gradient parameters in S.I. based units are given in the plot. The corresponding pulse parameters for the 20-cycle laser pulse are $\lambda = 160.4\,\mathrm{nm}$ and $I = 6.85 \cdot 10^{14}\,\mathrm{W/cm^2}$. Converged results for the simulator (hydrogen atom) were obtained with the basis set specified in Table C.1 (Table C.2).

the typical multi-peak structure (above-threshold-ionization peaks) where the peak distance reflects the frequency of the perturbing field. For the given parameters, the simulator and the hydrogen atom show very good agreement. Despite the different dimensionalities the TDSE solutions agree even quantitatively.

In order to investigate more carefully the influence of the dimensionality, the 1D solution of the hydrogen atom, i. e. the *soft*-Coulomb potential (in atomic units)

$$V(z) = -\frac{1}{\sqrt{2 + z^2}} \tag{17.1}$$

is considered. In agreement with the 3D Coulomb potential, it has an ionization potential for the ground state of $I_p = 0.5$ a.u. and a long-range behavior of $V(z) \approx -1/z$ for $z \gg 1$.

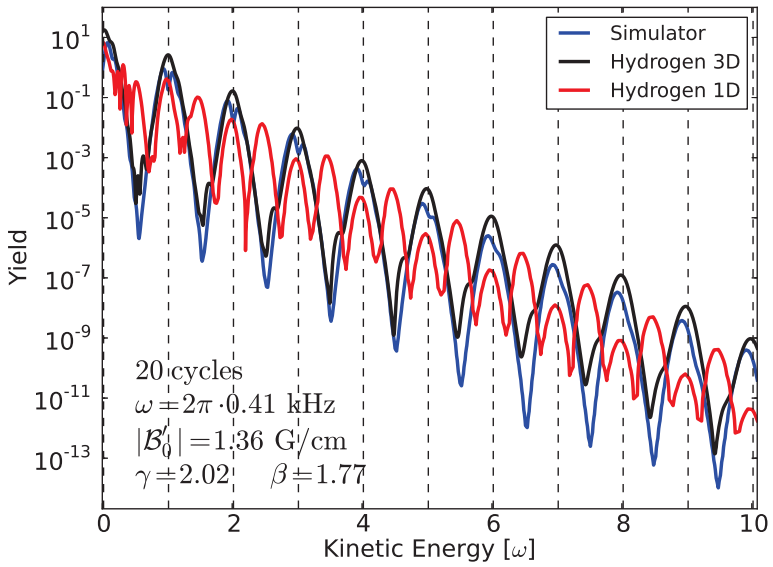

Figure 17.2: Same as Figure 17.1 but together with the 1D solution of the soft-Coulomb potential. Converged results for the soft-Coulomb potential were obtained with the basis set specified in Table C.3.

Figure 17.2 shows differential yields identical to the Figure 17.1 but together with the 1D hydrogen results. Compared to the spectra of the 3D hydrogen atom and the simulator that agree up to small-scale structures very well, the 1D hydrogen solution shows also structures besides the "multiphoton" peaks. Such a behavior is known from the transition to the quasi-static regime, where the multipeak structure disappears and a chaotic structure dominates. Another reason can be resonances. In fact, a view on the bound-state distributions in Figure 17.3 demonstrates that for the soft-Coulomb potential the first excited state is indeed close in energy to the first photon absorption of the ground state marked as red dashed horizontal line. Such a resonance is not present for the simulator system as also visible in Figure 17.3 where the first absorption energy lies in the gap region of the ground and first excited bound state. As a consequence, a second peak structure in between the main absorption peaks appears for the 1D *soft*-Coulomb potential that reflects the resonantly-enhanced multiphoton ionization from the resonantly populated first excited bound state.

In fact, if the Keldysh parameter is increased to reach further into the multiphoton regime with an excitation that is non-resonant, the typical peak structure is restored for the 1D soft-Coulomb potential as can be seen in Figure 17.4. While the peak

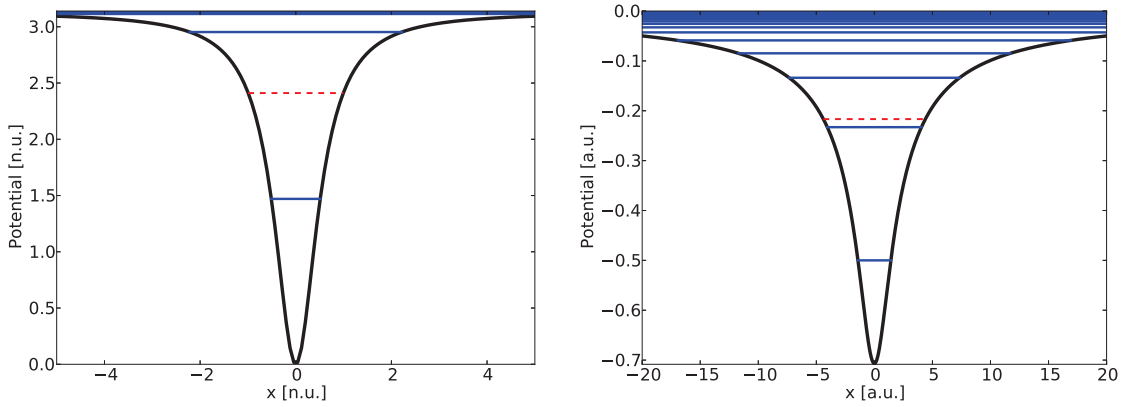

Figure 17.3: The trapping potential (black), the bound state energies (blue) and the excitation energies (red dashed) for $\omega = 0.94\,\text{n.u.}$ ($\omega_\text{e} = 0.283\,\text{a.u.}$) from the ground state for the quantum simulator (soft-Coulomb potential) on the left (right). The Lorentz potential of the simulator is specified by the parameters provided in Table C.7.

amplitude of the 1D hydrogen matches with the 3D hydrogen for the first four peaks, for the remaining peaks it agrees more with the simulator. The simulator peaks show almost a constant offset to smaller values compared to the 3D hydrogen atom. It should be also noted that the total yield (i. e. 0.89 in Figure 17.1 and 0.00033 in Figure 17.4 for the simulator) decreases with the gradient strength and the frequency. Moreover, the position of the multiphoton peaks is not constant, because their position is determined by the energy conservation $n_\text{ph}\omega - E_\text{b} - U_p$, and hence depends on U_p which itself depends on the gradient strength and the frequency.

To summarize, it is possible to recover the characteristic features of strong-field ionization in the multiphoton regime with ultracold atoms in a periodically varying magnetic field, whereas the slowdown of the processes is up to 14 orders of magnitude. Very importantly, such systems are experimentally realizable. This is truly remarkable.

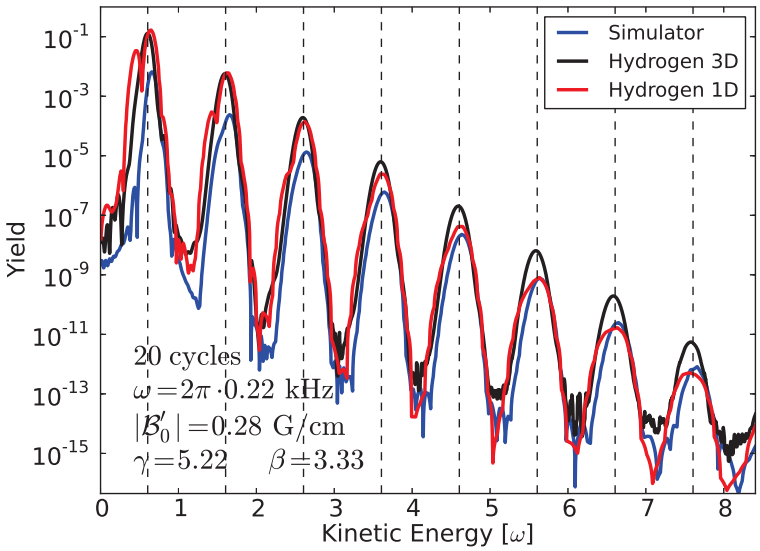

Figure 17.4: Energy-resolved spectra for the simulator, the 1D and 3D hydrogen atom obtained by the solution of the TDSE. The dashed vertical lines indicate the positions of the multiphoton peaks for an infinitely long pulse as expected from the subsequent absorption of field quanta. The magnetic-field gradient parameters in S.I. based units are given in the plot. The corresponding pulse parameters for the 20-cycle laser pulse are $\lambda = 302.95\,\mathrm{nm}$ and $I = 2.89 \cdot 10^{13}\,\mathrm{W/cm^2}$. The basis sets specified in Table C.1,Table C.2, and Table C.3 were used.

17.2 Quasistatic regime and rescattering

After having demonstrated that the simulator reproduces accurately the strong-field response of a hydrogen atom in the multiphoton regime, the quasistatic regime is investigated. As mentioned in Section 13.1, in the quasistatic regime the system is assumed to follow adiabatically the changes in the potential induced by the external time-dependent field. In contrast to the multiphoton regime where an absorption picture is adopted, here the bound particle is supposed to tunnel through or escape over the field-distorted potential barrier, see Figure 17.5a. For the escaped particles, a simple tunneling picture describes an exponential decrease in the energy-resolved spectra. Such a decrease can clearly be identified in the low-energy part (up to $2U_p$) in Figure 17.6 in which differential yields in the quasistatic regime are shown. Additional to the TDSE solutions for the simulator in Figure 17.6(a) and the hydrogen atom in 1D and 3D in Figure 17.6(b), the length gauge SFA solutions are shown that also show an exponential decrease of the direct atoms (electrons). In a periodically varying field, the emitted particle can, however, reverse its direc-

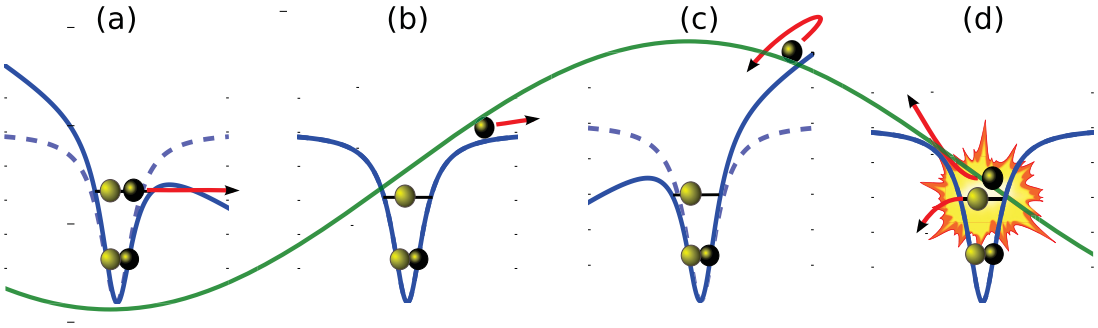

Figure 17.5: Behavior of two optically trapped atoms in a periodically driven magnetic-field gradient (solid green curve), as expected from the three-step model [186] in strong-field physics. After tunneling through the gradient distorted potential barrier (a) the escaped atom accelerates (b), reverses (c) and finally recollides (d) with the residual atoms. This sketch is also shown in [47].

tion and recollide. Such a recollision scheme for an atom in a trap is illustrated in Figure 17.5. The recollision is responsible for high harmonic generation when a liberated electron recombines with the parent ion. By evaluating a classical model it has been found [168] that high-harmonic spectra extend up to $3.17U_p + I_p$. The recollision process manifests in energy-resolved electron spectra as a plateau, because the escaped particles gain additional energy which results in a broad energy distribution[1] that was observed in [169]. Again, evaluating a classical model, the plateau is expected to extend from $2U_p$ to $10U_p$ [187]. It is truly astonishing how accurately the quantum simulator reproduces all expected features of the rescattering scenario. In addition, as visible in Figure 17.6, the extension of the plateau for the simulator lies very precisely in the region from $2U_p$, where the SFA and TDSE solutions loose their quantitative agreement up to $10U_p$ where the exponential decay of the TDSE starts again. Differently, for the 1D soft-Coulomb potential, the plateau starts at about $4U_p$ and for the 3D hydrogen at about $3U_p$. Moreover, for both, the 1D soft-Coulomb and the 3D hydrogen atom, the SFA and TDSE solutions for the direct electrons start to deviate significantly from the TDSE solution before the $2U_p$ threshold. Comparing the 1D and 3D solutions of the Coulombic systems with the simulator reveals, moreover, that the more pronounced structure in the plateau in case of the 1D spectra of the simulator and the 1D soft-Coulomb potential is an effect of dimensionality.

Rescattering is one of the major topics in attosecond science today. It is responsible for highly discussed effects like high-energy above-threshold ionization,

[1]The SFA can be modified to be able to describe rescattering [170]. Therefore, higher order terms of the S-matrix expansion have to be included and a rescattering potential has to be introduced.

non-sequential double ionization [188] and high-order harmonic generation [189]. In the example above the slow down of the simulator processes compared to the strong-field system is 13 orders of magnitude. Hence, the simulator allows to watch in "slow motion" the recollision dynamics under extremely controlled and versatile conditions.

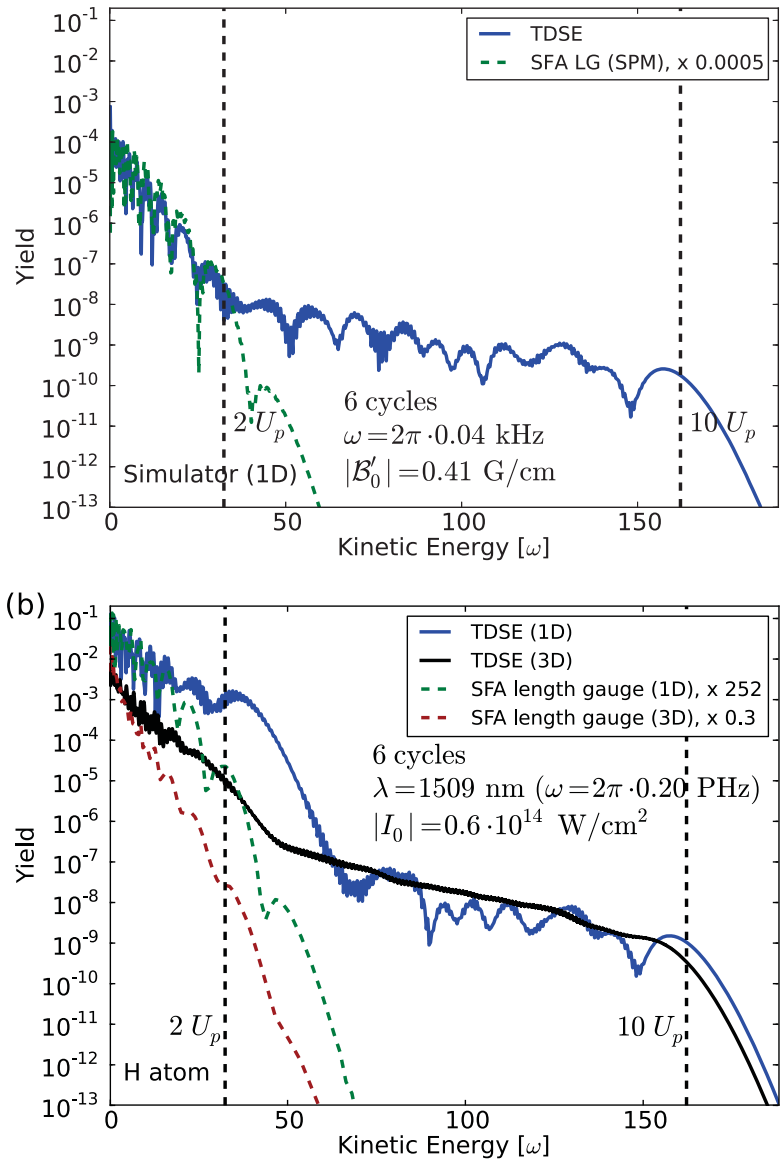

Figure 17.6: Differential yields for the simulator (a) and the 3D and 1D hydrogen atoms (b) in the quasistatic regime. The SFA yields are rescaled by a constant factor in order to agree with the total yield of the TDSE calculation. The factors are given in the legends. Converged results were obtained by using the basis sets specified in Table C.4,Table C.2, and Table C.5. The plots are also presented in [47].

17.3 Validation of the SFA

As already mentioned in Section 14.6, compared to the Coulombic systems, the simulator incorporates variable and shorter-ranged trap and interaction potentials and therefore better fulfills the effective short-range assumptions entering the SFA. In order to quantify these effects a comparison of energy-resolved SFA with TDSE spectra is performed. In order to obtain comparable spectra, for the evaluation of the 3D hydrogen atom the SFA amplitudes need to be integrated over all angles $\alpha \in [0, \pi]$ of the momentum $\mathbf{p}$ relative to the direction of the electric field which is equivalent to an integration of $\cos(\alpha) = \frac{1}{|\mathbf{E}||\mathbf{p}|}\mathbf{E} \cdot \mathbf{p}$ over the interval $[-1, 1]$, i. e.

$$|M_p|^2 = \int_{-1}^{1} d\cos(\alpha)\ |M_{\mathbf{p}}|^2 \quad . \tag{17.2}$$

It is very important to note that the integration is performed over the absolute square of the amplitude (in contrast to taking the square of the integral over the amplitude). In this way the total amplitude corresponds to the sum over measurements in an experiment where the photo-detector is placed in the different angles with respect to the field direction. Integrating over the amplitude and not the absolute squares would result in interferences that are, however, not reflecting a measurement scenario and are not comparable with the TDSE results.

To compare the quality of the SFA for the simulator and the hydrogen atom, the results of Figure 17.1 of the multiphoton regime are reconsidered first. There, the agreement of the energy-resolved spectra of the simulator and the hydrogen atom was even quantitatively excellent. In Figure 17.7 the energy-resolved spectra for the simulator and the hydrogen atom together with SFA results in length and velocity gauge are visible. The SFA reproduces well the ATI peaks in both systems, the simulator and the hydrogen atom. However, while for the first two peaks a quantitative agreement of the SFA in length and velocity gauge to the TDSE results can be found, the results for the hydrogen atom are over-estimating the yield by about *three orders* of magnitude. These results provide evidence that the SFA is indeed better applicable to the less long-ranged Lorentz potential than to the Coulomb potential of an hydrogen atom in the multiphoton regime.

Additionally, the gauge dependence of the SFA can be discussed. While for the simulator the velocity-gauge SFA gives quantitative agreement for almost the entire energy range, the length gauge SFA looses accuracy for larger kinetic energies. For the hydrogen atom, the velocity gauge is accurate for about the 8th, 9th and 10th peak, the length gauge is wrong by at least two orders of magnitude over the entire energy range. The differential yield in velocity-gauge SFA decreases with the kinetic energy compared to the length-gauge SFA that tends to overestimate the yield.

Hence, the behavior of the gauges of the simulator is in accordance to the one of the hydrogen atom, except that for the dominant first three peaks quantitative agreement between the SFA in both gauges and TDSE solution is achieved only within the simulator.

In the adiabatic regime, the SFA can be evaluated by comparing the results of Figure 17.5 and Figure 17.6 for the direct electrons (atoms) up to about $2U_p$. As shown in Figure 17.8, the SFA for the simulator reproduces the rich structure of the TDSE remarkably accurately. The rescaling constant is due to the use of the saddle-point approximation (SPM) that turned out to be necessary to evaluate the SFA for the simulator because the direct SFA calculation (at least in its current form of numerical implementation) was found to loose accuracy due to the strongly oscillating integrals.

Differently, the SFA for the hydrogen atom reproduces the small-scale structure of the TDSE solution only up to about 5ω, then a transition to a rather smooth curve is visible which fails to reproduce the structure of the TDSE result. Moreover, compared to the TDSE, the SFA for the hydrogen atom results in a different slope which leads to a yield that is already about by two orders too small at $E_{\mathrm{kin}} = 25\omega$.

Hence, the results of the comparison of the TDSE and SFA in the multiphoton regime and particularly in the adiabatic regime demonstrate that the SFA is indeed significantly better applicable to the simulator system than to a hydrogen atom. Hence, the quantum simulator provides a novel and unique tool to systematically validate the SFA for complicated many-body systems where it is nowadays routinely adopted although its applicability is unclear.

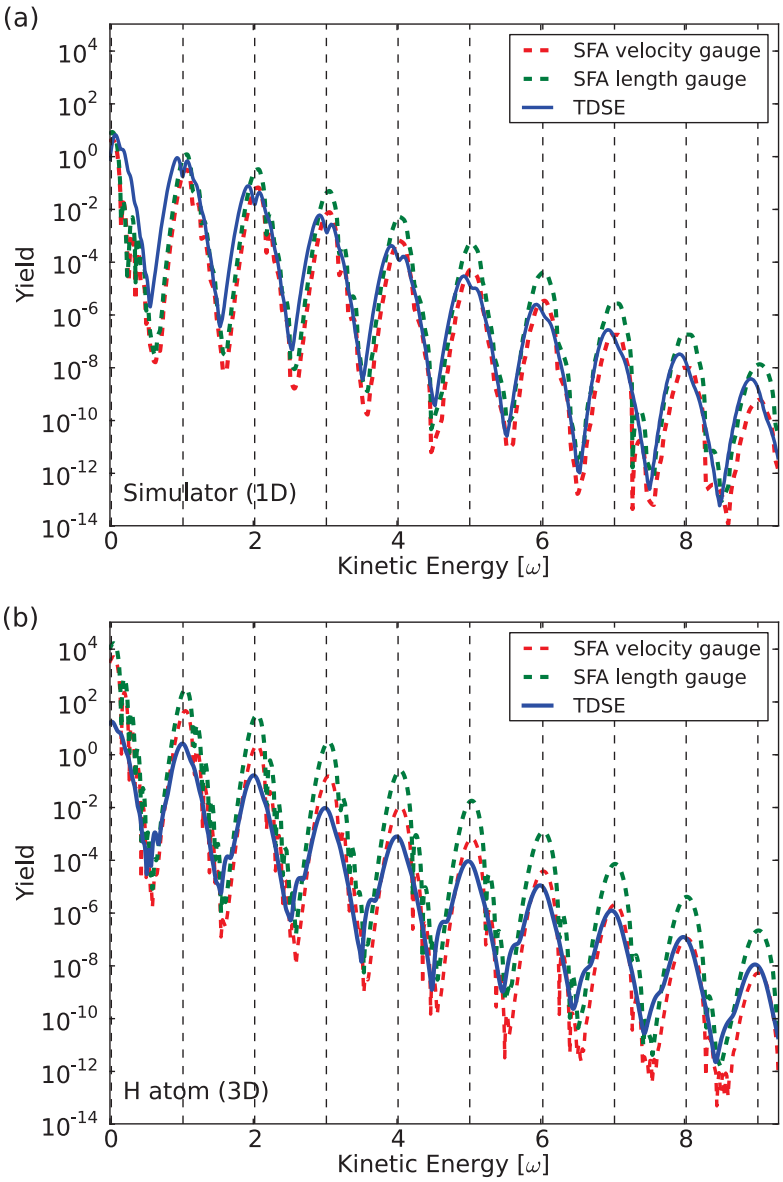

Figure 17.7: Same parameters as Figure 17.1 but simulator and hydrogen atom in different plots, including the length and velocity gauge SFA. The plots are also presented in [47].

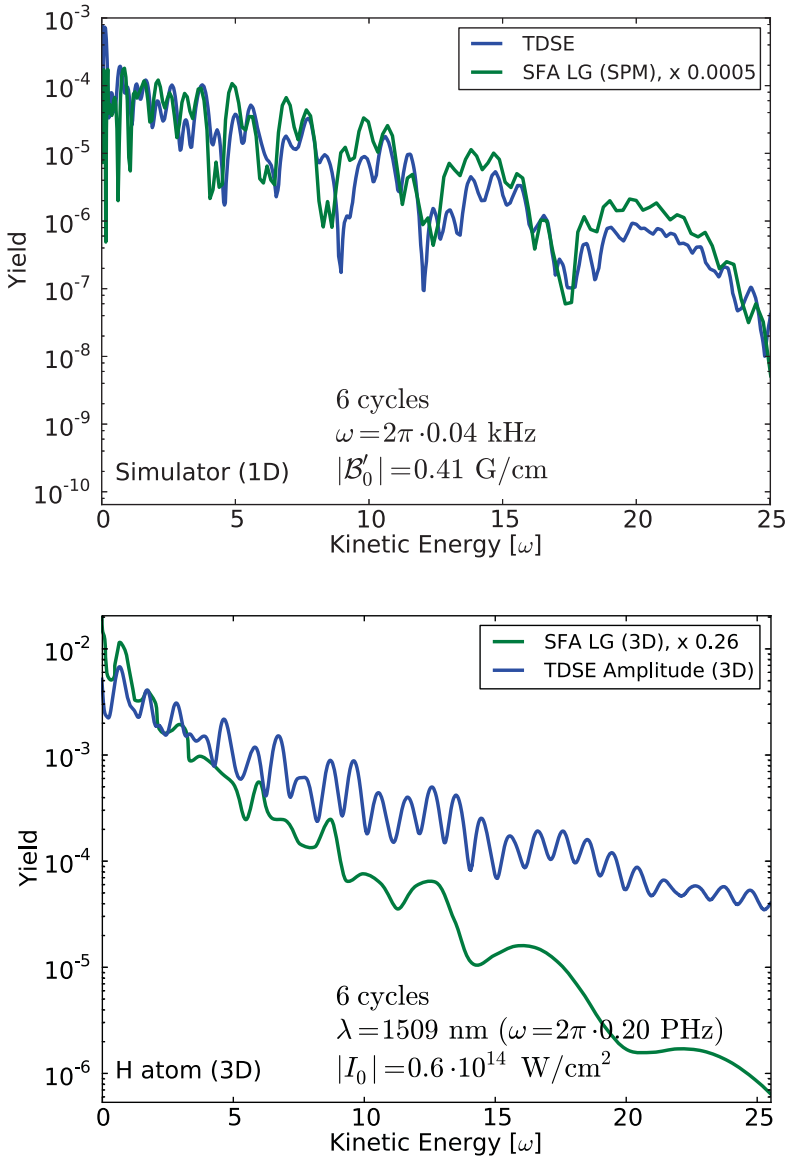

Figure 17.8: Comparison of TDSE and SFA results of the simulator and the H atom in the adiabatic regime. Same parameters as Figure 17.6 but for energies of the direct electrons (atoms). For the simulator the SFA is evaluated using the saddle-point approximation (SPM). For the TDSE the basis set specified in Table C.4 was used.

17.4 Imaging scheme for ultracold atoms

Certainly, a key benefit of the quantum simulator is to provide a novel tool that allows to systematically deepen the understanding in attosecond physics. On the other hand, a back action onto ultracold atoms can be generated.

In strong-field physics, the imaging of molecular orbitals can be performed by field-induced electron tunneling and diffraction. This process is based on rescattering that was shown to be quantitatively reproduced by the simulator in Section 17.2. Hence, by application of the simulator mapping, a controlled cold recollision may be used for the imaging of ultracold many-body systems.

Moreover, a novel imaging technique can be derived from the SFA in velocity gauge. The method relies on the applicability of the SFA for the simulator system, that was clearly demonstrated in Section 17.3. The SFA in velocity gauge for the quantum simulator

$$\mathcal{M}_{\mathbf{p}}^{\mathrm{VG}} = -i\tilde{\phi}_b(\mathbf{p}) \int_0^{t_f} dt\; e^{i(S_{\mathbf{p}}(t)+E_b t)} \left[\mathbf{p}\cdot\mathcal{A}(t) + \frac{1}{2}\mathcal{A}(t)^2\right] \quad . \tag{17.3}$$

contains the Fourier transform of the initial state $\tilde{\phi}_b(\mathbf{p})$, i. e. the momentum-space density $\tilde{\phi}$ as a factor. This provides a way to extract the momentum-space density of the initial state from the measured energy-resolved spectra if the velocity gauge SFA describes the systems behavior under the application of a periodically varying magnetic-field gradient accurately. A prerequisite for the imaging is of course the possibility to experimentally extract differential yields. It should be emphasized that in contrast to the strong-field experiments the pulse characteristics are known and controllable to a very high degree. Moreover, the binding energy can be measured to high precision. Since the time-integral in Eq. (17.3) only depends on these quantities, it can be determined without uncertainties. This provides a novel imaging technique which might serve as a valuable alternative to time-of-flight measurements.

18 Frustrated tunneling ionization

In a quantum simulator experiment such as proposed in Section 14.4, a measurement of the differential yield of atom escape requires further technical improvements. In analogy, in the early years of strong-field experiments also only total yields could be measured and an observation of differential quantities became only realizable with the onset of sophisticated technical advancements. However, the bound-state distribution after the pulse is directly accessible. In contrast, in strong-field physics the measurement of the excited state population is very challenging. It reveals, however, interesting effects. In [190] it was demonstrated that in the strong-field tunneling regime it is possible that a substantial fraction of neutral atoms survive the laser pulse in excited states despite its high intensity. Such a *frustrated tunneling ionization* (FTI) can be described within a semiclassical picture: In a first step, the electron tunnels out or escapes over the field-distorted potential barrier. Then the field amplitude changes sign, the electron did not gain enough drift velocity in the first step to fully escape the binding potential and gets recaptured in a highly excited (Rydberg) state.

Figure 18.1 shows the key result of the original work [190], i. e. the bound-state distribution that displays an enhanced population of highly excited bound states with quantum numbers between $n = 6$ and $n = 10$. The semiclassical picture was in [190] validated by the (semiclassical) Monte-Carlo simulation results that are displayed as red circles in Figure 18.1.

Experimental evidence for FTI has also been found in the fragmentation of H_2 [191] and D_2 [192] by the detection of excited H^* and D^* atoms, respectively. FTI was for the first time experimentally observed in polyatomic systems in the strong-field fragmentation and dissociation of D_3^+ [193]. In Chapter 18 the emergence of FTI within the quantum simulator is investigated.

18.1 Calculation of static rates

An important test of the semiclassical picture underlying FTI in [190] was the evaluation of a semiclassical Monte-Carlo calculation (performed in the group of Ulli Eichmann at the Max-Born Institute in Berlin). In the simulation, the escaping particle is initially placed at the semiclassical tunneling exit with a velocity of zero. Then, classical trajectories of the particle evolving in the external time-dependent

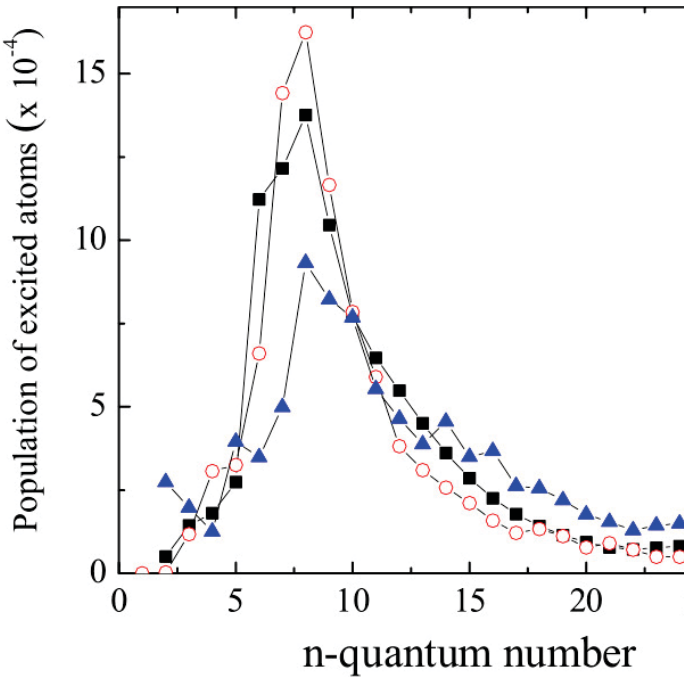

Figure 18.1: Distribution of the population of bound states in a system of Helium atoms exposed to a high-intense 30 fs Ti:sapphire laser pulse displaying FTI (see [190] for details). A quasi-one-electron (black boxes) and a full two-electron quantum mechanical calculation (blue triangles) are compared to a semiclassical Monte-Carlo simulation (red circles) at a laser intensity of $10^{15}\,\mathrm{W/cm^2}$. The Monte-Carlo simulation was normalized to the quasi-one-electron calculation at $n = 10$. The graph is taken from [190].

field are computed. The final energy is then projected on the eigenenergies of the bound states to obtain the bound state distribution after the pulse. As input the Monte-Carlo simulation moreover requires static tunneling rates, in order to scale the initial tunneling probability. For atomic systems, the tunneling rates in a static field are known analytically [152]. In order to perform the Monte-Carlo simulation also in the case of the quantum simulator, the static escape rate of an atom confined to the 1D Lorentz potential Eq. (14.14) is needed. Static tunneling rates are often calculated within the Wentzel-Kramers-Brillouin (WKB) approximation. However, since the considered gradient strengths are also in the over-the-barrier regime (where a tunneling theory such as WKB is inapplicable), a more general approach has to be adopted.

Static rates via TDSE

First, static rates are extracted from TDSE calculations with a static pulse of different plateau lengths. The ionization rate Γ for a static gradient can be defined by the rate equation

$$\frac{\mathrm{d}}{\mathrm{d}t}P_b(t) = -\Gamma P_b(t) \tag{18.1}$$

where P_b is the population of the bound part of the spectrum. Integrating this equation over the pulse duration $[0, t_f]$ leads to

$$\ln(P_b(t_f)) = -\Gamma t_f \tag{18.2}$$

and the total yield

$$Y(t_f) = 1 - \exp(-\Gamma t_f). \tag{18.3}$$

where the conservation of probability $Y + P_b = 1$ was used.

In order to find the rate from TDSE calculations, a static magnetic-field gradient pulse

$$\mathcal{B}'(t) = \begin{cases} \mathcal{B}'_0 \sin^2(\frac{\pi t}{2t_{\mathrm{ramp}}}) & \text{if } 0 \leq t \leq t_{\mathrm{ramp}} \\ \mathcal{B}'_0 & \text{if } t_{\mathrm{ramp}} < t \leq t_{\mathrm{ramp}} + t_{\mathrm{flat}} \\ \mathcal{B}'_0 \sin^2(\frac{\pi}{2} + \frac{\pi(t - t_{\mathrm{ramp}} - t_{\mathrm{flat}})}{2t_{\mathrm{ramp}}}) & \text{if } t_{\mathrm{ramp}} + t_{\mathrm{flat}} < t < t_f : \\ 0 & \text{else} \end{cases} \tag{18.4}$$

is used that has a ramp time t_{ramp}, a plateau time of t_{flat} and a total time of $t_f = 2t_{\mathrm{ramp}} + t_{\mathrm{flat}}$ which is continuous and differentiable. In order to extract Γ, TDSE calculations with static pulses are performed for a varying pulse length t_f, all with the basis set specified in Table C.4. The slope of a semilog plot of the bound population versus the pulse length then directly delivers Γ. Hereby, it has to be ensured that a variation of the ramp time does not change the rate. Although the procedure seems to be straightforward, there are several difficulties present. First, in the regimes where the yield is close to one and where it approaches zero, the equations Eqs. 18.3 and 18.2 loose their validity for a constant rate. This behavior is visible in Figure 18.3 where clearly for small yields the exponential law is not fulfilled. Also in the saturation the slope decreases. To overcome this issue it seems natural to choose only a smaller interval of the yield, e. g., $Y \in [0.2, 0.6]$. In Figure 18.4 the results of such a yield interval together with the linear regression to obtain the rate are visible. While for these gradient parameters the method

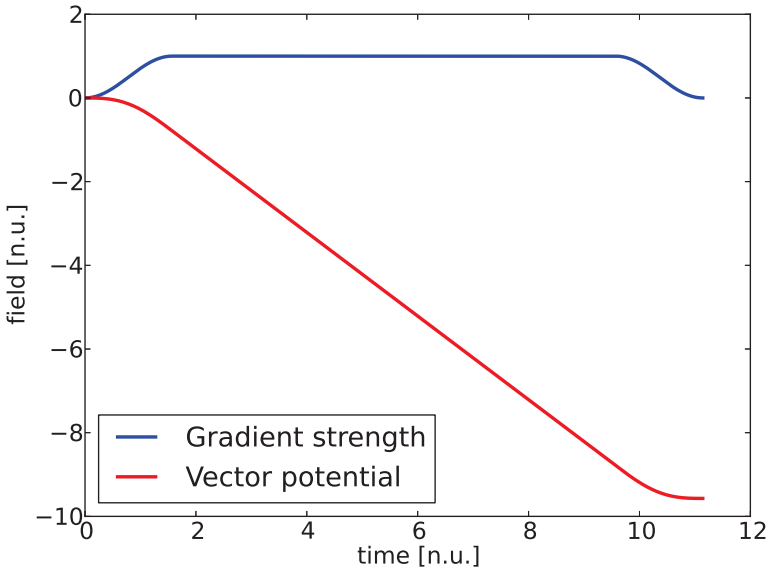

Figure 18.2: A generic magnetic-field gradient pulse and its vectorpotential for the evaluation of static rates with $\mathcal{B}_0' = 1n.u.$, $t_{\text{flat}} = 8n.u.$ and $t_{\text{ramp}} = \frac{\pi}{2}$.

to extract the rate seems appropriate, the approach suffers from complications. It has turned out that the starting point where the magnitude of the slope changes varies with the field strength. Hence, the valid interval, where the exponential law of Eq. (18.3) is valid varies with the gradient parameters. A systematic way to extract the yield would be to look in a region where the magnitude of the slope is maximal, but still in a large enough yield region. While the implementation of such an algorithm is straightforward, it is not worth the effort, since, as will be seen, the method gives inaccurate results, especially in the regime of low gradient strengths. Another difficulty of the method are very small gradient strengths where it is not clear where to measure the slope. Such a situation is shown in Figure 18.5.

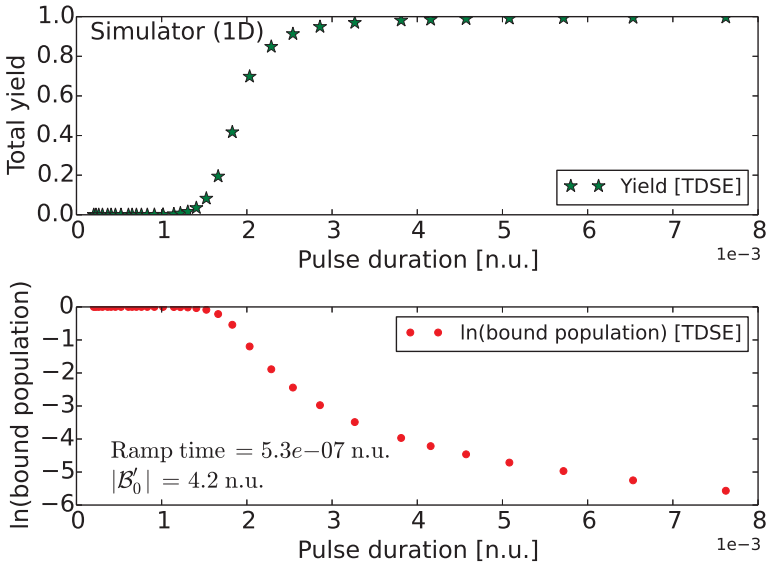

Figure 18.3: Total yield and population of the bound states for different values of the flat pulse duration.

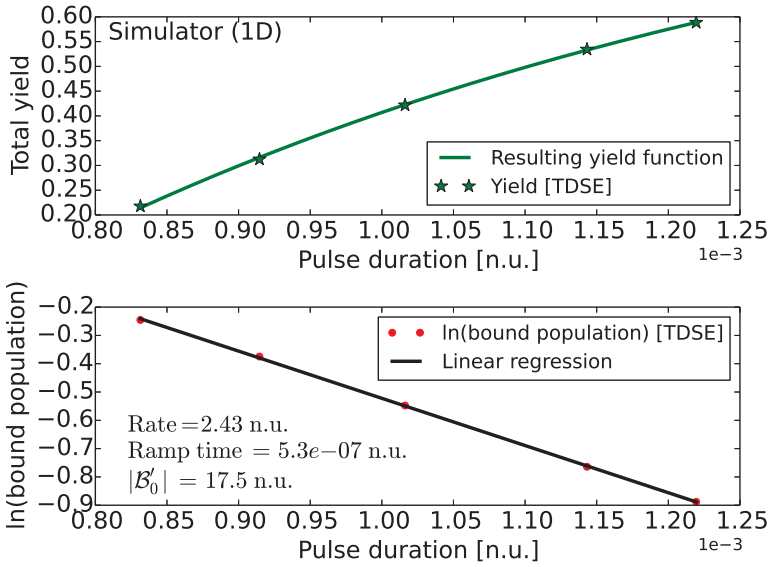

Figure 18.4: Total yield and population of the bound states for different values of the flat pulse duration. The rate is obtained from a linear regression (black line) of the TDSE results for the bound population. Green line indicates the expected yield for that rate based.

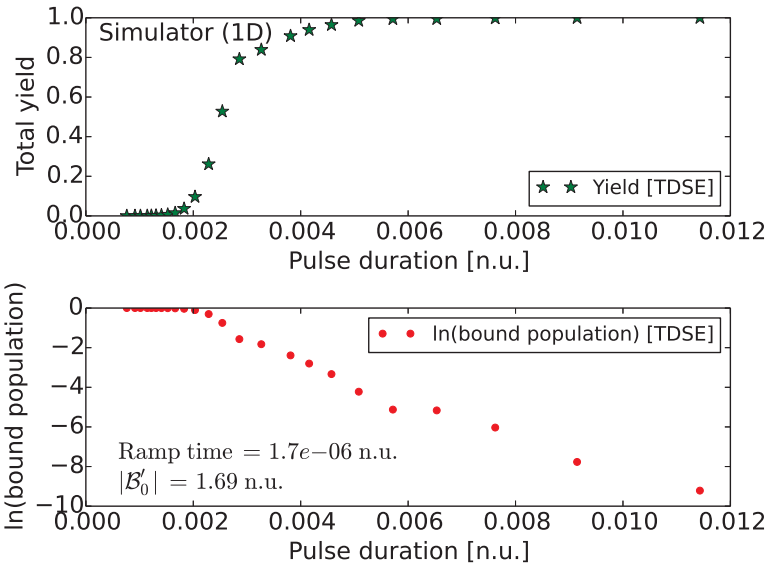

Figure 18.5: Total yield and population of the bound states for different values of the flat pulse duration. It is not clear where to evaluate the rate.

Static rates via complex scaling

The TDSE evaluation of static rates suffers from difficulties. To overcome these issues, static rates are extracted from complex scaling calculations. Complex scaling was first introduced in [194, 195] and later reviewed in [196–198].

In order to perform uniform complex scaling calculations, the matrix algorithm described in Section 15.1 is modified. The position x of Eq. (15.2) is scaled with an angle θ via

$$\hat{\mathrm{x}} \mapsto \hat{\mathrm{x}}\,\mathrm{e}^{i\theta} \quad . \tag{18.5}$$

Since the momentum operator in coordinate representation contains a spatial derivative, the momentum operator and the kinetic energy operator scale as

$$\hat{\mathrm{p}} \mapsto \hat{\mathrm{p}}\,\mathrm{e}^{-i\theta} \tag{18.6}$$

$$\hat{\mathrm{T}} \mapsto \hat{\mathrm{T}}\,\mathrm{e}^{-2i\theta} \quad , \tag{18.7}$$

respectively [1]. For all complex-scaling calculations shown in the following the basis set specified in Table C.1 was used.

For a vanishing gradient, the complex scaled spectrum shown in Figure 18.6 consists as expected on bound states that are real and continuum states that reach as rays into the complex plane under an angle of 2θ.

Applying a non-zero gradient leads to resonances that are visible as accumulation points in the spectrum. For these resonances

$$\frac{dE}{d\theta} = 0 \tag{18.9}$$

holds. Figure 18.7 shows the complex scaled energy spectrum for $\mathcal{B}' = 3.0$ n.u. Resonances are clearly visible in the zoomed part of the plot. At the resonance, the rate Γ can be directly extracted via the imaginary part of the resonance energy

$$\Gamma = -\frac{\mathrm{Im}\,E}{2} \quad . \tag{18.10}$$

[1] Note, the complex scaling performed here is *not* in complete analogy to the 3D case where only $r = |\mathbf{r}|$ is scaled. Such a scaling is equivalent to

$$\begin{cases} \hat{\mathrm{x}} \mapsto \hat{\mathrm{x}}\,\mathrm{e}^{i\theta} & \text{if } x \geq 0 \\ \hat{\mathrm{x}} \mapsto \hat{\mathrm{x}}\,\mathrm{e}^{i(\theta+\pi)} & \text{if } x < 0 \end{cases} \quad . \tag{18.8}$$

The scaling of the kinetic operator does not change then since $\mathrm{e}^{2\pi i} = 1$. However, this scaling was found to be inappropriate.

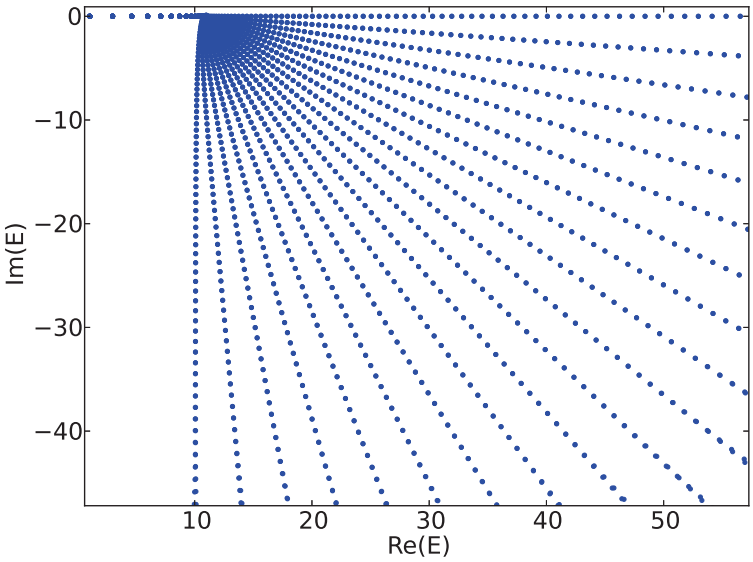

Figure 18.6: Complex scaled energy spectrum of the field-free Hamiltonian. Θ varies in between zero (where the energies are real) and $\pi/2$.

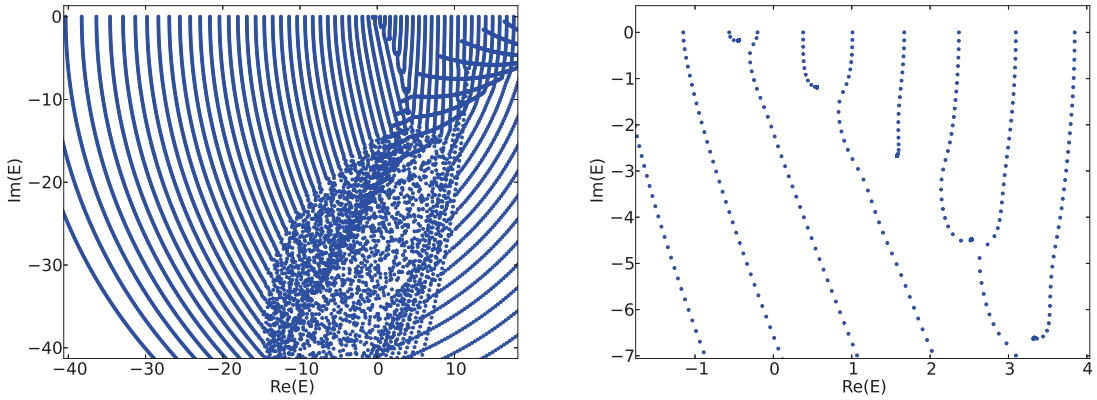

Figure 18.7: Complex scaled energy spectrum for a field strength of $\mathcal{B}' = 3\,\mathrm{n.u.}$, Θ varies in between zero and $\pi/2$. The tunneling resonances are clearly visible as accumulation points in the magnified right part.

Static rates via a semiclassical approach

Since the TDSE and the complex scaling gave (very) different results for the tunneling rate, a semiclassical evaluation was performed to decide on the validity of the methods. Semiclassically, the static tunneling rate Γ can be obtained by matching the bound state wavefunction $\psi_{\mathrm{b,pol}}$ that is polarized due to the static gradient with the outgoing (continuum) wavefunction. The tunneling rate

$$\Gamma = |v(z^{\mathrm{asym}})||\psi(z^{\mathrm{asym}})|^2 \tag{18.11}$$

is then given by the probability current through an asymptotic exit plane where the semiclassical velocity v is given by

$$v(z) = \sqrt{2(E_{\mathrm{b}} - U(z) + \mathcal{B}'z)} \tag{18.12}$$

containing the 1D Lorentz potential $U(z)$ of Eq. (14.14) used for the simulator. In WKB approximation this can also be expressed by [199, 200]

$$\Gamma = |v(z_0)||\psi_{\mathrm{b,pol}}(z_0)|^2 |a_{\mathrm{g}}(z_0, z_1)|^2 \tag{18.13}$$

where $z_0 = z_{t_1} + \xi(z_{t_2} - z_{t_1})$, $\xi \in (0,1)$ is a point inside the barrier between the inner and outer classical turning points z_{t_1}, z_{t_2} where the velocity is imaginary and $z_1 = z_{t_2}$ can be taken as the outer turning point [199, 200]. The turning points fulfill

$$U(z) - \mathcal{B}'z = 0 \quad . \tag{18.14}$$

The Gamow factor

$$a_{\mathrm{g}} = \exp\left[-\int_{z_0}^{z_1} dz\, \sqrt{2(U(z) - \mathcal{B}'z - E_{\mathrm{b}})}\right] \tag{18.15}$$

which is the probability that the particle can tunnel through the potential barrier (originally considered for the case of nuclear fusion) can be calculated analytically for the Lorentz potential of Eq. (14.14) resulting in

$$a_{\mathrm{g}} = \exp\left\{-\sqrt{2}\left[-pV z_{\mathrm{R}} \arctan\left(\frac{z}{z_{\mathrm{R}}}\right) - \frac{1}{2}\mathcal{B}'z^2 - E_{\mathrm{b}}z + pVz\right]_{z_0}^{z_1}\right\} \quad . \tag{18.16}$$

Also the turning points can be evaluated analytically. However, the general expression is not written down here, since it is (as a general complex solution of a cubic equation) very lengthy and provides no further inside. For gradient strengths that lie in the tunneling regime, all three turning points become real.

The exact bound state wavefunction $\psi_{\mathrm{b,pol}}(z)$ at z_0 can be calculated exactly based on a numerical solution, here the matrix method described in Section 15.1 is used. Alternatively, the value of the harmonic oscillator ground-state wavefunction (Eq. (3.22) for $n = 0$) may be chosen in analogy to [200] where it is proposed to use the unperturbed hydrogen ground state wavefunction for a calculation of $\psi_{\mathrm{b,pol}}(z_0)$ inside the barrier. In [200] it is also proposed to use a long-range approximation of the Gamow factor given by

$$a_{\mathrm{g}}^{(\mathrm{lr})} = \exp\left\{ -\int_{z_0}^{z_1} dz' \sqrt{\kappa^2 - 2\mathcal{B}' z'} \right\} \exp\left\{ -\int_{z_0}^{z_1} dz' \frac{U(z')}{\sqrt{\kappa^2 - 2\mathcal{B}' z'}} \right\} \tag{18.17}$$

to compensate the neglected polarization in the bound state. The Gamow factor can also be evaluated without taking into account polarization. It is then given by [200]

$$a_{\mathrm{g}}^{(\mathrm{nopol})} = \exp\left\{ -\frac{\kappa^3}{3\mathcal{B}'} + \kappa z_0 \right\} \exp\left\{ -\int_{z0}^{z_1} dz' \frac{U(z')}{\sqrt{\kappa^2 - 2\mathcal{B}' z'}} \right\} \tag{18.18}$$

In Figure 18.8 different approaches of the semiclassical approximation are compared to the corresponding results obtained by complex scaling. While the semiclassical approaches can only be evaluated in the tunneling regime, the complex scaling method allows also to calculate rates in the over-the-barrier regime. The complex scaling results are in excellent quantitative agreement to the semiclassical results using the exact expressions for the wavefunction and the Gamow factor. The latter method is independent on ξ (blue and red solid lines match), i. e. independent on where the asymptotic wavefunction is connected with the barrier-suppressed bound state. In an ideal case the rate should always be independent on ξ [200] but the results in Figure 18.8 prove differently for cases where ψ_{b} and a_{g} are *not* computed exactly within a numerical and an analytical computation, respectively. Replacing the exact polarized bound state by the harmonic-oscillator ground-state wavefunctions gives accurate results for small gradient strengths but starts to loose its accuracy close to the over-the-barrier threshold (brown dashed curve). The reason is that in this regime, the gradient-free solution significantly differs from the exact bound-state wavefunction that is strongly polarized. The results in which the Gamow factor is replaced by approximations give results that are incorrect by orders of magnitude. Hence, it is crucial for the accuracy of the semiclassical method to appropriately (analytically or numerically exact) calculate the Gamow factor.

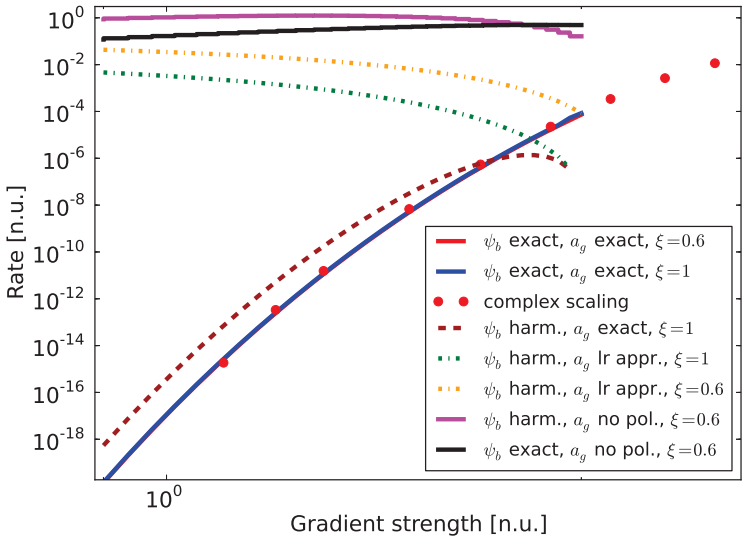

Figure 18.8: Static rates vs. gradient strength in natural units. Compared are the results obtained using complex scaling (red dots) with different semiclassical approaches (lines). In the legend, "ψ_b exact" indicates that the numerically exact polarized bound state is used, "ψ_b harm." indicates that the harmonic approximation has been adopted. "a_g exact", "a_g lr. appr.", "no pol.", indicates that the exact expression (Eq. (18.16)), the long-range approximation (Eq. (18.18)), or no polarization approximation was used, respectively. Note, the red and blue lines (ψ_b and a_g exact with $\xi = 0.6$ and $\xi = 1$) are nearly identical and hence lie almost above each other.

Final comparison of all methods, curve fitting of the rate

Finally, the results for the rates obtained by the different methods (TDSE, complex scaling, semiclassical approach) are compared in Figure 18.9. The almost perfect agreement of the complex scaling results and the semiclassical model using the numerically exact polarized bound-state wavefunction and the analytical expression for the Gamow factor for the tunneling regime was already demonstrated in Figure 18.8. However, only the complex scaling results allow for a prediction of the rate in the over-the-barrier regime. In principle, this is also possible with the TDSE method, but as visible in Figure 18.9, the results are completely inaccurate, depending on the field strength even by many orders of magnitude. In fact, the TDSE results are almost constant, i. e. independent on the gradient strengths. Even worse, the rate can locally decrease with an increasing gradient strength. Finally, for small gradient strengths, the method leads to inaccurate results by about seven orders of magnitude which demonstrates its inapplicability.

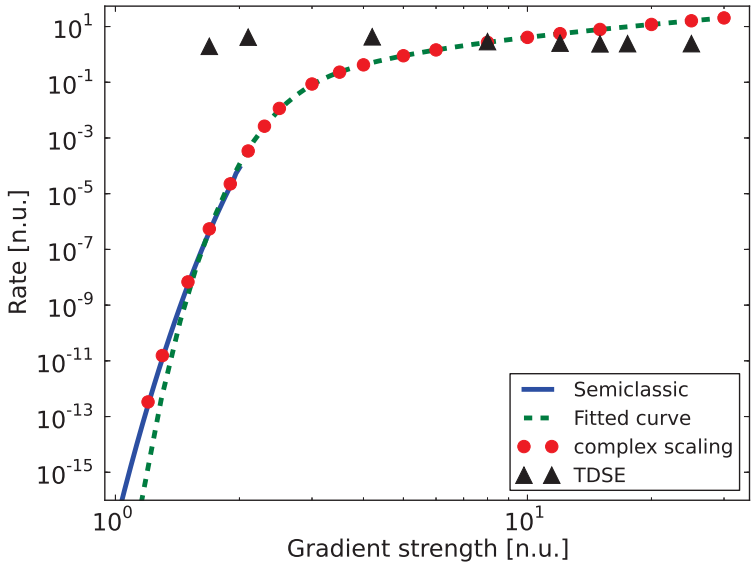

Figure 18.9: Static ionization rates vs. field strength in natural units. Compared are the results of the complex scaling, the TDSE with a ramp time of $5.3 \cdot 10^{-7}$ n.u. and the semiclassical evaluation with the numerical value of the bound state wavefunction within the barrier and the exact (analytic) expression of the Gamow factor. Moreover, the complex scaling values have been fitted (green dashed curve).

In Figure 18.9 the green dashed curve represents a fit to the complex scaling results. Such a curve is needed as an input for the Monte-Carlo simulation that was performed to investigate FTI for the quantum-simulator system. The regression function

$$\Gamma(\mathcal{B}') = \left(\frac{c_0}{\mathcal{B}'} + \frac{c_1}{\mathcal{B}'^3} + \frac{c_2}{\mathcal{B}'^5} + \frac{c_3}{\mathcal{B}'^9} + \frac{c_4}{\mathcal{B}'^{13}} + \frac{c_5}{\mathcal{B}'^{17}}\right) \exp\left(-e_0 \frac{\mathcal{B}' + \mathcal{B}'^2}{\mathcal{B}'^3}\right) \exp(-e_1 \mathcal{B}') \tag{18.19}$$

was used. The regression is performed using the Levenberg-Marquardt algorithm from MINPACK's `lmdif` and `lmder` algorithms that are accessible through the routine `leastsq` contained in the `optimize` package of Scipy. The resulting coefficients $c_0 = 8.5645 \cdot 10^2$, $c_1 = 8.0659 \cdot 10^4$, $c_2 = 1.3797 \cdot 10^7$, $c_3 = 2.2920 \cdot 10^{10}$, $c_4 = 4.8988 \cdot 10^{12}$, $c_5 = 1.3135 \cdot 10^{15}$, $e_0 = 4.2978 \cdot 10^1$, $e_1 = -3.423 \cdot 10^{-2}$ allow to evaluate the rate in natural units [2] for a wide range of gradient strengths in a closed-form

[2] To obtain Γ in SI units

$$\Gamma_{\mathrm{SI}}(\mathcal{B}'_{\mathrm{SI}}) = \alpha\Gamma(\beta\mathcal{B}'_{\mathrm{SI}}) \tag{18.20}$$

expression [3]. The fitted curve shows a deviation to the exact values for rates that fall below $\approx 10^{-9}$ which corresponds to $\mathcal{B}' \lesssim 1.5\,\mathrm{n.u.}$ The considered peak gradient strengths for the evaluation of FTI (following in the next section) are far above $\mathcal{B}' = 1.5\,\mathrm{n.u.}$ Hence, the Monte-Carlo results are not significantly influenced by these deviations because ionization occurs mainly around the pulse peak.

18.2 Bound-state populations – evidence for FTI

After having delivered a closed-form expression for the static (tunneling and over-the-barrier) rate for the 1D Lorentz potential in the previous section, in the following bound-state populations are investigated to search for FTI features in analogy to the ones displayed in Figure 18.1.

First, the behavior of the bound-state distributions are investigated in the adiabatic regime in the transition from the tunneling regime to the OTB regime. The bound-state distributions in Figure 18.10 are obtained from TDSE calculations of an atom initially in the ground state of the Lorentz potential with parameters specified in Table C.9 which were the parameters of the experiment at the time the calculations were performed (with the basis specified in Table C.4).

The upper row of Figure 18.10 (corresponding to $|\mathcal{B}_0'| = 0.39\,\mathrm{G/cm}$ and $|\mathcal{B}_0'| = 0.43\,\mathrm{G/cm}$) show bound-state distributions in the "true" tunneling regime which is characterized by $\gamma \ll 1$ and gradient strengths that do not yet lead to over-the-barrier escape. Although the absolute populations of the highly excited states is only on the order of 10^{-3}, and the ground states are still majorly populated (73.3% and 10.1%, respectively) the significant population of states with high quantum numbers indicates the existence of the FTI channel. It is important to note that these signatures also persist for gradient strengths that are just above the OTB threshold (OTBT=0.44 G/cm, see text in plots) as can be seen in the middle row, i. e. for gradient strengths of $|\mathcal{B}_0'| = 0.45\,\mathrm{G/cm}$ and $|\mathcal{B}_0'| = 0.46\,\mathrm{G/cm}$. Here the ground-state populations have further decreased to 2.9% and 0.44%, respectively. However, increasing the gradient strength even further into the OTB regime (lower row, $|\mathcal{B}_0'| = 0.72\,\mathrm{G/cm}$ and $|\mathcal{B}_0'| = 1.3\,\mathrm{G/cm}$) leads to an almost complete deexcitation of the ground state and also to a more random population of the bound states, i. e. while highly excited states are still populated also lower excited states show a

is to be used where Γ is the function defined in Eq. (18.19), $\alpha = 687.0$ is the conversion constant from frequency in n.u. to Hz and $\beta = 0.199$ is the conversion constant for a magnetic-field gradient in n.u. to G/cm (Note, here G/cm is used instead of T/m to conform with the experimental conventions, they differ by a factor 100, $100\,\mathrm{G/cm} = 1\,\mathrm{T/m}$).

[3] In [201] a 1D tunneling theory for the Lorentz potential is developed for two ultracold atoms that reproduces quantitatively the tunneling dynamics of the fermionization experiment [34]. In the limit of a single particle the theory is equivalent to the WKB approximation.

significant population. Hence, far in the OTB regime, the FTI peaks loose their unique characteristic.

In Figure 18.11 the bound-state distribution for a deeper potential is considered that supports a larger number of bound states ($n = 88$). The peak in the bound-state population for highly excited states indicates that FTI is also present in the deeper potential for gradient strengths just above the OTB threshold (left part, $|\mathcal{B}_0'| = 2.6\,\mathrm{G/cm}$) and further in the OTB regime (right part, $|\mathcal{B}_0'| = 3.3\,\mathrm{G/cm}$). In fact, this demonstrates that for a potential supporting a larger number of bound states and a sufficiently small frequency the distinct FTI peak survives even for gradient strengths more significantly in the OTB regime. Certainly, the gradient frequency of $\omega = 2\pi \times 0.5\,\mathrm{kHz}$ allowing for a 49 photon transition is extreme for today's experimental standards. It required the use of a very large box size (see Table C.6) to obtain converged results. The extremely small frequency that corresponds to a 4459 nm pulse for a hydrogen atom is necessary to push γ down below values of one. Still, the "true" tunneling regime is very narrow as it extends only from $2.2\,\mathrm{G/cm}$ up to $2.43\,\mathrm{G/cm}$.

Comment on symmetry

While in the original work on FTI the bound-state distributions are smooth as visible in Figure 18.1, in the 1D simulator system, the distributions follow often a zig-zag-pattern. This pattern stems from the 2-fold (*gerade*, *ungerade*) symmetry of the field-free eigenstates of the simulator Hamiltonian. Although these states are coupled and thus mixed during the time-propagation as can be deduced from the TDSE for the coefficients in Eq. (15.19), a symmetry dependent pattern survives for some pulses. Considering only states of a definite symmetry can recover the typical, more smooth curve. In 3D systems the bound-state populations are smooth although the *gerade/ungerade* is present. The reason is that different to 1D where the two symmetries have different energies, the symmetries for different L quantum numbers of the total angular momentum are energetically degenerate in 3D. Hence, for a given n quantum number different symmetries are summed up which flattens symmetry-dependent features.

Comparison to the semiclassical model

Finally, in order to validate the semiclassical picture underlying FTI, Monte-Carlo results are compared to the TDSE calculation. In Figure 18.12 the bound-state distribution for both approaches is shown for parameters that lead to large FTI-peak populations that exceed about 5%. Such peaks can be easily resolved in an

experiment [4]. While the TDSE as well as the semiclassical model both deliver no significant population of very highly excited states (n>20), the lower-lying bound states (n<10) show a higher population in the semiclassical result (relative to the maximum peak). Also the absolute quantity of the population is slightly different, i. e. the maximum peak in the TDSE calculation has a population of about 5.5%, the one in the Monte-Carlo evaluation of about 1.6%. However, the absolute quantities are not expected to agree very well since also in the original work [190] they differed.

Most importantly, the typical feature for FTI, i. e. a pronounced population at highly excited states is present in both systems. Both, the TDSE as well as the semiclassical evaluation, show a maximum population peak for n=13. This is a strong evidence that the semiclassical mechanism explained in [190] can be also applied to the simulator system. Moreover, it demonstrates that FTI is not only restricted to the tunneling regime, but is also present in the OTB regime. Finally, the result delivers a direct evidence that the strong-field effect of FTI is not restricted to 3D systems but is present also in 1D.

[4] In fact, with the present experimental setup only populations per state larger than about 4% of the total population can be measured.

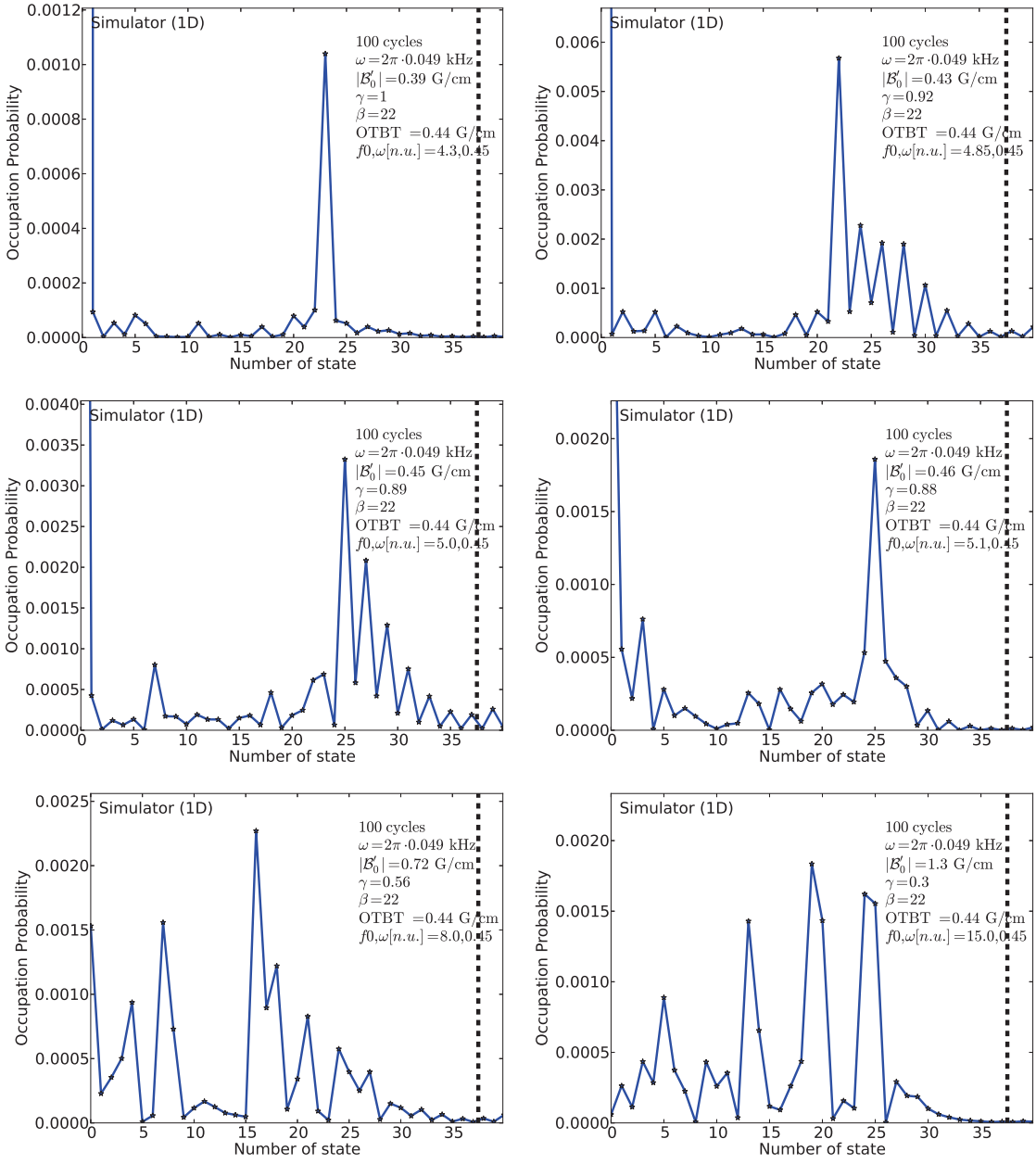

Figure 18.10: Bound-state distributions in the adiabatic regime for different magnetic-field gradient strengths (parameters are specified in the texts in the plots). While clear FTI features are present in the tunneling regime (upper row), these features persist for gradient strengths just above the OTB threshold (middle row). Far in the OTB regime the deexcitation of the ground state leads to excitations of also low lying excited bound states. The vertical dashed line indicates the continuum threshold.

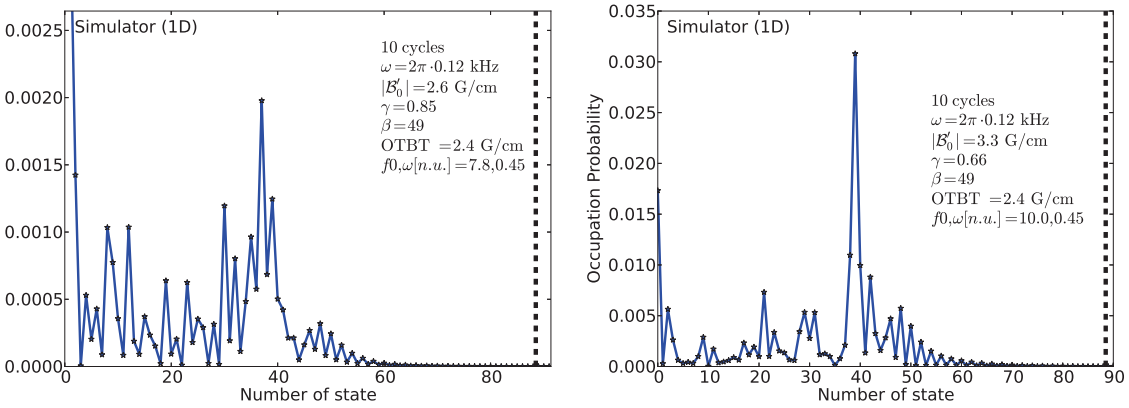

Figure 18.11: Bound-state distributions for the simulator for different gradient strengths for the Lorentz potential with parameters specified in Table C.10. Clear FTI features survive even far in the OTB regime.

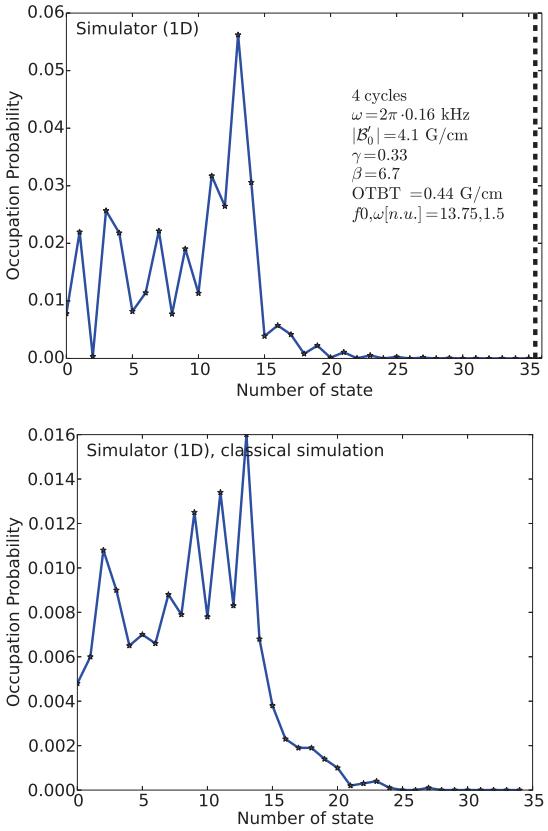

Figure 18.12: Bound-state distributions obtained from a TDSE calculation (upper plot) and a semiclassical Monte-Carlo evaluation (lower plot) for the Lorentz potential with parameters specified in Table C.9.

19 Behavior of the total yield

An analysis of FTI requires a measurement of the population of the bound states P_b. Such a measurement delivers directly the total atom-escape yield Y because $P_b + Y = 1$. In the strong-field regime, the total yields contain characteristic features that are analyzed in comparison to the quantum simulator.

19.1 ADK theory

An established theory for the description of total ionization yields in alternating fields in the adiabatic regime is the one introduced by Ammosov, Delone, and Krainov (ADK) [156] that is a simplified version of the Perelomov, Popov and Terent'ev (PPT) theory [153–155]. In order to validate the behavior of the total yields for the quantum simulator, it is interesting to compare to ADK theory. ADK delivers an expression for the ion rate. From the ion rate the corresponding ADK escape rate $\Gamma_{\mathrm{ADK}}(\mathcal{B}'(t))$ for the simulator is obtained by applying the simulator mapping Eq. (14.8). In order to extract from Γ_{ADK} the yield

$$Y_{\mathrm{ADK}} = 1 - \exp\left[-\int_0^T dt\, \Gamma_{\mathrm{ADK}}(|\mathcal{B}'_{\mathrm{e}}(t)|)\right] \quad , \tag{19.1}$$

an integration needs to be performed over the entire pulse duration $[0, T]$ and over the absolute value of the rate in which the *pulse envelope* $|\mathcal{B}'_{\mathrm{e}}|$ enters.

Based on the assumptions [156] entering the derivation of the ADK rate, it can only be expected to be valid for $\gamma \ll 1$. In contrast, the PPT rates allow for arbitrary γ and give improved results compared to ADK theory. Assuming that the dominant term in the rate expression of the PPT theory is the exponential one, a simple correction of the ADK rate is obtained by the transformation

$$\exp\left[-\frac{2\kappa^3}{3\mathcal{B}'}\right] \mapsto \exp\left[-\frac{2\kappa^3}{3\mathcal{B}'}\, g(\gamma)\right] \tag{19.2}$$

which maps the exponential of the ADK rate to the one of the PPT rate in which

$$g(\gamma) = \frac{3}{2\gamma}\left[\left(1 + \frac{1}{2\gamma^2}\right)\mathrm{arcsinh}\gamma - \frac{\sqrt{1+\gamma^2}}{2\gamma}\right] \quad . \tag{19.3}$$

The final expression which is referred to as *frequency-corrected ADK* (FC-ADK) [202] is then given by

$$\Gamma_{\mathrm{FC-ADK}}(\mathcal{B}') = \left(\frac{3\mathcal{B}'n^{*3}}{\pi Z^3}\right)^{1/2} \frac{Z^2}{2n^{*2}} \left(\frac{2\mathrm{e}}{n^*}\right)^{2n^*} \frac{1}{2\pi n^*} \frac{(2l+1)(l+|m|)!}{2^{|m|}|m|!(l-|m|)!} \times \left(\frac{2Z^3}{\mathcal{B}'n^{*3}}\right)^{2n^*-|m|-1} \exp\left(-\frac{2Z^3}{3n^{*3}\mathcal{B}'}\, g(\gamma)\right) \tag{19.4}$$

where $\kappa = \sqrt{2E_\mathrm{b}}$, $n^* = Z(2E_\mathrm{b})^{-1/2}$, $\mathrm{e} = \exp(1)$ is Euler's number, and $\mathcal{B}'$ is the magnetic-field gradient. The only frequency-dependent term is $g(\gamma)$. In the limit $\gamma \ll 1$, $g(\gamma) \to 1$ such that the FC-ADK rate reproduces the ADK rate.

In order to validate the correctness of the implementation of the (FC-)ADK rate, some results are compared to the implementation adopted in [202]. As demonstrated in Table 19.1 quantitative agreement is obtained for the tunneling rates in case of a 1s hydrogen atom.

F_0 [a.u.]	0.016880324	0.033760648	0.067521296
Γ_{ADK} of [202]	$2.493807603 \cdot 10^{-16}$	$6.641996898 \cdot 10^{-8}$	$9.115049499 \cdot 10^{-4}$
Γ_{ADK}	$2.493807603 \cdot 10^{-16}$	$6.641996898 \cdot 10^{-8}$	$9.115049499 \cdot 10^{-4}$
$\Gamma_{\mathrm{FC-ADK}}$ of [202]	$1.438708446 \cdot 10^{-10}$	$1.689754344 \cdot 10^{-6}$	0.001628164822
$\Gamma_{\mathrm{FC-ADK}}$	$1.438708647 \cdot 10^{-10}$	$1.689754433 \cdot 10^{-6}$	0.001628164842

Table 19.1: (FC-)ADK rates for different field strengths (specified in the first row) for a 1s hydrogen atom exposed to an alternating electric field with wavelength of 800 nm. Shown are the results for the numerical implementation adopted in [202] and the one of Eq. (19.4) used in this thesis. The ADK rate Γ_{ADK} is obtained from the FC-ADK rate $\Gamma_{\mathrm{FC-ADK}}$ of Eq. (19.4) by setting $g(\gamma) \equiv 1$. The values for the implementation adopted in [202] were provided by Johann Förster.

The ADK formula in atomic units can directly be used for the simulator in natural units by the use of the simulator mapping given in Eq. (14.8). Since the ADK formula is derived for the 3D hydrogen atom, for the use in the 1D simulator system $l = m = 0$ and $Z = 1$ are adopted. Although it seems unconventional to adopt a formula derived for a 3D system to a 1D potential, in strong-field physics the use of 1D models for, e. g., H, H_2^+, H_2, and He has a long tradition. Thus, it is interesting to validate the applicability of the (FC-)ADK yield for a 1D hydrogen system (soft-Coulomb potential) and even beyond the Coulombic potential (1D Lorentz system of simulator).

19.2 Yield vs. intensity

First, the behavior of the total yield for a varying pulse intensity is investigated. The 1D Lorentz potential of Eq. (14.14) with the parameters defined in Table C.8 in the appendix is chosen. In comparison to the trap used in Chapter 17 (see also Figure 17.3, right part), the larger waist results in a wider trap supporting more bound states ($n = 17$). The trap and the resulting bound-state distribution are visualized in Figure 19.1. The bound-state distribution becomes more "harmonic" as the gap between the ground state and the first excited state is reduced and the energy levels become more equidistant for low-lying states.

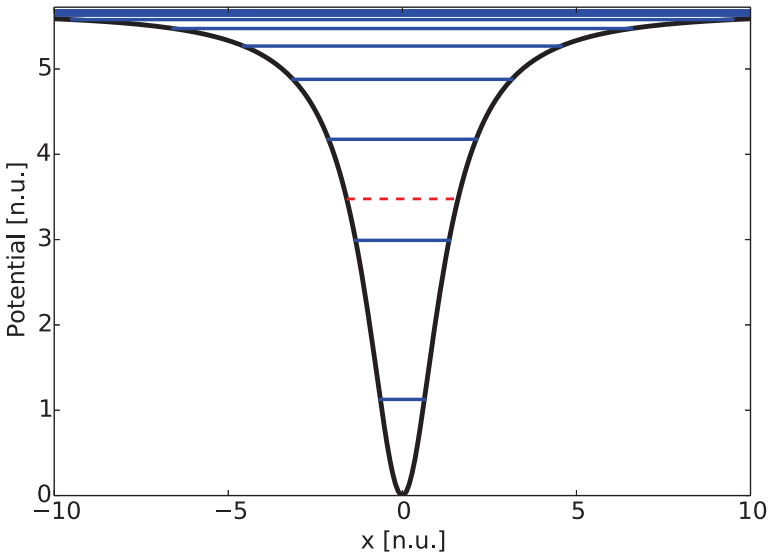

Figure 19.1: The trap potential (black), the bound-state energies (blue) and excitations (red dashed) from the ground state adopting a magnetic-field gradient of a frequency of $\omega = 2.35\,\text{n.u.}$ for the Lorentz potential with parameters specified in Table C.8.

The reason for this choice is that at the time when these calculations were performed, the experimental setup incorporated this waist size (which then changed again) and the primary goal of the calculations was to compare to the experiment.

In Figure 19.2, the total atom-loss yields for the simulator are compared to the ion yields of a 3D hydrogen atom and the 1D soft-Coulomb potential given in Eq. (17.1). In the multiphoton regime, lowest-order perturbation theory (LOPT) [161] predicts a behavior of the yield according to

$$\Gamma \propto I^N \tag{19.5}$$

where N is the minimum number of photons required for ionization. Thus, in a logarithmic plot, $\log(\Gamma) \propto N \log(I)$, such that LOPT predicts a line with a slope equal to N. These lines are indicated magenta dotted in Figure 19.2. The simulator as well as the Coulomb systems show the expected linear behavior in the multiphoton regime far from saturation.

Next, the behavior of the (FC-)ADK yield is considered. For the 1D soft-Coulomb potential the FC-ADK yield shows a quantitatively better agreement to the TDSE results compared to the solution for the 3D hydrogen atom, despite the fact that the ADK formula was originally derived for the 3D case. The better agreement is particularly visible for $\lambda = 176\,\mathrm{nm}$ at ,e. g., $I_0 = 10^{12}\,\mathrm{W/cm^2}$ where the 3D (1D) FC-ADK solution differs from the TDSE solution by about 2 (about 1) orders of magnitude. Hence, at least in the parameter regime of high photon frequencies (FC)-ADK is better suitable to describe 1D systems compared to 3D Coulomb systems. The reason is that in the (FC-)ADK theory tunneling along the field direction is considered and in 1D tunneling in the direction of the field is exaggerated compared to the 3D case where also other spatial degrees of freedom exist.

For the simulator, the accuracy of the FC-ADK depends on the frequency: at $\mathcal{B}_0'^2 = 0.1\,(\mathrm{G/cm})^2$ the FC-ADK yield underestimates the TDSE yield by 1 (2) orders of magnitude for $\omega/(2\pi) = 0.5\,\mathrm{kHz}$ ($\omega/(2\pi) = 0.3\,\mathrm{kHz}$). Hence, the quantitative deviation to the TDSE solution is comparable to the one for the Coulombic systems. This is remarkable, having in mind that in the derivation of the (FC-)ADK rate the long-range $1/r$ term of the ionic potential is explicitly taken into account.

Another evidence that the simulator reproduces typical strong-field effects is the occurrence of a channel closing for $\beta = 1.94$. The yields of all three systems show a "kink" directly after the position where the first channel closing appears (vertical dashed black lines). Such a channel closing is an effect that can occur in the multiphoton regime ($\gamma \gg 1$), when the ponderomotive energy that increases with the gradient (field) strength gets such large that the N photon ionization becomes prohibited and $N + 1$ photons are needed for ionization, i. e. for

$$F_{\mathrm{cc}} = \sqrt{(N\omega - E_{\mathrm{b}})4\omega^2} \quad . \tag{19.6}$$

The effect of the channel closing disappears for $\beta = 3.23$ since the first channel closing is already in the saturation regime where $\gamma \approx 1$.

Next, the influence of the waist size on the behavior of the yield is considered. In Figure 19.3, the atom-loss yield for the simulator for $\beta = 3.23$ (identical to the one in Figure 19.2) is considered in comparison to the one for a Lorentz potential with a wider waist of $w_0 = 1.66\,\mu\mathrm{m}$ (see Table C.9 for all parameters and the conversion

constants[1]). Both spectra show the typical LOPT slope (visible as agreement in the slope with the magenta dotted line). A comparison of the TDSE and the FC-ADK yield reveals a strong dependence of the ladder on the waist size. By increasing the waist size, the FC-ADK yield increases relative to the TDSE yield. In the regime $\gamma > 1$, the FC-ADK yield is smaller than the TDSE yield for the smallest waist ($w_0 = 1.1\,\mu$m, Figure 19.3 left), almost matches the TDSE yield for an increasing waist size ($w_0 = 1.66\,\mu$m, Figure 19.3 right), and is finally larger in case of the soft-Coulomb potential (Figure 19.2 middle right) because it has an even wider range.

Finally, an interesting effect in the structure in the saturation regime ($\gamma < 1$ for both waists) can be presented. A *stabilization* of the yield is visible such that the yield does not approach unity (full saturation) but rather seems to fluctuate at values far from saturation. This stabilization effect can neither be found for the smaller waist nor for the Coulombic systems shown in Figure 19.2. The essential difference between both waists is that the larger waist decreases the relative distance of the ground to the first excited state, i. e. an increase of the waist makes the eigenenergy spectrum more harmonic. This introduces stronger resonance effects. These are the explanation for the strong structure in the saturation regime and the stabilization of the yield far from unity. The detection of such a waist-size-dependent resonance-induced saturation gives an idea about the possibilities introduced by the flexibility and control of the quantum simulator.

[1] A manipulation of the waist changes also other quantities since the unit length that is defined by the size of the ground state varies.

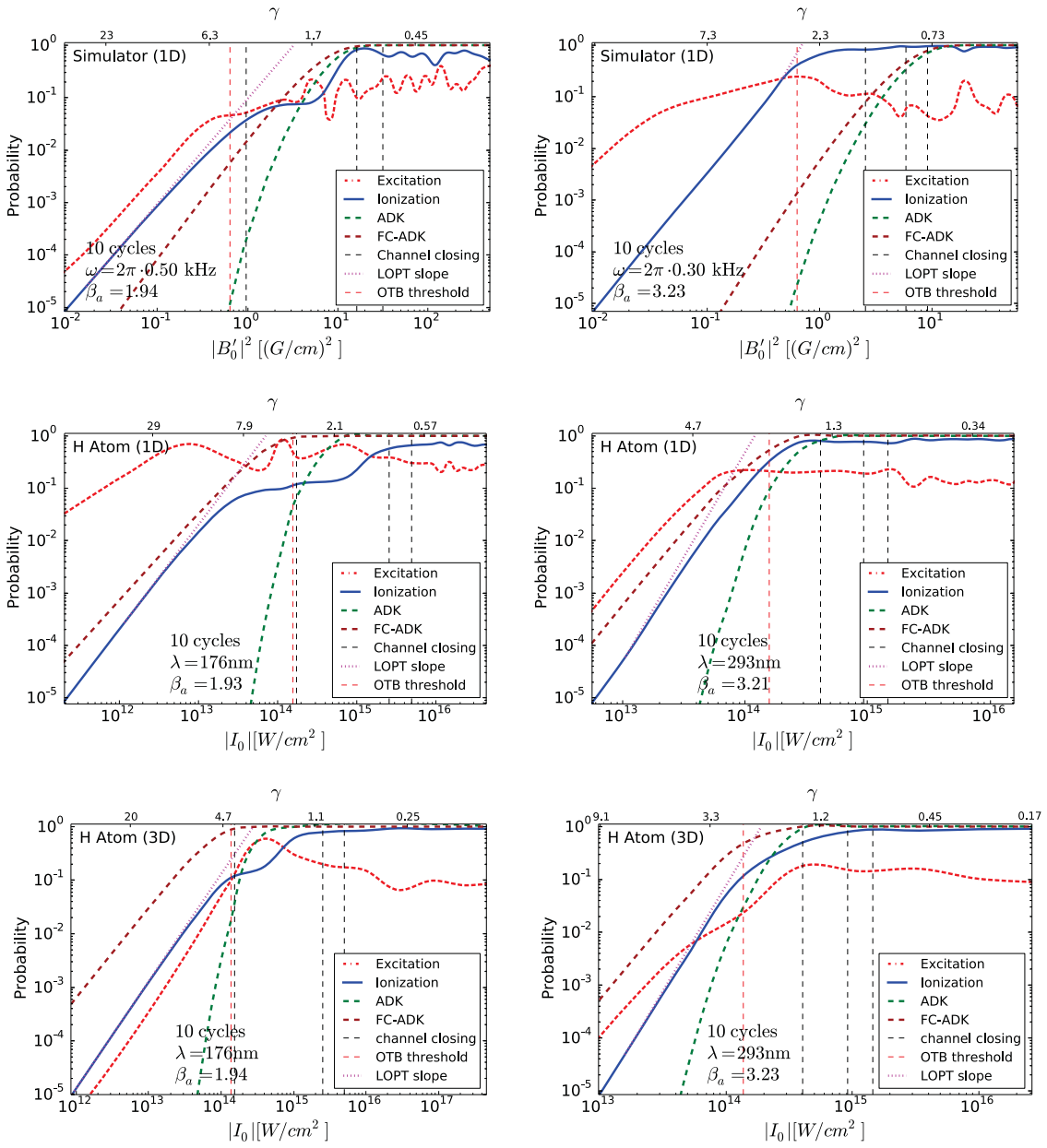

Figure 19.2: Total yields (solid blue lines) of the simulator (upper row) compared to the ones of the 1D soft-Coulomb potential (middle row) and 3D hydrogen atom (bottom row) for a variation of the magnetic-field gradient strength (laser intensity). The results shown in the left column correspond to a pulse frequency of $\omega = E_\mathrm{b}/1.94$. The ones in the right column correspond to $\omega = E_\mathrm{b}/3.23$. Additionally, the probabilities of an excitation (red dashed lines), the results of FC-ADK (brown dashed lines), ADK (green dashed lines) and the expected slope of the lowest order perturbation theory (magenta dotted lines) are presented. The vertical red dashed line indicates the OTB threshold, the vertical black dashed lines correspond to the position of channel closings. As a second scale the Keldysh parameter γ is shown at the top of the graphs. The same basis sets were used as specified in the caption of Figure 17.6.

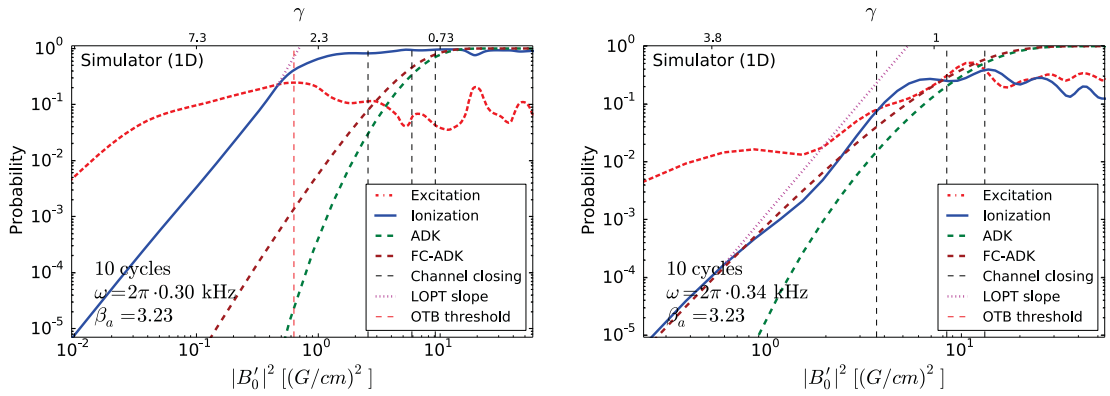

Figure 19.3: Total yields of the simulator as in Figure 19.2 but for $\omega = E_\mathrm{b}/3.23$ and trap potentials with waists of $w_0 = 1.1\,\mu$m (left) and $w_0 = 1.66\,\mu$m (right). For the solutions of the TDSEs the basis set specified in Table C.4 was used.

19.3 Yield vs. frequency

After having demonstrated that a variation of the intensity unveils interesting strong-field effects, frequency scans are performed. Typically, the dominant feature of frequency scans of the total yield are resonances occurring at N-photon ionization thresholds. These resonances are especially pronounced in the multiphoton regime as can be seen in the right column of Figure 19.4. There, the simulator shows resonantly enhanced yields around the N-photon thresholds in agreement to the Coulombic systems. These are the thresholds where $E_\mathrm{b} = N\omega$. The resonances are not reproduced by the (FC-)ADK calculations which are derived for the quasi-static regime and hence do not take into account the channel closing that is responsible for the resonances. The resonant peaks lead to an enhancement of the yield up to three orders of magnitude. Hence, the (FC-)ADK rates do not provide quantitative results but in the best case a prediction of the overall behavior.

The comparison of the excitation and ionization probabilities in Figure 19.4 reveal an opposing behavior for the higher intensities (left column) compared to the lower intensities (right column). While for the higher intensities (left column) the excitation and ionization probabilities follow each other (visible in the common enhancement at the channel-closing thresholds especially for the 1D systems for $n > 1$), for the lower intensities they show an opposing behavior (most significantly visible for $1 < n < 2$). It is a result of the conservation of probability $Y + P_e + P_g = 1$, i. e. the particle can either ionize (Y), end up in an excited state (P_e) or reside in the ground state (P_g). For high intensities the probability to stay in the ground state is small, such that the $P_g \approx 1 - Y$ which leads to the mentioned opposing behavior. Differently, at smaller intensities (right column), the probability to stay in the ground state is dominant, especially for small frequencies ($n < 3$). Consequently, with an increasing ionization probability also the excitation probability increases, e. g. both have a resonant character at the channel-closing thresholds.

On the first glance surprising, for all spectra the ionization and excitation probability show a crossing point almost exactly at the $n = 1$ photon threshold. The reason is that for a symmetric pulse envelope, at the $n = 1$ threshold half of the frequency (energy) width of the pulse which is given by the Fourier transform of the temporal pulse shape lies already in the continuum (leading to ionization) and the other half is below the continuum threshold leading to excitation. For $n > 1$ a rapid decrease of the excitation probability is observable because of direct ionization.

Interestingly, while for weaker field strengths (right column of Figure 19.4) the yields increase with the frequency ω of the external perturbation for lower intensities (left column of Figure 19.4) the yields rather fall with the intensities, especially in the transition regime between the multiphoton and the adiabatic regime ($0.9 \lesssim \gamma \lesssim 3$).

On the first glance this might be counter-intuitive since for an increasing photon energy the yield is expected to increase. However, an explanation of the decreasing yield is that with the transition from the adiabatic to the multiphoton regime the confined particle cannot escape from the trap anymore, because the spatial variation of the external field becomes too fast. In a semi-classical picture, ionization is damped because before the particle can escape the trap in one direction, the field direction has already reversed leading to an acceleration of the particle wavepacket to the opposite direction. The consequence is a dynamical trapping of the particle in the confining potential. In fact, this mechanism is similar to the one of FTI discussed in Chapter 18 where the particle was captured in a highly excited bound state because it could not gain enough drift velocity before the gradient reverses its direction. In fact, in the 1D systems, this dynamical-trapping effect is even more strongly pronounced which is understandable because in 3D there exist more versatile exit channels due to the higher dimensionality. On the contrary, in 1D the particle can only escape in the field direction.

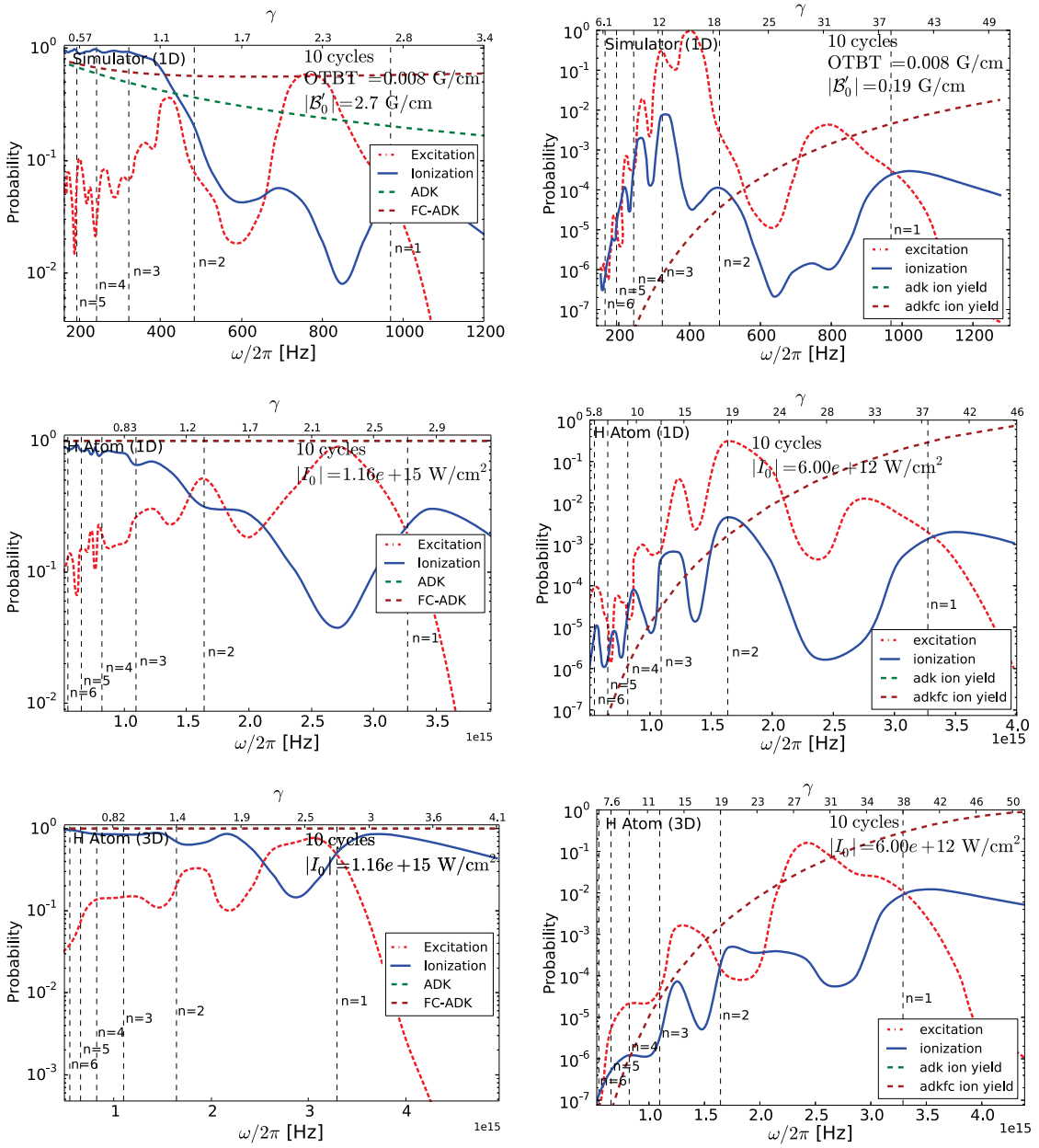

Figure 19.4: Total yields (solid blue lines) of the simulator (upper row) compared to the ones of the 1D soft-Coulomb potential (middle row) and 3D hydrogen atom (bottom row) for a variation of the frequency of the external perturbation. The gradient strength of the simulator result shown in the left (right) column of $|\mathcal{B}_0'| = 2.7\,\mathrm{G/cm}$ ($|\mathcal{B}_0'| = 0.054\,\mathrm{G/cm}$) correspond to a laser intensity $|I_0| = 1.16 \cdot 10^{15}\,\mathrm{W/cm^2}$ ($|I_0| = 4.64 \cdot 10^{15}\,\mathrm{W/cm^2}$) obtained by the parameter mapping described in Section 14.3. Additionally, the probabilities of an excitation (red dashed lines), the results of FC-ADK (brown dashed lines) and ADK (green dashed lines) are presented. The vertical black dashed lines correspond to the position of N-photon resonances. As a second scale the Keldysh parameter γ is shown.

20 Conclusion of Part III

A quantum simulator for attosecond physics based on ultracold atoms in an optical trap potential is presented. The simulator delivers a novel tool to systematically study strong-field many-body physics. Hence, it represents an assistance (or in the best case even an alternative) to corresponding strong-field experiments. The need for such a tool stems from the fact that *ab initio* calculations of the TDSE of strong-field many-body systems are extremely demanding and can only be performed for small systems. Today's state of the art is the treatment of H_2 and He. As a consequence, widely used simplified models cannot be verified. Moreover, constraints one faces in strong-field experiments, such as the limitation to a specific molecular geometry, a fixed number of electrons per element or molecule, fixed interaction strengths, and restricted pulse shapes are overcome in the simulator system. The simulation can even reach parameter regions which are beyond those nowadays realizable in strong-field experiments, including, e. g., exotic pulse shapes and effective pulse durations corresponding to the sub-attosecond regime. In fact, the proposed attosecond science in slow motion may shed light onto the ongoing debate on tunneling times [189, 203–205] by the unique control of the experimental setup and the extreme time resolution.

The connection of the strong-field and quantum-simulator Hamiltonian is established by the simulator mapping. For a specific experimental realization of the quantum simulator, a parameter mapping allows for the translation of a strong-field laser pulse to the corresponding magnetic-field gradient pulse.

In order to validate the quantum simulator numerically, a concrete realistic experimental realization is proposed that extends an existing sophisticated experimental setup. The numerical analysis of the TDSE and SFA results for this setup, a (1D) soft-Coulomb potential, and a (3D) hydrogen atom revealed that adopting experimentally realistic parameters the simulator accurately reproduces the physics in several regimes of the laser-matter interaction. In the multiphoton regime, the simulator replicates multiphoton peaks in agreement to the 3D hydrogen atom even quantitatively. In the adiabatic regime, the rescattering plateau between $2U_p$ and $10U_p$ is even more accurately realized as in the Coulombic case. The latter paves the way to investigate in "slow motion" the topical effects of rescattering. It is astonishing that the slowing-down of the ultra-fast strong-field processes is up to 14 orders of magnitude.

Moreover, it is demonstrated quantitatively that the extremely popular SFA is clearly better applicable to the quantum simulator system than to a hydrogen atom in all regimes of the laser-matter interaction. While the small-scale structure of the differential yield is reproduced by the SFA for the simulator in the adiabatic regime, the yields for the TDSE and SFA differ significantly for the hydrogen atom. In the multiphoton regime, the differential yield for the three dominant ATI peaks are overestimated by the SFA compared to the TDSE solution by about three orders of magnitude. In contrast, for the simulator the SFA is remarkably quantitatively accurate. This behavior is understandable since the effective short-range assumptions entering the SFA are better fulfilled for the simulator system. Hence, the quantum simulator delivers a method to stringently validate the SFA for complicated many-body systems where it is routinely adopted to interpret strong-field experiments although its validity is completely unclear. Importantly, the validity of the SFA for the simulator provides a novel technique to image momentum-space densities in ultracold atom experiments.

By analyzing bound-state distributions of the final TDSE solution the occurrence of frustrated tunneling ionization was detected in the quantum-simulator system in analogy to recent results in strong-field systems. In order to validate the semiclassical picture underlying FTI, the TDSE results were compared to semiclassical Monte-Carlo simulations. The latter required as input the static tunneling rates for a 1D Lorentz potential. An analysis demonstrated that the method of solving the TDSE with a pulse containing a long plateau fails miserably. In contrast, the static rates can be calculated accurately by complex scaling and in the tunneling regime by a semiclassical approach. However, differently than stated in literature, for the latter only if proposed approximations are neither applied to the bound state wavefunction nor to the Gamow factor. Finally, it was demonstrated that the semiclassical FTI picture is valid for the 1D simulator system, in fact, even in the OTB regime.

An investigation of the experimentally directly accessible total yields revealed that versatile features of the strong-field ionization are present in the simulator system. Beyond reproducing characteristic strong-field features, the variability of the simulator allows for the systematical investigation of interesting effects. For instance, a resonance-induced stabilization of the yield in the saturation regime can be observed. By varying the potential depth it was demonstrated that this effect is strongly dependent on the distribution of the bound states. The stabilization is enhanced when the bound-state distribution becomes more harmonic, i. e. if the gap between the ground and first excited bound state is reduced compared the Coulomb system introducing a resonantly enhanced population of excited bound states. Moreover, a dynamical trapping of the atom is revealed in the transition of the adiabatic to the multiphoton regime. Similar to the semiclassical picture of

FTI, ionization is damped because before the particle can escape the trap in one direction, the field direction has already reversed leading to an acceleration of the particle wavepacket in the opposite direction.

The experimental realization of the quantum simulator following the here presented proposal is under way. The author is very excited for first experimental results of attosecond science in slow motion.

21 Final summary and outlook

The first objective of this thesis was to develop the theory of inelastic CIR and to obtain a comprehensive understanding of c.m.-rel. motion coupling resonances. One major achievement was to present a thorough explanation of the Innsbruck loss experiment [39]. In particular, it was revealed why the splitting of the resonance position for a transversal anisotropic quasi-1D confinement and a resonance position for a negative value of the s-wave scattering length cannot be described by elastic CIR as first persistently presumed in the community. An intuitive reason is that at the elastic CIR the systems energy and square modulus of the wavefunction are equivalent to the one of non-interacting identical fermions which is not subject to loss resonances. A formal argument is that the ground trap state does not couple to a molecular eigenstate at the elastic CIR which would support for enhanced three-body losses. In contrast, inelastic CIR trigger a molecule formation and subsequent three-body collisions that lead to the observed losses. At the inelastic CIR a molecular bound state with c.m. excitation couples to a state of an unbound atom pair in the c.m. ground state due to the anharmonicity of the external confinement. Quantitative agreement is found between the experimental results [46] and the theory of inelastic CIR. The latter was presented in form of *ab initio* calculations as well as by a model that supports for easy-to-access analytical expressions for the resonance positions and coupling strengths. The model is demonstrated to give quantitatively accurate results for single-well potentials of sufficient depth. For multi-well potentials, the effect of particle loss at inelastic CIR was also identified by heavy *ab initio* calculations in accordance with loss measurements of an ultracold quantum gas of cesium atoms confined to a shallow 3D optical lattice [44]. There, starting in a Mott-insulator state the losses at the inelastic CIR go along with a tunneling process. However, inelastic CIR are also observed in connection with an unconventional ground state. Yet, the unique evidence that the losses in the many-body cesium systems [39, 44] are caused by inelastic CIR was only possible by performing an additional experiment that excludes other proposed mechanisms like elastic CIR, multichannel, cesium-specific, or many-body effects: the observation of a coherent molecule formation at inelastic CIR in a two-body system of lithium atoms initially prepared in the lowest trap state [42]. Quantitative agreement of the calculated and measured resonance positions, widths and coupling strengths confirms not only quantitatively the theory of inelastic CIR but also uniquely distinguishes them from

the elastic CIR that is adopted in the experiment to tune the 1D effective interaction strength. It was demonstrated explicitly that at the elastic CIR a molecule formation is absent.

The fact that the formation of molecules at the inelastic CIR can be performed fully coherently and even at a fixed interaction strength by a variation of the confinement geometry may pave the way for a coherent molecule association and controlled tuning of the interaction behavior in ultracold atom experiments where magnetic Feshbach resonances are inaccessible.

The universal nature of inelastic CIR was demonstrated recently for dipolar atoms and molecules [94] and even for Coulomb-interacting systems such as excitons and quantum dots [95]. There, the inelastic CIR were proposed for a novel kind of controlled single-photon source. At an inelastic CIR a variation of the exciton confinement leads to a redistribution of the charge density with subsequent increased annihilation probability of the electron-hole pair. Since this process can be steered *in situ* by a variation of the external confinement, single photons can be emitted on demand.

The universality of the concept of inelastic CIR might even be extensible to few-body systems where c.m. excited few-body bound states such as c.m. excited Efimov states may result in inelastic few-body CIR. In order to be able to treat computationally such ultracold few-body systems with a variable number of particles and variable trap potentials, a new theoretical method was developed. This was necessary because the treatment of inelastic CIR requires to abandon one of the most widely used approximations in ultracold research but especially in the theory of ultracold few-body systems, the harmonic approximation. The approach uses concepts of traditional computational quantum chemistry, i. e. Hartree-Fock and configuration interaction. In order to adopt these concepts a mapping of electronic structure systems onto ultracold atomic systems was performed. This is the identification and replacement of the Coulombic electron-electron interaction with a short-range atomic interaction and of the Coulombic nuclear-electronic interaction by an external, optically fabricated trap potential. In fact, while the replacement of the external potential is straightforward from a computational point of view, the usage of a short-range potential supporting bound states is inherently different to the electron-electron interaction that is solely repulsive, i. e. does *not* support for electron-electron bound states. The challenge of obtaining converged results stems form the introduction of two different lengths scales – the short-range bound-state regime, and the longer-range trap-state regime. Hence, short-range oscillatory structures in the relative motion need to be resolved by a Gaussian basis set that is distributed in a Cartesian frame.

By studying a finite-range Gaussian-shape interaction potential it has been demon-

strated that the effect of the contrary length scales can be overcome by widening the interaction range of the potential under the cost of introducing higher-order p and d-wave interactions, for instance. However, it is demonstrated that these contributions are negligible in energy which leads to a realistic description of the ultracold regime.

The investigation of a zero-range contact interaction potential discloses the need for a renormalization of the coupling constant. It turns out that this allows, at least in principle, to reconstruct the entire eigenenergy spectrum. Until converged results can be presented further optimizations to the code are necessary, including different initial densities, different types of basis sets such as Gaussian lobe functions, or a possible truncation of the CI space.

The next goals are, however, to directly apply the code to few-fermion systems. This is possible under full convergence in the mean-field regime. Here, the focus lies on the influence of multi-well potentials on few-body fermionic systems. Such systems are topical and intensively investigated experimentally.

The performed mapping of an electronic-structure system onto an ultracold-atom system by identifying the interaction and external potentials was, moreover, extended by a time-dependent linear perturbation. This leads to the prototype of an universal quantum simulator for attosecond science. The simulator proposal connects the very contrary physics of ultracold, trapped atomic gases and the one of atoms, ions, and molecules in ultra-intense, ultra-short laser pulses. In fact, it was demonstrated that in both systems equivalent physics is obtained within a slow-down of processes up to 14 orders of magnitude.

In fact, the quantum simulator delivers a novel tool for the systematic investigation of strong-field experiments that nowadays can only be interpreted by simplified and often unverifiable models. This unsatisfying situation in strong-field physics stems from the fact that, different to stationary problems in quantum chemistry, the time-evolution of perturbed quantum systems is computationally extremely demanding because all states including the continuum are coupled by the perturbation. As a consequence, the cutting edge of converged solutions of the TDSE are today atoms and molecules with a maximum number of two electrons, such as He and H_2. Attosecond-science experiments, however, routinely investigate complex many-body systems.

The core of the quantum simulator is built by the simulator mapping that identifies the field-free Hamiltonians in the very same way as already described for the few-body algorithm and additionally maps the electric charge, electric-field component and vectorpotential of the laser pulse on the atomic magnetic moment, magnetic-field gradient and temporal integral of the magnetic-field gradient, respectively. Moreover, natural units for the quantum simulator were introduced and a

parameter mapping was developed to translate parameters of a strong-field systems to corresponding parameters for the quantum simulator.

An experimental setup for the quantum simulator was proposed based on the extension of an existing experiment. Different studies were performed all under the prerequisite of experimental realizability. The theoretical investigation of the TDSE and SFA for a (1D) soft-Coulomb potential, a (3D) hydrogen atom, and the corresponding quantum simulator system revealed that the simulator accurately reproduces the physics in several regimes of the laser-matter interaction, including the behavior of total yields, channel closings and the topical effect of frustrated tunneling ionization. Moreover, the investigation of differential yields discloses that in the multiphoton regime *quantitative* agreement to the 3D hydrogen atom is achieved. In the adiabatic regime, strong-field rescattering models precisely describe the simulator system, even more accurate than 3D hydrogen. This is reflected by the fact that the theoretically predicted rescattering plateau is reproduced in highest accuracy within the simulator. Finally, the extremely popular SFA is more powerful for the quantum simulator system than for a hydrogen atom in all regimes of the laser-matter interaction. The reason is that the effective short-range assumptions of the SFA are better suited for the simulator system. Consequently, the quantum simulator delivers a novel and unique tool to systematically validate the SFA for many-body strong-field systems.

The quantum simulator proposal covers an interesting back action on ultracold atoms. The validity of the SFA for the quantum simulator can deliver a new technique to image momentum-space densities in ultracold quantum gases.

Beyond this thesis, the next step is the investigation of the quantum simulator for a realistic 3D Gaussian-beam potential. In comparison to the TDSE solution of, e. g., atomic hydrogen, the challenge is the coupling of all spatial coordinates by the Gaussian confinement. Such calculations can hopefully even more accurately guide a first quantum-simulator experiment. Moreover, a study of two confined ultracold atoms exposed to a periodically driven magnetic-field gradient is highly interesting. In comparison to the Coulomb interaction, it can reveal the influence of a short-range interaction in the strong-field regime.

In fact, the investigation of driven ultracold atomic systems is of great interest itself, also beyond the connection to attosecond physics. Similar to the transfer of ideas from condensed-matter physics to the physics of ultracold atoms in the early days of ultracold research, the field can benefit from a solid base of knowledge build in decades of strong-field physics research.

Bibliography

[1] M. H. Anderson, J. R. Ensher, M. R. Matthews, C. E. Wieman, and E. A. Cornell. Observation of Bose-Einstein condensation in a dilute atomic vapor. *Science*, 269:198, 1995.

[2] K. B. Davis, M. O. Mewes, M. R. Andrews, N. J. van Druten, D. S. Durfee, D. M. Kurn, and W. Ketterle. Bose-Einstein condensation in a gas of sodium atoms. *Phys. Rev. Lett.*, 75:3969, 1995.

[3] Herman Feshbach. Unified theory of nuclear reactions. *Ann. of Phys.*, 5:357, 1958.

[4] Cheng Chin, Rudolf Grimm, Paul Julienne, and Eite Tiesinga. Feshbach resonances in ultracold gases. *Rev. Mod. Phys.*, 82:1225, 2010.

[5] C. J. Pethick and H. Smith. *Bose-Einstein condensation in dilute gases*. Cambridge University Press, Cambridge, UK, 2002.

[6] Immanuel Bloch. Ultracold quantum gases in optical lattices. *Nat. Phys.*, 1: 23, 2005.

[7] Christof Weitenberg, Manuel Endres, Jacob F. Sherson, Marc Cheneau, Peter Schausz, Takeshi Fukuhara, Immanuel Bloch, and Stefan Kuhr. Single-spin addressing in an atomic Mott insulator. *Nature*, 471:319, 2011.

[8] F. Serwane, G. Zürn, T. Lompe, T. B. Ottenstein, A. N. Wenz, and S. Jochim. Deterministic preparation of a tunable few-fermion system. *Science*, 332 (6027):336, 2011.

[9] W. S. Bakr, A. Peng, M. E. Tai, R. Ma, J. Simon, J. I. Gillen, S. Fölling, L. Pollet, and M. Greiner. Probing the superfluid-to-Mott insulator transition at the single-atom level. *Science*, 329:547, 2010.

[10] Franco Dalfovo, Stefano Giorgini, Le P. Pitaevskii, and Sandro Stringari. Theory of Bose-Einstein condensation in trapped gases. *Rev. Mod. Phys.*, 71:463, 1999.

[11] P. S. Jessen, D. L. Haycock, G. Klose, and G. A. Smith. Quantum control and information processing in optical lattices. *Quant. Inf. Comp*, 1:20, 2001.

[12] A. Micheli, G. K. Brennen, and P. Zoller. A toolbox for lattice-spin models with polar molecules. *Nat. Phys.*, 2:341, 2006.

[13] P. Rabl, D. DeMille, J. M. Doyle, M. D. Lukin, R. J. Schoelkopf, and P. Zoller. Hybrid quantum processors: Molecular ensembles as quantum memory for solid state circuits. *Phys. Rev. Lett.*, 97:033003, 2006.

[14] Philipp-Immanuel Schneider and Alejandro Saenz. Quantum computation with ultracold atoms in a driven optical lattice. *Phys. Rev. A*, 85:050304, 2012.

[15] A. Marte, T. Volz, J. Schuster, S. Dürr, G. Rempe, E. G. M. van Kempen, and B. J. Verhaar. Feshbach resonances in rubidium 87: Precision measurement and analysis. *Phys. Rev. Lett.*, 89:283202, 2002.

[16] Cheng Chin, Vladan Vuletic, Andrew J. Kerman, Steven Chu, Eite Tiesinga, Paul J. Leo, and Carl J. Williams. Precision Feshbach spectroscopy of ultracold Cs_2. *Phys. Rev. A*, 70:032701, 2004.

[17] Artur Widera, Olaf Mandel, Markus Greiner, Susanne Kreim, Theodor W. Hänsch, and Immanuel Bloch. Entanglement interferometry for precision measurement of atomic scattering properties. *Phys. Rev. Lett.*, 92:160406, 2004.

[18] T. Zelevinsky, S. Kotochigova, and Jun Ye. Precision test of mass-ratio variations with lattice-confined ultracold molecules. *Phys. Rev. Lett.*, 100:043201, 2008.

[19] G. Zürn, T. Lompe, A. N. Wenz, S. Jochim, P. S. Julienne, and J. M. Hutson. Precise characterization of ^{6}Li feshbach resonances using trap-sideband-resolved rf spectroscopy of weakly bound molecules. *Phys. Rev. Lett.*, 110: 135301, 2013.

[20] D. Jaksch and P. Zoller. The cold atom hubbard toolbox. *Ann. of Phys.*, 315: 52, 2005.

[21] Martin W Zwierlein, André Schirotzek, Christian H Schunck, and Wolfgang Ketterle. Fermionic superfluidity with imbalanced spin populations. *Science (New York, N.Y.)*, 311(5760):492–6, 2006.

[22] U Schneider, L Hackermüller, S Will, Th Best, I Bloch, T A Costi, R W Helmes, D Rasch, and A Rosch. Metallic and insulating phases of repulsively interacting fermions in a 3D optical lattice. *Science*, 322(5907):1520–5, 2008.

[23] Yean-An Liao, Ann Sophie C Rittner, Tobias Paprotta, Wenhui Li, Guthrie B Partridge, Randall G Hulet, Stefan K Baur, and Erich J Mueller. Spin-imbalance in a one-dimensional Fermi gas. *Nature*, 467(7315):567–9, 2010.

[24] R. Gerritsma, G. Kirchmair, F. Zähringer, E. Solano, R. Blatt, and C. F. Roos. Quantum simulation of the Dirac equation. *Nature*, 463:68, 2010.

[25] Jonathan Simon, Waseem S. Bakr, Ruichao Ma, M. Eric Tai, Philipp M. Preiss, and Markus Greiner. Quantum simulation of antiferromagnetic spin chains in an optical lattice. *Nature*, 472:307, 2011.

[26] Manuel Endres, Takeshi Fukuhara, David Pekker, Marc Cheneau, Peter Schauss, Christian Gross, Eugene Demler, Stefan Kuhr, and Immanuel Bloch. The 'Higgs' amplitude mode at the two-dimensional superfluid/Mott insulator transition. *Nature*, 487:454, 2012.

[27] Belén Paredes, Artur Widera, Valentin Murg, Olaf Mandel, Simon Fölling, Ignacio Cirac, Gora V. Shlyapnikov, Theodor W. Hänsch, and Immanuel Bloch. Tonks-Girardeau gas of ultracold atoms in an optical lattice. *Nature*, 429:277, 2004.

[28] Toshiya Kinoshita, Trevor Wenger, and David S. Weiss. Observation of a one-dimensional tonks-girardeau gas. *Science*, 305:1125, 2004.

[29] Toshiya Kinoshita, Trevor Wenger, and David S. Weiss. Local pair correlations in one-dimensional bose gases. *Phys. Rev. Lett.*, 95:190406, 2005.

[30] Thilo Stöferle, Henning Moritz, Kenneth Günter, Michael Köhl, and Tilman Esslinger. Molecules of Fermionic atoms in an optical lattice. *Phys. Rev. Lett.*, 96:030401, 2006.

[31] C. Ospelkaus, S. Ospelkaus, L. Humbert, P. Ernst, K. Sengstock, and K. Bongs. Ultracold heteronuclear molecules in a 3D optical lattice. *Phys. Rev. Lett.*, 97:120402, 2006.

[32] E. Haller, M. Gustavsson, M. J. Mark, J. G. Danzl, R. Hart, G. Pupillo, and H.-C. Nägerl. Realization of an Excited, Strongly Correlated Quantum Gas Phase. *Science*, 325:1224, 2009.

[33] Elmar Haller, Russell Hart, Manfred J. Mark, Johann G. Danzl, Lukas Reichsöllner, Mattias Gustavsson, Marcello Dalmonte, Guido Pupillo, and Hanns-Christoph Nägerl. Pinning quantum phase transition for a Luttinger liquid of strongly interacting bosons. *Nature*, 466:597, 2010.

[34] G. Zürn, F. Serwane, T. Lompe, A. N. Wenz, M. G. Ries, J. E. Bohn, and S. Jochim. Fermionization of two distinguishable fermions. *Phys. Rev. Lett.*, 108:075303, 2012.

[35] M. Olshanii. Atomic scattering in the presence of an external confinement and gas of impenetrable Bosons. *Phys. Rev. Lett.*, 81:938, 1998.

[36] T. Bergeman, M. G. Moore, and M. Olshanii. Atom-atom scattering under cylindrical harmonic confinement: Numerical and analytic studies of the confinement induced resonance. *Phys. Rev. Lett.*, 91:163201, 2003.

[37] M. Girardeau. Relationship between systems of impenetrable bosons and fermions in one dimension. *J. Math. Phys.*, 1:516, 1960.

[38] Elliott H. Lieb and Werner Liniger. Exact analysis of an interacting Bose gas. i. the general solution and the ground state. *Phys. Rev.*, 130:1605, 1963.

[39] Elmar Haller, Manfred J. Mark, Russell Hart, Johann G. Danzl, Lukas Reichsöllner, Vladimir Melezhik, Peter Schmelcher, and Hanns-Christoph Nägerl. Confinement-induced resonances in low-dimensional quantum systems. *Phys. Rev. Lett.*, 104:153203, 2010.

[40] Shi-Guo Peng, Seyyed S. Bohloul, Xia-Ji Liu, Hui Hu, and Peter D. Drummond. Confinement-induced resonance in quasi-one-dimensional systems under transversely anisotropic confinement. *Phys. Rev. A*, 82:063633, 2010.

[41] Wei Zhang and Peng Zhang. Confinement-induced resonances in quasi-one-dimensional traps with transverse anisotropy. *Phys. Rev. A*, 83:053615, 2011.

[42] S. Sala, G. Zürn, T. Lompe, A. N. Wenz, S. Murmann, F. Serwane, S. Jochim, and A. Saenz. Coherent molecule formation in anharmonic potentials near confinement-induced resonances. *Phys. Rev. Lett.*, 110:203202, 2013.

[43] Simon Sala and Alejandro Saenz. Inelastic resonances due to the coupling of center-of-mass to relative motion, 2015. arXiv:1509.05799.

[44] M. J. Mark, S. Sala, F. Meinert, K. Lauber, E. Kirilov, A. Saenz, and H.-C. Nägerl. Observation of Ultra-narrow Feshbach Resonances and Inelastic Confinement-Induced Resonances in a Three Dimensional Optical Lattice, 2015. In preparation.

[45] D. Blume. Few-body physics with ultracold atomic and molecular systems in traps. *Rep. Prog. Phys.*, 75:046401, 2012.

[46] Simon Sala, Philipp-Immanuel Schneider, and Alejandro Saenz. Inelastic confinement-induced resonances in low-dimensional quantum systems. *Phys. Rev. Lett.*, 109:073201, 2012.

[47] Simon Sala, Johann Förster, and Alejandro Saenz. Ultracold-atom quantum simulator for attosecond science, 2013. arXiv:1311.2304.

[48] D. Jaksch, C. Bruder, J. I. Cirac, C. W. Gardiner, and P. Zoller. Cold Bosonic atoms in optical lattices. *Phys. Rev. Lett.*, 81:3108, 1998.

[49] M. Greiner, O. Mandel, T. Esslinger, T.W. Hänsch, and I. Bloch. Quantum phase transition from a superfluid to a Mott insulator in a gas of ultracold atoms. *Nature*, 415:39, 2002.

[50] C. Orzel, A. K. Tuchman, M. L. Fenselau, M. Yasuda, and M. A. Kasevich. Squeezed states in a bose-einstein condensate. *Science*, 291:2386, 2001.

[51] Andrew G. Truscott, Kevin E. Strecker, William I. McAlexander, Guthrie B. Partridge, and Randall G. Hulet. Observation of fermi pressure in a gas of trapped atoms. *Science*, 291:2570, 2001.

[52] T. Loftus, C. A. Regal, C. Ticknor, J. L. Bohn, and D. S. Jin. Resonant control of elastic collisions in an optically trapped fermi gas of atoms. *Phys. Rev. Lett.*, 88:173201, 2002.

[53] Sergey Grishkevich and Alejandro Saenz. Influence of a tight isotropic harmonic trap on photoassociation in ultracold homonuclear alkali-metal gases. *Phys. Rev. A*, 76:022704, 2007.

[54] A. R. Janzen and R. A. Aziz. An accurate potential energy curve for helium based on ab initio calculations. *The Journal of Chemical Physics*, 107(3):914, 1997.

[55] A. Derevianko, J. F. Babb, and A. Dalgarno. High-precision calculations of van der waals coefficients for heteronuclear alkali-metal dimers. *Phys. Rev. A*, 63:052704, 2001.

[56] T. Lahaye, C. Menotti, L. Santos, M. Lewenstein, and T. Pfau. The physics of dipolar bosonic quantum gases. *Rep. Prog. Phys.*, 72:126401, 2009.

[57] Florian Scheck. *Theoretische Physik 2, Nichtrelativistische Quantentheorie, Vom Wasserstoff zu den Vielteilchensystemen, 2. Auflage*. Springer, Berlin, Heidelberg, New York, 2005.

[58] Franz Schwabel. *Quantum Mechanics*. Springer, Berlin, Heidelberg, New York, 2007.

[59] Enrico Fermi. *La Ricerca Scientifica*, 7:13, 1936.

[60] K. Huang. *Statistical Mechanics*. New York: Wiley, 1963.

[61] Sergey Grishkevich, Philipp-Immanuel Schneider, Yulian V. Vanne, and Alejandro Saenz. Mimicking multichannel scattering with single-channel approaches. *Phys. Rev. A*, 81:022719, 2010.

[62] Thomas Busch, Berthold-Georg Englert, Kazimierz Rzazewski, and Martin Wilkens. Two cold atoms in a harmonic trap. *Found. Phys.*, 28:549, 1998.

[63] F. Deuretzbacher, K. Plassmeier, D. Pfannkuche, F. Werner, C. Ospelkaus, S. Ospelkaus, K. Sengstock, and K. Bongs. Heteronuclear molecules in an optical lattice: Theory and experiment. *Phys. Rev. A*, 77:032726, 2008.

[64] Sergey Grishkevich and Alejandro Saenz. Theoretical description of two ultracold atoms in a single site of a three-dimensional optical lattice using realistic interatomic interaction potentials. *Phys. Rev. A*, 80:013403, 2009.

[65] D. S. Petrov, M. Holzmann, and G. V. Shlyapnikov. Bose-Einstein condensation in quasi-2d trapped gases. *Phys. Rev. Lett.*, 84:2551, 2000.

[66] Bernd Fröhlich, Michael Feld, Enrico Vogt, Marco Koschorreck, Wilhelm Zwerger, and Michael Köhl. Radio-frequency spectroscopy of a strongly interacting two-dimensional fermi gas. *Phys. Rev. Lett.*, 106:105301, 2011.

[67] E. Haller and H.-C. Nägerl. private communication.

[68] Vanja Dunjko, Michael G. Moore, Thomas Bergeman, and Maxim Olshanii. Chapter 10 - confinement-induced resonances. In *Advances in Atomic, Molecular, and Optical Physics*, volume 60, pages 461 – 510. Academic Press, 2011.

[69] L. P. Pitaevskii and S. Stringari, editors. *Bose-Einstein Condensation*. Oxford University Press, Oxford, 2003.

[70] Zbigniew Idziaszek and Tommaso Calarco. Analytical solutions for the dynamics of two trapped interacting ultracold atoms. *Phys. Rev. A*, 74:022712, 2006.

[71] Eberhard Freitag and Rolf Busam. *Funktionentheorie 1*. Springer, Heidelberg, 2006.

[72] Jun-Jun Liang and Chao Zhang. Two ultracold atoms in a completely anisotropic trap. *Phys. Scr.*, 77:025302, 2008.

[73] Vladimir S. Melezhik and Peter Schmelcher. Multichannel effects near confinement-induced resonances in harmonic waveguides. *Phys. Rev. A*, 84: 042712, 2011.

[74] E. L. Bolda, E. Tiesinga, and P. S. Julienne. Ultracold dimer association induced by a far-off-resonance optical lattice. *Phys. Rev. A*, 71:033404, 2005.

[75] V. Peano, M. Thorwart, C. Mora, and R. Egger. Confinement-induced resonances for a two-component ultracold atom gas in arbitrary quasi-one-dimentional traps. *New J. Phys.*, 7:192, 2005.

[76] Vladimir Melezhik and Peter Schmelcher. Quantum dynamics of resonant molecule formation in waveguides. *New Journal of Physics*, 11(7):073031, 2009.

[77] Philipp-Immanuel Schneider, Sergey Grishkevich, and Alejandro Saenz. Ab initio determination of Bose-Hubbard parameters for two ultracold atoms in an optical lattice using a three-well potential. *Phys. Rev. A*, 80:013404, 2009.

[78] J. P. Kestner and L-M. Duan. Anharmonicity-induced resonances for ultracold atoms and their detection. *New J. Phys.*, 12:053016, 2010.

[79] G. Lamporesi, J. Catani, G. Barontini, Y. Nishida, M. Inguscio, and F. Minardi. Scattering in mixed dimensions with ultracold gases. *Phys. Rev. Lett.*, 104:153202, 2010.

[80] Manuel Valiente and Klaus Mølmer. Quasi-one-dimensional scattering in a discrete model. *Phys. Rev. A*, 84:053628, 2011.

[81] Sergey Grishkevich, Simon Sala, and Alejandro Saenz. Theoretical description of two ultracold atoms in finite three-dimensional optical lattices using realistic interatomic interaction potentials. *Phys. Rev. A*, 84:062710, 2011.

[82] I.S. Gradshteyn and I.M. Ryzhik. *Table of Integrals, Series, and Products*. Academic Press, 2007.

[83] J. Förster, A. Saenz, and U. Wolff. Matrix algorithm for solving Schrödinger equations with position-dependent mass or complex optical potentials. *Phys. Rev. E*, 86:016701, 2012.

[84] Sergey Grishkevich, 2009. PhD thesis, Humboldt-Universität zu Berlin.

[85] Shi-Guo Peng, Hui Hu, Xia-Ji Liu, and Peter D. Drummond. Confinement-induced resonances in anharmonic waveguides. *Phys. Rev. A*, 84:043619, 2011.

[86] Gerhard Zürn, 2012. PhD thesis, Ruprecht-Karls Universität Heidelberg.

[87] G. Zürn, T. Lompe, A. N. Wenz, S. Jochim, P. S. Julienne, and J. M. Hutson. Precise characterization of ^{6}Li feshbach resonances using trap-sideband-resolved rf spectroscopy of weakly bound molecules. *Phys. Rev. Lett.*, 110: 135301, 2013.

[88] T. Kraemer, J. Herbig, M. Mark, T. Weber, C. Chin, H.-C. Nägerl, and R. Grimm. Optimized production of a cesium bose–einstein condensate. *Applied Physics B*, 79(8):1013–1019, 2004.

[89] F. Meinert, M. J. Mark, E. Kirilov, K. Lauber, P. Weinmann, A. J. Daley, and H.-C. Nägerl. Quantum quench in an atomic one-dimensional ising chain. *Phys. Rev. Lett.*, 111:053003, 2013.

[90] A. D. Lange, K. Pilch, A. Prantner, F. Ferlaino, B. Engeser, H.-C. Nägerl, R. Grimm, and C. Chin. Determination of atomic scattering lengths from measurements of molecular binding energies near feshbach resonances. *Phys. Rev. A*, 79:013622, 2009.

[91] M. J. Mark, E. Haller, K. Lauber, J. G. Danzl, A. J. Daley, and H.-C. Nägerl. Precision measurements on a tunable Mott insulator of ultracold atoms. *Phys. Rev. Lett.*, 107:175301, 2011.

[92] A. J. Daley, J. M. Taylor, S. Diehl, M. Baranov, and P. Zoller. Atomic three-body loss as a dynamical three-body interaction. *Phys. Rev. Lett.*, 102:040402, 2009.

[93] M. J. Mark, E. Haller, K. Lauber, J. G. Danzl, A. Janisch, H. P. Büchler, A. J. Daley, and H.-C. Nägerl. Preparation and spectroscopy of a metastable mott-insulator state with attractive interactions. *Phys. Rev. Lett.*, 108:215302, 2012.

[94] Bruno Schulz, Simon Sala, and Alejandro Saenz. Resonances in ultracold dipolar atomic and molecular gases. *New J. Phys.*, 17:065002, 2015.

[95] Maria Troppenz, Simon Sala, Philipp-Immanuel Schneider, and Alejandro Saenz. Inelastic confinement-induced resonances in quantum dots, 2015. arXiv:1509.01159.

[96] V. Efimov. Energy levels arising from resonant two-body forces in a three-body system. *Phys. Lett. B*, 33:563, 1970.

[97] V. Efimov. Weakly bound states of three resonantly interacting particles. *Sov. J. Nucl. Phys.*, 12:598, 1971.

[98] V. Efimov. Energy levels of three resonantly interacting particles. *Nucl. Phys. A*, 210:157, 1973.

[99] Eric Braaten and H. W. Hammer. Universality in few-body systems with large scattering length. *Phys. Rep.*, 428:259–390, 2006.

[100] E. Braaten and H. W. Hammer. Efimov physics in cold atoms. *Ann. of Phys.*, 322:120, 2007.

[101] Jia Wang, J. P. D'Incao, B. D. Esry, and Chris H. Greene. Origin of the three-body parameter universality in efimov physics. *Phys. Rev. Lett.*, 108:263001, 2012.

[102] T. Kraemer, M. Mark, P. Waldburger, J. G. Danzl, C. Chin, B. Engeser, A. D. Lange, K. Pilch, A. Jaakkola, H.-C. Nägerl, and R. Grimm. Evidence for efimov quantum states in an ultracold gas of caesium atoms. *Nature*, 440: 315, 2006.

[103] G. Barontini, C. Weber, F. Rabatti, J. Catani, G. Thalhammer, M. Inguscio, and F. Minardi. Observation of heteronuclear atomic efimov resonances. *Phys. Rev. Lett.*, 103:043201, 2009.

[104] Noam Gross, Zav Shotan, Servaas Kokkelmans, and Lev Khaykovich. Observation of universality in ultracold ^{7}Li three-body recombination. *Phys. Rev. Lett.*, 103:163202, 2009.

[105] Scott E Pollack, Daniel Dries, and Randall G Hulet. Universality in Three- and Four-Body Bound States of Ultracold Atoms. *Science*, 326(5960):1683–1685, 2009.

[106] F. Ferlaino, S. Knoop, M. Berninger, W. Harm, J. P. D'Incao, H.-C. Nägerl, and R. Grimm. Evidence for universal four-body states tied to an efimov trimer. *Phys. Rev. Lett.*, 102:140401, 2009.

[107] J. R. Williams, E. L. Hazlett, J. H. Huckans, R. W. Stites, Y. Zhang, and K. M. O'Hara. Evidence for an excited-state efimov trimer in a three-component fermi gas. *Phys. Rev. Lett.*, 103:130404, 2009.

[108] M. Zaccanti, B. Deissler, C. D'Errico, M. Fattori, M. Jona-Lasinio, S. Müller, G. Roati, M. Inguscio, and G. Modugno. Observation of an Efimov spectrum in an atomic system. *Nat. Phys.*, page 10, 2009.

[109] Thomas Lompe, Timo B. Ottenstein, Friedhelm Serwane, Andre N. Wenz, Gerhard Zürn, and Selim Jochim. Radio-frequency association of efimov trimers. *Science*, 330(6006):940–944, 2010.

[110] Tao Yin, Peng Zhang, and Wei Zhang. Stable heteronuclear few-atom bound states in mixed dimensions. *Phys. Rev. A*, 84(5), 2011.

[111] Yujun Wang, W. Blake Laing, Javier von Stecher, and B. D. Esry. Efimov physics in heteronuclear four-body systems. *Phys. Rev. Lett.*, 108:073201, 2012.

[112] Trygve Helgaker, Poul Jorgensen, and Jeppe Olsen. *Molecular Electronic Structure Theory*. Wiley, Chichester, 2000.

[113] L. P. Pitaevsk. Vortex lines in an imperfect bose gas. *Soviet Physics JETP-USSR*, 13(2), 1961.

[114] E.P. Gross. Structure of a quantized vortex in boson systems. *Il Nuovo Cimento Series 10*, 20(3):454–477, 1961.

[115] Attila Szabo and Neil S Ostlund. *Modern Quantum Chemistry: Introduction to Advanced Electronic Structure Theory (Dover Books on Chemistry)*. Dover Publications, 1996.

[116] D.B. Cook. *Handbook of Computational Quantum Chemistry*. Dover books on chemistry. Oxford University Press, 1998.

[117] Richard P. Muller. PyQuante, Version 1.6.4, 2014. http://pyquante.sourceforge.net/.

[118] Pearu Peterson. F2PY: a tool for connecting Fortran and Python programs. *International Journal of Computational Science and Engineering*, 4(4):296, 2009.

[119] S. Behnel, R. Bradshaw, C. Citro, L. Dalcin, D.S. Seljebotn, and K. Smith. Cython: The best of both worlds. *Computing in Science Engineering*, 13(2): 31 –39, 2011.

[120] http://www.cython.org. December 27th, 2014.

[121] B. D. Esry and Chris H. Greene. Validity of the shape-independent approximation for Bose-Einstein condensates. *Phys. Rev. A*, 60:1451, 1999.

[122] Y. Alhassid, G. Bertsch, and L. Fang. New Effective Interaction for the Trapped Fermi Gas. *Phys. Rev. Lett.*, 100(23):230401, 2008.

[123] I. Stetcu, B. Barrett, U. van Kolck, and J. Vary. Effective theory for trapped few-fermion systems. *Phys. Rev. A*, 76(6):063613, 2007.

[124] I. Stetcu, B.R. Barrett, and U. van Kolck. No-core shell model in an effective-field-theory framework. *Phys. Rev. B*, 653(2-4):358–362, 2007.

[125] M. Rontani, S. Åberg, and S. M. Reimann. Configuration interaction approach to the few-body problem in a two-dimensional harmonic trap with contact interaction, 2008. arXiv:0810.4305.

[126] M. Rontani, J. Armstrong, Y. Yu, S. Åberg, and S. Reimann. Cold Fermionic Atoms in Two-Dimensional Traps: Pairing versus Hund's Rule. *Phys. Rev. Lett.*, 102(6):060401, 2009.

[127] P. R. Johnson, D. Blume, X. Y. Yin, W. F. Flynn, and E. Tiesinga. Effective renormalized multi-body interactions of harmonically confined ultracold neutral bosons. *New Journal of Physics*, 14:1–22, 2012.

[128] P. J. Knowles and N. C. Handy. A new determinant-based full configuration interaction method. *Chem. Phys. Lett.*, 111(4-5):315–321, 1984.

[129] B. Roos. A new method for large-scale ci calculations. *Chem. Phys. Lett.*, 15 (2):153 – 159, 1972.

[130] Jeppe Olsen, Bjorn O. Roos, Poul Jorgensen, and Hans Jorgen Aa. Jensen. Determinant based configuration interaction algorithms for complete and restricted configuration interaction spaces. *The Journal of Chemical Physics*, 89 (4):2185–2192, 1988.

[131] http://www.caam.rice.edu/software/ARPACK/. January 27th, 2014.

[132] Eric Braaten, Masaoki Kusunoki, and Dongqing Zhang. Scattering Models for Ultracold Atoms. *Ann. of Phys.*, 323(7):60, 2007.

[133] Richard P. Feynman. Simulating physics with computers. *International Journal of Theoretical Physics*, 21:467, 1982.

[134] Matthew P. A. Fisher, Peter B. Weichman, G. Grinstein, and Daniel S. Fisher. Boson localization and the superfluid-insulator transition. *Phys. Rev. B*, 40: 546, 1989.

[135] Thilo Stöferle, Henning Moritz, Christian Schori, Michael Köhl, and Tilman Esslinger. Transition from a strongly interacting 1D superfluid to a Mott insulator. *Phys. Rev. Lett.*, 92:130403, 2004.

[136] Peter Fulde and Richard A. Ferrell. Superconductivity in a Strong Spin-Exchange Field. *Physical Review*, 135(3A):A550–A563, 1964.

[137] A. I. Larkin and Yu. N. Ovchinnikov. Inhomogeneous State of Superconductors. *JETP*, 20:762, 1965.

[138] Stephan Arlinghaus and Martin Holthaus. Driven optical lattices as strong-field simulators. *Phys. Rev. A*, 81:063612, 2010.

[139] Immanuel Bloch, Jean Dalibard, and Sylvain Nascimbène. Quantum simulations with ultracold quantum gases. *Nature Physics*, 8(4):267–276, 2012.

[140] R. Blatt and C. F. Roos. Quantum simulations with trapped ions. *Nature Physics*, 8(4):277–284, 2012.

[141] Alán Aspuru-Guzik and Philip Walther. Photonic quantum simulators. *Nature Physics*, 8(4):285–291, 2012.

[142] Andrew A. Houck, Hakan E. Türeci, and Jens Koch. On-chip quantum simulation with superconducting circuits. *Nature Physics*, 8(4):292–299, 2012.

[143] P. M. Paul, E. S. Toma, P. Breger, G. Mullot, F. Augé, Ph. Balcou, H. G. Muller, and P. Agostini. Observation of a train of attosecond pulses from high harmonic generation. *Science*, 292:1689, 2001.

[144] S. Haessler, J. Caillat, W. Boutu, C. Giovanetti-Teixeira, T. Ruchon, T. Auguste, Z. Diveki, P. Breger, A. Maquet, B. Carré, R. Taïeb, and P. Salières. Attosecond imaging of molecular electronic wavepackets. *Nat. Phys.*, 6:200, 2010.

[145] J. Itatani, J. Levesque, D. Zeidler, Hiromichi Niikura, H. Pépin, J. C. Kieffer, P. B. Corkum, and D. M. Villeneuve. Tomographic imaging of molecular orbitals. *Nature*, 432:867, 2004.

[146] Yulian V. Vanne and Alejandro Saenz. Alignment-dependent ionization of molecular hydrogen in intense laser fields. *Phys. Rev. A*, 82:011403, 2010.

[147] E. Dehghanian, A. D. Bandrauk, and G. Lagmago Kamta. Enhanced ionization of the H_2 molecule driven by intense ultrashort laser pulses. *Phys. Rev. A*, 81:061403, 2010.

[148] G. S. J. Armstrong, J. S. Parker, and K. T. Taylor. Double-electron above-threshold ionization resonances as interference phenomena. *New J. Phys.*, 13 (1):013024, 2011.

[149] R. E. F. Silva, P. Rivière, and F. Martín. Autoionizing decay of H_2 doubly excited states by using XUV-pump infrared-probe schemes with trains of attosecond pulses. *Phys. Rev. A*, 85:063414, 2012.

[150] A. Palacios, H. Bachau, and F. Martín. Enhancement and control of H_2 dissociative ionization by femtosecond VUV laser pulses. *Phys. Rev. Lett.*, 96: 143001, 2006.

[151] R. E. F. Silva, F. Catoire, P. Rivière, H. Bachau, and F. Martín. Correlated electron and nuclear dynamics in strong field photoionization of H_2^+. *Phys. Rev. Lett.*, 110:113001, 2013.

[152] L. D. Landau and E. M. Lifshitz. *Quantum Mechanics*. Pergamon Press, Oxford, 1965.

[153] A. M. Perelomov, V. S. Popov, and M. V. Terent'ev. Ionization of atoms in an alternating electric field. *Sov. Phys. JETP*, 23:924, 1966.

[154] A. M. Perelomov and V. S. Popov. Ionization of atoms in an alternating electric field. ii. *Sov. Phys. JETP*, 24(1):207, 1967.

[155] A. M. Perelomov and V. S. Popov. Ionization of atoms in an alternating electric field. iii. *Sov. Phys. JETP*, 25(2):336, 1967.

[156] M. V. Ammosov, N. B. Delone, and V. P. Krainov. Tunnel ionization of complex atoms and of atomic ions in an alternating electromagnetic field. *Sov. Phys. JETP*, 64:1191, 1986.

[157] Heinrich Hertz. Über den Einfluss des ultravioletten Lichtes auf die elektrische Entladung. *Ann. der Phys.*, 267:983, 1887.

[158] Albert Einstein. Über einen die Erzeugung und Verwandlung des Lichtes betreffenden heuristischen Gesichtspunkt. *Ann. der Phys.*, 322:132, 1905.

[159] Maria Göppert-Mayer. Über Elementarakte mit zwei Quantensprüngen. *Ann. der Phys.*, 401(3):273–294, 1931.

[160] P. Lambropoulos. Multiphoton ionization of one-electron atoms with circularly polarized light. *Phys. Rev. Lett.*, 29:453, 1972.

[161] P. Lambropoulos. Topics on multiphoton processes in atoms. *Adv. At. Mol. Phys.*, 12:87, 1976.

[162] P. Agostini, F. Fabre, G. Mainfray, G. Petite, and N. K. Rahman. Free-free transitions following six-photon ionization of xenon atoms. *Phys. Rev. Lett.*, 42:1127, 1979.

[163] Y. Gontier, M. Poirier, and M. Trahin. Multiphoton absorptions above the ionisation threshold. *J. Phys. B*, 13:1381, 1980.

[164] D. B. Milošević, G. G. Paulus, D. Bauer, and W. Becker. Above-threshold ionization by few-cycle pulses. *J. Phys. B*, 39:R203, 2006.

[165] P. Kruit, J. Kimman, H. G. Muller, and M. J. van der Wiel. Electron spectra from multiphoton ionization of xenon at 1064, 532, and 355 nm. *Phys. Rev. A*, 28:248, 1983.

[166] Anne L'Huillier and Ph. Balcou. High-order harmonic generation in rare gases with a 1-ps 1053-nm laser. *Phys. Rev. Lett.*, 70:774, 1993.

[167] T. F. Gallagher. Above-threshold ionization in low-frequency limit. *Phys. Rev. Lett.*, 61:2304, 1988.

[168] P. B. Corkum. Plasma perspective on strong field multiphoton ionization. *Phys. Rev. Lett.*, 71:1994, 1993.

[169] K. J. Schafer, Baorui Yang, L. F. DiMauro, and K. C. Kulander. Above threshold ionization beyond the high harmonic cutoff. *Phys. Rev. Lett.*, 70: 1599, 1993.

[170] M. Lewenstein, Ph. Balcou, M. Yu. Ivanov, Anne L'Huillier, and P. B. Corkum. Theory of high-harmonic generation by low-frequency laser fields. *Phys. Rev. A*, 49:2117, 1994.

[171] Peter Hertel, 2011. Natural units. Lecture notes. Available (January 12th, 2015) at http://www.home.uni-osnabrueck.de/phertel/aps/nunits.pdf.

[172] Friedhelm Serwane, 2011. PhD thesis, University of Heidelberg.

[173] S. Jochim and G. Zürn. private communication.

[174] A. Saenz. On the influence of vibrational motion on strong-field ionization rates in molecules. *J. Phys. B*, 33:4365, 2000.

[175] Yulian Vanne, 2010. PhD thesis, Humboldt University Berlin.

[176] F. N. Fritsch and R. E. Carlson. Monotone Piecewise Cubic Interpolation. *SIAM Journal on Numerical Analysis*, 17(2):238–246, 1980.

[177] L. V. Keldysh. Ionization in the field of a strong electromagnetic wave. *Sov. Phys. JETP*, 20:1307, 1965.

[178] F. H. M. Faisal. Multiple absorption of laser photons by atoms. *J. Phys. B*, 6: L89, 1973.

[179] Howard R. Reiss. Effect of an intense electromagnetic field on a weakly bound system. *Phys. Rev. A*, 22:1786, 1980.

[180] Y. V. Vanne and A. Saenz. Generalized gauge-invariant formulations of the strong-field approximation. *Phys. Rev. A*, 79:023421, 2009.

[181] Zijian Long and Wing-ki Liu. Keldysh theory of strong-field ionization. *Can. J. Phys*, 88:227–245, 2010.

[182] W. Becker, A. Lohr, M. Kleber, and M. Lewenstein. A unified theory of high-harmonic generation: Application to polarization properties of the harmonics. *Phys. Rev. A*, 56:645–656, 1997.

[183] G.A. Evans and J.R. Webster. A high order, progressive method for the evaluation of irregular oscillatory integrals. *Applied Numerical Mathematics*, 23(2):205–218, 1997.

[184] D. Milošević, G. Paulus, and W. Becker. Phase-Dependent Effects of a Few-Cycle Laser Pulse. *Physical Review Letters*, 89(15):7–10, 2002.

[185] Yulian V. Vanne and Alejandro Saenz. Exact Keldysh theory of strong-field ionization: Residue method versus saddle-point approximation. *Phys. Rev. A*, 75:033403, 2007.

[186] P. B. Corkum and Ferenc Krausz. Attosecond science. *Nat. Phys.*, 3:381, 2007.

[187] G. G. Paulus, W. Becker, W. Nicklich, and H. Walther. Rescattering effects in above-threshold ionization: a classical model. *J. Phys. B*, 27:L703, 1994.

[188] Boris Bergues, Matthias Kübel, Nora G. Johnson, Bettina Fischer, Nicolas Camus, Kelsie J. Betsch, Oliver Herrwerth, Arne Senftleben, A. Max Sayler, Tim Rathje, Thomas Pfeifer, Itzik Ben-Itzhak, Robert R. Jones, Gerhard G. Paulus, Ferenc Krausz, Robert Moshammer, Joachim Ullrich, and Matthias F. Kling. Attosecond tracing of correlated electron-emission in non-sequential double ionization. *Nat. Commun.*, 3:813, 2012.

[189] D. Shafir, H. Soifer, B. D. Bruner, M. Dagan, Y. Mairesse, S. Patchkovskii, M. Y. Ivanov, O. Smirnova, and N. Dudovich. Resolving the time when an electron exits a tunnelling barrier. *Nature*, 485:343, 2012.

[190] T. Nubbemeyer, K. Gorling, A. Saenz, U. Eichmann, and W. Sandner. Strong-field tunneling without ionization. *Phys. Rev. Lett.*, 101:233001, 2008.

[191] B. Manschwetus, T. Nubbemeyer, K. Gorling, G. Steinmeyer, U. Eichmann, H. Rottke, and W. Sandner. Strong laser field fragmentation of H_2: Coulomb explosion without double ionization. *Phys. Rev. Lett.*, 102:113002, 2009.

[192] J. McKenna, S. Zeng, J. J. Hua, A. M. Sayler, M. Zohrabi, Nora G. Johnson, B. Gaire, K. D. Carnes, B. D. Esry, and I. Ben-Itzhak. Frustrated tunneling ionization during laser-induced D_2 fragmentation: Detection of excited metastable D^* atoms. *Phys. Rev. A*, 84:043425, 2011.

[193] J. McKenna, A. M. Sayler, B. Gaire, Nora G. Kling, B. D. Esry, K. D. Carnes, and I. Ben-Itzhak. Frustrated tunnelling ionization during strong-field fragmentation of D_3^+. *New Journal of Physics*, 14(10):103029, 2012.

[194] J. Aguilar and J. Combes. *Comm. Math. Phys.*, 22:269, 1971.

[195] E. Balslev and J. Combes. *Comm. Math. Phys.*, 22:280, 1971.

[196] B. R. Junker. Recent computational developments in the use of complex scaling in resonance phenomena. *Adv. At. Mol. Phys.*, 18:207, 1982.

[197] William P. Reinhardt. Complex coordinates in the theory of atomic and molecular structure and dynamics. *Annu. Rev. Phys. Chem.*, 33:223, 1982.

[198] Nimrod Moiseyev. Quantum theory of resonances: calculating energies, widths and cross-sections by complex scaling. *Phys. Rep.*, 302:211, 1998.

[199] Ryan Murray, Wing-Ki Liu, and Misha Yu. Ivanov. Partial Fourier-transform approach to tunnel ionization: Atomic systems. *Physical Review A*, 81(2): 023413, 2010.

[200] Misha Ivanov. Tunnel Ionization Revisited. Available (January 15th, 2015) at http://www.nccr-must.ch/libraries.files/TunnelIonizationTalk4.pdf.

[201] Massimo Rontani. Tunneling theory of two interacting atoms in a trap. *Phys. Rev. Lett.*, 108:115302, 2012.

[202] Johann Förster, Yulian V. Vanne, and Alejandro Saenz. Ionization behavior of molecular hydrogen in intense laser fields: Influence of molecular vibration and alignment. *Phys. Rev. A*, 90:053424, 2014.

[203] M. Uiberacker, Th. Uphues, M. Schultze, A. J. Verhoef, V. Yakovlev, M. F. Kling, J. Rauschenberger, N. M. Kabachnik, H. Schröder, M. Lezius, K. L. Kompa, H.-G. Muller, M. J. J. Vrakking, S. Hendel, U. Kleineberg, U. Heinzmann, M. Drescher, and F. Krausz. Attosecond real-time observation of electron tunnelling in atoms. *Nature*, 446:627, 2007.

[204] Adrian N. Pfeiffer, Claudio Cirelli, Mathias Smolarski, Darko Dimitrovski, Mahmoud Abu-samha, Lars Bojer Madsen, and Ursula Keller. Attoclock reveals natural coordinates of the laser-induced tunnelling current flow in atoms. *Nat. Phys.*, 8:76, 2012.

[205] P. Eckle, A. N. Pfeiffer, C. Cirelli, A. Staudte, R. Dörner, H. G. Muller, M. Büttiker, and U. Keller. Attosecond ionization and tunneling delay time measurements in helium. *Science*, 322:1525, 2008.

Appendices

A Confinement-induced resonances

A.1 Basis sets

In the following the basis sets for the calculation of two atoms with the method specified in Section 3.4 are specified. In all orbital calculations, B splines of the order 8 were used. In the orbital calculation of the rel. motion, a linear-geometric grid (see [81] for details) was used with a knot sequence of 15 a.u. for the linear part including 50 B splines. For the c.m. orbital calculation, the B splines are distributed linearly over the entire box size.

Orbital calculation	
Box size [a.u.]	$\sqrt{12} \cdot 15000$
Rel. motion	
B splines	100
Angular momenta	30
C.m. motion	
B splines	60
Angular momenta	32
Configuration interaction	
Rel. active orbitals	
Number of bound states	2
Total number of states	101
Symmetries	A_g
C.m. active orbitals	
A_g symmetry	41

Table A.1: Basis set No. A.1.

Orbital calculation	
Box size [a.u.]	$\sqrt{12} \cdot 35000$
Rel. motion	
B splines	110
Angular momenta	26
C.m. motion	
B splines	100
Angular momenta	26
Configuration interaction	
Rel. active orbitals	
Number of bound states	2
Total number of states	111
Symmetries	A_g
C.m. active orbitals	
A_g symmetry	41

Table A.2: Basis set No. A.2.

Orbital calculation	
Box size [a.u.]	$\sqrt{12} \cdot 25000$
Rel. motion	
B splines	180
Angular momenta	34
C.m. motion	
B splines	160
Angular momenta	34
Configuration interaction	
Rel. active orbitals	
Number of bound states	30
Total number of states	160
Symmetries	A_g
C.m. active orbitals	
A_g symmetry	80

Table A.3: Basis set No. A.3.

Orbital calculation	
Box size [a.u.]	$\sqrt{12} \cdot 18000$
Rel. motion	
B splines	150
Angular momenta	18
C.m. motion	
B splines	100
Angular momenta	18
Configuration interaction	
Rel. active orbitals	
Number of bound states	20
Total number of states	200
Symmetries	A_g
C.m. active orbitals	
A_g symmetry	50

Table A.4: Basis set No. A.4.

Orbital calculation	
Box size [a.u.]	$\sqrt{12} \cdot 15000$
Rel. motion	
B splines	150
Angular momenta	10
C.m. motion	
B splines	100
Angular momenta	10
Configuration interaction	
Rel. active orbitals	
Number of bound states	2
Total number of states	120
Symmetries	A_g
C.m. active orbitals	
A_g symmetry	30

Table A.5: Basis set No. A.5.

B Few-body algorithm

In the following small but important code excerpts of the few-body FCI code are given to demonstrate the conceptual clarity of key parts of the code. Note, parts of the non-optimized Python version of the code are shown here due to readability. The highly-optimized Cython implementation of the code was used for calculations. The speedup is two to three orders of magnitude. Additionally, basis sets are detailed.

B.1 The coding of the Graph object

```
class Graph(object):
  """ graph object determining vertex weights and arc weights in
  reverse lexical ordering.

  Attention: orbital numbering starts with 0!
  Attention: address starts also with 0!

  """


  def __init__(self, n_orbs, n_electron):
      """
      n_orbs      :       number of orbitals
      n_electron  :       number of electrons
      """
      self.n_orbs = n_orbs
      self.n_electron = n_electron
      self.get_vertex_weights()
      self.get_arc_weights()
      self.get_occupations()

      assert int(binom(self.n_orbs,self.n_electron))
                                  == len(self.occupations)



  def get_vertex_weights(self):
      """ get the vertex weights

      vertices are indexed as a two-dimensional n_orbs+1 x
      n_electron+1 array:

      rows: orbitals
      columns: number of electrons
      """
```

```
        self.vert_weights = np.zeros((self.n_orbs+1,self.n_electron+1),
                                     dtype=np.int32)
        self.vert_weights[0,0] = 1
        for row in xrange(1,self.n_orbs+1):
            for column in xrange(self.n_electron+1):

                if column > row:
                    """ upper triangle is left out """
                    continue
                if row > column+ self.n_orbs - self.n_electron:
                    continue

                if column==0:
                    """check if vertex is allowed"""
                    self.vert_weights[row,column]=
                         self.vert_weights[row-1,column]
                else:
                    self.vert_weights[row,column]=
                         self.vert_weights[row-1,column]
                       + self.vert_weights[row-1,column-1]



    def get_arc_weights(self):
        """ get the arc weights

        arc weigths for vertical arcs. Represented as (n,N) array

        """
        self.arc_weights = np.zeros((self.n_orbs, self.n_electron),
                                    dtype=np.int32)
        for row in xrange(self.n_orbs):
            for column in xrange(self.n_electron):
                if column > row:
                    """ upper triangle is left out """
                    continue
                if row > column+ self.n_orbs - self.n_electron:
                    """ lower part """
                    continue

                self.arc_weights[row,column] =
                    self.vert_weights[row,column+1]



    def address(self, occupation):
        """ get the address of a string given its occupation as, e.g.,
        (0,2,3) means string a^+_0 a^+_2 a^+_3

        Attention: orbital numbering starts with 0!
        Attention: address starts also with 0!
```

```
        occupation : sorted list of creation operators (integers)
        """
        address = 0
        for index in xrange(self.n_electron):
            address += self.arc_weights[occupation[index],index]
        return address



    def get_occupations(self):
        """ return a list of occupations (list of lists) in reverse
        lexical order

        Strategy:
        create all occupations and the sort by address.
        """
        occs = list(itertools.combinations(range(self.n_orbs),
                    self.n_electron))
        occs = sorted(occs, key=lambda occ:self.address(occ))
        self.occupations = occs
```

B.2 The coding of E^{γ}_{pq}

```
def e_pq_on_string(p,q,string):
    """
    apply the excitation operator a^+_p a_q on a string

    This gives new string and a phase factor.

    It must have been checked that q is in string and p is not!
    """

    if q not in string:
        """ annihilate vacuum """
        return 0,0
    if p in string and p!=q:
        """ try to create already occupied orbital which was
        not destroyed """
        return 0,0

    e_pq_string = list(string)
    # determine phase factor
    q_index = e_pq_string.index(q)
    phase_q = (-1)**q_index
    # apply annihilator q and creator p (in place of q)
    e_pq_string[q_index] = p
    # sort to get p in the right place
    e_pq_string.sort()
    phase_p = (-1)**e_pq_string.index(p)

    return phase_p*phase_q, e_pq_string
```

B.3 Basis sets

Gaussian exponents	
s	0.05 0.1 0.3 0.5 0.7 1.0 5.
p	0.05 0.1 0.3 0.5 0.7 1.0 5.
d	0.05 0.1 0.5 1.0 5.
f	0.05 0.1 0.5 1.0 5.

Table B.1: Basis set No. B.1.

Gaussian exponents	
s	0.05 0.1 0.3 0.5 0.7 0.9 5.
p	0.05 0.1 0.3 0.5 0.7 0.9 5.
d	0.1 0.5 1.0

Table B.2: Basis set No. B.2.

C Attoscience quantum simulation

In the following the basis sets for the TDSE calculations of Part III are specified. Moreover the parameters of the Lorentz potentials of the proposed quantum simulator experiment are given that are used throughout the thesis.

C.1 Basis sets

Computation of gradient-free eigenstates	
Box size [n.u.]	800
Number of points	3201
Time propagation	
Number of states	2001
Relative tolerance of ODE solver	10^{-6}

Table C.1: Specification of basis set No. C.1 for the TDSE solution of the quantum simulator.

Computation of field-free eigenstates	
Box size [a.u.]	2000
Number of B splines	4000
Order of B splines	12
Knot sequence	linear
Number of angular momenta l of Y_{lm}	50
Time propagation	
Energy cutoff [a.u.]	10

Table C.2: Specification of basis set No. C.2 for the TDSE solution (performed by Johann Förster) of the 3D hydrogen atom.

Computation of field-free eigenstates	
Box size [a.u.]	800
Number of points	3201
Time propagation	
Number of states	1001
Relative tolerance of ODE solver	10^{-6}

Table C.3: Specification of basis set No. C.3 for the TDSE solution of the soft-Coulomb potential.

Computation of gradient-free eigenstates	
Box size [n.u.]	1200
Number of points	4001
Time propagation	
Number of states	3001
Relative tolerance of ODE solver	10^{-6}

Table C.4: Specification of basis set No. C.4 for the TDSE solution of the quantum simulator.

Computation of field-free eigenstates	
Box size [a.u.]	1200
Number of points	4201
Time propagation	
Number of states	2001
Relative tolerance of ODE solver	10^{-6}

Table C.5: Specification of basis set No. C.5 for the TDSE solution of the soft-Coulomb potential.

Computation of gradient-free eigenstates	
Box size [n.u.]	2500
Number of points	10001
Time propagation	
Number of states	5001
Relative tolerance of ODE solver	10^{-6}

Table C.6: Basis-set specification C.6 for the TDSE solution of the quantum simulator.

C.2 Trap and natural unit specifications

Parameter	Value [n.u.]	Value [S.I. based]
w_0 [n.u.]	0.307	$0.6\,\mu$m
V_0 [n.u.]	156.54	$3.3\,\mathrm{k_b}\,\mu$K
λ	0.544	1064 nm
p	0.02	0.02

Unit	Conversion constant
Length	$1.9559 \cdot 10^{-6}$
Energy	$2.9106 \cdot 10^{-31}$
Frequency	2760.0
Mass	$9.9879 \cdot 10^{-27}$
Charge	$8.7937 \cdot 10^{-16}$

Table C.7: Trap parameters No. C.7 in n.u. and S.I.-based units (upper table) and corresponding conversion constants (lower table) from n.u. to S.I. (multiply the n.u. value with the constant to get S.I. units).

Parameter	Value [n.u.]	Value [S.I. based]
w_0 [n.u.]	0.3915	$1.1\,\mu$m
V_0 [n.u.]	567.858	$5.8\,\mathrm{k_b}\,\mu$K
λ	0.3787	1064 nm
p	0.01	0.01

Unit	Conversion constant
Length	$2.80997 \cdot 10^{-6}$
Energy	$1.41017 \cdot 10^{-31}$
Frequency	1337.2
Mass	$9.98789 \cdot 10^{-27}$
Charge	$8.79365 \cdot 10^{-16}$

Table C.8: Trap parameters No. C.8 in n.u. and S.I.-based units (upper table) and corresponding conversion constants (lower table) from n.u. to S.I. (multiply the n.u. value with the constant to get S.I. units).

Parameter	Value [n.u.]	Value [S.I. based]
w_0 [n.u.]	0.42343	$1.66\,\mu$m
V_0 [n.u.]	1105.3	$5.8\,\mathrm{k_b}\,\mu$K
λ	0.2714	1064 nm
p	0.01	0.01

Unit	Conversion constant
Length	$3.92033 \cdot 10^{-6}$
Energy	$7.2449 \cdot 10^{-32}$
Frequency	687.0
Mass	$9.98789 \cdot 10^{-27}$
Charge	$8.79365 \cdot 10^{-16}$

Table C.9: Trap parameters No. C.9 in n.u. and S.I.-based units (upper table) and corresponding conversion constants (lower table) from n.u. to S.I. (multiply the n.u. value with the constant to get S.I. units).

Parameter	Value [n.u.]	Value [S.I. based]
w_0 [n.u.]	0.655	1.66 μm
V_0 [n.u.]	462.0	$5.8\ \mathrm{k_b}\,\mu$K
λ	0.42	1064 nm
p	0.05	0.05

Unit	Conversion constant
Length	$2.53456 \cdot 10^{-6}$
Energy	$1.73329 \cdot 10^{-31}$
Frequency	1643.6
Mass	$9.98789 \cdot 10^{-27}$
Charge	$8.79366 \cdot 10^{-16}$

Table C.10: Trap parameters No. C.10 in n.u. and S.I.-based units (upper table) and corresponding conversion constants (lower table) from n.u. to S.I. (multiply the n.u. value with the constant to get S.I. units).

Abbreviations

Abbreviation	Description
BEC	Bose-Einstein condensate
rel.	Relative (motion)
c.m.	Center of mass (motion)
CIR	Confinement-induced resonance
MOT	Magneto-optical trap
FWHM	Full width half maximum
HF	Hartree Fock
CI	Configuration interaction
FCI	Full configuration interaction
LOPT	Lowest order perturbation theory
ATI	Above-threshold ionization
REMPI	Resonantly enhanced multiphoton ionization
LG	Length gauge
VG	Velocity gauge
TDSE	Time-dependent Schrödinger equation
SFA	Strong-field approximation
SPM	Saddle-point approximation
a.u.	Atomic units
n.u.	Natural units (of the quantum simulator)
ADK	Ammosov, Delone and Krainov (rate)
FC-ADK	Frequency-corrected Ammosov, Delone, and Krainov (rate)
FTI	Frustrated tunneling ionization
WKB	Wentzel-Kramers-Brillouin (approximation)
OTB	Over the barrier
OTBT	Over-the-barrier threshold

List of Figures

List of Tables

Selbständigkeitserklärung

Ich erkläre, dass ich die Dissertation selbständig und nur unter Verwendung der von mir gemäß §7 Abs. 3 der Promotionsordnung der Mathematisch-Naturwissenschaftlichen Fakultät, veröffentlicht im Amtlichen Mitteilungsblatt der Humboldt-Universität zu Berlin Nr. 126/2014 am 18.11.2014 angegebenen Hilfsmittel angefertigt habe.

Ich habe mich nicht anderwärts um einem Doktorgrad im Promotionsfach Physik beworben und besitze keinen Doktorgrad im Promotionsfach Physik.

Die Promotionsordnung der Mathematisch-Naturwissenschaftlichen Fakultät, veröffentlicht im Amtlichen Mitteilungsblatt der Humboldt-Universität zu Berlin Nr. 126/2014 am 18.11.2014 habe ich zur Kenntnis genommen.

Berlin, 26. September 2015 .....

Acknowledgment

First and foremost I would like to thank my supervisor Alejandro Saenz. He guided me excellent but in the same time allowed me to work independently on my own ideas. I learned a lot from his deep knowledge and far-reaching experience, in scientific means but also in terms of formal matters and writing. I can not stress enough how thankful I am that he proof-read the entire thesis before its submission. Finally, from a personal point of view, the countless hours we worked together during the last years were very enjoyable.
Next, I would like to thank Phillip-Immanuel Schneider and Bruno Schulz for the many illuminating discussions about ultracold topics. I want to give a special thank to Johann Förster who did not only introduce me to the wide field of strong-field physics but was also an excellent contact for technical discussions.
Moreover, I want to thank Selim Jochim, Gerhard Zürn, Thomas Lompe and Andre Wenz. The entire collaboration on coherent molecule formation which had its roots at the DPG spring meeting was a total success.
I want to thank Manfred Mark for the pleasant cooperation and especially for being such patient and with the seemingly endless calculation times for the multi-well systems.
I acknowledge the "Studienstiftung des deutschen Volkes" not only for financial support but also for excellent seminars and meetings that allowed me to get in touch with very fascinating people.
Outside physics, I want to thank my sister for all the warmhearted time. I want to thank my parents. You built the cornerstone for my scientific career. I am infinitely grateful for your unconditional parental love.
Anna, I wish to express my deepest gratitude to you for your expansive support. You were certainly most affected by my time-consuming studies. I could always count on your backup that I needed most in the last months before submission. One hand washes the other.
Although you do not yet understand, I want to thank my children who were both born during the time of this thesis, Johannes and David. Besides turning off unexpectedly the power supply of my computer you are closely connected to this work. The joy you give me is beyond words.